ABSTRACT

Title of Dissertation:	THE IMPACT OF ENGINEERED MECHANICAL CONFINEMENT ON MESENCHYMAL STEM CELL AND LUNG FIBROBLAST MECHANOBIOLOGY
	Mary Teresa Doolin, Doctor of Philosophy, 2020
Dissertation directed by:	Assistant Professor Dr. Kimberly M. Stroka, Fischell Department of Bioengineering

Mechanical cues have been shown to influence cell gene expression, cell protein expression, and cell behaviors critical for homeostasis and disease progression. Cells experience the mechanical cue of confinement *in vivo*, such as within the extracellular matrix, and *in vitro*, such as within tissue engineered scaffolds. Despite its prevalence, the impact of mechanical confinement on cell fate is poorly understood. Cues from the mechanical microenvironment are primarily sensed and responded to by the cytoskeleton, which transmits forces to the nucleus and can thereby alter gene expression. The nucleus itself is also a mechanosensor, sensing external forces and again altering gene expression. Mesenchymal stem cells (MSCs) and lung fibroblasts are known to be sensitive to mechanical forces, yet the effect of mechanical confinement on these cells is unclear.

In this dissertation, we investigated how mechanical confinement induced by engineered microchannels influences MSC morphology and migration. Notably, we

show that confinement alters the relative contributions of cytoskeletal and contractile machinery in MSC migration in unconfined and confined spaces. We next investigated how mechanical confinement induced by microchannels influences MSC and fibroblast nucleus volume. When certain cytoskeletal machinery was inhibited, nucleus volume was altered only in MSCs in wide channels, suggesting diverging roles of the cytoskeleton in regulating nuclear deformation and migration in different degrees of confinement and in different cell types. While performing this work, we observed a lack of assays that provide precise control over the degree of confinement induced on cells, yield a large sample size, enable long-term culture, and enable easy visualization of cells over time. Therefore, we designed, created, and validated a confining micropillar assay that achieves these requirements. Using these confining micropillars, we investigated the effect of confinement on lung fibroblast to myofibroblast transition (FMT), a hallmark of idiopathic pulmonary fibrosis. Cell density was more predictive of FMT than the degree of confinement induced by micropillar arrays. These results improve our understanding of how MSCs and lung fibroblasts respond to confinement, which will aid in the rational design of MSC-based therapies and FMT-targeting therapies.

THE IMPACT OF ENGINEERED MECHANICAL CONFINEMENT ON MESENCHYMAL STEM CELL AND LUNG FIBROBLAST MECHANOBIOLOGY

by

Mary Teresa Doolin

Dissertation submitted to the Faculty of the Graduate School of the
University of Maryland, College Park, in partial fulfillment
of the requirements for the degree of
Doctor of Philosophy
2020

Advisory Committee:
Assistant Professor Kimberly M. Stroka, Chair
Assistant Professor Gregg Duncan
Professor John P. Fisher
Professor Wolfgang Losert
Assistant Professor Giuliano Scarcelli

Personal Acknowledgements

So many people have helped me throughout the making of this dissertation. While I cannot exhaustively thank everyone who has assisted me along the way, I will try.

I would like to thank Dr. Kim Stroka for her endless support, optimism, and mentorship. She has taught me valuable lessons about science, life, and everything in between. I will be happy if I can be a fraction of the wonderful woman she is.

Thank you to Dr. Helim Aranda Espinoza for convincing me that maybe I'm an alright scientist, and for teasing me on a constant basis. Your sense of humor, conversation, and support helped get me through the last year of my PhD.

I would like to thank my lab mates, past and present. Dr. Kelsey Gray for her support and the joy she brought to lab. Dr. Marina Pranda for her sense of humor and diversions throughout the day. Ariana Decastro for being an ideal travel partner and staying grounded when some of us are not so much. Dr. Li Yan for her kind spirit. Rebecca Moriarty for being a true friend, an excellent conversationalist, and an amazing scientist.

I would like to thank all my friends within the department, especially Michelle Bookstaver, Emily Gosselin, and Sarah Van Belleghem for their support and for continuing to be my friends even after living with me for a whole year. Also thank you to my incredible friends Sarah Williams, Molly O'Lena, Sara Goss, Lucy Lee, and Sophie Stypeck for their love and for being the most fun people I know.

I would like to thank my boyfriend's family, of which there are too many to list, who have accepted me into their family with such open arms. Specifically, I would like

to thank Kim, Keith, Glee, Gail, and Austin for their love and support, which includes letting me hang around their house in my pajamas all day while eating all their food.

I would like to thank my parents, Eileen and Len, for being the best role models anyone could ask for. Thank you to my mom for listening to me gripe when I was down and celebrating with me when I was up. Thank you for making me laugh, keeping me sane, always knowing what to say, and being an inspiration. I hope to be as cool of a woman as you are. Thank you to my dad for instilling in me a love of learning, knowledge, and science and for showing me the power of calm and logical thinking. I would never have obtained a PhD if not for his work ethic, support, and guidance, and because I value his opinion so deeply.

I would also like to thank my sister, Tricia, and my brother, Kyle, for always supporting me and being the second best role models anyone could ask for (sorry, Mom and Dad come first, you understand). Thank you to Kyle for being the funniest human I know, always showing me new music and games, and accepting me as I am without question. Thank you to Tricia for showing me how to advocate for myself without shame and showing me that it is possible to be smart, sophisticated, and a complete goofball. Also thank you to their partners, Jess and Anthony, for being so kind and fun and for not judging our family (at least not out loud).

Finally, I would like to thank my boyfriend and best friend, Brandyn Mark, for being my partner through this whole journey. He makes me laugh every day and helps me put things in perspective. Thank you for taking care of me when I was too busy to do it myself. Thank you for encouraging me, listening to me, and making sure I relax

and have fun. Thank you for doing all of this while working hard and going to school yourself. Your perseverance in achieving your goals inspires me.

Oh, and thank you to my cat Farrah, for sitting on my laptop whenever I need to be productive and running away whenever I need to pet you. At least you're cute.

Scientific Acknowledgements

I would like to thank and acknowledge the following:

- Dr. Kim Stroka for her mentorship and feedback regarding results, data analysis, manuscript editing, and data presentation.
- My committee members Dr. John Fisher, Dr. Gregg Duncan, Dr. Giuliano Scarcelli, and Dr. Wolfgang Losert for their continued support and feedback.
- The University of Maryland Imaging Core Facility for providing resources for confocal imaging.
- The BioWorkshop core facility in the Fischell Department of Bioengineering at the University of Maryland for confocal microscope, plate reader, and gel imager resources.
- The Maryland NanoCenter at the University of Maryland: its FabLab for providing photolithography resources and its AIMLab for providing SEM resources.

Chapter 2

- Rebecca Moriarty for co-authoring several sections in this chapter.

Chapter 4

- Thea Ornstein for her work on setting up experiments, imaging cells, and co-authoring the introduction and methods of this section.

Chapter 5

- Dr. Sz-Chian Liou for his assistance with sample preparation and acquisition of SEM images.

Chapter 8

- Katelyn Kunert for her work on experiments and analysis of MSCs treated with Trichostatin A.
- Dr. Daniel Conway for providing the adenovirus and lentivirus DN-KASH constructs and continued support in its use.
- Dr. Alexander Dunn and Steven Tan for providing the FRET tension sensor and consistent support in its use.

Funding sources

- University of Maryland
    - Graduate School Summer Fellowship
    - Graduate School Jacob K. Goldhaber Travel Awards
- BMES Student Travel Award
- NIH (NHLBI) F31 Fellowship #F31HL145991

Table of Contents

List of Tables

List of Figures

List of Abbreviations

AFM – atomic force microscopy

CSC – cancer stem cell

ECM – extracellular matrix

FMT – fibroblast to myofibroblast transition

FA – focal adhesion

FBS – fetal bovine serum

FRET – Förster resonance energy transfer

HDAC – histone deacetylase

HLF – human lung fibroblast

IPF – idiopathic pulmonary fibrosis

KASH - Klarsicht, ANC-1, Syne homology

LAD – lamina-associated domain

LINC – linker of the nucleoskeleton and cytoskeleton

MMP – matrix metalloproteinase

MSC – mesenchymal stem cell

MSC-CM – mesenchymal stem cell-conditioned media

MRTF-A – Myocardin Related Transcription Factor A

NMMII – non-muscle myosin II

PBS – phosphate-buffered saline

PDMS – polydimethylsiloxane

PEG – polyethylene-glycol

ROCK – Rho-associated protein kinase

RGD – Arginylglycylaspartic acid

SMA – smooth muscle actin

SUN – Sad1 and UNC-84

TGF-β – transforming growth factor-β

TSA – Trichostatin A

YAP/TAZ – Yes-associated protein/transcriptional co-activator with PDZ-binding motif

Chapter 1: Introduction

Mechanical cues such as stiffness and shear stress have been shown to influence cell gene expression, cell protein expression, and cell behaviors critical for homeostasis and disease progression [1], [2]. Cells physically attach to extracellular matrix (ECM) components via focal adhesions, which consist of integrins and associated helper proteins, and focal adhesions subsequently attach to the intracellular cytoskeleton [3]. The cytoskeleton, which consists of actin filaments, microtubules, and intermediate filaments, is a critical component of a cell's mechanosensing machinery [4]. The cytoskeletal network transmits mechanical forces to the nucleus via the linker of the nucleoskeleton and cytoskeleton (LINC) complex, which can thereby alter gene expression [5]. The nucleus itself is also a mechanosensor, sensing external forces and altering gene expression directly [6].

Investigation of cell mechanosensing and ECM mechanics has led to advancements in almost all facets of bioengineering, including regenerative medicine and drug development. Consideration of the mechanical microenvironment has led to improved scaffolds for tissue engineering [7]. Additionally, several drugs targeting ECM stiffness have been approved to treat a variety of pathologies [8]. In addition to stiffness, cells experience the mechanical cue of confinement *in vivo*, such as within the ECM, and *in vitro,* such as within tissue engineered scaffolds. For example, cells may be confined within channels between connective tissue and the basement membrane of muscle, nerve and epithelium [9], [10], during cell intravasation and extravasation [11],

in the tumor microenvironment [12], and in interstitial tissue [13]. Despite its prevalence, the impact of mechanical confinement on cell fate is poorly understood.

Mesenchymal stem cells (MSCs) are multipotent cells found within adult tissues, such as the bone marrow [14]. MSCs are increasingly studied due the myriad of beneficial properties they possess [15]. MSCs can differentiate into other cell types, potentially aiding in tissue regeneration, and they can secrete immunomodulatory factors, potentially aiding in the treatment of several pathologies [16]. Despite their extreme promise, very few MSC-based therapies have gained clinical approval [17]. In part, this is a result of the inability to precisely control MSC behavior, due to the lack of fundamental knowledge regarding how MSCs respond to various mechanical microenvironments, including mechanical confinement.

Idiopathic pulmonary fibrosis (IPF) is one such disease where MSCs are being used as a potential therapy [18], [19]. IPF is a deadly disease, with an average mortality rate after diagnosis of 3-5 years and with no effective treatments currently available [20]. This highlights a basic lack of understanding regarding IPF progression. IPF is believed to be caused and perpetuated by a rampant inflammatory response within the lung, and it is characterized by fibroblastic foci consisting of dense ECM, fibroblasts, and myofibroblasts [21]. Myofibroblasts are contractile, ECM producing cells that contribute heavily to IPF progression [22]. These cells are largely not present in healthy lung tissue, but originate from the fibroblast to myofibroblast transition induced by factors such as inflammation and increased tissue stiffness [23], [24]. As myofibroblasts persist within the lung interstitial tissue, they deposit ECM that induces a higher degree of confinement on lung fibroblasts.

The overall goal of this dissertation is to investigate the impact of engineered mechanical confinement on mesenchymal stem cell and lung fibroblast mechanobiology in order to improve mesenchymal stem cell-based therapies and improve our understanding of idiopathic pulmonary fibrosis. We use two forms of engineered mechanical confinement: a confining microchannel assay and a confining micropillar assay (Fig. 1.1). We subsequently use these assays to investigate MSC migration, morphology, and nucleus volume as well as the lung fibroblast to myofibroblast transition (FMT).

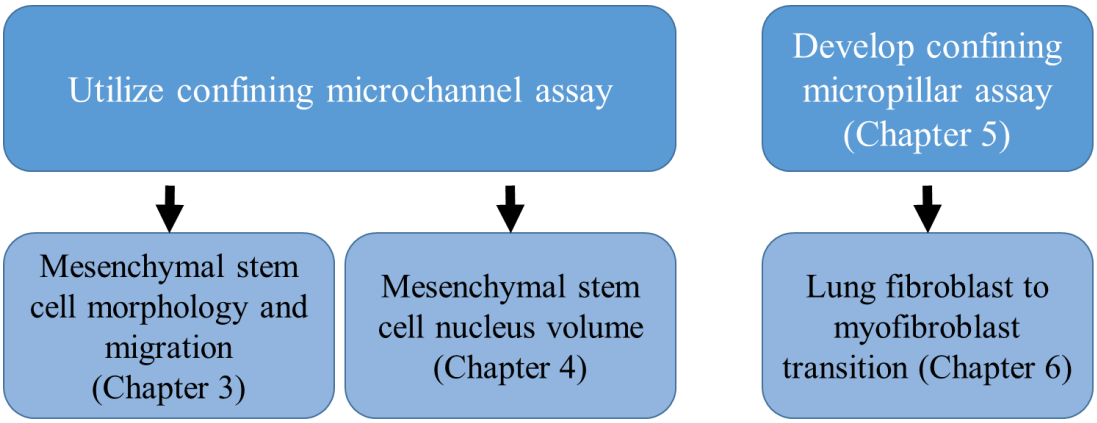

Figure 1.1 Dissertation overview.

In this dissertation, we investigated how mechanical confinement induced by engineered microchannels influences MSC morphology, migration efficiency, and migration mechanism (Chapter 3). In this chapter, we systematically varied the degree of confinement experienced by MSCs using a collagen-coated polydimethylsiloxane (PDMS)-based microfluidic device which was previously designed and characterized [25], [26]. The microchannels are 10 μm tall and of varying widths (3, 6, 10, 20, and 50

μm). These dimensions are representative of pores found *in vivo*, such as within capillaries and ECM microtracks [27], [28], and *in vitro*, as in tissue engineered scaffolds. We found that MSC migration speed is modestly biphasic as a function of microchannel width, and inhibitors of various cytoskeletal machinery affect MSC differently in confining microchannels compared to wider microchannels (Chapter 3). These results improve our mechanistic understanding of the mechanobiology of stem cell migration and outline the cytoskeletal and contractile machinery that contribute to migration in confined and unconfined microenvironments.

We next investigated how mechanical confinement induced by microchannels influences MSC and fibroblast nuclear volume (Chapter 4). In this chapter, we characterized the 3D morphology of nuclei within various cell types in response to physical confinement induced by the same microchannels used in Chapter 3. MSCs and L929 cells were chosen for experimentation due to their differences in 2D nuclear morphology in response to confinement. Our results suggest that cell identity may possess a larger role in governing nuclear deformation than the force of confinement alone (Chapter 4). When certain cytoskeletal machinery was inhibited, nuclear deformation was altered only in MSCs in wide channels, suggesting diverging roles of the cytoskeleton in regulating nuclear deformation and migration in different degrees of confinement and in different cell types.

While performing the work reported in Chapters 3 and 4, we observed a lack of assays that provide precise control over the degree of confinement induced on cells, yield a large sample size, enable long-term culture, and enable easy visualization of cells over time. Therefore, we designed, created, and validated a confining PDMS-based

micropillar assay that achieves these requirements (Chapter 5). The data show that MSCs alter their cell and nucleus morphology in response to confinement induced by micropillars. Furthermore, it appears that MSCs may alter their migration mode based on the degree of confinement experienced or by the mere existence of micropillars (Chapter 5). This micropillar assay will provide new fundamental information about cellular mechanobiology in response to physical confinement.

Using the confining micropillar assay designed in Chapter 5, we investigated the effect of confinement on lung fibroblast to myofibroblast transition (FMT), a hallmark of IPF (Chapter 6). Cell density was more inductive of FMT than the degree of confinement induced by micropillar arrays (Chapter 6). Ultimately, the results presented herein improve our understanding of how MSCs and lung fibroblasts respond to confinement, which will aid in the rational design of MSC-based therapies and FMT-targeting therapies.

Chapter 2: Background[1]

2.1 Mesenchymal stem cells

Mesenchymal stem cells (MSCs) are generally defined as cells that can self-renew or generate cells of a different lineage, also defined as multipotent. The definition of MSCs is a topic of ongoing debate, but the most widely accepted definition is laid out by the International Society for Cell Therapy [29]. This definition includes that MSCs be plastic adherent, be able to differentiate into osteoblasts, chondrocytes, and adipocytes *in vitro,* and that MSCs be positive for a set of surface markers and negative for a different set of surface markers [29]. MSCs can be isolated from a variety of different sources, most commonly from bone marrow [30].

MSC have many properties that make them attractive for cell-based therapies. These properties include immunomodulatory paracrine activity, immunomodulation via cell-cell contact, and the ability to differentiate and integrate into a host tissue [15]. Due to these attractive properties, MSCs are increasingly involved in clinical trials, where they are slowly progressing [31]. Since 2015, 6% of all MSC-based clinical trials were in stage 3 [17], [31]. This is in contrast overall drug development, where 10.8% of all trials are in stage 3 [32], [33], but similar to oncology drugs, where 4.9% of trials are in phase 3 [33]. Despite extremely promising pre-clinical results, there are only 3 clinically approved MSC-based therapies [31]. The scarcity of approved MSC-based therapies to

[1] Includes sections adapted from M.T. Doolin*, R.A. Moriarty*, and K.M Stroka, Mechanosensing of Physical Confinement by Mesenchymal-Like Cells, Frontiers in Physiology 11:365 (2020) (* indicates co-first author).

date can be attributed to many factors, including the complex regulatory landscape, variability in MSC dosing, and variability in MSC maintenance [34]. Additionally, there exists a basic lack of knowledge concerning MSCs and how they respond to their microenvironment. It is critical to continue investigation into how the MSC microenvironment influences MSC behaviors in order to ultimately develop off-the-shelf MSC-based therapies.

Biochemical factors have been known to influence stem cell differentiation for several decades, but the role of mechanical cues in MSC differentiation is a more recent field of investigation. In 2006, substrate stiffness was shown to alter MSC lineage commitment in a seminal paper for the stem cell mechanobiology field [1]. This sparked the notion that mechanical cues need to be considered when using MSCs. Subsequently, MSCs have been shown to respond to shear stress, adhesion size and pattern, topography, strain, and other mechanical forces by altering their lineage commitment, migration, cytoskeletal arrangement, and other phenotypes [35]–[39]. Much of the preliminary stem cell mechanobiology work to date was performed on 2D surfaces. However, scientists have begun to unearth the effects of a 3D confining microenvironment on MSCs. An overview of how MSCs respond to mechanical confinement is reviewed in section 2.3 of this chapter. In Chapters 3 and 4, we investigate how mechanical confinement influences MSC migration efficiency, migration mechanism, and nucleus volume.

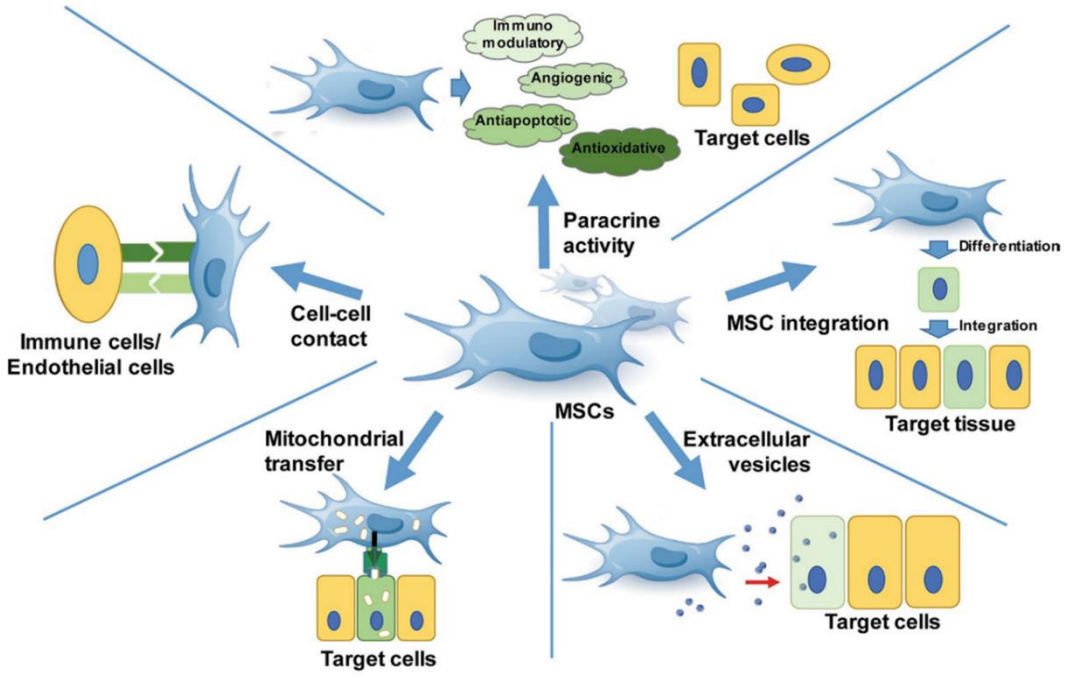

Figure 2.1 Mesenchymal stem cells have a myriad of properties that may be harnessed for use in therapies. Image adapted from [15].

2.2 Idiopathic pulmonary fibrosis

2.2.1 Introduction to idiopathic pulmonary fibrosis

Idiopathic pulmonary fibrosis (IPF) is a chronic disease of the lung characterized by the differentiation of resident fibroblasts into contractile myofibroblasts that deposit excessive extracellular matrix (ECM) [21]. There are no effective treatments for IPF, and the median survival time after diagnosis is approximately 3 years [40]. Tissue explanted from lungs diagnosed with IPF is stiffer than healthy lung tissue, due to the increased protein content of the ECM and altered collagen crosslinking [41], [42]. Additionally, the protein content of the ECM changes with disease progression. For

example, lung tissue from early stage IPF is typically dominated by collagen III, but the majority of late stage ECM protein content is collagen I [43]. Concomitant with increased ECM deposition and crosslinking, there is increased confinement experienced by cells. In Chapter 6, we examine how confinement influences the fibroblast to myofibroblast transition, a key aspect of IPF progression.

A characteristic feature of IPF is the presence of fibroblastic foci within the lung, which consist of activated fibroblasts and myofibroblasts [41]. Myofibroblasts are contractile, ECM depositing cells that express α-smooth muscle actin (α-SMA) in association with f-actin stress fibers. Although the origin of myofibroblasts in IPF is debated, there is evidence that resident fibroblasts can differentiate into myofibroblasts when given certain physical and/or chemical cues [44]. It has been shown that fibroblasts cultured on stiff substrates are more likely to differentiate into myofibroblasts than those on soft substrates, due to increased actomyosin contractility [44]. Concomitantly, stiff matrices encourage stress fiber formation within cells, which compress the nucleus [45]. However, it is unknown to what degree direct nuclear compression in the absence of increased actomyosin contractility alters fibroblast phenotype. In Chapter 6, we investigate how mechanical confinement, which induces high nuclear compression with low actomyosin contractility, affects FMT.

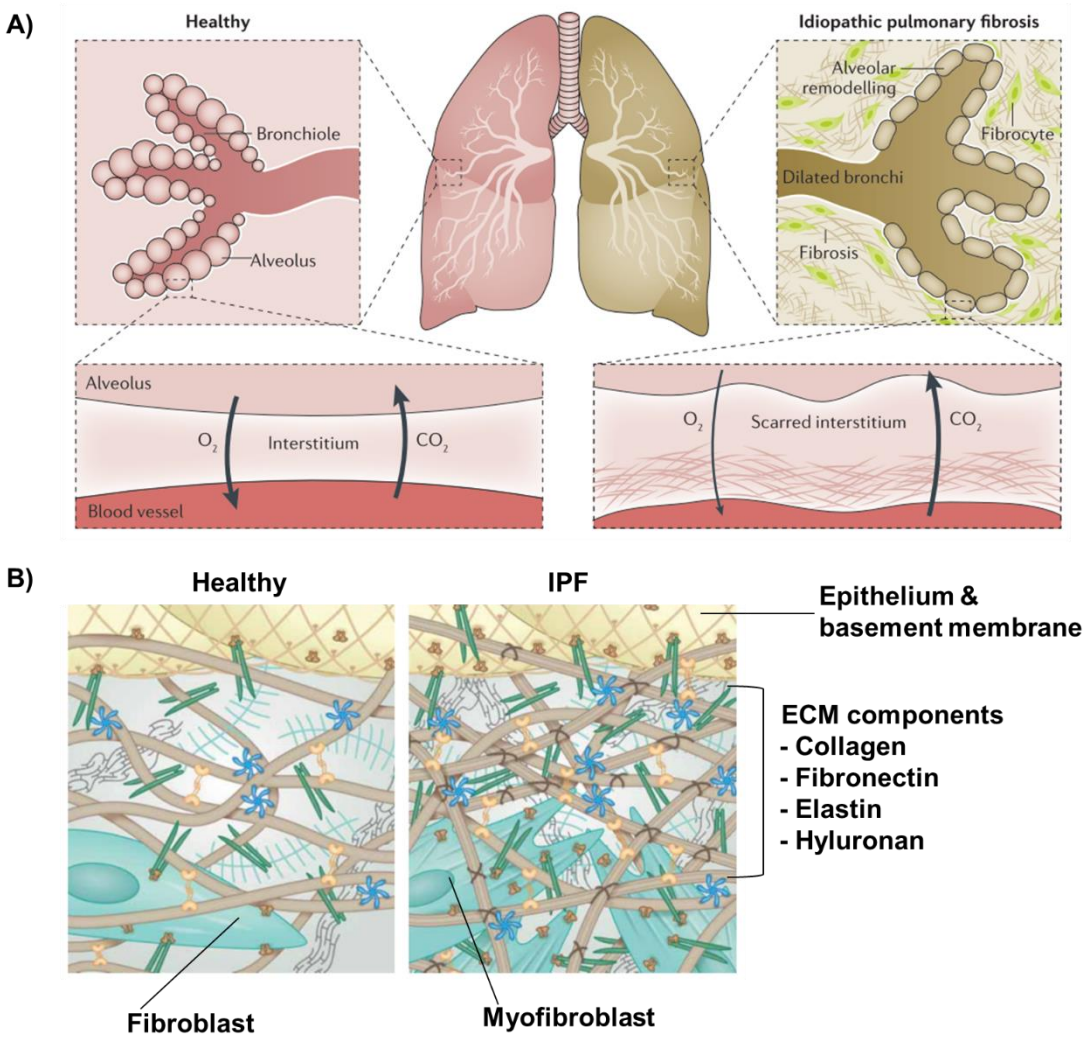

Figure 2.2 Idiopathic pulmonary fibrosis. A) IPF damages alveoli and impairs lung function. Image adapted from [21]**. B) IPF is characterized by increased ECM deposition by myofibroblasts. Image adapted from** [41]**.**

2.2.2 Mechanosensing in FMT

Lung fibroblasts respond to mechanical cues in their microenvironment through several pathways. Fibroblasts cultured on stiff substrates are more likely to differentiate into myofibroblasts than those on soft substrates, with increased

actomyosin contractility playing an important role in this process [44], [46]. Stiffness may induce FMT through the activation of signal transducer and activator of transcription 3 (STAT3) and megakaryoblastic leukemia 1 (MKL1) via Rho/Rho-associated protein kinase (ROCK) and Janus kinase 2 (JAK2) signaling pathways [47], [48]. Indeed, both ROCK isoforms, ROCK1 and ROCK2, play a role in FMT [49]. Conversely, hypoxia reduces FMT through RhoA activity [50]. Transforming growth factor (TGF)-β1 is commonly used to induce FMT, and TGF-β1 treated fibroblasts display "supermature" focal adhesions atop ED-A fibronectin, supporting the highly contractile myofibroblast phenotype [51]. Fibroblasts are not only mechanosensitive to stiffness, but to strains. Cyclic mechanical loading comparable to that induced on cells *in vivo* by breathing reduces α-SMA expression in lung fibroblasts, potentially due to reduced autocrine TGF-β1 secretion [52]. In Chapter 6, we begin to investigate mechanosensing of lung fibroblasts in response to cell density and mechanical confinement.

2.2.3 Mesenchymal stem cell therapies for IPF

The number of registered clinical trials involving MSCs is growing rapidly, and nearly tripled from 2011 to 2015 [17], [53]. In the case of IPF, MSC injection is being targeted as a prospective therapy [54]. Several pre-clinical trials have proved MSCs effective in ameliorating inflammation and fibrosis, motivating the initiation of clinical trials [18], [55]. However, other studies indicate that MSC therapy worsens outcome, particularly in late stage IPF [19]. Less than 1% of all injected MSCs remain in the body one week after systemic injection, suggesting a paracrine mechanism of action [56].

Accordingly, secreted factors derived from MSCs have been shown to block fibroblast differentiation into myofibroblasts [57]. In Chapter 6, we investigate how confinement may affect MSC paracrine activity and if MSC secreted factors influence FMT.

2.3 Confinement

2.3.1 Clinical relevance of confinement

Biochemical cues are well known to influence stem cell differentiation [58], [59]. However, in the past decade or so, researchers have determined that mechanical signals are similarly important in specifying stem cell fate [1], [36], [60]–[62]. One such mechanical cue is confinement, which cells experience in tissues *in vivo* as well as in tissue engineered constructs and laboratory assays [63]. Confinement can significantly impact a multitude of cell behaviors. For example, a variety of cell types such as fibroblasts, cancer cells, and epithelial cells, can migrate via different mechanisms in response to a confined microenvironment [64]–[67].

The use of MSCs in clinical trials increased approximately four-fold from 2011 to 2016, yet there are only 3 clinically approved MSC-based therapies [31]. Despite the extreme promise of MSC-based therapies, a major limitation in the field of regenerative medicine is the ineffectiveness in directing MSCs to target tissues following injection into a patient [68]. Furthermore, direct control over stem cell fate *in vivo* is still difficult to achieve [69]. Within the past decade, it has been shown that mechanical cues can direct stem cells down a particular lineage. The effect of mechanical cues such as

stiffness, shear stress, and loading on stem cell fate have been investigated, but research on the effects of confinement on stem cell fate is still in its early stages [1], [70].

Stem cells experience mechanical confinement during the homing process *in vivo* as they migrate through endothelial barriers and tissues towards a target, and also *in vitro* during integration into engineered scaffolds [71]. Stem cell homing has been defined as the arrest of stem cells on the vasculature, followed by transmigration across the endothelium; this process is critical to the function of both native stem cells and stem cells delivered systemically as therapy [14]. When administered locally, MSCs are implanted in close proximity to the target site and may migrate through extracellular matrix or along epithelial surfaces towards the target [72]. When administered intravenously, stem cells extravasate from the blood vessel towards the target site, and subsequently through extracellular matrix [73]. In both cases, stem cells experience mechanical confinement as they migrate across endothelial barriers, through tissues, and towards a target. Indeed, MSCs have been shown to transmigrate through pores of 1-2 μm diameter within the endothelial monolayer both transcellularly and paracellularly [74]. Furthermore, MSCs are commonly integrated into tissue engineered scaffolds, which likely impose varying degrees of confinement on the cells, depending on scaffold porosity and architecture [71]. Understanding how MSCs respond to confinement could allow for improved systemic and localized stem cell therapies, as well as improved regenerative therapies. It is possible that physical confinement, in combination with other microenvironmental cues, can be optimized to engineer stem cells for use in regenerative therapies or as anti-inflammatory agents.

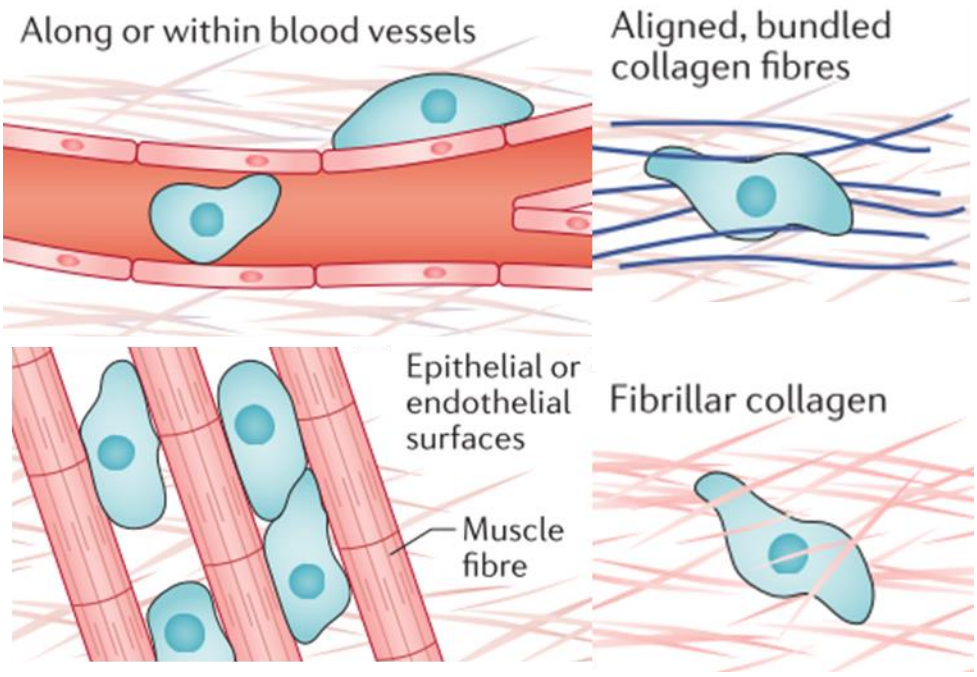

Figure 2.3 Cells experience confinement *in vivo*. Adapted from [12].

2.3.2 Mechanosensing of confinement

In the past two decades, there have been significant strides in understanding how cells sense mechanical forces in 2D environments, and the field is now moving towards understanding mechanosensing in 3D environments. To attach to a 2D substrate, cells form nascent adhesions which may mature to focal adhesions or disassemble [75]. Traction forces are generated as cells adhere to a substrate and contract via actomyosin, thereby moving the cell forward [76]. Traction forces are highly dependent on, or inter-linked with, actin dynamics, cell morphology, and cell migratory state [76], all of which may be altered by confinement. For example, MSC spreading, proliferation, and migration are suppressed when cells are not able to build up sufficient tension on non-deformable collagen gels [77]. Not only do traction forces inform cell migration, but

traction forces have been shown to ultimately influence MSC differentiation [78], [79]. Hence, if MSC traction forces are also reduced in confinement, there may be profound effects on cell behaviors.

Within polyethylene glycol (PEG) hydrogels, fibroblasts interrogate the 3D matrix via strong inward traction forces near the ends of long, slim extensions [80]. Additionally, fibroblast adhesions to 3D matrices are much more stable over time than adhesions to 2D matrices [81], and 3D adhesions can be distinct from 2D adhesions in phosphorylation of focal adhesion kinase [82]. Integrin clustering appears to be more important than stiffness for MSC differentiation in 3D hydrogels [78], though tuning the hydrogel's mechanical properties towards faster relaxation promotes enhanced MSC spreading, proliferation, and osteogenic differentiation in 3D [83]. Diffuse focal adhesions have previously been correlated with different lineage selection preferences in collagen hydrogels [77].

Despite their diffuse appearance, these focal adhesion proteins still play a role in protrusive and matrix deforming activity [84], and are found in regions of curvature or edges [85], for instance, as cells begin to enter confinement. During these protrusive events, α4β1 integrins engage with paxillin to drive myosin II-mediated contractility [65]. Increased membrane tension, as may be observed in confinement, compresses the lamellipodium and subsequently aligns focal adhesions in fibroblasts [86]. Increased membrane tension also inhibits SCAR/WAVE complex recruitment and RAC activation, which inhibits protrusion and leading-edge signals in migrating neutrophils [87]. Hence, although in some situations focal adhesions appear more diffuse and punctate in confinement, reportedly leading to lower cell traction forces, these protein

complexes still seem to play an important role in cellular mechanosensing of the physical environment, albeit in a possibly different manner than the classical 2D model. Doyle and Yamada provide an excellent comprehensive review on cell mechanosensing in 3D microenvironments [88].

2.4 The cytoskeleton response to confinement

Typically, a force experienced by a cell at its membrane is transmitted to the cell's cytoskeleton. Physical alterations of boundaries around MSCs influence actin filaments, focal adhesions, and cell contractility [85]. Actin stress fiber formation is enhanced in MSCs of intermediate volume with sharp edges, possibly due to the increased concentration of RhoA and Arp 2/3 [85]. Conversely, MSCs and carcinoma cells within microchannels show diffuse actin and microtubule structures that polarize to the leading and lagging edges of the cell [26], [64]. A well-known mechanosensitive ion channel is the Piezo1 Ca^{2+} gated ion channel, which can respond to both external and internal stimuli to alter Ca^{2+} levels in the cell. Mechanical stresses induced by confinement in Chinese hamster ovary cells lead to increases in intracellular calcium levels via increased tension activation of the Piezo1 stretch-activated cation channel, kick starting a feed-forward signaling loop to drive the phosphodiesterase type 1-dependent suppression of protein kinase A [89] and possibly enhancing myosin II activity. It is also interesting to note that in the context of stem cells, Piezo 1 can direct lineage specific differentiation in neural stem cells, and an increase in its activity on stiff substrates can drive increased Ca^{2+} intracellular levels leading to increased neuronal lineage differentiation [90]. The actin cytoskeleton reorganizes in response to

physical barriers, partially due to blocking of the membrane transport protein EphA2 [91], and in coordination with loss of linear, mature focal adhesions [26], [92]. Remodeling of the cytoskeleton also takes place during epithelial-to-mesenchymal transition, when cells adopt a more vimentin-based than keratin-based composition [93]. Vimentin is critical for coupling to myosin to generate adhesion and traction forces [94], whereas keratin aids in cell to cell adhesions common in epithelial cells [95]. Furthermore, accumulation of Yes-associated protein/transcriptional co-activator with PDZ-binding motif (YAP/TAZ) in the cytosol, as opposed to the nucleus, is seen in cells that have undergone actin remodeling during ciliogenesis [96], shedding light on yet another possible mechanosensing mechanism for confined cells.

The cytoskeletal reorganization observed in confinement can also be driven by protein kinase C inhibition, which was shown to attenuate migration in conjunction with retinoic acid [97]. Additionally, organelle positioning, which may vary in confinement, can regulate cell behaviors. For example, nuclear position can be a key factor in determining when a fibroblast undergoes fast or slow migration [98]. Anterior localization of mitochondria in confined environments, via rhoGTPase-1 trafficking on microtubules, ahead of the nucleus in the direction of cell migration, increases cell velocities and directional persistence [99].

2.5 The nucleus response to confinement

The nucleus is a dynamic organelle, with its volume changing in response to altered extracellular environments [100]. Nuclei from a variety of cell types have the capacity to deform in an anisotropic manner in response to applied force from an atomic

force microscope tip [101]. Environmental radii of less than 7 μm seem to be the threshold for nucleus remodeling [102], [103], though this value likely depends on unconfined nuclear size. The nucleus as a mechanosensor has previously been reviewed extensively [104], [105], and it is likely that nuclear deformation is a critical pathway for cell mechanosensing of physical confinement.

Lamin A/C, a protein in the nuclear lamina that supports the nuclear envelope, has been shown to play a critical role in the successful migration of cells in confinement [106]. It was demonstrated that in stem cells, low nuclear stress promotes lamin A/C degradation and turnover, while cytoskeletal stress and tension promote lamin A/C maintenance [107]. This pathway acts through myosin contractility and turnover, and it ultimately influences gene expression [107]. Lamin A/C overexpression has been shown to increase the degree of anisotropic nuclear deformation in response to an applied force, underscoring its importance in nuclear mechanics and response to external forces [101]. Nuclear envelope rupture due to actin bundle accumulation at areas of low lamin A levels causes nuclear compression or stretching [108]. This compression or stretch leads to herniation of chromatin or double stranded DNA breaks, but the nuclear envelope integrity is restored by endosomal sorting complexes required for transport III (ESCRTIII), a membrane remodeling protein, rapidly after cells clear confinement [13], [109]. This process has also been modeled extensively during transmigration studies [110].

Lamins and the cytoskeleton can transmit mechanical forces between each other via the linker of the nucleoskeleton and cytoskeleton (LINC) complex. The LINC complex consists of KASH-domain proteins, which reside in the outer nuclear

membrane, and SUN-domain proteins, which reside in the inner nuclear membrane [111]. KASH-domain proteins include nesprin -1, -2, -3, and -4 which each contain binding sites for one or two cytoskeletal elements, and SUN-domain proteins include the commonly expressed Sun1 and Sun2, as well as the testis-specific Sun -3, -4, and -5. [112]. Microtubules link to Dynein/Lis1, which connect to members of the LINC complex (nesprin to SUN to lamin A) to transmit forces across the nuclear membrane [113]. In addition, nesprin-2 works synergistically with non-muscle myosin IIB to transmit forces to the nucleus [114], [115].

Disruption of the LINC complex prohibits cells from responding to low magnitude vibrations, further indicating the LINC complex as a critical component of the MSC mechanosensing machinery [116]. In line with this, transfer of strain from the cytoskeleton to the nucleus via the LINC complex has been shown to be essential for stretch-induced activation of the YAP/TAZ pathway [117], and nuclear localization of YAP/TAZ is increased in confined MSCs [85]. The YAP/TAZ mechanotransduction pathway plays a fundamentally important role in regulating gene expression and MSC differentiation and seems to present differently in different confined environments and cell types. The nuclear lamina interacts with the genome via lamina associated domains (LADs), controlling the location and accessibility of the genome [118]. In fact, lamin A/C deficient cells have defective gene transcription regulated by NF-κB in response to mechanical strain [119]. This is particularly important to MSCs, as their differentiation is responsive to NF-κB [120].

In addition to lamin A/C, confinement has been shown to alter chromatin dynamics. When confined to 2 μm diameter pores, cancer cells show nuclei with ~100%

chromatin and ~0% mobile proteins like those involved in DNA repair or nucleases, yet mobile proteins move into the nucleus unhindered when cells encounter 8 μm diameter pores [121]. Both the cytoskeleton and nucleoskeleton have been shown to control chromatin dynamics within the nucleus. In one study, confined, isotropic cells contained lower lamin A/C levels and more dynamic heterochromatin foci [122]. Conversely, polarized, elongated cells generated higher stress on the nucleus, had higher lamin A/C levels, and had less dynamic heterochromatin foci [122]. These results have been confirmed by others who have shown that loss of lamin A/C leads to increased chromatin dynamics [123].

Histone acetylation patterns may also be affected by confinement. Nuclear levels of histone deacetylase 3 (HDAC3) were lower in cells with intermediate volume (3600-4800 μm^3), and higher when actomyosin contractility was inhibited with blebbistatin [85]. Stiffer embryonic stem cell nuclei with higher lamin A/C content have decreased histone H3 acetylation, which is correlated with increased f-actin levels and increased nuclear localization of myocardin-related transcription factor A (MRTF-A) [124]. MRTF-A, in turn, influences MSC differentiation by helping to maintain homeostasis in MSC osteogenesis and adipogenesis [125]. Nuclear confinement leads to alteration of around 180 genes, including increased expression of histones 4 and 3 [126]. Disruption of chromatin structure via chromatin decondensation can decrease fibroblast mechanosensitivity and dampen the anisotropic deformation of nuclei in response to an applied force [101]. In summary, the structure and composition of the LINC complex, nuclear lamina, and nuclear contents can be altered by mechanical confinement, and may subsequently alter gene expression.

The nucleus is the largest organelle in the cell and is generally the stiffest organelle [127]. Consequently, nuclear passage into a pore is widely regarded as the rate limiting step in migration through confinement [127]. The steric hindrance presented by the nucleus is not trivial, and it has been shown that cell migration is inhibited in cells with larger nuclei [128]. Specifically, migration is arrested in various cell types when trying to migrate through a pore that is less than 10% the size of their nuclear cross section [129]. It should be noted that the nucleus does not get through a constriction without help. In dendritic cells, it has been shown that Arp2/3 nucleated actin accumulates at the portion of nucleus inserted into a constriction, allowing actin to compress the nucleus further and allow further entry into a pore [130]. Similarly, non-muscle myosin (NMM) -IIA and –IIB have been shown to play differential roles in cancer cell invasion, with NMMIIA facilitating cell protrusion and NMMIIB facilitating nuclear translocation through small pores [114]. Migration through small constrictions has lasting effects on the nucleus, as Harada et al. showed that the MSC nucleus deforms irreversibly after migration through small pores, due to its high lamin A: lamin B ratio [131]. Nuclear positioning within the cell has also been suggested to impact migration speed [98]. It has been demonstrated that the nucleus is a key factor in determining when a fibroblast undergoes undergo periods of fast, persistent migration or periods of slow, random migration [98]. While the actin cap is intact, the nucleus translocates and the cell moves quickly and persistently. However, when the actin cap is dissolved, the nucleus rounds and rotates, during which the cell slows and moves randomly [98]. Motivated by the importance of the nucleus to cell migration and cell mechanosensing, we investigate how confinement alters nucleus volume in Chapter 4.

2.6 Cellular confinement assays

Cells experience confinement in many different environments, whether in the context of *in vitro* or *in vivo* assays, and to many different degrees. As a result, published literature varies greatly when discussing confinement, and many labs have distinct strategies and devices to study cell behavior in confinement. The various models of confined cell migration have been reviewed extensively elsewhere [10], [132], so we do not detail all methods extensively here. However, we do emphasize that there is a growing need to "define confinement" in quantitative physical terms, since there are many different assays that could impose a confining force on cells. Hydrogels, polydimethylsiloxane (PDMS), silicon, PEG, glass, and collagen are examples of the many materials applied in various confining devices [132]. Cells can be confined on a 2D surface through chemical modifications of the growth surface or with plasma lithography [133], [134]. For example, micropatterned lines of adhesive protein can create a 1D track upon which cells can migrate [135], [136]. This 1D system can be easily fabricated and imaged, and it is a useful technique for single cell studies. Additionally, fibroblast migration on 1D lines has some similarities to its migration in 3D substrates [135]. 1D patterning techniques are most similar to the migration of cells along extracellular matrix protein "tracks" *in vivo* [137]. Similarly, grooved substrates have been harnessed to confine cell migration through a phenomenon known as contact guidance [138]–[140]. Contact guidance aligns cytoskeletal features parallel to the grooves in a substrate, directing cell migration along the grooved axis [141].

Many groups study confinement using microfabricated devices, including uni-axial “sandwich” confinement [142], [143] and bi-axial confinement [144]–[146]. One such method encourages cell migration through confining microchannels or nanotubes of various widths [25], [26], [147]–[149]. Useful to the study of cell mechanotransduction, these channels may be modified to measure forces exerted by cells or to exert forces on cells [150]–[152]. Beyond microfluidic devices, confining cells within micropillar arrays can be an effective method to systematically control degree of confinement while simultaneously assessing cell behavior [153]–[156]. Furthermore, microtracks can be created in softer materials, by patterning microchannels in polyacrylamide gels [157], or by fabricating collagen microtracks via micromolding [158] or two-photon laser microsurgery [159].

Complete 3D confinement can be achieved by encapsulating cells in 3D hydrogels or scaffolds, though the degree of confinement may be difficult to systematically control in these assays [129], [160]–[162]. Within hydrogels, cell seeding may be manipulated by external forces [163], [164] or confinement may be dynamically controlled, for example by light-triggered expansion of gelatin hydrogel microstructures [165]. Cells may also be confined within spheroids, where they experience increased cell-cell interactions and confinement due to intercellular pressures [166]. Lastly, cells are confined as they intravasate and extravasate into or out of the vasculature, and numerous groups have modeled transmigration in this facet, usually either through Boyden chambers or cell monolayers [167]–[170]. While these assays do not fully confine the entire cell at once, they do present *in vivo*-like constrictive environments through which the cell body, and its nucleus, must squeeze. Regardless of the confining

mechanism used, mechanical confinement has the potential to drastically alter cell behavior when compared to traditional 2D culture. We utilize a confining microchannel assay within Chapters 3 and 4. Chapter 5 details the development and validation of a confining micropillar assay, which is subsequently used in Chapter 6.

2.7 Effect of confinement on MSC behaviors

2.7.1 Morphology

MSCs exhibit several distinct changes in cell body and nucleus morphology with increased mechanical confinement. Indeed, different scaffolds can push MSCs into various morphologies in one, two, or three dimensions [171]. While migrating within channels, MSCs exhibit marked elongation, with increased aspect ratio of the cell body and nucleus [64]. Interestingly, MSCs display a constant nuclear major axis length as a function of microchannel width [64], [172], which is compensated by increased nuclear height as microchannels become more narrow [172], while sarcoma cells display an increasing nuclear major axis length as confinement increases [173]. Nuclear elongation during confined migration has been shown to be due, in part, to increased lamin-A:B ratio [131]. Within micropillars, MSCs tend to branch less than fibroblasts, maintaining a highly anisotropic morphology [153]. MSC morphology in confinement is also stiffness dependent. When cultured within micropillar arrays of anisotropic stiffness, MSCs preferentially align along the stiffer direction [154]. Notably, meso-scale cues have a greater influence on MSC alignment than micro-scale cues at certain lengths [174], and when microniches are too large or too small, no actin stress fibers are

observed within MSCs [85]. Finally, MSC spreading can be hindered by increased crosslink density of 3D gels at early time points, but there is a monotonic increase in cell spreading with increasing adhesivity [175].

2.7.2 Migration

The detailed mechanisms of confined migration of several cell types has been reviewed extensively elsewhere [127], [176]–[178]. Therefore, we focus herein on studies of particular relevance to MSCs. Of note, nuclear passage into a pore is widely regarded as the rate limiting step in migration through confinement, likely because the nucleus significantly stiffer than the surrounding cytoplasm and other organelles [127]. Of note for stem cells, lamin A/C is critical for successful confined migration, and the expression level of lamin A/C can influence the migration rate of cells through small pores. For example, overexpression or knockout of lamin A/C reduces cell migration rate, but a moderate knockdown of lamin A/C expression increases the migration rate of fibroblasts, MSCs, and tumor cells [102], [106], [131], [179]. Furthermore, migration is arrested in tumor cells, T cells, and neutrophils during migration through pores that are less than 10% the size of their nuclear cross-section [129]. Hence, nuclear deformability, nuclear morphology, and lamin A/C expression are all critical components in determining cell migration response in confined environments.

Notably, the effect of confining channels on MSC migration is highly dependent on the population doubling level. MSC invasiveness of MSCs into spaces between micropillars with 8 μm spacing increases with increased passage due to transition of cells from a viscoelastic fluid to a viscoelastic solid [153]. Similarly, in comparing

MSCs from different donors, the less deformable MSCs are more likely to enter small channels [153]. This emphasizes the need to consider passage-dependent effects on behavior in MSCs. Additionally, this study highlights the inherent differences between MSCs from different donors and the MSCs' subsequent response to confinement.

Confinement in glass microtubes alters the migration phenotype of neural stem cells in comparison with 2D substrates, and these confining microtubes also better recapitulate the *in vivo* neural stem cell morphology than does culture on 2D substrates [148]. MSC migration efficiency in 3D scaffolds has been shown to be strongly dependent on pore size, with MSCs being most migratory in scaffolds of 12 μm pore diameter [180]. However, MSC migration is unaffected by tortuosity or contraction of wide 3D channels [181]. MSCs have also been shown to migrate through small physiologic pores. For example, MSCs can transmigrate through pores of 1-2 μm diameter within the endothelial monolayer, exhibiting non-apoptotic blebbing to facilitate migration [74].

Other physiological cues, such as stiffness or adhesivity, coupled with confinement may also influence MSC migration. Stiff 3D hydrogels may hinder migration by limiting cells' ability to deform its ECM [182]. Similarly, cell speed decreases with increasing crosslink density, but persistence of migration is unaffected [175]. Gels with lower crosslinking density and high adhesivity support cells with more sustained polarization, higher migration speeds and higher spreading [175]. In contrast, low adhesion and vertical confinement causes mesenchymal cells to migrate faster and more amoeboid-like [183]. Similarly, MSC spheroids entrapped in alginate gels with a high concentration of RGD binding ligands or no RGD ligands have minimal

outgrowths, while MSC spheroids in alginate gels of low RGD ligand concentration have more migration and outgrowth [184]. When placed within matrix metalloproteinase (MMP)-degradable PEG gels, MSC migration is inhibited by an MMP inhibitor or blebbistatin [185], indicating the importance of MMPs and myosin II-mediated contractility for MSC migration in these environments. Additionally, migration occurs in regions of complete or near-complete hydrogel erosion [185]. Wnt signaling is also involved in the effective migration and invasion of MSCs [186]. Finally, cancer stem cells (CSCs) have enhanced motility in aligned collagen matrices, while the overall population of cancer cells does not have enhanced motility [187]. Smaller cell size, plasticity, and higher degrees of protrusive activity lead to faster cancer stem cell migration as opposed to other breast carcinoma cells where the nucleus is a limiting factor [187]. In Chapter 3, we demonstrate that confinement influences both the speed and migration mechanism of MSCs.

2.7.3 Invasiveness

Invasiveness, or the ability to permeate confined spaces, is another critical property of stem cells. For the sake of this chapter, we chose not to describe phenotypic changes in cells transmigrating through an endothelium, but rather we describe the effects of longer, sustained confining forces. MSCs are able to negate contact-inhibition and migrate around other cells on narrow micropatterned fibrillar structures, where they would normally retract from cell-cell contact. This increase in migratory behavior in MSCs may be due to the decreased N-cadherin expression [181]. Additionally, confinement can be more important than stiffness in determining how cells invade into

surrounding 3D collagen matrices [188] and which migration mechanism they use [189]. Confinement within the ECM can inhibit the number of cancer stem cells (CSCs) and their scattering from a cancer cell mass [190]. However, this inhibition may be overcome by increased CSC motility or increased proteolysis [190].

2.7.4 Differentiation

There is growing evidence that confinement can alter MSC differentiation (Fig. 2.4). Scaffold pores, an example of circular spatial constraints, alter the differentiation of MSCs. Scaffolds with pore sizes of 300 μm result in higher levels of MSC chondrogenesis than scaffolds with 94 or 130 μm pores [191]. Interestingly, a different study found that 100-150 μm diameter pores enhance osteogenic differentiation, potentially due to actin and focal adhesion rearrangement involving α2 integrins, α5 integrins, and vinculin [192]. When MSCs are seeded within gelatin–glutaraldehyde scaffolds, increased confinement of pores to an area of ~30 μm^2 (~6 μm diameter) enhances osteogenic differentiation [193]. Additionally, pore size may be more important than bulk scaffold properties in directing lineage specification [193]. Although pore size alters MSC differentiation, crosslink density has little influence on stem cell fate in non-degradable covalently crosslinked systems, even when the network presents adhesive ligands [79]. Conversely, MSCs have a higher differentiation capacity in gels with a fibrillar collagen density more similar to conditions *in vivo* [194]. Confining individual MSCs to intermediate volumes enhances alkaline phosphatase expression and reduces MSC lipid content [85]. It has also been asserted that adhesion-ligand presentation matters more to MSC differentiation than cell morphology [78].

MSC differentiation is also altered in other confining environments that increase cell-cell contacts. For example, culturing MSCs in 3D spheroids yields better adipogenic and osteogenic differentiation efficiency than culture in a 2D monolayer [195]. Additionally, MSC colonies confined within agarose walls show increased adipogenic differentiation at the center of colonies, osteogenic differentiation slightly closer to the edge, and more undifferentiated cells at the extreme edge of colonies next to the wall [196]. 3D confinement or lateral confinement can speed up and enhance or induce, respectively, de-differentiation of fibroblasts to induced pluripotent stem cells [197]–[199]. However, despite potential advantages described above, there are risks to confining MSCs. DNA damage to MSCs, as may be induced in extreme confinement, has been shown to promote MSC senescence, limiting their differentiation and proliferation capacity [200].

Adipogenesis

Construct	Optimal microenvironment	Elements Involved	Reference
100 μm diameter spheroid	Spheroid > 2D	Downregulation of stemness genes	(Wang et al., 2009)
PLL-coated glass encircled by agarose wall	Center of culture > outer edge of culture	Reduced traction forces at center	(Tanaka et al., 2017)
Methacrylated hyaluronic acid hydrogel microniches (10 kPa)	Larger volumes (4800, 9200 μm^3) > smaller volumes (3600, 2800 μm^3)	RhoA diluted in larger cells, more G-actin, more cytosolic YAP/TAZ, increased nuclear HDAC3	(Bao et al., 2017)

Chondrogenesis

Construct	Optimal microenvironment	Elements Involved	Reference
Collagen-hyaluronic acid scaffolds (0.5 kPa)	300 μm pore > 94 μm or 130 μm pore	Rounded as opposed to flat morphology, reduced scaffold surface area	(Matsiko et al., 2015)

Osteogenesis

Construct	Optimal microenvironment	Elements Involved	Reference
Gelatin foam scaffold (3-4 kPa)	100-150 μm pore > 45 μm or 200 μm pore	Increase in vinculin localization to FAs, increased protrusion, mediated by α2 and α5 integrins	(Lo et al., 2016)
100 μm diameter spheroid	Spheroid > 2D	Downregulation of stemness genes	(Wang et al., 2009)
PLL-coated glass encircled by agarose wall	Edge of culture > center of culture or wall	Increased traction forces at periphery	(Tanaka et al., 2017)
Methacrylated hyaluronic acid hydrogel microniches (10 kPa)	intermediate volumes (3600 μm^3) > smaller volumes (2800 μm^3) or larger volumes (4800, 9200 μm^3)	FA formation, more myosin IIa, YAP/TAZ nuclear localization, reduced nuclear HDAC3	(Bao et al., 2017)
Gelatin-glutaraldehyde scaffold	30 μm pore: 15 kPa > 50 kPa	Pore size > bulk stiffness	(McAndrews et al., 2014)

Figure 2.4 Unique conditions for each confining construct enhance MSC differentiation towards a particular lineage.

2.7.5 Cell secretome

There are a few studies that suggest the cell secretome may be altered by confinement. When embryoid bodies made of human pluripotent stem cells are cultured in microwells, ectoderm and endoderm genes are upregulated, while mesoderm genes are upregulated in cells in suspension [201]. This effect may be due to the accumulation

of secreted factors within microwells [201]. Additionally, 3D spheroid culture of MSCs increases the secretion of anti-inflammatory factors when compared to 2D culture [202]. However, conditioned media from the 3D spheroid culture does not have an anti-inflammatory effect on LPS (endotoxin) -treated cells [202]. Recently, manipulating the physical microenvironment, such as by applying strain or altering substrate protein coating, has been shown to alter the MSC secretome, which includes cytokines and extracellular vesicles [203]. To obtain MSC secreted factors, MSCs are typically cultured in 2D on standard tissue culture plastic and their media harvested [204], [205]. However, MSCs cultured in 3D spheroids have been shown to have enhanced therapeutic effects [206]. The effect of confinement on the MSC secretome is of special interest, as MSC-derived extracellular vesicles and MSC-conditioned media are increasingly being investigated for their therapeutic potential. However, due to the presence of confounding and inseparable conditions in current studies, the field is lacking an overall systematic evaluation of how confinement affects the MSC secretome. In Chapter 6, we investigate how confinement may affect MSC paracrine activity and if MSC secreted factors influence FMT.

2.7.6 Gene and protein expression

Ultimately, the phenotypic changes in cell behavior can usually be traced back to changes in gene and protein expression. Although we touched on this in previous sections, we highlight some findings here. On 2D surfaces, cells are able to control gene expression via spatial control of regulatory proteins [207], and studies are investigating if the same effect could be occurring in confinement. In general, deformation of the

nucleus can subsequently alter gene expression. For example, force on the nucleus can open nuclear pores to YAP/TAZ entry [208]. Additionally, MSC differentiation is altered based on the amount of nuclear "sagging" when seeded atop micropillar arrays [209].

MSCs in spheroids exhibit higher levels of adipogenic and osteogenic mRNA expression as well as stem cell maintenance mRNA, in comparison with MSCs in 2D monolayer culture [195]. This result was confirmed by Zhang et al., who revealed MSC spheroids within a microgel display increased mRNA expression of chondrogenic and osteogenic markers without induction media, and increased mRNA expression of chondrogenic, adipogenic, or osteogenic markers after applying induction media, compared to 2D [210]. MSCs in spheroids also display increased mRNA expression of stemness biomarkers, anti-inflammatory biomarkers, angiogenic biomarkers, and differentiation biomarkers relative to monolayer culture [211]. Again, it is difficult to determine whether confinement specifically is responsible for these effects, or whether there are confounding effects from altered cell-cell contacts, build-up of trophic factors within the spheroid, or other factors.

2.8 Conclusion

Due to the pervasive nature of mechanical confinement *in vivo*, it is critical to understand how and why confinement alters cell behaviors. Furthermore, it is becoming increasingly evident that we must also make these links in the context of the specific (physical or biochemical) microenvironment. Herein, we explore how mechanical confinement influences MSC and lung fibroblast mechanobiology. Together, this

knowledge has the potential to improve MSC-based therapeutics or tissue engineered constructs, as well as IPF-targeting therapies.

Chapter 3: Physical confinement alters cytoskeletal contributions towards human mesenchymal stem cell migration[2]

3.1 Introduction

The use of mesenchymal stem cells (MSCs) in clinical trials is rapidly increasing. According to data from the National Library of Medicine and the National Institutes of Health, the number of completed clinical trials involving mesenchymal stem cells nearly doubled from April 2015 to April 2017 (www.clinicaltrials.gov). Such trials include systemic or targeted delivery of MSCs in patients for the treatment of a variety of conditions such as graft-versus-host disease, osteoarthritis, and myocardial infarction. Additionally, tissue-engineered constructs that incorporate MSCs are becoming increasingly viable and complex [212]–[214]. The *in vivo* or the *in vitro* stem cell microenvironment is critical for providing signaling cues to regulate the balance between quiescence and activation or differentiation of stem cells and to control tissue formation and repair [74], [215]. Biochemical cues are well known to regulate stem cell behavior, and more recently, mechanical cues such as matrix stiffness and topography have been identified as important regulators of stem cell morphology, migration, proliferation, and differentiation [1], [35]–[37]. An additional mechanical cue is confinement, which MSCs encounter as they home to a target.

[2] Adapted from M.T. Doolin and K.M. Stroka, Physical confinement alters cytoskeletal contributions towards human mesenchymal stem cell migration, Cytoskeleton, 75(3): 103-117 (2018).

The homing process is critical to the success of *in vivo* stem cell therapies, yet it is still poorly understood. Similarly, cellular infiltration into or out of a construct is critical to the success of many tissue engineered scaffolds. Stem cells experience mechanical confinement during the homing process as they migrate through endothelial cell-lined vasculature and tissues towards a target, and also during integration into porous tissue-engineered scaffolds. Mounting evidence has indicated that a variety of cell types, including fibroblasts, cancer cells, and epithelial cells, undergo migrational plasticity and use different migration mechanisms for confined migration than for unconfined migration [65]–[67]. Specifically, confinement alters the migration phenotype of mesenchymal cells, making them faster and more amoeboid-like when there is also low adhesion [183]. Furthermore, confinement in reductionist models such as glass microtubes alters the migration phenotype of neural stem cells in comparison with two-dimensional (2D) substrates, and these confining microtubes also better recapitulate the *in vivo* neural stem cell morphology than does culture on 2D substrates [148]. Finally, MSC migration efficiency in 3D scaffolds has been shown to be strongly dependent on pore size, implying that confinement has an effect on MSCs *in vitro*, as well as *in vivo* [180]. Despite such studies, the effect of confinement on MSC response and the mechanism MSCs use to sense and respond to confinement are poorly understood. Understanding the mechanistic behavior of MSCS in confinement is crucial for specific and tunable control of MSC infiltration into tissue engineered scaffolds and homing to distinct tissues *in vivo*.

In this work, our approach was to systematically vary the degree of confinement experienced by human mesenchymal stem cells (MSCs) using a collagen-coated

polydimethylsiloxane-based microfluidic device which we have previously designed and characterized [25], [26], and subsequently visualize and quantify MSC chemotaxis. We verified that MSCs were able to successfully migrate though microchannels 10 μm tall and of varying widths (3, 6, 10, 20, and 50 μm) in response to a chemotactic gradient created by fetal bovine serum (FBS). Intriguingly, we found that MSC migration speed is modestly biphasic as a function of microchannel width, and inhibitors of various cytoskeletal machinery affect MSC differently in confining microchannels compared to wider microchannels. Our results improve our mechanistic understanding of the mechanobiology of stem cell migration and outline the cytoskeletal and contractile machinery that contribute to migration in confined and unconfined microenvironments.

3.2 Materials and Methods

3.2.1 Cell culture and reagents

Bone marrow-derived human mesenchymal stem cells (donor: 20 year-old female) were purchased from RoosterBio, Inc. (Frederick, MD, USA). Cells were removed from liquid nitrogen and grown in RoosterBio basal media with media booster (RoosterBio, Inc.) for the first day post-thaw. Thereafter, cells were cultured in media composed of Dulbecco's Modified Eagle's Medium with high glucose (ThermoFisher Scientific, Waltham, MA, USA), 10% Fetal Bovine Serum (FBS) (ThermoFisher Scientific), and 1% Penicillin-Streptomycin 10,000 U/mL (ThermoFisher Scientific). Cells were cultured and used until a population doubling level of 20, which occurred at passage 5, and cells were passaged at or below 80% confluency. Cells were washed with

Phosphate-Buffered Saline (PBS) (VWR, Radnor, PA, USA), and detached with TrypLE Express Enzyme (ThermoFisher Scientific). All cells were cultured at 37°C, 50% humidity, and 5% CO2:95% air.

3.2.2 Microfluidic device fabrication

A polydimethylsiloxane (PDMS) microchannel device was prepared as previously described [25], [26]. All photolithography procedures were carried out in the University of Maryland Nanocenter FabLab. Briefly, a mask was made in AutoCAD (AutoDesk, San Rafael, CA, USA) to represent the microchannels or the feed lines. A layer of SU-8 3010 negative photoresist (MicroChem, Westborough, MA, USA) was spin coated onto a 4-inch diameter silicon wafer (University Wafer, Boston, MA, USA). Using an EVG620 mask aligner (EVG Group, Albany, NY, USA), the mask in the image of microchannels was placed over the wafer and exposed to ultraviolet (UV) light to crosslink. Excess SU-8 3010 was dissolved using SU-8 developer (MicroChem), and a layer of SU-8 3025 negative photoresist (MicroChem) was spin coated onto the wafer. Using an EVG620 mask aligner, the mask in the image of the feed lines was placed over the wafer, and the features were UV crosslinked. Excess SU-8 3025 was dissolved. Finished wafers were silanized using tridecafluoro-1,1,2,2,tetrahydrooctyl-1-trichlorosilane (97%) (Pfaltz & Bauer, Waterbury, CT, USA) overnight in a vacuum desiccator. The resulting silicon master contained microchannels with 50 μm, 20 μm, 10 μm, 6 μm, and 3 μm width, 10 μm height, and 200 μm length. The cell seeding channels were 50 μm tall. PDMS (Robert McKeown Company, Branchburg, NJ, USA) was mixed at a 10:1 base:curing agent ratio, poured over the silicon master, and

degassed in a vacuum desiccator. The PDMS and master were baked for at least two hours at 85°C, then the PDMS device was cut and removed from the master. A hole punch was used to create the media inlets and outlets in the PDMS device. The PDMS devices and 25 mm by 75 mm #1 glass coverslips (Electron Microscopy Sciences, Hatfield, PA, USA) were cleaned with ethanol and RO water, air dried, baked at 85°C, then placed in a plasma cleaner (Harrick Plasma, Ithaca, NY, USA) and plasma treated for 2.5 minutes. The devices were then bonded to the coverslips for 5 minutes while applying pressure, and the coverslip-device construct was UV sterilized for 10 minutes. 20 μg/mL collagen I (SigmaAldrich, St. Louis, MO, USA) was added to all wells of the devices and incubated for at least one hour at 37°C. The collagen I solution was then removed, and devices were washed twice with PBS.

3.2.3 Migration experiments

Cells were rinsed with PBS, detached with TrypLE, collected with media and centrifuged. Cells were then resuspended in FBS-free media and centrifuged. Cells were then re-suspended in FBS-free media to yield $1x10^5$ to $2x10^5$ cells per 25 μL. Twenty-five μL of cell suspension was added to the cell inlet of each microchannel device, and devices were incubated for at least 5 minutes at 37°C. Excess liquid was removed, then 50 μL of FBS-free media was added to the cell inlet and bottom two media inlets, and 50 μL of FBS-containing media was added to the top media inlet to induce a chemotactic gradient. For experiments using any inhibitor, aside from latrunculin-A, media containing the drug or appropriate vehicle control was added at this time. For experiments using latrunculin-A, cells were incubated with the chemotactic gradient for

2 hours so cells migrated fully into the channels. Then, media was removed and media containing latrunculin-A or its appropriate vehicle control was added. The drugs included latrunculin-A (2 μM, Cayman Chemical, Ann Arbor, Michigan, USA), blebbistatin (50 μM, SigmaAldrich), nocodazole (10 μM, SigmaAldrich), and Y27632 (10 μM, Cayman Chemical). Dimethyl sulfoxide (SigmaAldrich) served as vehicle control in all cases except latrunculin-A, where ethanol served as vehicle control. Imaging began immediately after the proper media was added to the device. Images were acquired on an Olympus IX83 microscope (Olympus, Center Valley, PA, USA) using a 10x objective. A chamber adjusted to 37°C, 50% humidity, and 5% CO_2:95% air was used on the microscope stage in order to sustain cell viability. Images were taken at 5-10 minute intervals overnight.

3.2.4 Immunofluorescence

The following steps were carried out at room temperature, unless otherwise specified, and reagents were added to all wells of the device. Cells were fixed in 3.7% formaldehyde (FisherScientific, Fair Lawn, NJ, USA) for 10 minutes, washed in 0.1 M glycine, then washed twice in PBS (VWR). Cells were permeabilized with 0.5% Triton-X 100 (SigmaAldrich) for 5 minutes, washed in PBS thrice, and blocked for nonspecific binding in 2.5% goat serum (Abcam, Cambridge, MA, USA) for at least one hour. Primary antibody in 1% goat serum was added to cells and incubated at 4°C overnight. Primary antibodies and dilutions used were mouse anti-α-tubulin (ThermoFisher Scientific, 1:100) and rabbit anti-phospho-paxillin (Cell Signaling Technology, Danvers, MA, USA, 1:100). Cells were washed thrice in PBS, incubated in 2.5% goat

serum for at least one hour, and incubated with AlexaFluor 488 Phalloidin (ThermoFisher Scientific, 1:500), Hoechst (ThermoFisher Scientific, 1:2500), and a fluorescently labelled secondary antibody for one hour. Secondary antibodies and dilutions used were AlexaFluor 568 goat anti-mouse (ThermoFisher Scientific, 1:200) and AlexaFluor 568 goat anti-rabbit (ThermoFisher Scientific, 1:200). Cells were washed thrice in PBS, then imaged. Images were acquired on an Olympus IX83 microscope (Olympus) using a 40x or 60x oil immersion objective for cell morphology measurements. Images were acquired on a PerkinElmer UltraVIEW Vox confocal spinning disk microscope (PerkinElmer, Waltham, MA, USA) using a 60x oil immersion objective to visualize actin, microtubules, and focal adhesions. Fluorescence settings were kept constant for each experiment, unless otherwise specified. Use of the PerkinElmer confocal microscope was performed courtesy of the University of Maryland imaging core.

3.2.5 Data analysis

Cell migration in the channels was manually tracked in ImageJ by tracking the center of mass of the cell as it migrated through the channels. Tracking began once a cell was entirely within the channel and ceased once a portion of the cell protruded from the channel. Cells were not tracked if they divided or died while in the channel. Mean speed and chemotactic index were calculated for each cell using a custom Matlab program. Chemotactic index was calculated as the end-to-end distance travelled divided by the total distance travelled. For cell morphology, cells and nuclei were manually traced in ImageJ. Aspect ratio, circularity, area, solidity, and roundness were extracted

using ImageJ built in morphology measurements. Inverse aspect ratio was equated to the roundness. Focal adhesion area was quantified in ImageJ by applying the same threshold to all immunofluorescence images for py-paxillin and measuring the area of each focal adhesion with the particle analyzer. We excluded any particles greater than 5 μm^2, to remove any background staining.

3.2.6 Statistical analysis

Data for cells from at least three independent trials was pooled for statistical analysis. A student's t-test, in the case of normally distributed data, or Mann-Whitney test, in the case of non-normally distributed data, was performed between drug-treated and control groups. A one way ANOVA, in the case of normally distributed data, or Kruskal-Wallis test, in the case of non-normally distributed data, was performed between channel widths. A significance level of 0.05 was used. Error bars report the standard error of the mean (SEM).

3.3 Results

3.3.1 Confinement alters MSC morphology

Our first goal was to determine whether MSCs were capable of migrating through collagen-coated microchannels down to 3 μm wide (and 10 μm tall), and if so, whether cell morphology and migration speed depended on degree of confinement. We have previously shown that metastatic cancer cells can successfully migrate through the microchannel devices used here [65], [67], [152], and we predicted that MSCs, which also possess an innate requirement for efficient cell migration through confining 3D

matrices, were also sufficiently deformable to squeeze through the narrowest channels. Indeed, MSCs seeded in the microfluidic chemotaxis devices migrated completely through all channel widths ranging from 3 μm to 50 μm wide, in response to a fetal bovine serum (FBS) chemoattractant gradient (Fig. 3.1A, 3.1B). Given the obvious morphological differences observed via phase contrast microscopy in narrow (Fig. 3.1A) vs. wide (Fig. 3.1B) microchannels, we hypothesized that MSC cytoskeletal arrangement also depended on degree of confinement. Thus, MSCs were fixed while migrating through the microchannels, and subsequently stained for actin and tubulin. Both the actin and microtubule networks appeared more diffuse and less fibrillar in confining narrow (3 μm) channels, compared to wide (50 μm) channels (Fig. 3.1C, 3.1D). Furthermore, MSCs in narrow channels appeared to occupy the entire height of the channel (Fig. 3.1C; y-z plane), while MSCs in wide channels occupied just a fraction of the channel height (Fig. 3.1D; y-z plane). Interestingly, in narrow channels (where the nucleus was deformed significantly in the x-y plane), the nucleus height in the z-direction occupied the majority of the height of the channel (Fig. 3.1C). In wider channels (where the nucleus was not laterally confined in the x-y plane), the nucleus height in the z-direction was significantly less than the channel height (Fig. 3.1D). Due to the apparent differences in MSC shape and structure between channel widths (Fig. 3.1C, 3.1D), we quantified several cell and nucleus morphological parameters. Both cell area and nucleus area in the XY plane decreased with decreasing channel width (Fig. 3.1E, 3.1F). Cell inverse aspect ratio, which is a measure of the minor axis over the major axis of an ellipse fitted to the cell, also increased monotonically from 3 μm to 50 μm channels (Fig. 3.1G). It was previously shown that force application to 3T3

fibroblasts causes the nucleus to deform in an anisotropic manner [101]. Thus, we also quantified the lengths of the major and minor axes of MSC nuclei by approximating the nucleus as an ellipse. In agreeance with an anisotropic model, the nucleus major axis length was independent of channel width, while the minor axis significantly decreased with decreasing channel width, even within 50 μm-wide channels, when compared to 2D substrates (Fig. 3.1H).

Figure 3.1 Effects of confinement on MSC cytoskeletal organization and cellular and nuclear morphological parameters. Phase contrast timelapse sequence of MSCs migrating in A) narrow, 3 μm channels, or B) wide, 50 μm channels. Scale bar on panel (B) represents 50 μm and applies to panels (A) and (B). MSC cytoskeleton in C) a 3 μm narrow channel, or D) a 50 μm wide channel, shown in both the XY and YZ planes. In panels (C) and (D) cells were fixed and stained for α-tubulin (red), actin (green), and the nucleus (blue). Color channels were altered individually, yet to the same degree for panels (C) and (D). Scale bar on panels (C) and (D) represents 9 μm and applies to panels (C) and (D). Area of E) MSCs and F) MSC nuclei as a function of channel width. G) Inverse aspect ratio of MSCs as a function of channel width. H) MSC nucleus major axis length and minor axis length as a function of channel width. Bar graphs report mean ± SEM. **p<0.01, ***p<0.001, ****p<0.0001. (Number on individual bars indicates total number of pooled cells from N≥5 independent experiments).

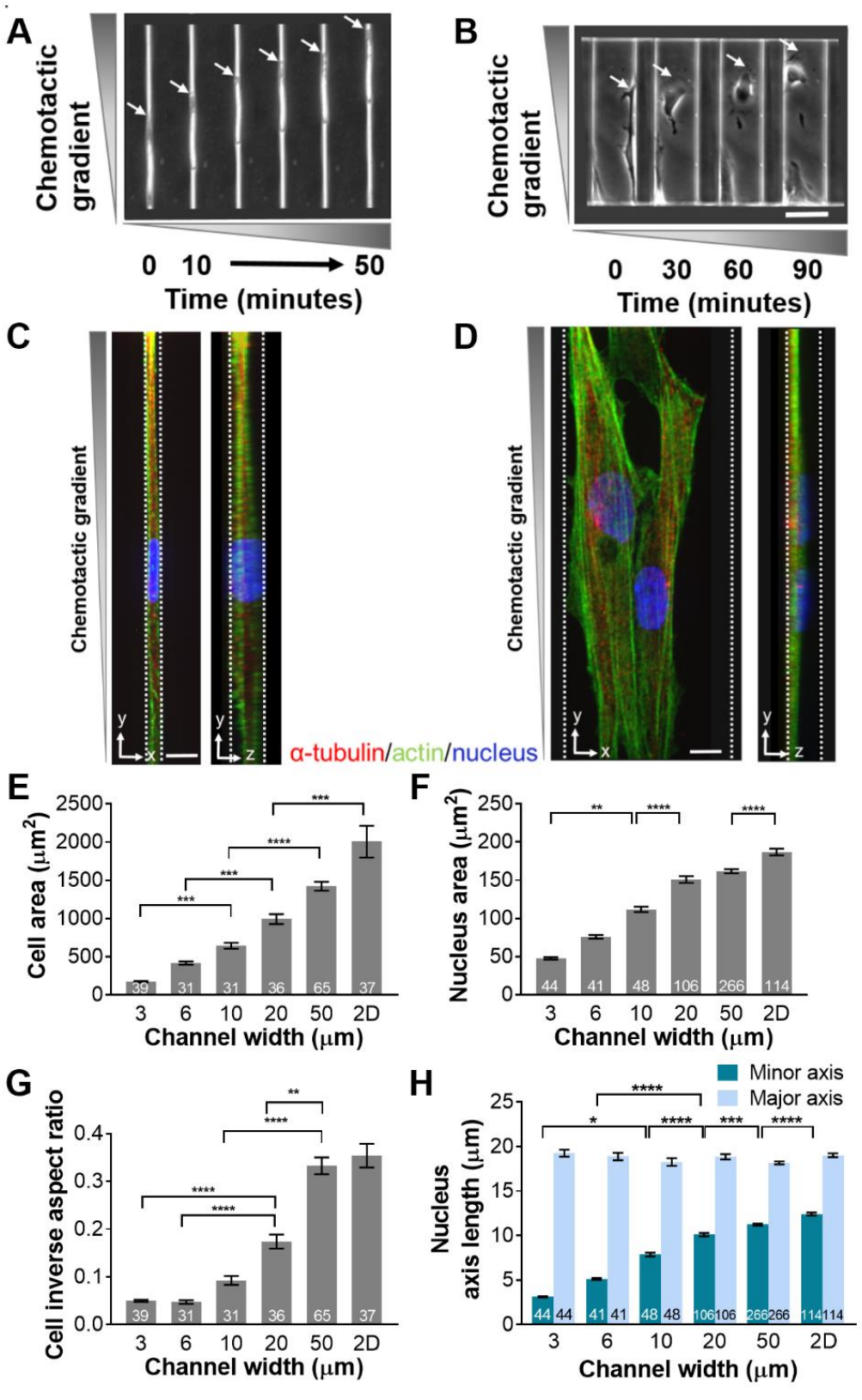
A
Chemotactic gradient
0 10 50
Time (minutes)
B
Chemotactic gradient
0 30 60 90
Time (minutes)
C
Chemotactic gradient
y
x
y
z
α-tubulin/actin/nucleus
D
Chemotactic gradient
y
x
y
z
E
Cell area (μm²)
2500
2000
1500
1000
500
0
***
***
***
****
***
39 31 31 36 65 37
3 6 10 20 50 2D
Channel width (μm)
F
Nucleus area (μm²)
250
200
150
100
50
0
**
****
****
44 41 48 106 266 114
3 6 10 20 50 2D
Channel width (μm)
G
Cell inverse aspect ratio
0.4
0.3
0.2
0.1
0.0
**
****
****
****
39 31 31 36 65 37
3 6 10 20 50 2D
Channel width (μm)
H
Minor axis
Major axis
Nucleus axis length (μm)
25
20
15
10
5
0
****
*
****
***
****
44 44 41 41 48 48 106 106 266 266 114 114
3 6 10 20 50 2D
Channel width (μm)

3.3.2 Passage number alters MSC speed and chemotactic index in response to confinement

Previous reports have shown that increasing MSC passage number decreases the invasiveness and bioactivity of MSCs [153], [216], so we investigated MSC speed as a function of passage and of confinement. MSCs at passage 3, 4, or 5 (P3, P4, or P5) were seeded in the microfluidic device, and the speed of MSCs migrating within microchannels was subsequently tracked. We found that P3 and P4 MSCs displayed a modest biphasic relationship between migration speed and microchannel width (Fig. 3.2A and 3.2B). Meanwhile, P5 MSCs showed no significant difference in speed among channel widths (Fig. 3.2C). Intriguingly, when data from all passages were plotted together but without being pooled, it became evident that MSCs tended to move slower as a function of increasing passage number for all channel widths (Fig. 3.2D). However, this difference was not significant in the narrowest channel (Fig. 3.2D).

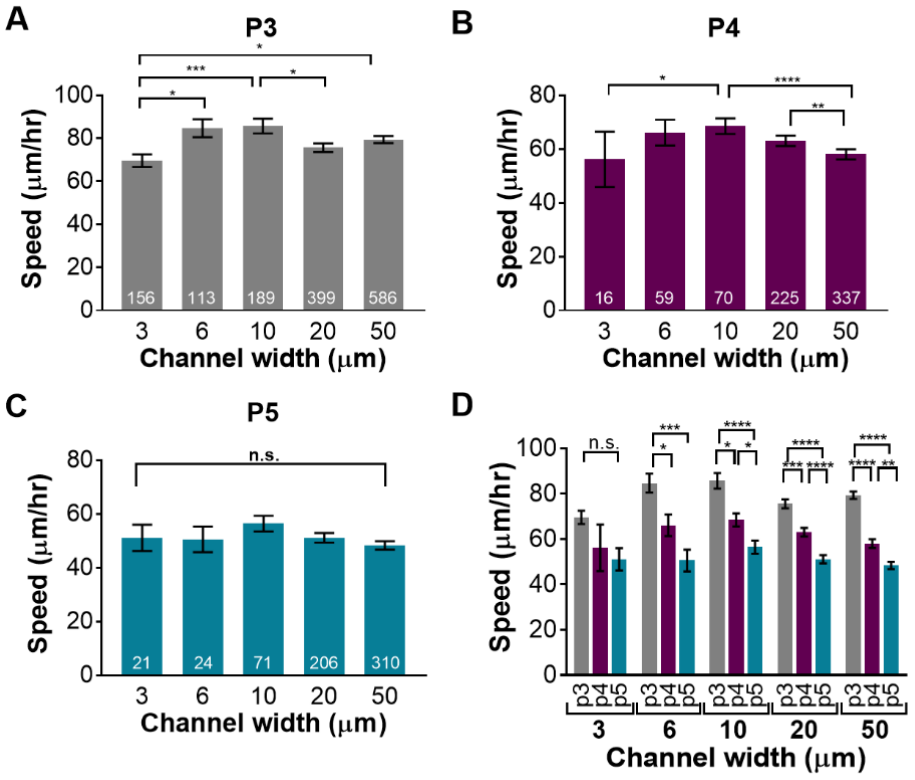

Figure 3.2 Effects of confinement and passage on MSC speed. Speed of A) passage 3 (p3), B) passage 4 (p4), or C) passage 5 (p5) MSCs as a function of channel width. D) MSC speed as a function of channel width, replotted to highlight differences across passages. Bar graphs represent mean ± SEM. For panels A-C, number on individual bars indicates total number of pooled cells from N=3 independent experiments for each passage. *P<0.05, **p<0.01, ***p<0.001, ****p<0.0001.

We next calculated the chemotactic index of each cell migrating within the microchannels, which is defined as the end-to-end distance travelled divided by the total distance travelled; in this measurement, a value of 1 indicates perfectly persistent migration. P3 MSCs moved with a significantly greater chemotactic index in 50 μm wide channels than in 6 μm wide channels (Fig. 3.3A). However, MSCs moved with a

significantly lower chemotactic index in 50 μm wide channels than 20 μm wide channels (Fig. 3.3A). P4 MSCs moved with a significantly higher chemotactic index in 6 μm wide channels than 3 μm, 20 μm, or 50 μm wide channels (Fig. 3.3B). Furthermore, MSCs moved with a significantly greater chemotactic index in 50 μm wide channels than in 10 μm wide channels (Fig. 3.3B). P5 MSCs displayed no significant difference in chemotactic index among channel widths (Fig. 3.3C). When all passages were plotted together but without being pooled, it became evident that, in general, P4 MSCs migrated most persistently in comparison with P3 and P5 MSCs in all channel widths, though chemotactic index was not statistically different across passages in the narrowest 3 μm channels (Fig. 3.3D).

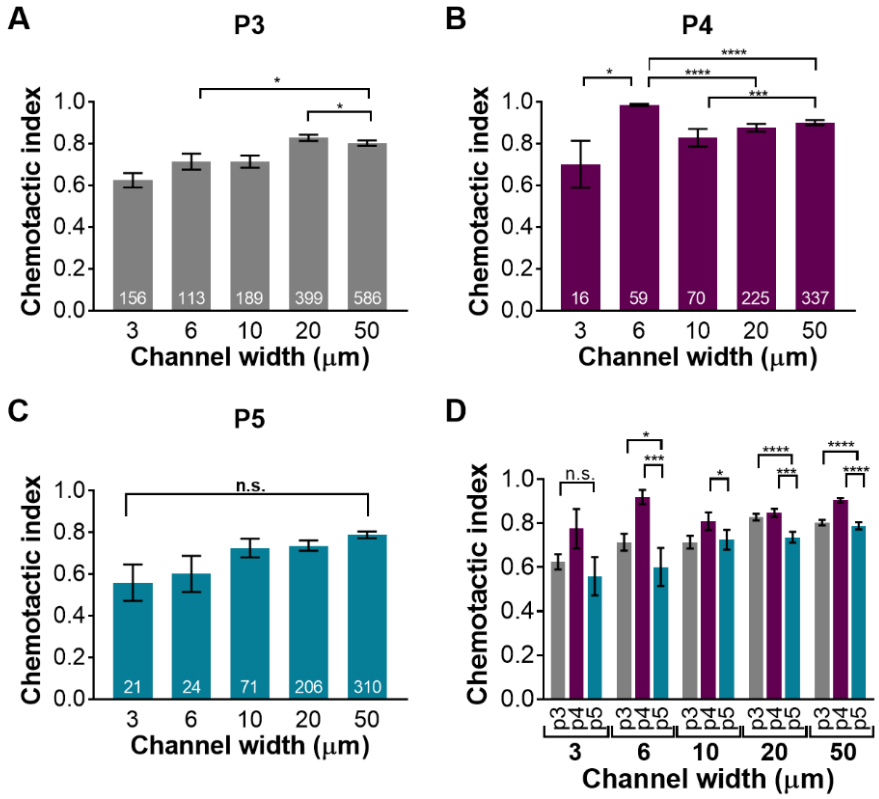

Figure 3.3 Effects of confinement and passage on MSC chemotactic index. Chemotactic index of A) passage 3 (p3), B) passage 4 (p4), or C) passage 5 (p5) MSCs as a function of channel width. D) MSC chemotactic index as a function of channel width, replotted to highlight differences across passages. Bar graphs represent mean ± SEM. For panels A-C, number on individual bars indicates total number of pooled cells from N=3 independent experiments for each passage. *P<0.05, **p<0.01, ***p<0.001, ****p<0.0001.

3.3.3 Inhibition of microtubule polymerization does not affect MSC migration in confinement

We have previously shown that microtubule polymerization is indispensable for MDA-MB-231 tumor cell migration in confined (3 μm wide) microchannels [26]. However, given the diffuse microtubule network observed in MSCs in narrow (3 μm) channels (Fig. 3.1C), we hypothesized that MSC migration in confinement may depend less on microtubule polymerization. Hence, we inhibited microtubule polymerization in MSCs by treating cells with nocodazole as they entered and migrated through the microchannels. Vehicle control-treated cells in 50 μm wide channels exhibited a distinct microtubule network that was visibly disrupted after nocodazole treatment (Fig. 3.4A). Microtubule inhibition also resulted in alteration of the actin cytoskeleton, with a visual reduction in stress fiber content and overall F-actin organization in nocodazole-treated cells in 50 μm wide channels (Fig. 3.4A). Meanwhile, nocodazole did not affect visual organization of the microtubule network in MSCs in narrow (3 μm) channels, where vehicle control- and nocodazole-treated cells both contained a diffuse α-tubulin network rather than distinct microtubules (Fig. 3.4B).

Given the differential effects of nocodazole on microtubule organization in MSCs in wide vs. narrow channels, we next wanted to determine whether these effects carried over to migration potential of MSCs. Indeed, we found that nocodazole treatment significantly decreased the speed of MSCs in 20 μm and 50 μm wide channels but had no effect on MSC migration speed in narrower channels (Fig. 3.4C). Meanwhile, nocodazole treatment significantly increased the chemotactic index of MSCs in 6 μm

and 10 μm wide channels, but significantly decreased the chemotactic index of MSCs migrating through 50 μm wide channels (Fig. 3.4D). Microtubule depolymerization has been shown to result in release of guanine exchange factor-H1 (GEF-H1), leading to increased cell contractility via activation of RhoA, ROCK, and myosin II, [217]–[219], increased traction forces [220], and, possibly, decreased cell speed and persistence. To determine if a potential nocodazole-induced increase in cell contractility caused a significant effect on MSC migration, we treated cells with a combination of blebbistatin, which decreases cell contractility, and nocodazole, which putatively increases contractility. Similar to nocodazole treatment alone, a combination of blebbistatin and nocodazole treatment significantly decreased the speed of cells that migrated through 20 μm and 50 μm wide channels (Fig. 3.4E). The chemotactic index of MSCs with combinatorial blebbistatin and nocodazole treatment was significantly increased for cells that migrated through 6 μm wide channels (Fig. 3.4F).

Figure 3.4 Effects of inhibition of microtubule polymerization on MSC migration in confinement. A) Control and nocodazole-treated MSCs in 50 μm wide channels. B) Control and nocodazole-treated MSCs migrating through 3 μm narrow channels. In panels (A) and (B) cells were fixed and stained for α-tubulin (red), actin (green), and the nucleus (blue). C) Effects of inhibition of microtubule polymerization on MSC speed and D) persistence. Also shown are percent changes in MSC E) speed or F) chemotactic index, with respect to the vehicle control, for cells treated with nocodazole, blebbistatin, or a combination of nocodazole and blebbistatin. Bar graphs report mean ± SEM. Scale bars represent 9 μm and apply to both control and nocodazole condition for each of panels (A) and (B). *p<0.05, **p<0.01, ****p<0.0001. For panels (C-D), number on individual bars indicates total number of pooled cells from N=3 independent experiments for each condition. In panels (E-F), data points represent nocodazole treated cells presented in (C-D), blebbistatin treated cells presented in Figs. 6C and 6D, and pooled nocodazole and blebbistatin treated cells from N=4 independent experiments for each condition as follows: n(3 μm channel, control)=62, n(3 μm channel, nocodazole and blebbistatin)=15, (6 μm channel, control)=12, n(6 μm channel, nocodazole and blebbistatin)=10, n(10 μm channel, control)=16, n(10 μm channel, nocodazole and blebbistatin)=14, n(20 μm channel, control)=59, n(20 μm channel, nocodazole and blebbistatin)=12, n(50 μm channel, control)=100, n(50 μm channel, nocodazole and blebbistatin)=21.

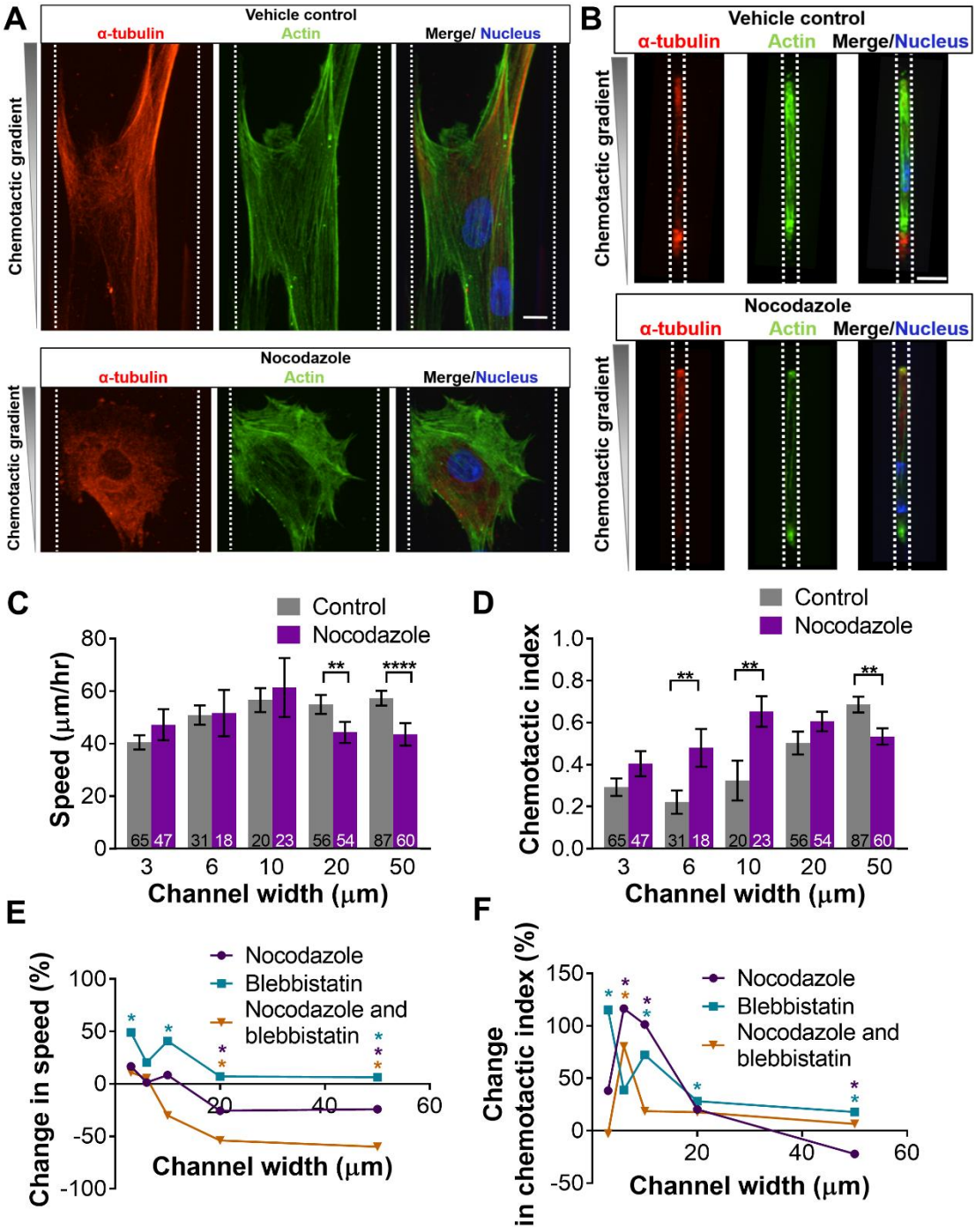

In view of the differences we observed in MSC speed and chemotactic index with increasing passage (Fig. 3.2D, 3.3D), we sought to investigate whether passage affects MSC response to nocodazole. Hence, we replotted our data from Fig. 3.4C and

Fig. 3.4D to separate out MSCs by passage (Fig. 3.5). Notably, the numbers of P4 and P5 MSCs entering into the narrower channels (10, 6, 3 μm) were much lower than P3 MSCs, as indicated by the n values shown on the data bars in Figure 3.5, leading to differences in statistical differences when comparing data from individual passages. Interestingly, nocodazole treatment did not alter the speed of P3 MSCs in any channel width (Fig. 3.5A). However, nocodazole treatment significantly decreased the speed of P4 and P5 MSCs in 20 μm and 50 μm wide channels (Figs. 3.5B, 3.5C). Conversely, the chemotactic index of nocodazole-treated P3 MSCs most similarly followed the pooled data (Figs. 3.5D, 3.4D). Nocodazole treatment significantly increased the chemotactic index of P3 MSCs in 6 μm and 10 μm wide channels, but significantly decreased the chemotactic index of P3 and P5 MSCs migrating through 50 μm wide channels (Fig. 3.5D, 3.5F). There were no statistical differences in the chemotactic index of nocodazole-treated P4 MSCs when compared to the respective vehicle control (Fig. 3.5E).

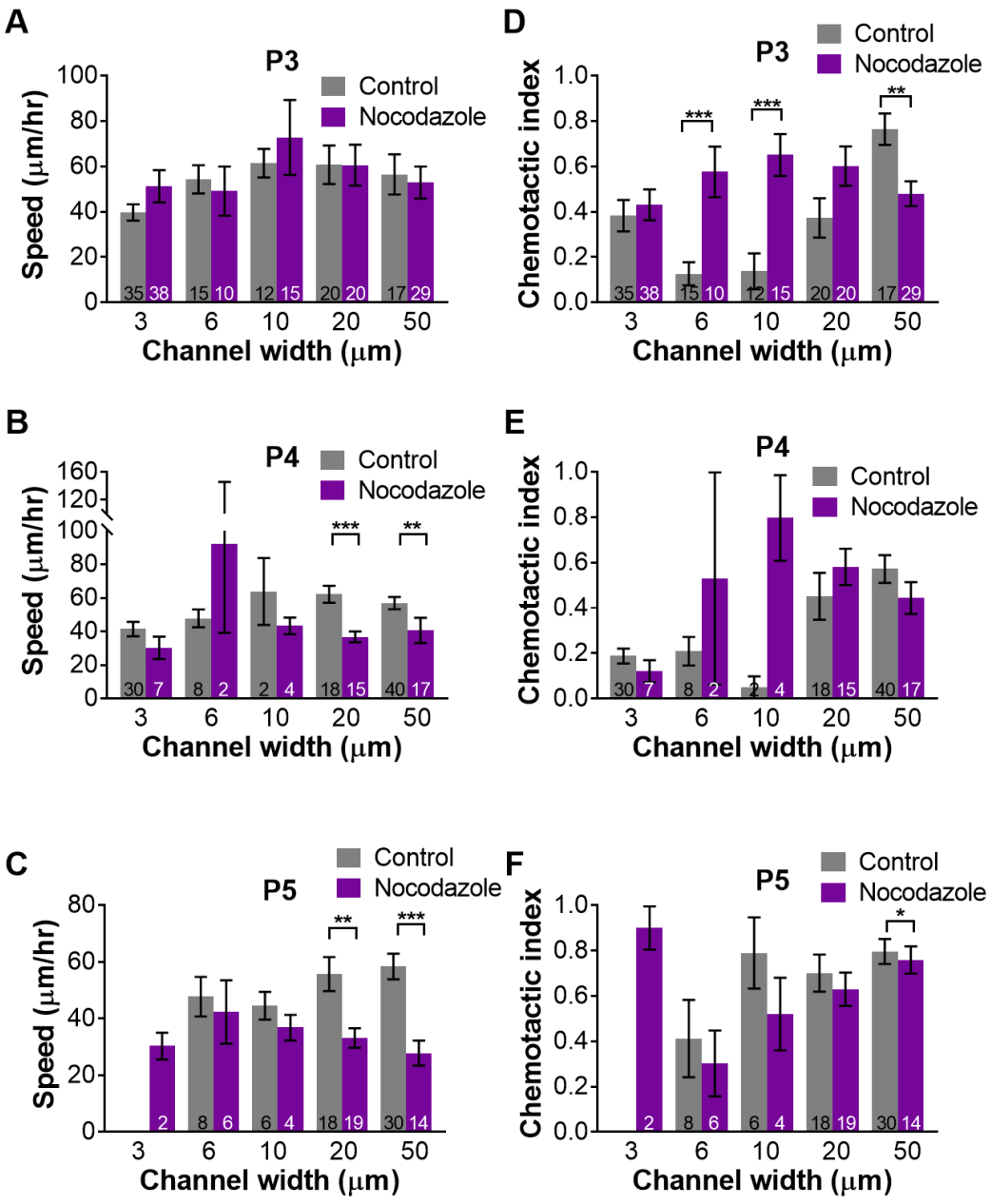

Figure 3.5 Effects of inhibition of microtubule polymerization on hMSCs in Figure 3.4 broken out by passage. Effects of nocodazole on speed for hMSCs of A) P3, B) P4, and C) P5. Effects of nocodazole on chemotactic index for hMSCs of D) P3, E) P4, and F) P5. Bar graphs report mean ± SEM. *P<0.05, **p<0.01, ***p<0.001.

3.3.4 Inhibition of myosin II-mediated contractility enhances MSC migration

The typical mesenchymal migration model involves an interplay between actin polymerization and actin-associated myosin II-mediated cell contractility, so we next investigated the role of myosin II in confined MSC migration. To inhibit myosin II-mediated contractility, MSCs were treated with blebbistatin while they entered and migrated through the microchannels. There were no apparent changes in the MSC cytoskeleton between blebbistatin- and vehicle control-treated cells, with both groups exhibiting defined fibrillar actin and microtubule networks in wide channels (Fig. 3.6A) and diffuse actin and tubulin structures in confinement (Fig. 3.6B). However, blebbistatin-treated cells presented an increase in protrusions and exhibited lengthier, more spindle-like cell bodies (Figs. 3.6A, 3.6B). Inhibition of myosin II contractility significantly increased the speed of cells in 3 μm, 10 μm, and 50 μm wide channels in comparison with the vehicle control (Fig. 3.6C). Notably, the p-value for statistical significance decreased with decreasing channel width, indicating that blebbistatin had a larger effect on cell migration speed in narrower channels (Fig. 3.6C). Chemotactic index was significantly increased for blebbistatin-treated cells migrating in all channel widths except for 6 μm (Fig. 3.6D).

3.3.5 Inhibition of ROCK enhances MSC migration in wide channels

Given the effects of inhibiting myosin II on cell migration speed in confined vs. unconfined channels, we hypothesized that upstream targeting of the contractility pathway would also lead to differential migration patterns in narrow vs. wide channels.

Hence, we next investigated the effects of inhibition of Rho-associated protein kinase (ROCK) on MSC migration by treating cells with the pharmacological inhibitor Y27632 as they entered and migrated through the microchannels. ROCK was chosen not only because it is upstream of myosin II in the contractility pathway, but also because it has been shown to influence stem cell fate [36]. Surprisingly, Y27632-treated MSCs migrated significantly faster in 50 μm wide channels, in comparison with vehicle control-treated cells (Fig. 3.6E). However, Y27632-treated cells had a significantly higher chemotactic index in all channel widths, compared to control (Fig. 3.6F). Interestingly, ROCK inhibition via Y27632 led to a greater percent increase in cell speed (over the vehicle control) in wide channels (50 μm) in comparison with narrow channels (3 μm), where there was no significant change in cell speed after blebbistatin treatment (Fig. 3.6E). Notably, this trend was opposite the effects of blebbistatin (Fig. 3.6E), even though both ROCK and myosin II act in the contractility pathway. Both ROCK inhibition and myosin II inhibition significantly increased the chemotactic index of cells in both narrow and wide channels (Fig. 3.6F).

Figure 3.6 Effects of inhibition of myosin II- and ROCK-mediated contractility on MSC migration in confinement. The microtubule and actin networks of control and blebbistatin-treated MSCs in A) 50 μm (wide) and B) 3 μm (narrow) channels. In panels (A) and (B) cells were fixed and stained for α-tubulin (red), actin (green), and the nucleus (blue). Fluorescence exposure times differ between panels (A) and (B). The red channel was altered individually, yet to the same degree for panels (A) and (B). In panels (A) and (B), scale bars represent 9 μm. C) Effects of blebbistatin on MSC speed and D) chemotactic index. Also shown are percent changes in MSC E) speed or F) chemotactic index, with respect to the vehicle control, for cells treated with Y27632 or blebbistatin. Bar graphs report mean ± SEM. (C-D) *p<0.05, **p<0.01, ***p<0.001, ****p<0.0001. (E-F) *p<0.05. For panels (C-D), number on individual bars indicates total number of pooled cells from N=4 independent experiments for each condition. In panels (E-F), data points represent blebbistatin treated cells presented in panels (C-D) and pooled Y27632 treated cells from N=3 independent experiments for each condition as follows: n(3 μm channel, control)=48, n(3 μm channel, Y27632)=110, (6 μm channel, control)=26, n(6 μm channel, Y27632)=31, n(10 μm channel, control)=37, n(10 μm channel, Y27632)=48, n(20 μm channel, control)=105, n(20 μm channel, Y27632)=192, n(50 μm channel, control)=155, n(50 μm channel, Y27632)=325.

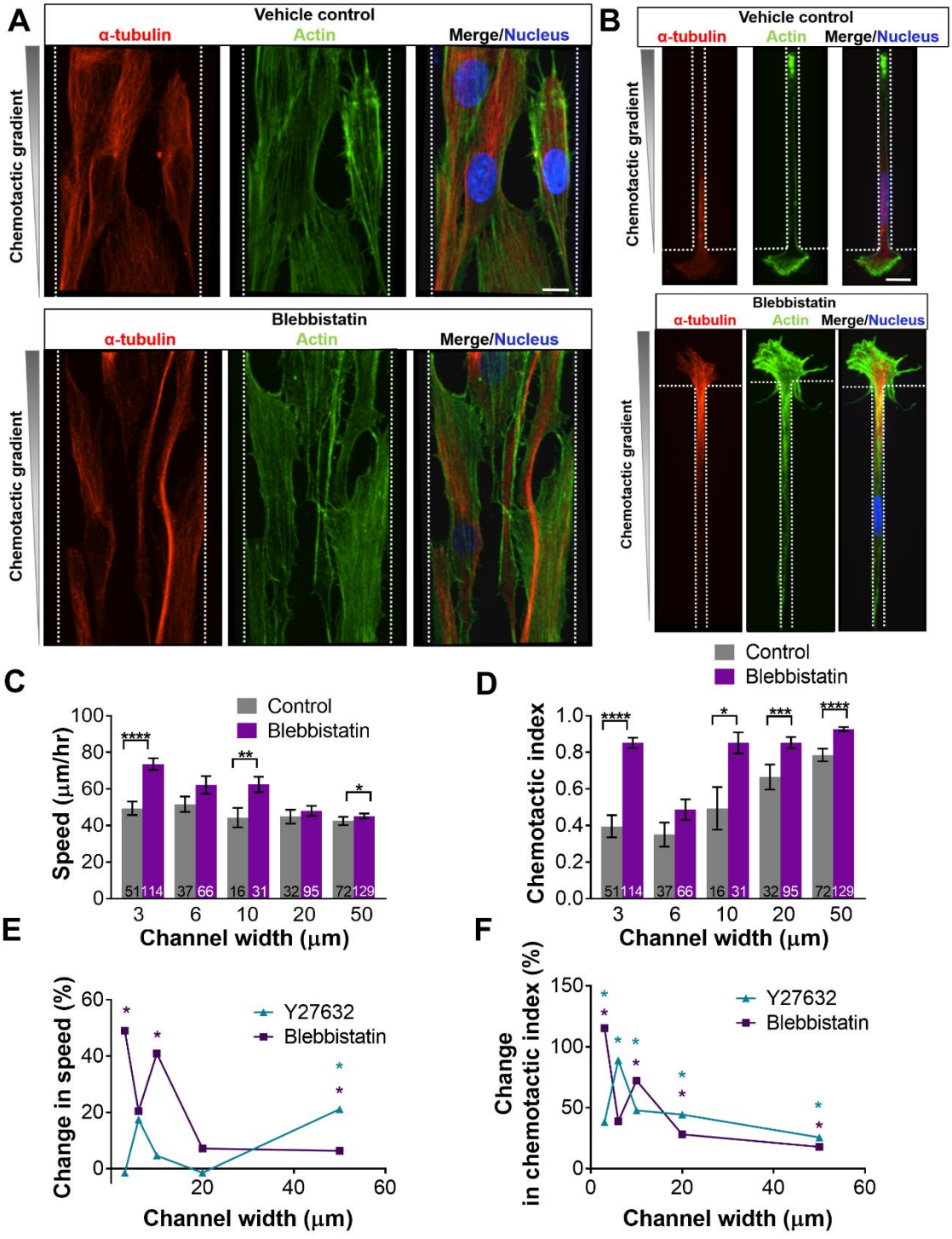
A
Vehicle control
α-tubulin
Actin
Merge/Nucleus
Chemotactic gradient
Blebbistatin
B
C
Control
Blebbistatin
Speed (μm/hr)
Channel width (μm)
D
Chemotactic index
E
Change in speed (%)
Y27632
F
Change in chemotactic index (%)

As with nocodazole treatment, we investigated whether blebbistatin affected MSCs differently with increasing MSC passage (Fig. 3.7). The speed of blebbistatin-treated MSCs of all passages was either not significantly different or (in a few cases) significantly greater than vehicle control for all channel widths (Figs. 3.7A, 3.7B, 3.7C). For example, most strikingly, similar to the pooled data, the speed of P3 MSCs in 3 μm narrow channels was significantly increased after blebbistatin treatment (Fig. 3.7A). In addition, the chemotactic index of blebbistatin-treated MSCs of all passages was either not significantly different or significantly greater than vehicle control for all channel widths (Figs. 3.7D, 3.7E, 3.7F). For example, similar to the pooled data, the chemotactic index of P3 MSCs in 3 μm, 20 μm, and 50 μm wide channels was significantly increased after blebbistatin treatment (Fig. 3.7D).

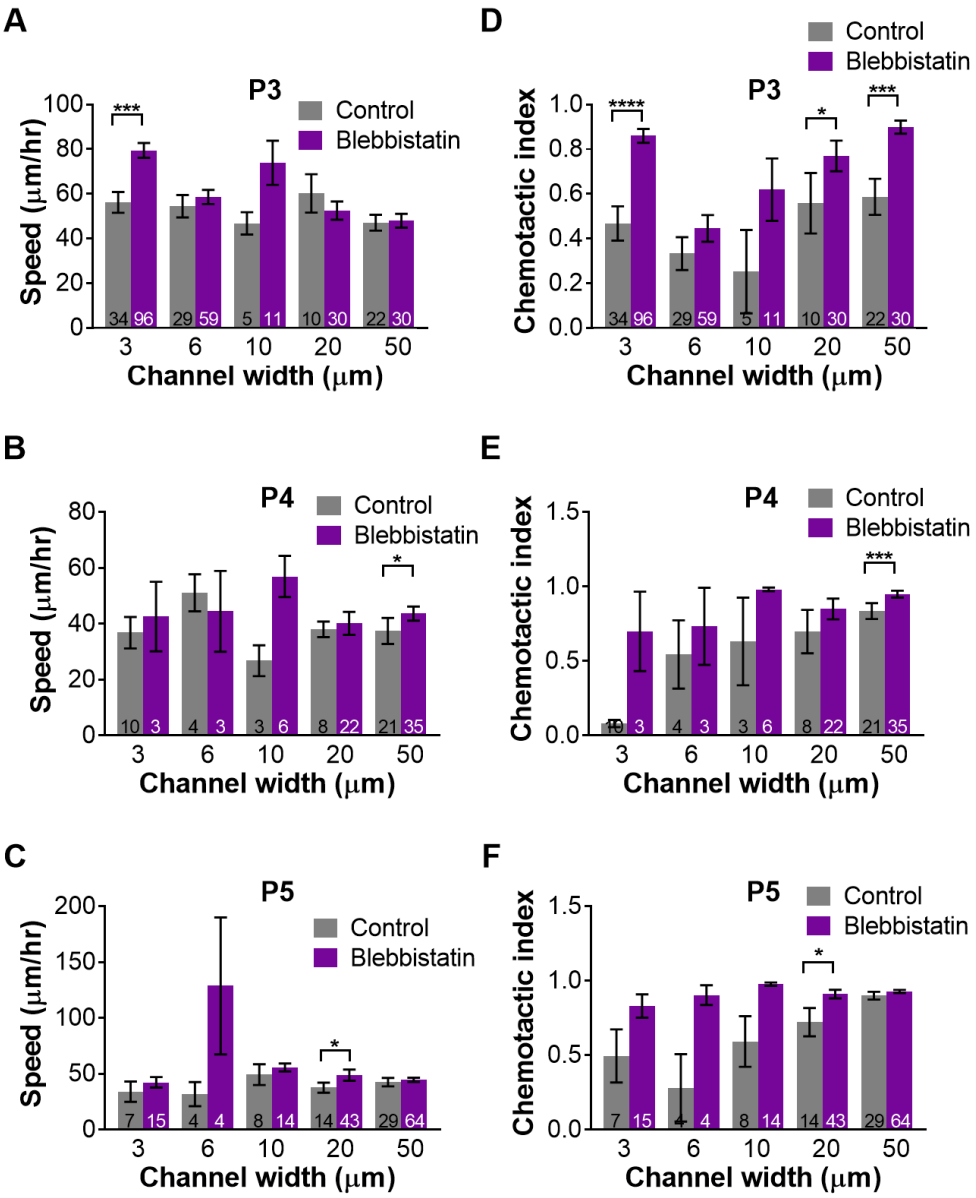

Figure 3.7 Effects of inhibition of myosin II contractility on hMSCs in Figure 3.6 broken out by passage. Effects of blebbistatin on speed for hMSCs of A) P3, B) P4, and C) P5. Effects of nocodazole on chemotactic index for hMSCs of D) P3, E) P4, and F) P5. Bar graphs report mean ± SEM. *P<0.05, ***p<0.001, ****p<0.0001.

3.3.6 Inhibition of actin polymerization completely disrupts MSC migration

We previously reported that migration of MDA-MB-231, S180, and CH2879 metastatic tumor cells in narrow (3 μm) microchannels can persist during inhibition of actin polymerization [26], [67]. To assess whether actin polymerization contributes to confined MSC migration, cells were treated with latrunculin-A after entering the microchannels in order to inhibit actin polymerization. The F-actin network was visibly disrupted in latrunculin-A-treated cells, compared to vehicle control cells, and latrunculin-A-treated cells appeared rounded with reduced area regardless of channel width (Fig. 3.8A, 3.8B). Immunostaining of α-tubulin similarly revealed significant disruption of the microtubule network in the latrunculin-A-treated cells (Fig. 3.8A, 3.8B). Migration speed of latrunculin-A-treated cells was significantly decreased in all channel widths in comparison with the vehicle control (Fig. 3.8C), and therefore cells were unable to migrate across the microchannels after latrunculin-A treatment, regardless of width. This trend was maintained for P3, P4, and P5 MSCs and thus only pooled data area shown. Table 1 provides a summary of our results indicating the effects of various cytoskeletal and contractile machinery on MSC migration and persistence.

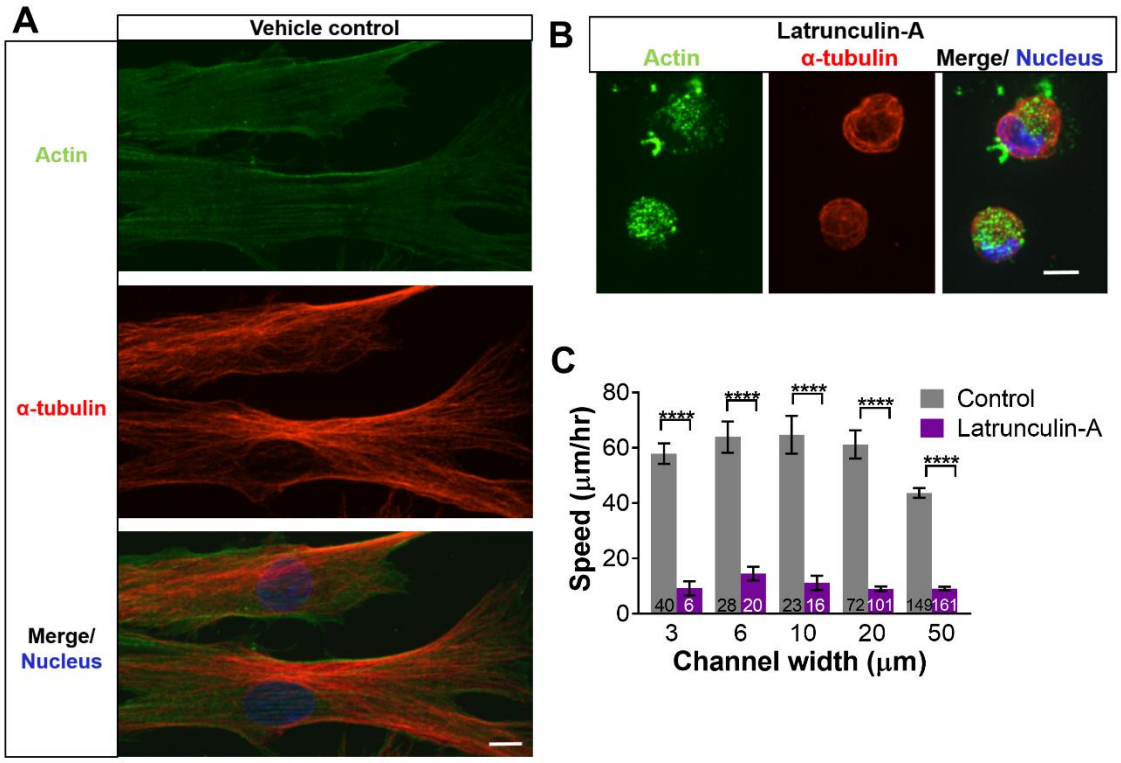

Figure 3.8 Effects of inhibition of actin polymerization on MSC migration in confinement. A) The cytoskeletal network in control cells and B) cells treated with latrunculin-A. In panels (A) and (B) cells were fixed and stained for α-tubulin (red), actin (green), and the nucleus (blue). In panels (A) and (B), scale bars represent 9 μm. C) Effect of latrunculin A on speed of MSCs as a function of channel width. Bar graphs report mean ± SEM. ****p<0.0001. For panel (C), number on individual bars indicates total number of pooled cells from N=3 independent experiments for each condition.

Table 3.1 MSCs migrate with different mechanisms in narrow channels than in wide channels.

Speed	Actin polymerization	Myosin II contractility	ROCK activity	Microtubule polymerization
Wide channels	(++++)	(-)	(----)	(++++)
Narrow channels	(++++)	(----)	No effect	No effect

Chemotactic index	Actin polymerization	Myosin II contractility	ROCK activity	Microtubule polymerization
Wide channels	No effect	(++++)	(++++)	(--)
Narrow channels	(+)	(++++)	(+)	No effect

(+) and (-) indicate relative magnitude of effects of each mechanistic process, on either speed (top half of table) or chemotactic index (bottom half of table).

3.3.7 pY-paxillin-positive focal adhesions are mostly absent in MSCs migrating in confinement.

Actin stress fibers typically terminate at focal adhesions on the cell's basal surface, and given the lack of a distinct actin stress fiber network in MSCs in narrow channels, we hypothesized that MSCs in confinement might also lack focal adhesions, a result we have previously reported for MDA-MB-231 tumor cells [26]. Thus, MSCs in the microchannel device were immunostained for tyrosine-phosphorylated (py)-paxillin, a protein which localizes to focal adhesions in cells. Tyrosine phosphorylation of paxillin is promoted by myosin II activity [221], and thus myosin II activity, and

possibly cell contractility, have been approximately indicated by the presence of py-paxillin-positive focal adhesions [65]. We found that mature py-paxillin-rich focal adhesions were mostly absent in cells migrating in 3 μm, 6 μm, or 10 μm narrow channels, where py-paxillin appeared punctate and disperse, with no visible F-actin stress fibers at which to terminate (Fig. 3.9A, 3.9B, 3.9C). Mature, py-paxillin-rich, linear focal adhesions appeared in MSCs migrating in wide channels (Fig. 3.9D, 3.9E). Furthermore, F-actin and py-paxillin were localized and aligned along the axis of migration of MSCs in 50 μm channels, indicative of mature focal adhesions (Fig. 3.9E). Accordingly, cells exiting narrow (3 μm) channels had few mature py-paxillin-rich focal adhesions on their basal surface in confinement, but exhibited mature focal adhesions at their unconfined leading edge (Fig. 3.9F). Interestingly, immediately upon exit from the channel, the actin stress fiber network appeared to begin to reform (Fig. 3.9F), though organization of stress fibers was much more disorganized in comparison with cells in wide channels or on a 2D surface (Fig. 3.1D, 3.4A, 3.6A, 3.8A). While the average area of focal adhesions decreased slightly with decreasing channel width (Fig. 3.9G), the percent cell area covered by focal adhesions decreased drastically with decreasing channel width (Fig. 3.9H).

Figure 3.9 Localization of py-paxillin-rich focal adhesions in MSCs in confinement. py-paxillin in MSCs migrating in A) 3 μm, B) 6 μm, C) 10 μm, D) 20 μm, and E) 50 μm wide channels. F) MSCs exiting 3 μm narrow channels. In panels (A-F) cells were fixed and stained for py-paxillin (red), actin (green), and the nucleus (blue). G) Average area of focal adhesions. H) Percentage of cell area occupied by focal adhesions. Bar graphs report mean ± SEM. *$p<0.05$. Scale bars represent 10 μm for panels (A-F).

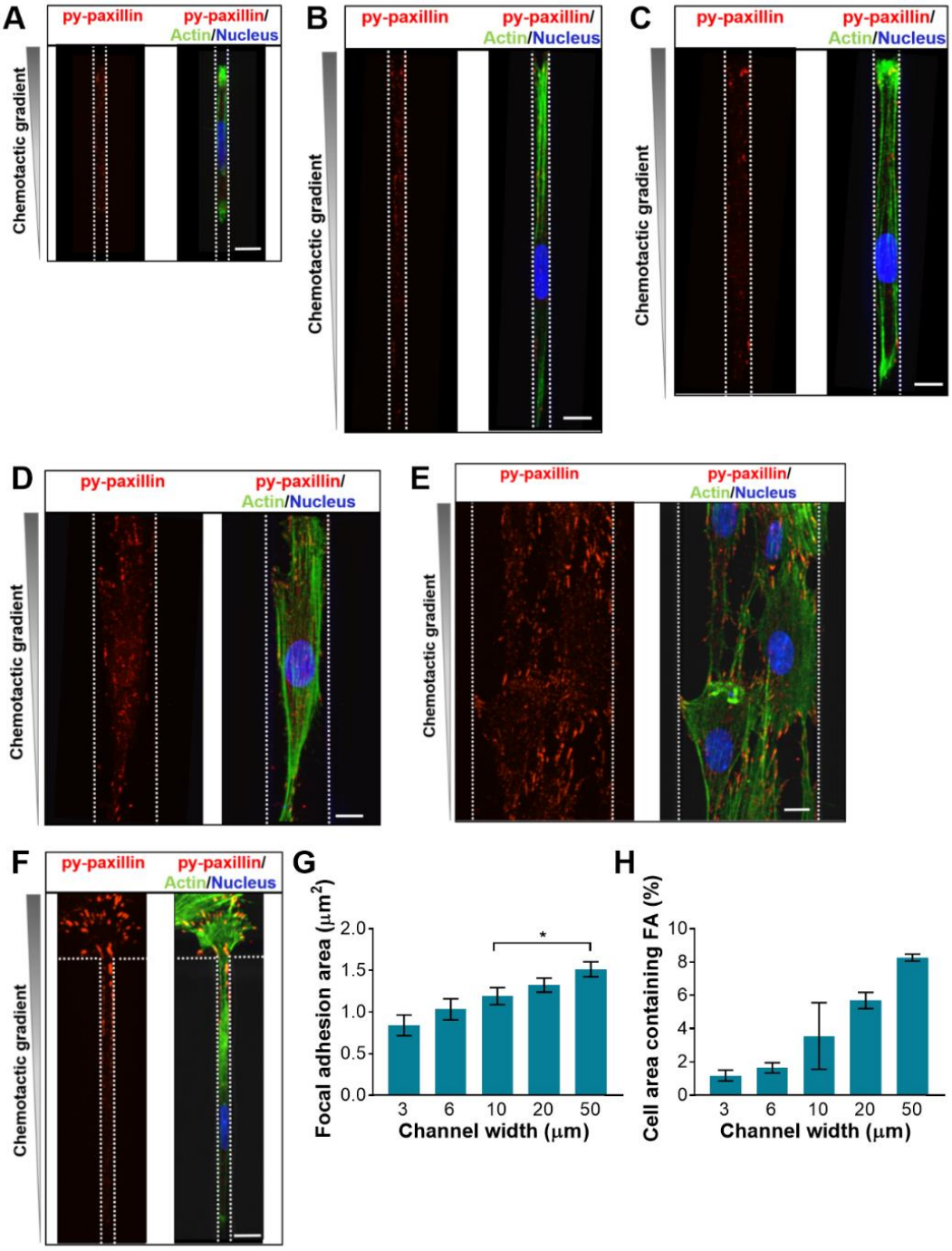
A
py-paxillin
py-paxillin/
Actin/Nucleus
Chemotactic gradient
B
py-paxillin
py-paxillin/
Actin/Nucleus
Chemotactic gradient
C
py-paxillin
py-paxillin/
Actin/Nucleus
Chemotactic gradient
D
py-paxillin
py-paxillin/
Actin/Nucleus
Chemotactic gradient
E
py-paxillin
py-paxillin/
Actin/Nucleus
Chemotactic gradient
F
py-paxillin
py-paxillin/
Actin/Nucleus
Chemotactic gradient
G
Focal adhesion area (μm²)
2.0
1.5
1.0
0.5
0.0
*
3
6
10
20
50
Channel width (μm)
H
Cell area containing FA (%)
10
8
6
4
2
0
3
6
10
20
50
Channel width (μm)

3.4 Discussion

Effective control of MSC localization in porous tissue engineered scaffolds and mobilization to distinct tissue sites during homing after clinical therapy requires an understanding of how MSCs navigate complicated 3D microenvironments with various physico-chemical stimuli, one of which is mechanical confinement. Mounting evidence has accumulated, demonstrating that other highly migratory cell types, such as metastatic cancer cells, can change their mode of migration, depending on the degree to which they are confined in a 3D environment (for recent reviews, see [12], [222]). In order to systematically evaluate the cytoskeletal elements contributing to migration of MSCs in confined vs. unconfined spaces, we introduced MSCs into chemotaxis-based, collagen-coated microfluidic devices containing microchannels of varying width and of fixed height, which we have characterized previously [25], [26]. The chemotactic gradient within the microfluidic devices is stable for 14 hours after addition into channels [25], which is approximately the length of time over which migration was analyzed. We subsequently treated the cells with pharmacological inhibitors of various migration machinery, visualized cytoskeletal organization, and quantified migratory potential. Our experiments have led to several novel and significant insights regarding MSC migration in confined spaces: (1) MSC actin and microtubule networks appear more diffuse rather than fibrillar in confined microchannels; (2) MSC migratory potential (i.e., speed and persistence) varies modestly with passage and degree of confinement; (3) inhibition of myosin II activity (via blebbistatin) leads to enhanced MSC migration, most significantly in confined microchannels; (4) inhibition of actin

polymerization (via latrunculin-A) leads to loss of migration in both confined and unconfined microchannels, while inhibition of microtubule polymerization (via nocodazole) leads to slowed migration in only unconfined microchannels; (5) mature, py-paxillin-rich focal adhesions are diminished in MSCs in confined microchannels.

Similar to past observations on metastatic tumor cells [26], MSCs displayed obvious differences in actin and microtubule cytoskeletal arrangement from wide channels to narrow channels. Confinement significantly altered MSC body morphological parameters, as MSCs exhibited a decrease in both area and inverse aspect ratio with decreasing channel width. Additionally, confinement significantly altered several MSC nucleus morphology parameters, and MSC nuclei began to deform in 50 μm wide channels. Unlike 3 μm, 6 μm, and 10 μm channels (where only one cell body can fit inside the channel width-wise), cells commonly migrate alongside each other in 20 μm and 50 μm wide channels. Accordingly, cell-cell interactions may have played a role in the observed nuclear deformation in wide (20 μm and 50 μm) channels. Future work could be aimed at determining whether nuclear deformation seen here in wide channels is due to channel crowding or if contact guidance of MSCs by channel walls can lead to cells "sensing" confinement wider than their cell body. We also note that while there is no statistical difference in cell inverse aspect ratio from 10 μm to 6 μm, or from 6 μm to 3 μm channels, the nucleus minor axis significantly decreases from 10 μm to 3 μm. Furthermore, the nucleus minor axis width equaled the microchannel width in 6 and 3 μm-wide channels, while in larger channels the nucleus minor axis was smaller than the channel width, thus indicating that full nuclear confinement along the minor axis length occurs at channel widths less than 10 μm. Thus, we hypothesize that

the modest decrease in MSC speed going from 6 or 10 μm channels down to 3 μm channels (i.e., in P3 and P4 cells) could be due to nuclear deformation rather than cell body deformation. Interestingly, MSC nuclei were strained along their minor axes, while the major axes maintained the same length in all levels of confinement. This is in agreeance with previous work, which showed that nuclei from 10 different cell types deform in an anisotropic manner and preferentially deform along their minor axis when an active force is applied by an atomic force microscope tip [101]. MSCs herein experience a passive force while migrating through microchannels, suggesting that anisotropic nuclear deformation can result from both active and passive forces.

Previous reports have indicated that MSC behavior can be passage dependent, as increased passage leads to loss of MSC proliferative capacity and multipotency [223], and also reduced exosome production and invasiveness [153], [216]. Therefore, we hypothesized that passage number would influence MSC migration, possibly as a function of confinement. Indeed, even in a range of "low passages" (i.e., 3, 4, and 5, corresponding to a population doubling level below 21), we observed significant differences in MSC speed and chemotactic index as a function of passage, with MSC speed decreasing with increased passage number for all channel widths except 3 μm, where there was no difference in cell speed across passages. MSCs have been shown to stiffen with increasing passage doubling (PD) from PD2 to PD17 due to coarsening of the cytoskeleton and increase in actin stress fiber radius [224]. Similarly, increased passage of MSCs to P100 has been reported to decrease the expression of genes associated with focal adhesion formation and cytoskeletal turnover [225]. Often, MSCs entered narrow channels, only to back out the way they came in, yielding a chemotactic

index of approximately 0.5. P3 MSCs were much more likely to enter and migrate through the narrowest channels, which would be expected if the MSCs were stiffening in the P3-P5 passage range, as suggested in Maloney *et al*. Meanwhile, for all passages, MSCs in wide channels more often migrated to the end of the channel and exited the other side.

Furthermore, the biphasic relationship between MSC speed and microchannel width is similar to other cell types, such as S180 sarcoma cells (unpublished data) and MDA-MB-231 highly metastatic breast tumor cells [146], [147], but in contrast to other cell types. For example, the biphasic trend is in contrast to human osteosarcoma cells in microchannels, where cell speed monotonically decreases in response to confinement [25], and NIH-3T3 fibroblasts on 1D microphotopatterned lines, where cell speed monotonically increases in response to spatial confinement [135]. Interestingly, contact guidance seems to determine the path of cell migration in channels that are larger than its cell body [141]. Future work should investigate whether the biphasic relationship seen here between cell migration speed and confinement is due to the presence of an optimal channel width that is narrow enough to present contact guidance cues, yet wide enough not to severely constrict the nucleus during migration.

Inhibition of microtubule polymerization via nocodazole did not affect MSC migration in confinement, but slowed cells in wide (20 μm and 50 μm) channels and decreased persistence in 50 μm channels. Nocodazole has been shown to decrease total traction force generation in cells on a planar surface and reduce actin intensity and organization in addition to loss of microtubule intensity and organization [226]. We hypothesize that the reduced speed of nocodazole-treated cells in wide channels may be

due to the loss of a defined fibrillar microtubule network or simultaneous loss of actin organization. Confinement alone, in absence of any drug treatments, led to dissolution of the microtubule network, and thus we hypothesize the effects of nocodazole treatment on cell migration may have been more apparent in MSCs in wide channels, where the microtubules were more organized and fibrillar. Contrarily, metastatic breast tumor cells migrating in confinement were significantly slowed by microtubule inhibiting drugs of concentrations comparable to the one used herein [26], [147]. MSC cell cycle has been shown to be only partially affected by nocodazole [227], whereas cancer cells enter cell cycle arrest post-nocodazole treatment [228], and hence there may be secondary effects on other processes such as mitosis that may explain the differential effects of nocodazole on confined migration between MSCs and cancer cells. Future investigations may elucidate the cause for discrepancies between these cell types.

On the other hand, nocodazole has also been suggested to increase contractility and traction force generation [217], [220] through a microtubule depolymerization-associated release of GEF-H1, which activates RhoA [217]–[219], so we explored whether our results were a direct effect of microtubule depolymerization, an effect of increased traction forces, or both. We chose an approach based on a previous study, which demonstrated that the nocodazole-mediated increase in cell contractility was abrogated by combined treatment with blebbistatin [220]. In our work, MSCs treated with both nocodazole and blebbistatin responded similarly to nocodazole-treated cells rather than blebbistatin-treated cells, and exhibited the largest changes in speed compared to control, especially in wide channels. Thus, we hypothesize that slowed MSC migration in wide channels after nocodazole treatment is not due to an increase in

contractility. Furthermore, these results suggest that decreased contractility via blebbistatin, or blebbistatin itself, may exacerbate the effects of microtubule inhibition in wide channels.

Inhibition of myosin II contractility via blebbistatin significantly enhanced MSC speed in 3 μm, 10 μm, and 50 μm wide channels. However, the percent change in speed for blebbistatin-treated cells from vehicle control cells was greatest for narrow channels, and decreased as channels widened. Additionally, blebbistatin enhanced MSC persistence in all channel widths except 6 μm. This result is supported by previous work, which showed that the inhibition of myosin II via blebbistatin in metastatic breast tumor cells significantly increased cell speed in confinement [26]. Cell softening has been associated with blebbistatin treatment, [229], which may have allowed cells to more easily squeeze through the narrowest channels. Conversely, blebbistatin had no effect on neural stem cell speed in microtubes [148], perhaps demonstrating the different roles myosin II contractility may play in different stem cell types. Our results for nocodazole and blebbistatin treatment are both in opposition to what has been seen for NIH-3T3 fibroblasts migrating on a 1D line or in 3D matrix [135].

Cells were treated with Y27632 in order to inhibit ROCK, a signaling protein upstream from myosin contractility. Inhibition of ROCK enhanced MSC migration in wide channels, with dissimilar effects on cell speed than was seen with blebbistatin treatment. Similar results were found for MSCs migrating on a planar surface under shear stress [38] and MSCs migrating in a chemotaxis assay [230], where inhibition of ROCK increased MSC migration. Conversely, metastatic breast tumor cells were shown to have a significantly increased speed in response to Y27632 in 3 μm wide channels

[26]. However, other studies have shown Y27632 to reduce the metastatic potential of cancer cells [231], and increased ROCK expression is correlated with poor clinical outcome in breast cancer patients [232]. We found that ROCK inhibition increased MSC persistence and increased the percentage of cells that entered channels (data not shown), similar to blebbistatin. Also similar to blebbistatin treatment, cell softening has been observed after Y27632 treatment [233], which may have allowed cells to more easily deform while squeezing into the narrowest channels.

Inhibition of actin polymerization via latrunculin-A halted MSC migration, regardless of channel width. This is in accordance with previous work investigating the migration of neural stem cells in microtubes [148]. However, these results differ from the behavior of metastatic breast cancer and sarcoma cells, which were able to migrate efficiently in confinement despite having been treated with latrunculin-A [26], [67]. Sarcoma cells were shown to harness ion pump and aquaporin function to migrate in confinement via an osmotic engine model [67]. Though we did not assess ion pump and aquaporin expression or the osmotic engine model in the MSCs, our results suggest that a water permeation-based mechanism in the absence of actin polymerization is not sufficient to enable migration in this benign cell type.

Given the diffuse actin network in narrow channels, we hypothesized that mature focal adhesions would be absent in cells in narrow channels. Indeed, the presence of mature, py-paxillin-rich focal adhesions in MSCs decreased with decreasing channel width. Similarly, metastatic breast cancer cells display smaller and less mature focal adhesions as confinement increases [26]. In 3D gels, breast epithelial cells and

fibrosarcoma cells demonstrate a decrease in focal adhesion formation and a more disperse distribution of focal adhesion associated proteins [84], [234].

3.5 Conclusion

In summary, we have shown that MSCs respond differently to pharmacological inhibitors of cytoskeletal and contractile machinery in narrow vs. wide microchannels, suggesting that cells rely on these machinery to different degrees in confined vs. unconfined microenvironments. Inhibition of actin significantly hindered cell migration in both confined and unconfined microchannels. However, MSC migration in narrow channels was overall less sensitive to perturbations to the MSC cytoskeleton than MSCs in wide channels. These insights could allow for specific control of MSC infiltration into tissue engineered scaffolds and could also inform whether the degree of confinement in microchannels between anatomical structures directs cell migration during homing *in vivo*. Furthermore, it is possible that physical confinement, in conjunction with other microenvironmental cues, can be exploited to engineer and direct stem cells for use in regenerative therapies and/or *in vitro* models. A next step towards this goal is to further explore how mechanical confinement impacts nuclear morphology (Chapter 4), since deformation of the cell nucleus can influence many processes leading to altered cell behavior.

Chapter 4: Nuclear Deformation in Response to Mechanical Confinement is Cell Type Dependent[3]

4.1 Introduction

The way a cell senses and responds to a physical force can vary based on cell type or tissue microenvironment, potentially altering downstream events such as migration, homeostasis, differentiation, proliferation, or tumorigenesis [235], [236]. An important element in the force transmission pathway is the nucleus, the largest and stiffest cell organelle [237]. The nucleus has been characterized as a mechanosensor of the cell and transmits external forces emanating from the cellular microenvironment to the nuclear envelope housing the chromatin [6], [105], [126]. Mechanical forces propagate from the extracellular matrix (ECM) to mechanosensitive focal adhesions and cytoskeletal structures. Cytoskeletal structures are then connected to the nuclear lamina, below the nuclear envelope, through the linker of nucleoskeleton to cytoskeleton (LINC) complex [6]. Additionally, direct force application to the nucleus can induce chromatin stretch and transcriptional upregulation of a reporter transgene without involvement of the nucleo-cytoskeleton network [238]. Isolated and intracellular nuclei can deform anisotropically in response to both active and passive externally-applied forces. Active forces include atomic force microscopy (AFM) [101], biaxial stretching devices [239], and magnetic tweezers [240], while passive forces include glass

[3] Adapted from M.T. Doolin*, T.S. Ornstein*, and K.M. Stroka, Nuclear Deformation in Response to Mechanical Confinement is Cell Type Dependent, Cells, 8(5): 427 (2019) (* indicates co-first authorship by undergraduate student mentored by Mary Doolin).

microtubes [241], three-dimensional (3D) hydrogels [128] or microfluidic devices [25], [26], [64], [146], [173]. Using AFM and micropipette nuclear aspiration, the nucleus can physically deform with as little as a few nanonewtons of force [101], [242]. Specifically, differentiated and undifferentiated nuclei alike preferentially deformed along their minor (short) axis in reaction to an applied force [101], [239], [243]. We have previously shown that the nuclear major (long) axis in human mesenchymal stem cells (MSCs) maintains a constant length with increasing degrees of lateral confinement [64]. In contrast, we have also shown that nuclear major (long) axis in mouse sarcoma (Ab3) cells increases in length with increasing degrees of lateral confinement [173]. While anisotropic deformation has been found to be inherent to nuclei of many different cell types, nuclear axis lengths in three dimensions have not been quantified in confinement.

Physical confinement is experienced by cells *in vivo* in many contexts. For example, cells may be confined within channels between connective tissue and the basement membrane of muscle, nerve and epithelium [9], [10], during cell intravasation and extravasation [11], in the tumor microenvironment [12], and in interstitial tissue [13]. Indeed, the migration modes of several cell types is altered by the degree of confinement induced [9], [13], [66], [67], [244]. Although a vast array of cell types experience mechanical confinement, the components involved in mechanotransduction can differ among cell types. Cytoskeleton prestress, the composition of the LINC complex, and the organization of the nucleoskeleton can differ based on cell type [240]. Specifically, increased expression of lamin-A has been shown to correlate with increased nuclear, cell, and tissue stiffness [245]. Furthermore, the sensitivity of a

particular cell type to nuclear anisotropy is influenced by lamin-A expression as well as chromatin organization, and lamin-A over-expression results in an increase in strain along the nuclear minor axis [101]. Additionally, the deformation of the nuclear major and minor axes can be influenced by microtubule and actin structures. In short-term biaxial stretching experiments with epithelial monolayers, it was discovered that microtubules resist deformation along the major axis while actin resists deformation along the minor axis [239]. Microtubule and actin networks have also been known to regulate cell volume, which can dynamically alter nuclear morphology [246]. In micro-engineered 3D environments, the ratio of cellular to nuclear volume is conserved, but the specific volumes of the nucleus and cell is dependent on cell type [247]. It remains unknown whether these cytoskeletal proteins dictate nuclear deformability and nuclear volume in confined migration and if their role is different in varying cell types.

In this work, we characterized the 3D morphology of nuclei within various cell types in response to physical confinement. Cell types were chosen for experimentation due to their differences in tissue origin, organism origin, disease pathology, and level of differentiation potency. To recapitulate and control the degree of confinement experienced by cells *in vitro*, we employed polydimethylsiloxane (PDMS)-based microchannels that were 30, 60, 100, 200, or 500 μm^2 in cross-sectional area and previously designed and characterized [25], [26]. Nuclear deformation in the XYZ planes as well as nuclear area and volume were quantified using immunofluorescence and Image J software. The effects of myosin II inhibition and microtubule depolymerization on nuclear deformation were additionally investigated. Our results suggest that cell identity may possess a larger role in governing nuclear deformation

than the force of confinement alone and that actin and microtubules may not independently modulate nuclear anisotropy in confined cell migration.

4.2 Materials and methods

4.2.1 Cell culture and reagents

Bone marrow-derived human MSCs (donor: 20 year- old female) were purchased (RoosterBio Inc., Frederick, MD) and experimentally used up until passage 5, which is when the population reaches a doubling level of 20. Human breast adenocarcinoma highly metastatic cells (MDA-MB-231 cells; American Type Culture Collection, Manassas, VA, USA) were used up to a passage of 30 after purchase. Finally, adult mouse fibroblasts (L929 cells) were gifted from Dr. John Fisher (Fischell Department of Bioengineering at the University of Maryland, College Park) and were used up to a passage of 10.

All cell types were cultured in either T-25 or T-75 polystyrene, plasma-treated flasks (VWR, Radnor, PA) and grown in medium comprised of 89% Dulbecco's modified Eagle's medium with high glucose (DMEM; ThermoFisher Scientific, Waltham, MA), 10% heat inactivated fetal bovine serum (FBS; ThermoFisher Scientific), and 1% penicillin/streptomycin 1000 U/mL (P/S; ThermoFisher Scientific). All cells were cultured at 37 °C, 50% humidity, and 5% CO2: 95% air and passaged at or below 90% confluency. Cells to be passaged were first washed in phosphate buffered saline (PBS; VWR, Radnor, PA) and detached from the flasks with 0.25% Trypsin-

EDTA (ThermoFisher Scientific), except for MSCs, which were treated with TrypLE Express Enzyme (ThermoFisher Scientific).

4.2.2 Microfluidic device manufacturing and cell seeding

Polydimethylsiloxane (PDMS) microfluidic devices were prepared according to previously described protocols [25], [26], [64]. The devices contain a variety of channel widths or a repeating, single channel width. All photolithography procedures were carried out in the University of Maryland Nanocenter FabLab. In summary, separate masks were designed in AutoCAD (AutoDesk, San Rafael, CA) for the channels (first feature) and the seeding and collection reservoirs (second feature). A 4-inch diameter silicon wafer (University Wafer, Boston, MA) was spin coated with a 10-mm thick layer of SU-8-3010 negative photoresist (MicroChem, Westborough, MA), and the mask representing the channels was placed over the coated wafer using the EVG620 mask aligner (EVG Group, Albany, NY). The layers were then selectively exposed to UV to complete crosslinking of the SU-8-3010 in the areas dictated by the mask. Remaining SU-8-3010 was then dissolved using SU-8 developer (MicroChem). To create the second feature, a layer of SU-8 3025 negative photoresist (MicroChem) was spin coated onto the wafer. Then the EVG620 mask aligner was used to place the mask of the seeding and collection reservoirs over the coated wafer. The system was once again selectively exposed to UV and the extra SU-8-3010 was removed. The completed wafers were silanized using 97% tridecafluoro-1,1,2,2, tetrahydrooctyl-1-trichlorosilane (UCT Inc., Bristol, PA, USA) overnight in a vacuum desiccator. The finished silicon masters contained the mold for manufacturing multi- or single

microchannel devices, defined by the widths of their channels, which included 50, 20, 10, 6, and 3 μm. Regardless of channel width, all channels were 10 μm in height and 200 μm in length.

From the silicon masters, PDMS devices were fabricated. PDMS (Krayden, Denver, CO, USA) was weighed and mixed at a 10:1 base: curing agent ratio, poured into a silicon master, degassed in a vacuum desiccator for approximately 30 minutes and baked at 80 °C for at least 1 hour. Devices were cut out of the silicon master and holes were punched into the PDMS to create cell and media inlets and outlets. Microchannels and 25 mm by 75 mm #1 glass coverslips (Electron Microscopy Sciences, Hatfield, PA) were washed with ethanol and reverse osmosis or MilliQ water, dried for 5 minutes at 80°C and plasma treated in the plasma cleaner (Harrick Plasma, Ithaca, NY) for 2.5 minutes. The devices were then bonded to the glass coverslips by applying pressure for 3 minutes and UV sterilized for 10 minutes. Finally, devices were coated with 20 ug/mL collagen I (Sigma Aldrich, St. Louis, MO) for 1 hour at 37°C. After incubation, collagen was removed, devices were washed twice with PBS, and cells were immediately seeded into the cell inlet.

During the collagen I coating incubation time period, cells were prepared for device seeding. Cells were removed from the incubator, washed once with PBS and detached with the addition of trypsin for 5 minutes. FBS-containing media was then added, and the cells were centrifuged at 1000 RPM for 5 minutes. Cells were resuspended in FBS-free media, counted, centrifuged again, and resuspended again in FBS-free media to yield 100,000 cells per 25 μl. Twenty five microliters of cell suspension was pipetted into the cell inlets of the devices and incubated. After 5

minutes, the cell suspension was removed and 50 µl of FBS-free media was added to the cell inlet and bottom two media inlets, and 50 µl of FBS-containing media was added to the topmost inlet to create a chemoattractant gradient. For studies including blebbistatin (50 µM, Sigma Aldrich) or nocodazole (10 µM, Sigma Aldrich), the inhibitor was added to both FBS-free and FBS-containing media, such that it was in equal concentrations throughout the device. Dimethyl sulfoxide (Sigma Aldrich) served as the vehicle control in all experiments. Cells were incubated overnight to allow for migration through the channels. All microchannel devices containing cells were cultured at 37°C, 50% humidity, and 5% CO2: 95% air.

4.2.3 Immunofluorescence

Following an overnight incubation period, cells and media were removed from the inlets and outlets. In all future steps listed below, when a reagent was added, it is implied that the same volume was added to all wells. Cells were washed once with PBS and immediately fixed with 3.7% formaldehyde (Fisher Scientific, Fair Lawn, NJ). After a 10-minute incubation at room temperature, cells were washed thrice with PBS. Cells were permeabilized by the addition of 0.5% Triton-X 100 (Sigma Aldrich) for 5 minutes, followed by three PBS washes. Nonspecific binding was then blocked with 2.5% goat serum (Abcam, Cambridge, MA) for 1 hour at room temperature. Primary antibody diluted in PBS and 1% goat serum was added and samples were incubated overnight at 4°C. Primary antibodies used were mouse anti-α-tubulin (ThermoFisher Scientific #A11126, 1:100 or 1:200). The next day, cells were washed twice or thrice in PBS, incubated in 2.5% goat serum for at least 1 hour and incubated with AlexaFluor

488 Phalloidin (ThermoFisher Scientific, 1:500), Hoechst (ThermoFisher Scientific, 1:500 or 1:2500) and a fluorescently labeled secondary antibody for 1 hour. Secondary antibody and dilution used was AlexaFluor 568 goat anti-mouse (ThermoFisher Scientific #A11004, 1:200). Cells were washed twice or thrice in PBS and imaged immediately or within a few days when Fluoromount-G (ThermoFisher Scientific) was added for preservation.

4.2.4 Imaging

Widefield or confocal microscopy was used to extrapolate nuclear dimensions. MSC, MDA-MB-231 and L929 images for 2D measurement extrapolation were acquired on an Olympus IX83 microscope (Olympus, Tokyo, Japan) using a 40x or 60x oil immersion objective. All Z stack images were taken using a PerkinElmer UltraVIEW Vox confocal spinning disk microscope (PerkinElmer, Waltham, MA) with a 100x oil immersion objective. Z-step size was 0.1 μm or 0.2 μm, and the boundaries of the stack were defined as the planes in which no staining could be observed. Use of the PerkinElmer confocal microscope was performed courtesy of the University of Maryland imaging core. In all experiments, fluorescence intensity and sensitivity were adjusted manually to optimize visualization.

4.2.5 Data analysis in 2D

All data analysis for calculating 2D nuclear major axis length, minor axis length and area was completed in ImageJ using the built-in morphology measurements. Widefield images were used for analysis. Nuclei were manually traced and measured,

then dimensions originally output as pixels were converted into microns for analysis. Specifically, to calculate nuclear major and minor axes lengths, ImageJ fitted the traced nuclei to ellipses.

4.2.6 Data analysis in 3D

ImageJ was used to quantify volume from acquired Z-stacks. First, the edges of Z-stacks were cut according to the built in ImageJ feature, Find Edges. This was completed to minimize the effects of background fluorescence during thresholding. The top and bottom planes were defined as the first and last image plane, respectively, in which an edge of the nucleus was visible. Next, IsoData thresholding was performed. IsoData threshold can be expressed mathematically as $Threshold = \frac{average\ background + average\ objects}{2}$. This automated thresholding method was chosen to exclude any bias in the analysis and for its ability to threshold consistently for nuclei in all channel widths. Thresholding was calculated based on the middle plane of the stack and applied to all other planes in the stack. After thresholding, the ImageJ feature, Fill Holes, was used to correct any large holes in the interior of the nuclei caused by excess thresholding or low fluorescence signal. The ImageJ plugin "3D Object Counter" was then used to automatically calculate volume based on the number of voxels of the object. 3D object Counter also yielded the length, width, and height of the object bounding box. This methodology was validated by seeding 10 μm, yellow-green fluorescent polystyrene microspheres (ThermoFisher Scientific) inside the channels and completing a similar imaging protocol to experimental conditions. In a 50 μm wide channel and a Z step size of 0.15 μm, the volume calculated of the microsphere with the described

methodology was 570 μm^3, in comparison to the expected volume of 524 μm^3, which yields a percent error of 8.8%.

4.2.7 Statistical Analysis

To compare nuclear dimensions in different channel widths, a one-way ANOVA, in the case of normally distributed data, or Kruskal-Wallis test with a Dunn's post hoc test, in the case of non-normally distributed data, was completed. Data were pooled from at least three independent trials, except in 2D data for MSC and MDA-MB-231, which were pooled from two independent trials. A significance level of 0.05 was used. Error bars report the standard error of the mean. Select graphs were unable to fit all comparisons, in which case we refer readers to the supplementary tables for full statistical analysis.

4.3 Results

4.3.1 Nuclear deformation as a function of confinement is cell type-dependent

We have previously shown that MSC morphology and cytoskeletal arrangement is altered with increasing confinement [64], and here we aimed to determine whether cells from different species origin, tissue location, and disease state display similar behaviors. We chose to examine MSCs, MDA-MB-231 cells, and L929 cells. These cell types were chosen due to their differences in tissue origin (bone marrow, mammary gland, and subcutaneous connective tissue, respectively) organism origin (human, human, and mouse), and disease pathology (healthy, cancerous, and healthy).

Furthermore, these cells are extensively used throughout literature in many different applications and therefore we found them to be relevant cell models. We first visualized nuclear morphology of the three cell types within microchannels of varying width (Fig. 4.1). We note that 50 μm wide channels served as our "unconfined" control, where cells were not constrained in the x-y plane. Indeed, cell nuclei in 3 μm narrow channels consistently appeared quite elongated and ellipsoidal in the x-y plane (Fig. 4.1A, 4.1C, 4.1E). As the channels widened, the nucleus became more circular in the x-y plane as the cells themselves became more spread (Fig. 4.1B, 4.1D, 4.1F). We first quantified whether there were differences in x-y nucleus area, major axis length, or minor axis length (Fig. 4.1G) with increasing confinement (i.e., decreasing channel width). In all cell types, nucleus area decreased with increasing confinement, albeit with different levels of significance (Fig. 4.1H and Table 4.1). Similarly, the nucleus minor axis decreased with increasing confinement for all cell types (Fig. 4.1I and Table 4.2). Note that due to manual tracing of widefield microscopy images, some minor axis values were slightly above their respective microchannel width. We maintain that this variability is consistent across all channel widths. Interestingly, cell type-dependent trends emerged for nucleus major axis length. MSCs and MDA-MB-231 cells maintained a fairly constant nucleus major axis length as a function of channel width, with some exceptions (Fig. 4.1J and Table 4.3). L929 cells showed a marked increase in nucleus major axis length with increasing confinement (Fig. 4.1J and Table 4.3). These trends in L929 cell nuclei are similar to what we have previously shown in mouse sarcoma cells [173]. In summary, the nucleus major axis deformed differently in response to confinement for MSCs and MDA-MB-231 cells than for L929 cells (and

our previously published mouse sarcoma cells). Having made these 2D observations in the x-y plane, we next investigated if there were cell type-dependent differences in nucleus height and volume during deformation in confinement.

Figure 4.1 Quantification of 2D nuclear morphology in confinement. Images are shown for MSCs within microchannels of width A) 3 μm and B) 50 μm. Images are shown for L929 cells within microchannels of width A) 3 μm and B) 50 μm. Images are shown for MDA-MB-231 cells within microchannels of width E) 3 μm and F) 50 μm. In panels (A-F) cells were fixed and stained for actin (green) and the nucleus (blue). Color channels were altered individually for optimal visualization. Scale bar represents 10 μm in panels (A-F). G) Definition of nuclear major and minor axis. Also shown is quantification of nucleus H) area, I) minor axis, and J) major axis of MSCs, MDA-MB-231 cells, and L929 cells. Markers on line graphs report mean ± SEM of n cells, pooled from N≥2 independent experiments with n(3 μm, MSC)=9, n(3 μm, MDA-MB-231)=178, n(3 μm, L929)=26, n(6 μm, MSC)=25, n(6 μm, MDA-MB-231)=114, n(6 μm, L929)=21, n(10 μm, MSC)=21, n(10 μm, MDA-MB-231)=98, n(10 μm, L929)=80, n(20 μm, MSC)=104, n(20 μm, MDA-MB-231)=288, n(20 μm, L929)=44, n(50 μm, MSC)=289, n(50 μm, MDA-MB-231)=620, n(50 μm, L929)=136. Full statistical information for panels H-J is provided in Tables 4.1-4.3. Thea Ornstein captured microscopy images and analyzed data.

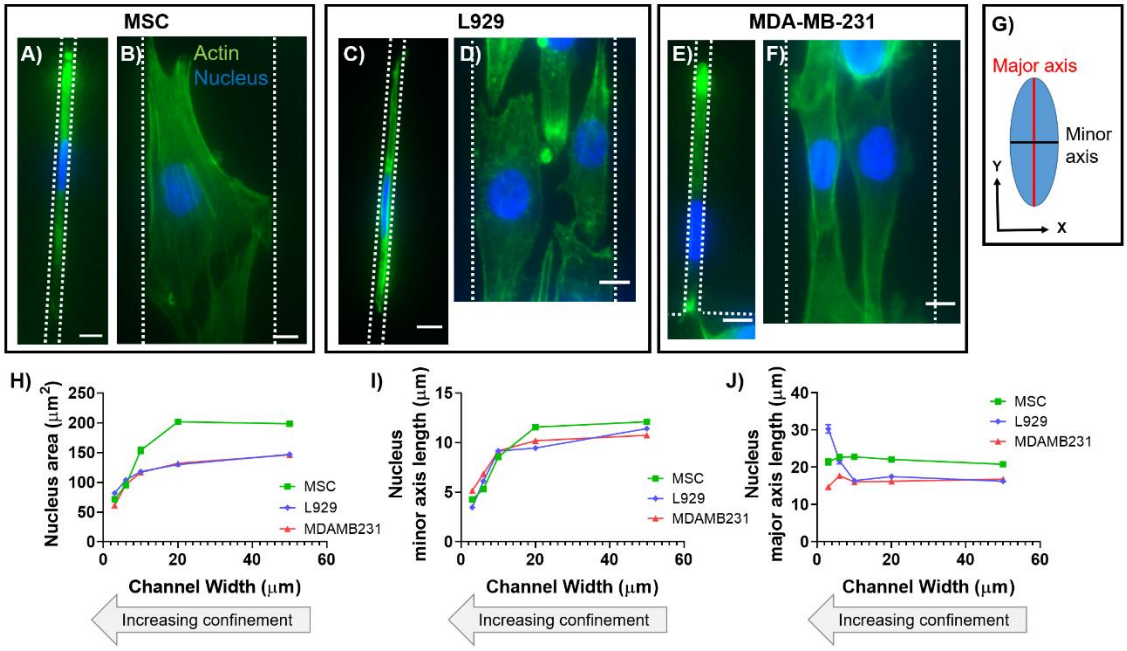

Table 4.1 Statistics for nucleus area for MSCs, L929 cells, and MDA-MB-231 cells, ns=not significant, *p<0.05, **p<0.005, ****p<0.0001.

Area	MSC	L929	MDAMB231
3 vs 6 μm	ns	ns	****
3 vs 10 μm	ns	****	****
3 vs 20 μm	****	****	****
3 vs 50 μm	****	****	****
6 vs 10 μm	ns	ns	**
6 vs 20 μm	****	*	****
6 vs 50 μm	****	****	****
10 vs 20 μm	****	ns	*
10 vs 50 μm	****	****	****
20 vs 50 μm	ns	ns	ns

Table 4.2 Statistics for nucleus minor axis for MSCs, L929 cells, and MDA-MB-231 cells, ns=not significant, *p<0.05, **p<0.005, ***p<0.0005, ****p<0.0001.

Minor axis	MSC	L929	MDAMB231
3 vs 6 µm	ns	ns	**
3 vs 10 µm	****	****	****
3 vs 20 µm	****	****	****
3 vs 50 µm	****	****	****
6 vs 10 µm	****	***	****
6 vs 20 µm	****	****	****
6 vs 50 µm	****	****	****
10 vs 20 µm	****	ns	**
10 vs 50 µm	****	****	****
20 vs 50 µm	*	****	ns

Table 4.3 Statistics for nucleus major axis for MSCs, L929 cells, and MDA-MB-231 cells, ns=not significant, *p<0.05, **p<0.005, ***p<0.0005, ****p<0.0001.

Major axis	MSC	L929	MDAMB231
3 vs 6 µm	ns	ns	****
3 vs 10 µm	ns	****	ns
3 vs 20 µm	ns	****	ns
3 vs 50 µm	ns	****	***
6 vs 10 µm	ns	****	***
6 vs 20 µm	ns	*	****
6 vs 50 µm	*	****	***
10 vs 20 µm	ns	ns	ns
10 vs 50 µm	**	ns	ns
20 vs 50 µm	***	ns	ns

4.3.2 Nuclear deformation in 3D is cell type-dependent

To investigate the effects of confinement on nuclear height and volume, we narrowed our experimental cell lines to two. We selected MSCs and L929 cells due to their opposing trends in major axis length with increasing confinement, as measured from 2D images. Using confocal microscopy, we captured z-stacks of cells within each

microchannel width. Using ImageJ, we quantified nuclear volume and the length, width, and height of the nucleus (Fig. 4.2). Due to a high level of background fluorescence, we calculated nuclear volume of a shortened z-stack, as indicated by the "Find edges" tool in ImageJ. However, the images herein show the full z-stack. Therefore, a high amount of background fluorescence is evident above the confining microchannel in some figures. Both MSCs and L929 cells in 3 μm narrow channels appeared elongated, with diffuse microtubule structures and a defined actin ring around the cell perimeter (Fig. 4.3A-B and Supplementary Movie S1-S2, captions for all movies found in the Appendix). As the channels widened, more actin stress fibers formed within MSCs, and the MSC nucleus became flattened in the z-axis (Fig. 4.3C and Supplementary Movie S3). In contrast, L929 cell nuclei maintained similar height in the z-axis as channels widened, and their cytoskeletal structures remained more diffuse than MSCs (Fig. 4.3D and Supplementary Movie S4). Length was comparable to major axis in 2D and width was comparable to minor axis in 2D. Nuclear volume in 20 μm wide channels was significantly increased in both MSC and L929 cells when compared to 3 μm wide channels (Fig. 4.3E-F). Additionally, L929 nuclei within 10 μm or 50 μm wide channels were significantly larger in volume than nuclei within 3 μm wide channels (Fig. 4.3F). In MSCs, nuclei in 3 μm and 6 μm channels were significantly smaller in width than MSCs in 50 μm channels, but nuclear length and height were unchanged with decreasing channel width (Fig. 4.3G and Tables 4.4-4.5). Similarly, L929 cell nuclei in 3 μm, 6 μm, and 10 μm wide channels all had significantly shorter widths than cell nuclei within 20 μm channels (Fig 3.3H and Table 4.6-4.7). In contrast to MSCs, the L929 nuclear length in 3 μm wide channels was significantly longer than nuclei in 20 μm or 50 μm wide

channels (Fig. 4.3H and Table 4.6-4.7). Despite similar trends in nuclear volume, L929 cells and MSCs differed in nuclear dimensionality. MSCs remained rather anisotropic in all channel widths; MSC nuclear length was significantly longer than nuclear width and height in all channel widths (Fig. 4.3G). L929 cell nuclei had similar anisotropic behavior in 3, 6, and 10 μm wide channels. However, L929 nuclei in 20 and 50 μm wide channels were isotropic, with no differences in nuclear length, width, or height (Fig. 4.3H). Upon observing differences in nuclear volume and dimensionality with increasing confinement, we questioned if this behavior would be altered by perturbations to the cytoskeleton.

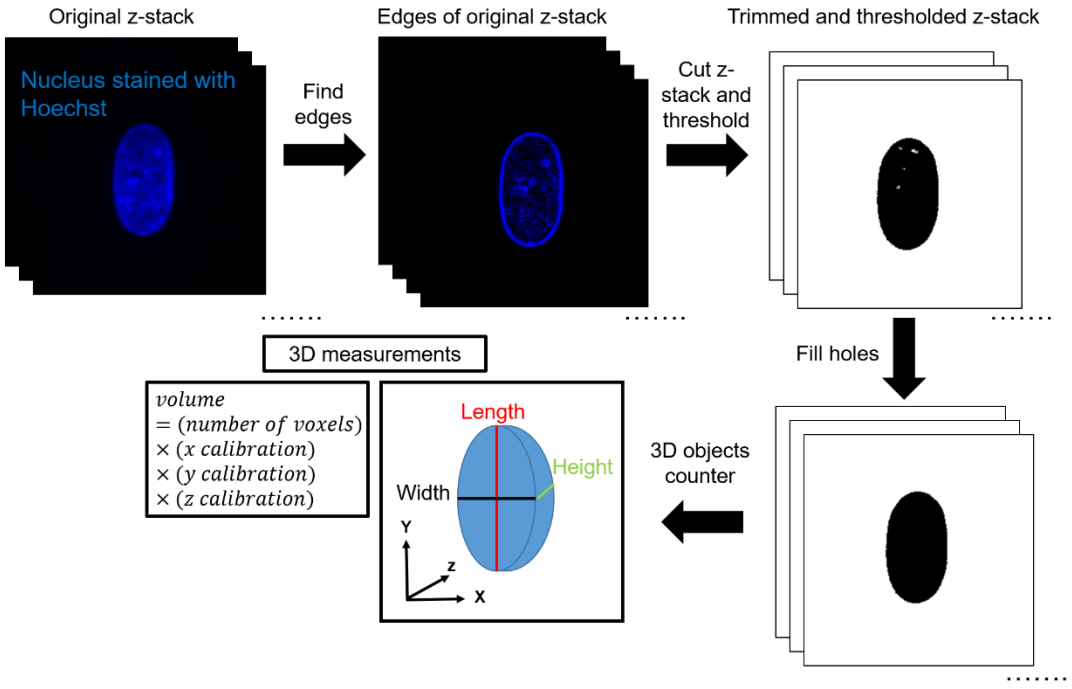

Figure 4.2 Workflow for calculating 3D morphological parameters of the nucleus.

Figure 4.3 Orthogonal views of A) MSC or B) L929 cell within 3 μm narrow channel. Orthogonal views of C) MSC or D) L929 cell within 50 μm wide channel. In panels (A-D) cells were fixed and stained for α-tubulin (red), actin (green), and the nucleus (blue). Color channels were altered individually for optimal visualization. Scale bar represents 10 μm and applies to panels (A-D). 3D renderings of nuclei shown in panels A-D are provided in Supplemental Movies S1-S4. Also shown are quantifications of the nucleus volume of E) MSCs or F) L929 cells, along with nucleus length, width, and height of G) MSCs or H) L929 cells. Dot plots report mean ± SEM. *p<0.05, **p<0.005, ***p<0.0005, ****p<0.0001. (Each dot indicates one cell, pooled from N≥3 independent experiments). Full statistical information for panels G-H is provided in Tables 4.4-4.7. Thea Ornstein captured microscopy images.

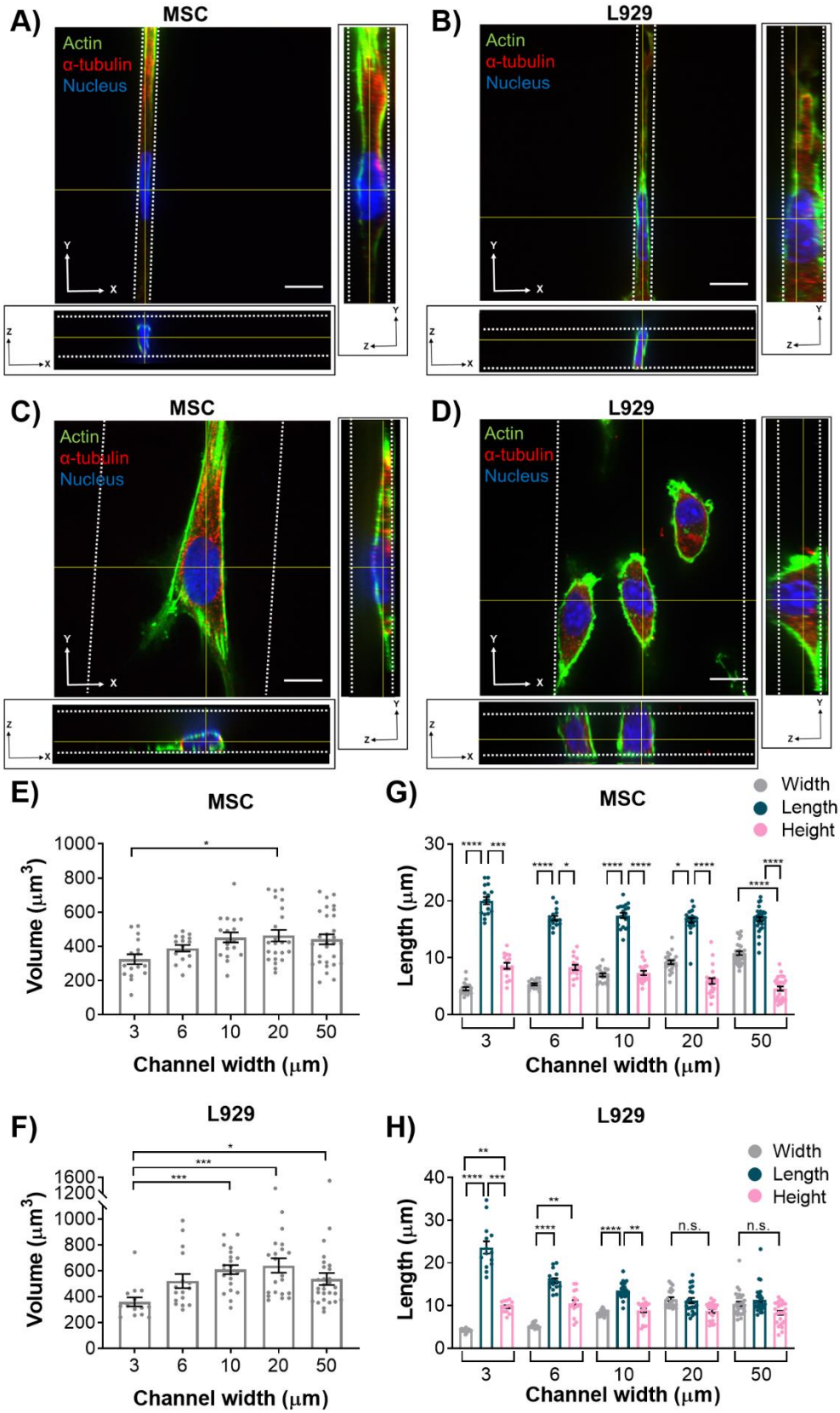
A)
MSC
Actin
α-tubulin
Nucleus
B)
L929
Actin
α-tubulin
Nucleus
C)
MSC
Actin
α-tubulin
Nucleus
D)
L929
Actin
α-tubulin
Nucleus
E)
MSC
Volume (μm3)
Channel width (μm)
F)
L929
Volume (μm3)
Channel width (μm)
G)
MSC
Width
Length
Height
Length (μm)
Channel width (μm)
H)
L929
Width
Length
Height
Length (μm)
Channel width (μm)
n.s.

Table 4.4 Statistics for MSC nucleus dimensions, ns = not significant, **p<0.005, ****p<0.0001.

	Width	Length	Height
3 vs 6 µm	ns	ns	ns
3 vs 10 µm	ns	ns	ns
3 vs 20 µm	**	ns	ns
3 vs 50 µm	****	ns	ns
6 vs 10 µm	ns	ns	ns
6 vs 20 µm	ns	ns	ns
6 vs 50 µm	**	ns	ns
10 vs 20 µm	ns	ns	ns
10 vs 50 µm	ns	ns	ns
20 vs 50 µm	ns	ns	ns

Table 4.5 Statistics for MSC nucleus dimensions, ns = not significant, *p<0.05, **p<0.005, ***p<0.0005, ****p<0.0001.

	Channel width (µm)				
	3	**6**	**10**	**20**	**50**
Width vs. length	****	****	****	*	ns
Width vs. height	ns	ns	ns	ns	****
Length vs. height	***	*	****	****	****

Table 4.6 Statistics for L929 cell nucleus dimensions, ns = not significant, *p<0.05, **p<0.005, ***p<0.0005, ****p<0.0001.

	Width	Length	Height
3 vs 6 µm	ns	ns	ns
3 vs 10 µm	ns	ns	ns
3 vs 20 µm	****	**	ns
3 vs 50 µm	****	**	ns
6 vs 10 µm	ns	ns	ns
6 vs 20 µm	****	ns	ns
6 vs 50 µm	***	ns	ns
10 vs 20 µm	*	ns	ns
10 vs 50 µm	ns	ns	ns
20 vs 50 µm	ns	ns	ns

Table 4.7 Statistics for L929 cell nucleus dimensions, ns = not significant, *p<0.05, **p<0.005, ***p<0.0005, ****p<0.0001.

	Channel width (µm)				
	3	**6**	**10**	**20**	**50**
Width vs. length	****	****	****	ns	ns
Width vs. height	**	**	ns	ns	ns
Length vs. height	***	ns	**	ns	ns

4.3.3 Microtubule polymerization is not necessary to maintain nuclear morphology in confinement

To investigate the role of the microtubule network in maintaining nuclear volume and dimensionality in confinement, we inhibited microtubule polymerization in MSCs or L929 cells by adding 10 µM nocodazole to cell media. Nocodazole-treated cells within 3 µm narrow channels appeared similar to control, with diffuse cytoskeletal features in both cell types (Fig. 4.4A-B and Supplementary Movie S5-S8). However, in

50 μm wide channels, nocodazole-treated MSCs and L929 cells appeared rounder, with less evidence of linear microtubule structures (Fig. 4.4C-D and Supplementary Movie S9-S12). MSCs treated with nocodazole in 10 and 50 μm wide channels contained nuclei with significantly larger volume than control (Fig. 4.5A). Although the nuclear heights appeared slightly larger in nocodazole treated cells compared to control, there was no significant difference in nuclear axis lengths between nocodazole treated and control groups for the same channel widths (Fig. 4.5B and Table 4.8-4.9). L929 cells treated with nocodazole showed no difference in volume or nuclear axis lengths from controls of the same channel width (Fig. 4.5C-D and Table 4.10-4.11).

Figure 4.4 Orthogonal views of MSC treated with 10 μM nocodazole or vehicle control within A) 3 μm narrow channel and B) 50 μm wide channel. Orthogonal views of L929 cell treated with 10 μM nocodazole or vehicle control within C) 3 μm narrow channel and D) 50 μm wide channel. Cells were fixed and stained for α-tubulin (red), actin (green), and the nucleus (blue). Color channels were altered individually for optimal visualization. Scale bar represents 10 μm. 3D renderings of nuclei shown in panels A-D are provided in Supplemental Movies S5-S12. Thea Ornstein captured microscopy images.

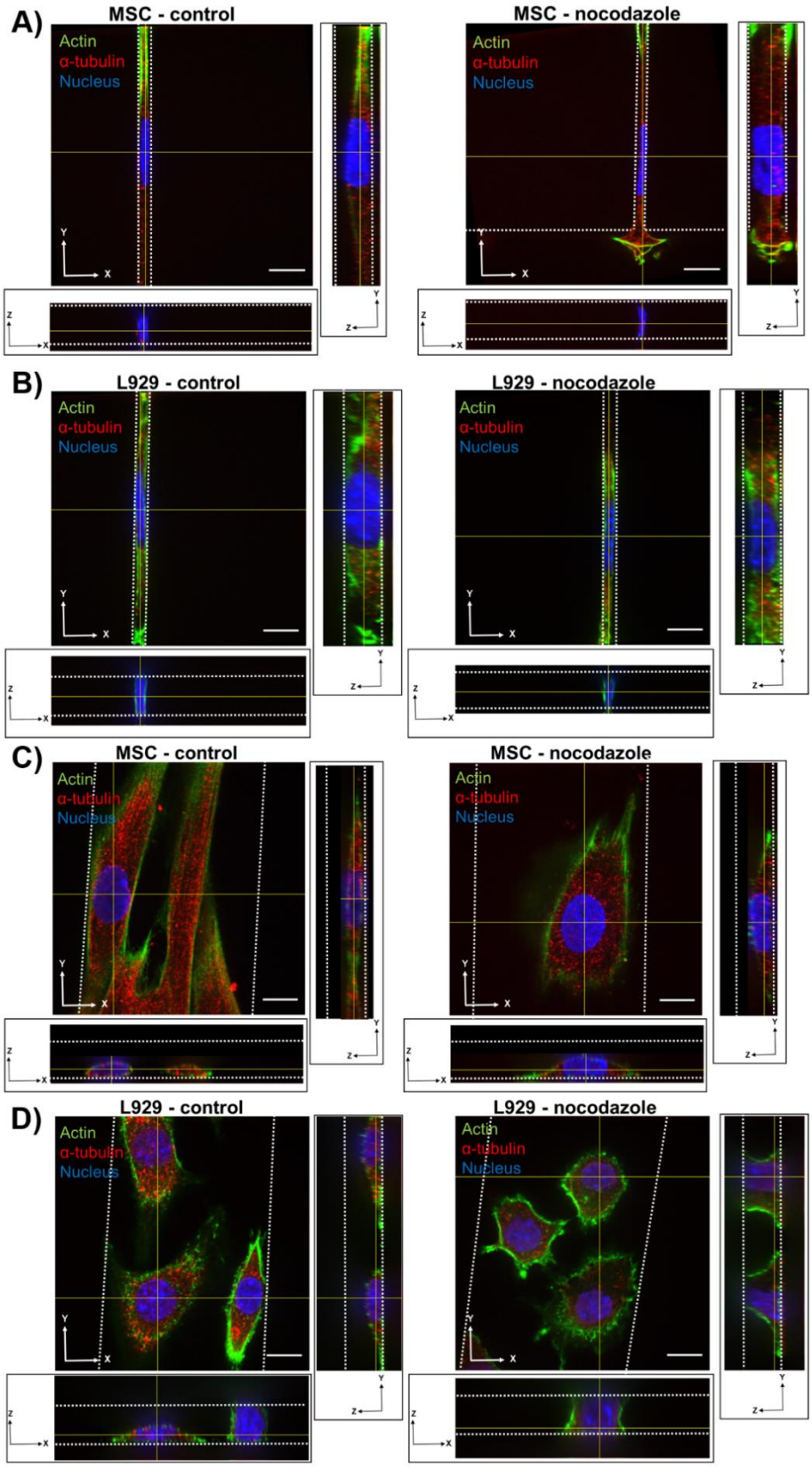
A)
MSC - control
Actin
α-tubulin
Nucleus
MSC - nocodazole
Actin
α-tubulin
Nucleus
B)
L929 - control
Actin
α-tubulin
Nucleus
L929 - nocodazole
Actin
α-tubulin
Nucleus
C)
MSC - control
Actin
α-tubulin
Nucleus
MSC - nocodazole
Actin
α-tubulin
Nucleus
D)
L929 - control
Actin
α-tubulin
Nucleus
L929 - nocodazole
Actin
α-tubulin
Nucleus

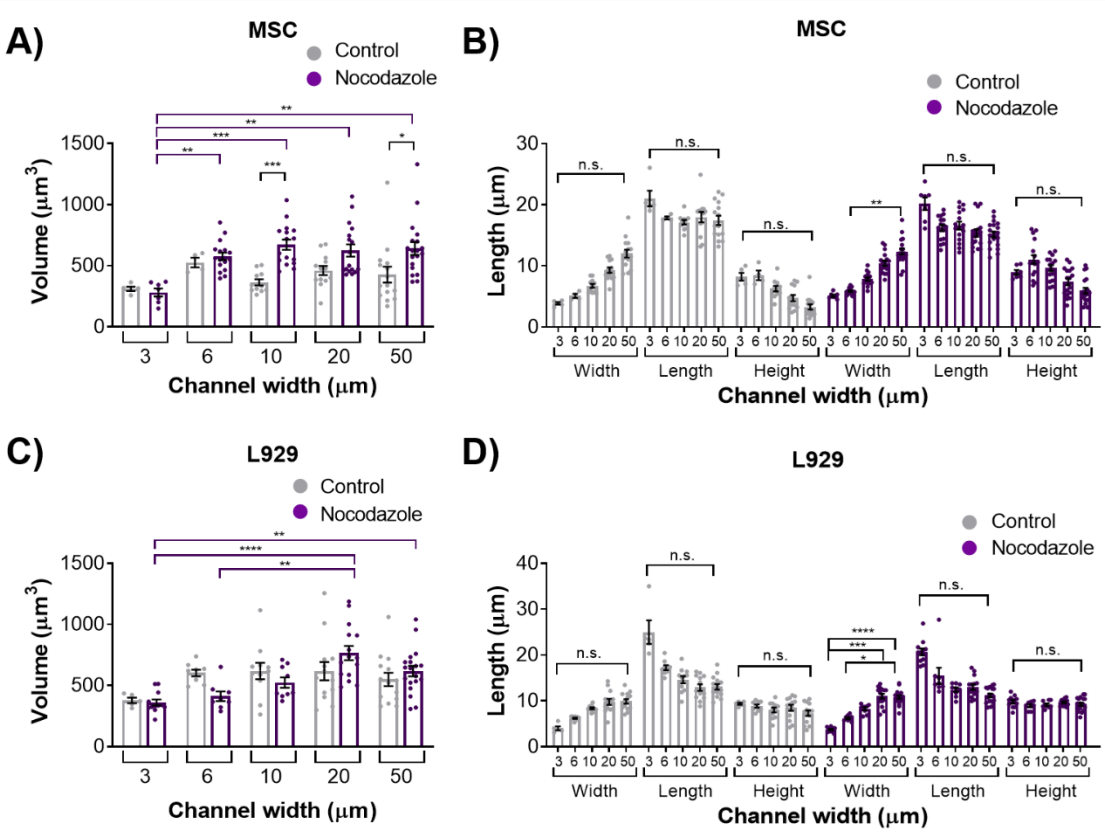

Figure 4.5 Nucleus A) volume or B) length, width, and height of MSCs treated with 10x µM nocodazole or vehicle control. Nucleus C) volume or D) length, width, and height of L929 cells treated with 10 µM nocodazole or vehicle control. Dot plots report mean ± SEM. *p<0.05, **p<0.005, ***p<0.0005, ****p<0.0001. (Each dot indicates one cell, pooled from N≥3 independent experiments). Full statistical information for panels B and D is provided in Tables 4.8-4.11.

Table 4.8 Statistics for MSC nucleus dimensions when treated with 10 µM nocodazole or vehicle control ns = not significant, **p<0.005, ***p<0.0005, ****p<0.0001.

		Channel width (µm)				
Comparison		**3**	**6**	**10**	**20**	**50**
Control	W vs. L	***	ns	***	ns	ns
	W vs. H	ns	ns	ns	ns	***
	L vs. H	ns	ns	***	****	****
Nocodazole	W vs. L	****	****	**	ns	ns
	W vs. H	ns	ns	ns	ns	**
	L vs. H	ns	ns	ns	**	****
W	Cont. vs. Noc.	ns	ns	ns	ns	ns
L	Cont. vs. Noc.	ns	ns	ns	ns	ns
H	Cont. vs. Noc.	ns	ns	ns	ns	ns

Table 4.9 Statistics for MSC nucleus dimensions when treated with 10 µM nocodazole or vehicle control ns = not significant, **p<0.005.

		Dimension		
Comparison		W	L	H
Control	3 vs. 6 µm	ns	ns	ns
	3 vs. 10 µm	ns	ns	ns
	3 vs. 20 µm	ns	ns	ns
	3 vs. 50 µm	ns	ns	ns
	6 vs. 10 µm	ns	ns	ns
	6 vs. 20 µm	ns	ns	ns
	6 vs. 50 µm	ns	ns	ns
	10 vs. 20 µm	ns	ns	ns
	10 vs. 50 µm	ns	ns	ns
	20 vs. 50 µm	ns	ns	ns
Nocodazole	3 vs. 6 µm	ns	ns	ns
	3 vs. 10 µm	ns	ns	ns
	3 vs. 20 µm	ns	ns	ns
	3 vs. 50 µm	ns	ns	ns
	6 vs. 10 µm	ns	ns	ns
	6 vs. 20 µm	ns	ns	ns
	6 vs. 50 µm	**	ns	ns
	10 vs. 20 µm	ns	ns	ns
	10 vs. 50 µm	ns	ns	ns
	20 vs. 50 µm	ns	ns	ns

Table 4.10 Statistics for L929 cell nucleus dimensions when treated with 10 µM nocodazole or vehicle control ns = not significant, *p<0.05, **p<0.005, ***p<0.0005, ****p<0.0001.

		Channel width (µm)				
Comparison		**3**	**6**	**10**	**20**	**50**
Control	W vs. L	****	****	**	ns	ns
	W vs. H	ns	ns	ns	ns	ns
	L vs. H	ns	**	**	ns	***
Nocodazole	W vs. L	****	***	ns	ns	ns
	W vs. H	ns	ns	ns	ns	ns
	L vs. H	*	ns	ns	ns	ns
W	Cont. vs. Noc.	ns	ns	ns	ns	ns
L	Cont. vs. Noc.	ns	ns	ns	ns	ns
H	Cont. vs. Noc.	ns	ns	ns	ns	ns

Table 4.11. Statistics for L929 cell nucleus dimensions when treated with 10 µM nocodazole or vehicle control ns = not significant, *p<0.05, ***p<0.0005, ****p<0.0001.

		Dimension		
Comparison		W	L	H
Control	3 vs. 6 µm	ns	ns	ns
	3 vs. 10 µm	ns	ns	ns
	3 vs. 20 µm	ns	ns	ns
	3 vs. 50 µm	ns	ns	ns
	6 vs. 10 µm	ns	ns	ns
	6 vs. 20 µm	ns	ns	ns
	6 vs. 50 µm	ns	ns	ns
	10 vs. 20 µm	ns	ns	ns
	10 vs. 50 µm	ns	ns	ns
	20 vs. 50 µm	ns	ns	ns
Nocodazole	3 vs. 6 µm	ns	ns	ns
	3 vs. 10 µm	ns	ns	ns
	3 vs. 20 µm	***	ns	ns
	3 vs. 50 µm	****	ns	ns
	6 vs. 10 µm	ns	ns	ns
	6 vs. 20 µm	ns	ns	ns
	6 vs. 50 µm	*	ns	ns
	10 vs. 20 µm	ns	ns	ns
	10 vs. 50 µm	ns	ns	ns
	20 vs. 50 µm	ns	ns	ns

4.3.4 Myosin II contractility is not necessary to maintain nuclear morphology in confinement

To investigate the role of the actomyosin network in maintaining nuclear volume and dimensionality in confinement, we inhibited myosin II-mediated contractility by adding 50 µM blebbistatin to cell media. In both wide and narrow microchannels, the actin organization did not appear drastically different between blebbistatin and control

groups (Fig. 4.6 and Supplementary Movie S13-S20). Some blebbistatin-treated L929 cells in wide channels exhibited a longer trailing edge than control cells (Fig. 4.6D). We have previously shown that MSCs in microchannels do not exhibit altered microtubule structure upon blebbistatin treatment (Chapter 3). MSCs treated with blebbistatin in 20 μm wide channels displayed nuclei with significantly less volume than MSCs treated with vehicle control (Fig. 4.7A). However, MSCs treated with blebbistatin did not show any differences in any axis lengths from control (Fig. 4.7B and Table 4.12-4.13). L929 cells treated with blebbistatin showed no difference in volume or nuclear axis lengths from control (Fig. 4.7C-D and Table 4.14-4.15).

Figure 4.6 Orthogonal views of MSC treated with 50 μM blebbistatin or vehicle control within A) 3 μm narrow channel and B) 50 μm wide channel. Orthogonal views of L929 cell treated with 50 μM blebbistatin or vehicle control within C) 3 μm narrow channel and D) 50 μm wide channel. Cells were fixed and stained for actin (green) and the nucleus (blue). Color channels were altered individually for optimal visualization. Scale bar represents 10 μm. 3D renderings of nuclei shown in panels A-D are provided in Supplemental Movies S13-S20. Thea Ornstein captured microscopy images.

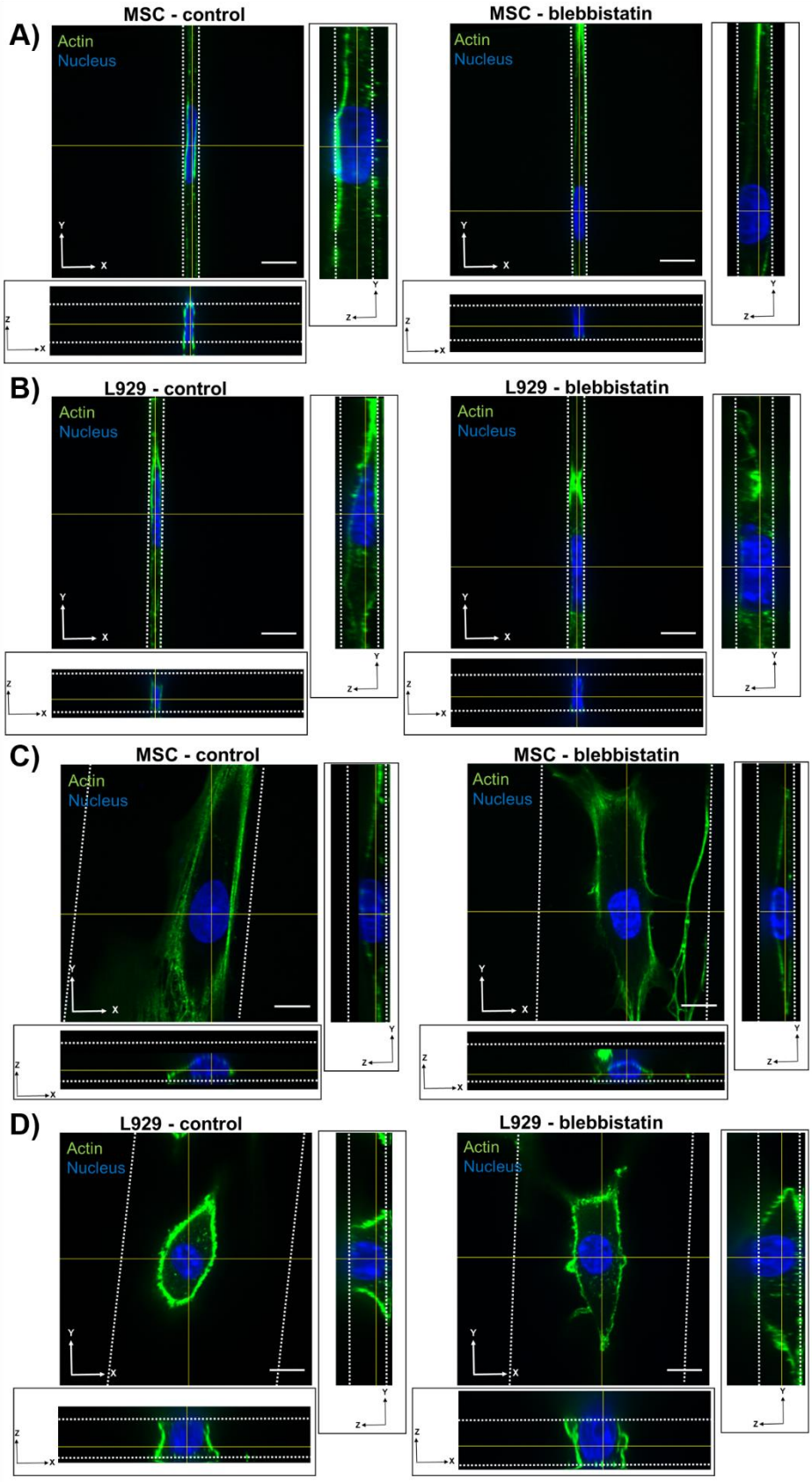
A)
MSC - control
Actin
Nucleus
MSC - blebbistatin
Actin
Nucleus
B)
L929 - control
Actin
Nucleus
L929 - blebbistatin
Actin
Nucleus
C)
MSC - control
Actin
Nucleus
MSC - blebbistatin
Actin
Nucleus
D)
L929 - control
Actin
Nucleus
L929 - blebbistatin
Actin
Nucleus

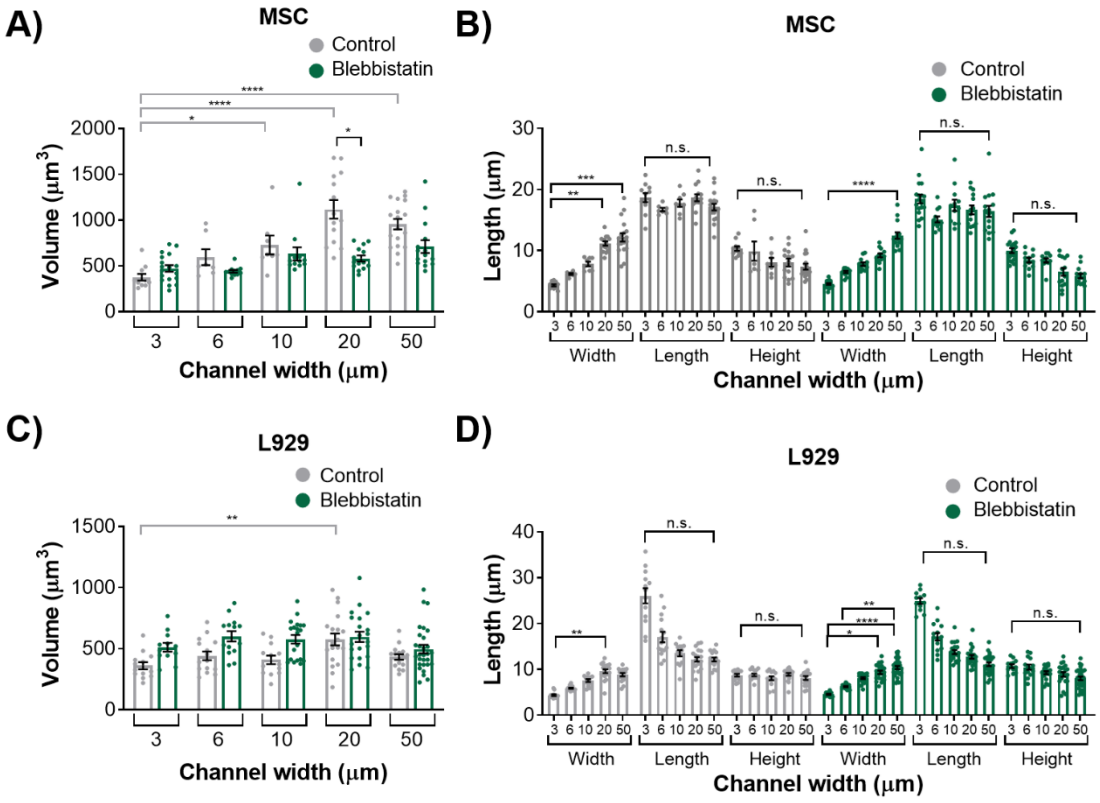

Figure 4.7 Nucleus A) volume or B) length, width, and height of MSCs treated with 50 μM blebbistatin or vehicle control. Nucleus C) volume or D) length, width, and height of L929 cells treated with 50 μM blebbistatin or vehicle control. Dot plots report mean ± SEM. *p<0.05, **p<0.005, ***p<0.0005, ****p<0.0001. (Each dot indicates one cell, pooled from N≥3 independent experiments). Full statistical information for panels B and D is provided in Tables 4.12-4.15.

Table 4.12 Statistics for MSC nucleus dimensions when treated with 50 µM blebbistatin or vehicle control ns = not significant, *p<0.05, **p<0.005, ***p<0.0005, ****p<0.0001.

		Channel width (µm)				
Comparison		**3**	**6**	**10**	**20**	**50**
Control	W vs. L	****	*	ns	ns	ns
	W vs. H	ns	ns	ns	ns	ns
	L vs. H	ns	ns	ns	***	****
Blebbistatin	W vs. L	****	**	**	ns	ns
	W vs. H	**	ns	ns	ns	**
	L vs. H	*	ns	*	****	****
W	Cont. vs. Bleb.	ns	ns	ns	ns	ns
L	Cont. vs. Bleb.	ns	ns	ns	ns	ns
H	Cont. vs. Bleb.	ns	ns	ns	ns	ns

Table 4.13 Statistics for MSC nucleus dimensions when treated with 50 µM blebbistatin or vehicle control ns = not significant, **p<0.005, ***p<0.0005, ****p<0.0001.

		Dimension		
Comparison		W	L	H
Control	3 vs. 6 µm	ns	ns	ns
	3 vs. 10 µm	ns	ns	ns
	3 vs. 20 µm	**	ns	ns
	3 vs. 50 µm	***	ns	ns
	6 vs. 10 µm	ns	ns	ns
	6 vs. 20 µm	ns	ns	ns
	6 vs. 50 µm	ns	ns	ns
	10 vs. 20 µm	ns	ns	ns
	10 vs. 50 µm	ns	ns	ns
	20 vs. 50 µm	ns	ns	ns
Blebbistatin	3 vs. 6 µm	ns	ns	ns
	3 vs. 10 µm	ns	ns	ns
	3 vs. 20 µm	ns	ns	ns
	3 vs. 50 µm	****	ns	ns
	6 vs. 10 µm	ns	ns	ns
	6 vs. 20 µm	ns	ns	ns
	6 vs. 50 µm	ns	ns	ns
	10 vs. 20 µm	ns	ns	ns
	10 vs. 50 µm	ns	ns	ns
	20 vs. 50 µm	ns	ns	ns

Table 4.14 Statistics for L929 cell nucleus dimensions when treated with 50 µM blebbistatin or vehicle control ns = not significant, *p<0.05, ***p<0.0005, ****p<0.0001.

		Channel width (µm)				
Comparison		**3**	**6**	**10**	**20**	**50**
Control	W vs. L	****	****	***	ns	ns
	W vs. H	ns	ns	ns	ns	ns
	L vs. H	****	***	*	ns	*
Blebbistatin	W vs. L	****	****	****	ns	ns
	W vs. H	***	*	ns	ns	ns
	L vs. H	ns	ns	*	*	*
W	Cont. vs. Bleb.	ns	ns	ns	ns	ns
L	Cont. vs. Bleb.	ns	ns	ns	ns	ns
H	Cont. vs. Bleb.	ns	ns	ns	ns	ns

Table 4.15 Statistics for L929 cell nucleus dimensions when treated with 50 µM blebbistatin or vehicle control ns = not significant, *p<0.05, **p<0.005, ****p<0.0001.

		Dimension		
Comparison		W	L	H
Control	3 vs. 6 µm	ns	ns	ns
	3 vs. 10 µm	ns	ns	ns
	3 vs. 20 µm	**	ns	ns
	3 vs. 50 µm	ns	ns	ns
	6 vs. 10 µm	ns	ns	ns
	6 vs. 20 µm	ns	ns	ns
	6 vs. 50 µm	ns	ns	ns
	10 vs. 20 µm	ns	ns	ns
	10 vs. 50 µm	ns	ns	ns
	20 vs. 50 µm	ns	ns	ns
Blebbistatin	3 vs. 6 µm	ns	ns	ns
	3 vs. 10 µm	ns	ns	ns
	3 vs. 20 µm	*	ns	ns
	3 vs. 50 µm	****	ns	ns
	6 vs. 10 µm	ns	ns	ns
	6 vs. 20 µm	ns	ns	ns
	6 vs. 50 µm	**	ns	ns
	10 vs. 20 µm	ns	ns	ns
	10 vs. 50 µm	ns	ns	ns
	20 vs. 50 µm	ns	ns	ns

4.4 Discussion

In this study, we investigated how the passive force of confinement in microchannels affected nuclear deformation of various cell types. In 2D, nuclei of MSCs and MDA-MB-231 cells maintained a fairly constant major axis length when the minor axis was forcibly decreased by confining microchannel walls. In contrast, nuclei of L929 cells increased their major axis length as the minor axis was forcibly decreased by

microchannels, which is similar to what we have previously shown in mouse sarcoma cells [173]. It has also been reported in literature that the nuclei of several cell lines deform anisotropically in response to an applied force, with the minor axis exhibiting higher strain than the major axis [101]. These results were demonstrated to be both intrinsic to the nucleus and controlled by the cytoskeleton, and it was postulated that microtubules resist nuclear deformation along the major axis and actin resists deformation along the minor axis [101].

We initially hypothesized that nuclear volume would not change with increasing confinement, leading us to a second hypothesis that the height of the MSC nuclei would increase with increasing confinement, whereas the height of L929 nuclei would remain constant. However, interestingly, nuclei of MSCs and L929 cells decreased in volume when they experienced the highest degree of confinement. This result is consistent with other studies that have reported changes in nuclear volume in response to the mechanical microenvironment. For example, nuclear volume was altered by nanotopography, potentially mediated by focal adhesion arrangement [100]. When confined to microwells, nuclear volume decreased with decreasing microwell volume [85]. Additionally, we observed a large range in the values of nucleus volume, and these values are on par with what others have reported [128], [246], [247]. Interestingly, nucleus volume has been shown to scale with cell volume [247], [248]. Mouse MSCs have been shown to have a nucleus volume of approximately 250 μm^3 when osmotically compressed to a cell volume of approximately 1,000 μm^3, which is in line with the nucleus volume we observed of MSCs and L929 cells in confinement [248]. When MSCs were confined to microwells in a previous study, their nuclear volume was less

than observed here. Nucleus volumes ranged from approximately 170-230 μm^3 when cell volume was modulated from 2800-9200 μm^3 [85]. However, the microwells were approximately 10 kPa in elastic modulus, whereas the microchannels herein are approximately 1 MPa in elastic modulus, suggesting that there may be a complex interplay between physical confinement and matrix stiffness in regulating nuclear volume.

MSC nuclei were anisotropic in all channel widths, while L929 cell nuclei were anisotropic in the narrowest channels and isotropic in the widest channels. MSCs exhibited more defined actin stress fibers than L929 cells in wide channels. Given the flattened morphology of MSCs in wide channels, we hypothesize that actin stress fibers compress the MSC nucleus in wide channels, thereby reducing the nuclear height and increasing the nuclear width with decreasing confinement. MSCs increased nuclear height in response to increasing confinement, as nuclear width was forced to decrease. Interestingly, the MSC nuclear length remained constant in all channel widths. Conversely, L929 cells maintained the same nuclear height in all channel widths. We suggest that this is due to minimal stress fiber formation and minimal cytoskeletal tension in L929 cells which were more rounded. To compensate, L929 cells increased nuclear length in response to increasing confinement, as nuclear width was forced to decrease. It is interesting to note that L929 cells and MSCs have different origins – from mouse adipose and human bone marrow, respectively. It was previously observed that nuclear stiffness scales with tissue stiffness due to differences in lamin A content [45]. Although adipose and bone marrow are both soft tissues, MSCs have higher lamin A content than cells derived from fat or lung tissue [45]. Chromatin condensation may also

affect nuclear deformation in confinement. It has been shown that chromatin decondensation leads to a more isotropic deformation of fibroblast nuclei [101]. Additionally, it has been shown that polarized, elongated cells (similar to MSCs in wide channels) generate higher stress on the nucleus, have higher lamin A/C levels, and have less dynamic heterochromatin foci [122]. Conversely, isotropic cells contain a rounder nucleus, lower lamin A/C levels, and more dynamic heterochromatin foci [122]. These chromatin dynamics may ultimately influence nuclear deformation.

We observed that inhibition of microtubule polymerization via nocodazole increased MSC nuclear volume within wider 10 and 50 μm channels. Nocodazole has been shown to increase nuclear volume and increase major axis strain in 2D [101], [246]. In two dimensions, microtubules seem to exert a force on the nucleus, as evidenced by a crescent shaped nucleus around the microtubule organizing center (MTOC) when lamin A is knocked out [249] and decreases in nuclear envelope fluctuations after nocodazole treatment [250]. Furthermore, inhibition of microtubule polymerization in the long term decreases elasticity of fibroblasts in 2D [251]. Similarly, we showed previously that nocodazole did not affect cell migration speed in confinement, but reduced cell speed in wide channels (Chapter 3). It is possible that microtubule polymerization has a reduced role in regulating nuclear morphology in confinement in comparison with 2D microenvironments. Nocodazole did not, however, affect the nuclear volume or dimensions of L929 cells in any channel width. The microtubule network in L929 cells already appeared quite diffuse in all channel widths before treatment, suggesting that microtubules in these cells contribute little to maintaining nuclear morphology even in 2D microenvironments.

We also observed that inhibition of myosin II contractility decreased nuclear volume of MSCs in 20 μm wide channels. Blebbistatin is often used to decrease the stiffness of cortical actin [229], and may have reduced the force on the nucleus exerted by the actin network. Inhibition of myosin II by blebbistatin has been shown to decrease the force on the nucleus and increase the levels of phosphorylated lamin A/C, which is typically associated with lamin A/C turnover and rounding nuclei [252]. Untreated L929 cells did not appear to have many actin stress fibers in any channel width, and hence they may have a low-contractile basal state. Therefore, the addition of blebbistatin did not seem to alter the cytoskeletal structure of L929 cells. In reporting these results, we also note an inherent limitation in our methods; confocal microscopy is a costly and time-consuming technique, so it is difficult to obtain a significantly large sample size for quantification of nuclear 3D volume and dimensions. Future studies could work towards developing a high throughput method of confining and imaging cells could enable larger sample sizes to support our conclusions.

It does not appear that the external effectors of cell contractility or microtubule polymerization are key determinants of nuclear dimensions in confinement, which leaves the question if internal nuclear effectors control nuclear volume in confinement. Future studies may investigate the effects of chromatin decondensation or lamina disruption on nuclear volume, as these have both been demonstrated to decrease or increase, respectively, the anisotropic nucleus deformation in response to force [101]. Additionally, the LINC complex has been demonstrated to control the homeostatic position of the nucleus [253]. It is possible that the LINC complex may have a role in nuclear volume regulation or nuclear deformation in response to force. Internal nuclear

effectors ought to be investigated for their role in nuclear deformation in three dimensions.

4.5 Conclusion

In summary, we observed that different cell types deform differently in response to mechanical confinement. Microtubule polymerization and myosin II contractility do not appear essential in L929 cells for regulation of nuclear volume and dimensionality. Conversely, microtubule polymerization and myosin II contractility seem to play a role in maintaining nuclear volume and dimensionality in unconfined, but not confined, MSCs. This work informs our understanding of nuclear mechanics in microenvironments related to tissue homeostasis and disease and suggests diverging roles of the cytoskeleton in regulating nuclear deformation in different cell types.

While the microchannel device used in this Chapter and in Chapter 3 was useful for learning new mechanobiological behavior of MSCs in confinement, exploration of a longer-term process, such as progression of IPF, requires a system that can support long-term culture and downstream biological readouts, while still exerting known amounts of mechanical confinement and retaining easy visualization of cells over time. Therefore, in the next Chapter, we designed, created, and validated confining micropillar arrays that achieves these requirements and, in Chapter 6, will enable us to explore the mechanobiology of IPF progression.

Chapter 5: Integration of Mesenchymal Stem Cells into a Novel Micropillar Confinement Assay[4]

5.1 Introduction

While biological cues have long been recognized as important regulators of cell behavior, mounting evidence indicates that mechanical cues also have critical influences on cell migration, division, differentiation, and other essential cell processes [1], [64], [173]. Understanding and capitalizing on the effects of these mechanical cues can promote the successful outcome of tissue engineering strategies for repair and regeneration of tissues. Relevant external mechanical cues may include stiffness, topography, shear stress, viscoelasticity, and, as we discuss specifically herein, confinement. The field is recognizing that a variety of cell types, including fibroblasts, cancer cells, and epithelial cells, undergo migrational plasticity and enlist different mechanisms for confined migration than for unconfined migration [65]–[67]. For example, we have shown that confinement reduces the influence of microtubule polymerization on mesenchymal stem cell (MSC) migration (Chapter 3).

Intravital imaging has revealed that cells indeed experience physical confinement *in vivo* [72], [254]. In addition, cells integrated into tissue engineered scaffolds likely experience physical confinement depending on the porosity and organization of the scaffold at the microscale. Three-dimensional cellular assays are

[4] Adapted from M.T. Doolin and K.M. Stroka, Integration of Mesenchymal Stem Cells into a Novel Micropillar Confinement Assay, Tissue Engineering Part C: Methods, 25(11): 662-676 (2019).

becoming increasingly popular, but many labs also have distinct methods and devices to study cell behavior in confinement. One approach uses micropatterned lines of a particular adhesive protein or grooves, creating 1D tracks upon which cells can migrate [135], [136], [138], [140]. This technique is advantageous due to its simplicity of production, ease of live cell imaging, and potential for single cell studies. While 1D patterning techniques can be similar to the migration of cells along extracellular matrix protein "tracks" *in vivo*, they do not account for the compression of the cell body and nucleus that a cell may experience in 3D *in vivo* microenvironments [137]. To mimic *in vivo* cell compression, systems have been designed to confine cells vertically, in which cell migration can be markedly different than on a 2D substrate [126], [143], [183]. However, in this method, cells are limited to only one axis of confinement [143]. Boyden chambers are also often employed for studying the effects of 3D confined migration on cell behavior [167]. While Boyden chambers are a useful tool for post-confinement readouts, they do not allow for easy live visualization of cells within the chamber and do not easily allow for long-term culture in confinement [255]. Hydrogels are also commonly used to confine cells in a 3D microenvironment [129], [161]. However, hydrogels can lack precise control over the degree of 3D confinement experienced by the cells, and it is difficult to image and accurately track cells in 3D hydrogels over time. To address these shortcomings, we and others have analyzed cell migration through confining microchannels of various widths [25], [26], [144], [147], [148]. While this approach offers precise control over the degree of confinement experienced and ease of imaging, it provides a relatively small sample size that is inadequate for proteomic or genetic analysis. Additionally, microfluidic devices often

require the introduction of a chemotactic gradient to encourage migration into small channels [25], [26], which may or may not be physiologically relevant for a given tissue engineering strategy.

Here, we have developed a novel micropillar confinement assay that allows for precise control over the degree of confinement experienced by cells, enables visualization of cells in real time (on the order of weeks), and provides a large sample size for downstream biological assays. Our data show that MSCs alter their cell and nuclear morphology in response to confinement induced by micropillars. Furthermore, it appears MSCs may alter their migration mode based on the degree of confinement experienced or by the mere existence of micropillars. Overall, this micropillar assay will provide new fundamental information about cellular migration and mechanobiology in response to physical confinement.

5.2 Materials and Methods

5.2.1 Cell culture and reagents

Bone marrow-derived human mesenchymal stem cells (Donor 1: 20 year-old female, Donor 2: 22 year-old male) were purchased from RoosterBio, Inc. (Frederick, MD, USA). Experiments were performed with Donor 1 unless otherwise noted in the figure caption. Cells were removed from liquid nitrogen and grown in RoosterBio basal media with media booster (RoosterBio, Inc.) for the first day post-thaw. Thereafter, cells were cultured in media composed of Dulbecco's Modified Eagle's Medium with high glucose (ThermoFisher Scientific, Waltham, MA, USA), 10% Fetal Bovine Serum

(FBS) (ThermoFisher Scientific), and 1% Penicillin-Streptomycin 10,000 U/mL (ThermoFisher Scientific). Cells were cultured and used until a population doubling level of 20 and cells were passaged at or below 80% confluency. Cells were washed with Phosphate-Buffered Saline (PBS) (VWR, Radnor, PA, USA), and detached with TrypLE Express Enzyme (ThermoFisher Scientific). All cells were cultured at 37°C, 50% humidity, and 5% CO2:95% air.

5.2.2 Micropillar device fabrication

A polydimethylsiloxane (PDMS) micropillar device with micropillars of different spacing (Fig. 5.1A) was prepared via photolithography, as previously described [25], [26]. All photolithography procedures were carried out in the University of Maryland Nanocenter FabLab. Briefly, a mask was made in AutoCAD (AutoDesk, San Rafael, CA, USA) to represent the micropillars of different spacings. A layer of SU-8 3010 negative photoresist (MicroChem, Westborough, MA, USA) was spin coated onto a 4-inch diameter silicon wafer (University Wafer, Boston, MA, USA). Using an EVG620 mask aligner (EVG Group, Albany, NY, USA), the mask in the image of micropillars was placed over the wafer and exposed to ultraviolet (UV) light to crosslink. Excess SU-8 3010 was dissolved using SU-8 developer (MicroChem). Finished wafers were silanized using tridecafluoro-1,1,2,2,tetrahydrooctyl-1-trichlorosilane (OTS, 97%) (UCT Inc., Bristol, PA, USA) overnight in a vacuum desiccator. The resulting silicon master contained micropillars with 50 μm, 20 μm, 10 μm, and 5 μm spacing, and 13-17 μm height. These distances were chosen because they are representative of the dimensions of *in vivo* tracks and *in vitro* scaffold pores [28].

PDMS micropillar arrays were manufactured based on previously described protocols [143], [154]. PDMS (Krayden, Denver, CO, USA) was mixed at a 10:1 base:curing agent ratio, poured over the silicon master, and degassed in a vacuum desiccator. The PDMS and master were baked for at least 10 minutes at 100°C, and then the PDMS mold was cut and removed from the silicon master. The PDMS mold was then placed in a plasma cleaner (Harrick Plasma, Ithaca, NY, USA) and plasma treated for 2.5 minutes. Finished molds were silanized using OTS (97%) overnight in a vacuum desiccator. PDMS was mixed at a 10:1 base:curing agent ratio, poured over the PDMS mold, and degassed in a vacuum desiccator. Glass coverslips (thickness #1, Fisher Scientific, Fair Lawn, NJ, USA) were then applied to each set of micropillars while applying gentle pressure. The PDMS and coverslips were baked overnight at 80°C, then the coverslip-PDMS micropillar constructs were carefully removed from the PDMS mold. The PDMS-coverslip construct ensured that the base PDMS layer was sufficiently thin for microscopy, but that cell would sense PDMS on all sides.

PDMS blocks were coated in 8% Pluronic F127 (SigmaAldrich, St. Louis, MO, USA) solution for 1 hour at room temperature, then washed with DI water. Meanwhile, micropillar arrays were plasma treated for 2.5 minutes. Micropillar arrays were subsequently stamped with the Pluronic F127-coated PDMS blocks, and placed into 6-well plates. The plates were UV sterilized for 10 minutes. 20 μg/mL collagen I (SigmaAldrich) was added to all wells and incubated for at least one hour at 37°C. The collagen I solution was then removed, and devices were washed twice with PBS before seeding cells at a density of $5x10^4$ cells/well (Fig. 1B). Cell media was changed every 2-3 days.

5.2.3 Scanning electron microscopy

All SEM images were acquired in the University of Maryland Nanocenter AimLab by Dr. Sz-Chian Liou. SEM images were acquired using Hitachi SU-70 FEG SEM to visualize pillar spacing and Tescan XEIA FEG SEM/FIB to visualize pillar height. Pillar spacing and diameter were measured in ImageJ, and height was measured using Tescan microscope software.

5.2.4 Immunofluorescence

The following steps were carried out at room temperature, unless otherwise specified. Cells were fixed in 3.7% formaldehyde (Fisher Scientific) for 10 minutes, then washed two to three times in PBS (VWR). Cells were permeabilized with 0.5% Triton-X 100 (SigmaAldrich) for 5 minutes, washed in PBS two to three times, and blocked for nonspecific binding in 2.5% goat serum (Abcam, Cambridge, MA, USA) for at least one hour. Primary antibody in 1% goat serum was added to cells and incubated at 4°C overnight. Primary antibodies and dilutions used were mouse anti-α-tubulin (ThermoFisher Scientific #A11126, 1:100) and rabbit anti-phospho-paxillin (Cell Signaling Technology #2541S, Danvers, MA, USA, 1:100). Cells were washed two to three times in PBS, incubated in 2.5% goat serum for at least one hour, then incubated with AlexaFluor 488 Phalloidin (ThermoFisher Scientific, 1:500), Hoechst (ThermoFisher Scientific, 1:2500), and a fluorescently labelled secondary antibody for one hour. Secondary antibodies and dilutions used were AlexaFluor 568 goat anti-mouse (ThermoFisher Scientific #A11004, 1:200) and AlexaFluor 568 goat anti-rabbit (ThermoFisher Scientific #A11011, 1:200). Cells were washed two to three times in

PBS, then imaged. Images were acquired on an Olympus IX83 microscope (Olympus) using a 20x objective for cell morphology measurements or using a 60x objective for high magnification images. Images were acquired on a PerkinElmer UltraVIEW Vox confocal spinning disk microscope (PerkinElmer, Waltham, MA, USA) using a 20x objective to obtain z-stacks and to visualize actin, nucleus, microtubules, and focal adhesions. Use of the PerkinElmer confocal microscope was performed courtesy of the University of Maryland imaging core.

5.2.5 Migration experiments

Cells were seeded onto micropillar arrays and allowed to incubate overnight. The following day, media was changed and imaging began thereafter. Images were acquired on an Olympus IX83 microscope (Olympus) using a 20x objective. A chamber adjusted to 37°C, 50% humidity, and 5% CO_2:95% air was used on the microscope stage in order to sustain cell viability. Images were taken at 10 minute intervals overnight.

5.2.6 Data analysis

For cell density, images of cell nuclei were thresholded and analyzed with the ImageJ Particle Analyzer. Cell density for each image was calculated by dividing the number of nuclei in an image by the total image area. For cell morphology, cells and nuclei were manually traced in ImageJ. Area, circularity, solidity, roundness, major axis, and minor axis were extracted using ImageJ built in morphology measurements. Roundness is equated to the inverse aspect ratio. Solidity was defined as the cell area divided by the convex area. To track cell migration in ImageJ, the cell centroid was

manually identified for each frame. Only cells that stayed within frame for the duration of the timelapse were tracked. A custom MATLAB program was implemented to calculate the speed, trajectory, mean squared displacement (MSD), and turning angle for each cell based on the position of the cell centroid. To calculate cell migration parameters every 30 minutes, we considered the position of the cell centroid every 3rd frame since images were originally captured every 10 minutes. Skewness of turning angle distributions was calculated in Graphpad.

5.2.7 Statistical analysis

Data for cells from at least two independent trials was pooled for statistical analysis. A one-way ANOVA with Holm-Sidak's multiple comparisons test, in the case of normally distributed data, or Kruskal-Wallis test with Dunn's multiple comparisons test, in the case of non-normally distributed data, was performed to determine differences in data from micropillar arrays of different spacing and differences between time points. A significance level of 0.05 was used. Error bars report the standard error of the mean (SEM) or standard deviation (SD), as indicated in figure or table captions.

5.3 Results

5.3.1 MSCs completely infiltrate into micropillar arrays

To entrap cells into the micropillar arrays, we aimed to encourage cell infiltration between pillars via cell attachment to the sides of the micropillars and migration on the cells' own accord. The tops of the pillars were stamped with Pluronic F127, a common surfactant used to minimize cell adhesion, using a microcontact

printing method described previously [154]. The remaining surface area was coated in collagen type I to enable cell attachment to the micropillar sides and base (Fig. 5.1B).

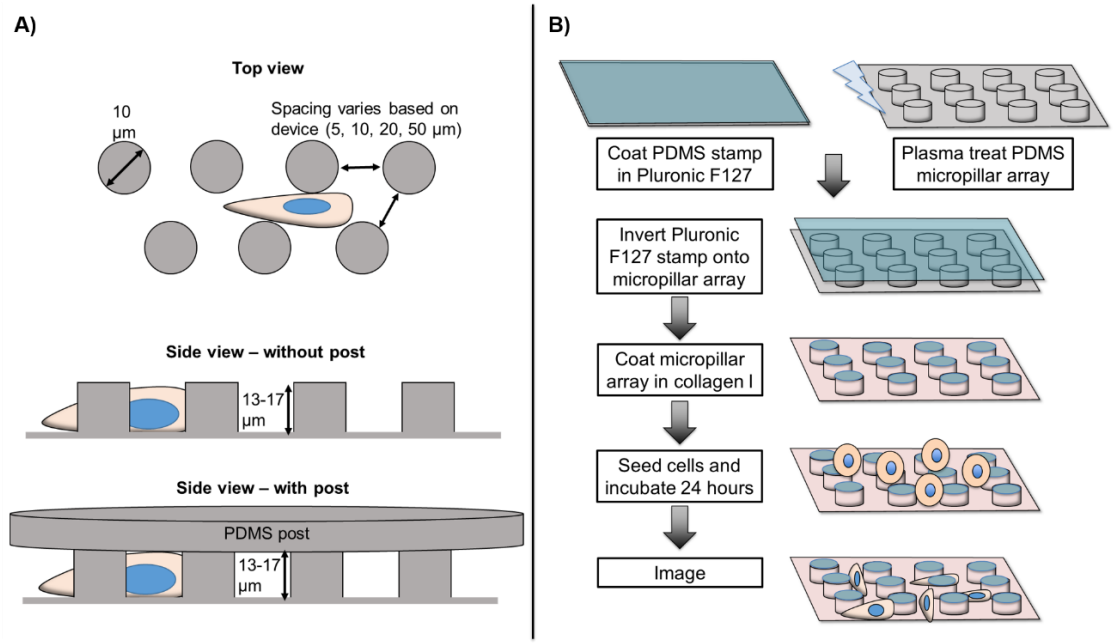

Figure 5.1 Micropillar preparation. A) Design of micropillar arrays. B) Representative workflow of micropillar array preparation.

We next investigated whether cells were completely entrapped within the pillars (for a full confinement effect), or whether they protruded above the pillar height (for only partial confinement). Our goal was for cells to only "feel" the basal PDMS plane and the walls of the micropillars. When posts were shorter, with a height of approximately 11 μm, parts of the cell body protruded above the micropillars, and the cell appeared to extend over the tops of pillars in spots (Fig. 5.2A). Hence, we fabricated 14 μm tall pillars and confirmed that these arrays fully confined the cell body and nucleus below the pillar tops (Fig. 5.2B).

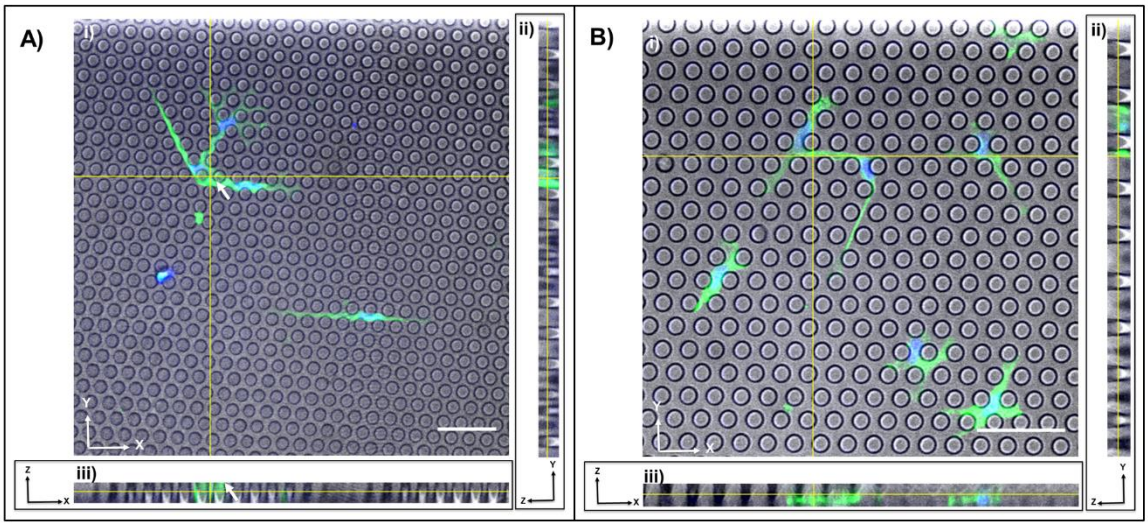

Figure 5.2 Micropillar specifications selection. Confocal images of MSCs within A) 11 µm tall micropillars or B) 14 µm tall micropillars. For both panels i) shows the XY plane, ii) shows the YZ plane, and iii) shows the XZ plane. White arrows indicate cell regions atop the micropillars. Cells were fixed and stained for actin (green) and the nucleus (blue). Scale bars represent 50 µm.

Next, we verified the dimensions of the 14 µm tall micropillars using scanning electron microscopy (SEM, Fig. 5.3). Micropillars with spacing of 5, 10, 20, and 50 µm were indeed measured to be approximately the theorized spacing, and the micropillar diameter was ~9 µm for all micropillar spacings (Fig. 5.3A-D, Table 5.1). Micropillars with spacing of 5, 10, 20, and 50 µm were approximately 13, 14, 13, and 17 µm tall, respectively, as measured by SEM (Fig. 5.3E-H, Table 5.1). We speculate that this height discrepancy could be minimized if each micropillar array was manufactured on its own silicon wafer, such that each array has its own optimized parameters during photolithography. However, because we achieved micropillar arrays that fully confined

cells without their protruding onto the micropillar tops, we moved forward with this fabrication technique.

Figure 5.3 Micropillar specifications validation. SEM images of micropillar array distribution with spacings of A) 5 µm, B) 10 µm, C) 20 µm, and D) 50 µm. SEM images of micropillar array height with spacings of E) 5 µm, F) 10 µm, G) 20 µm, and H) 50 µm. Quantification of pillar spacing and dimensions are shown in Table 5.1.

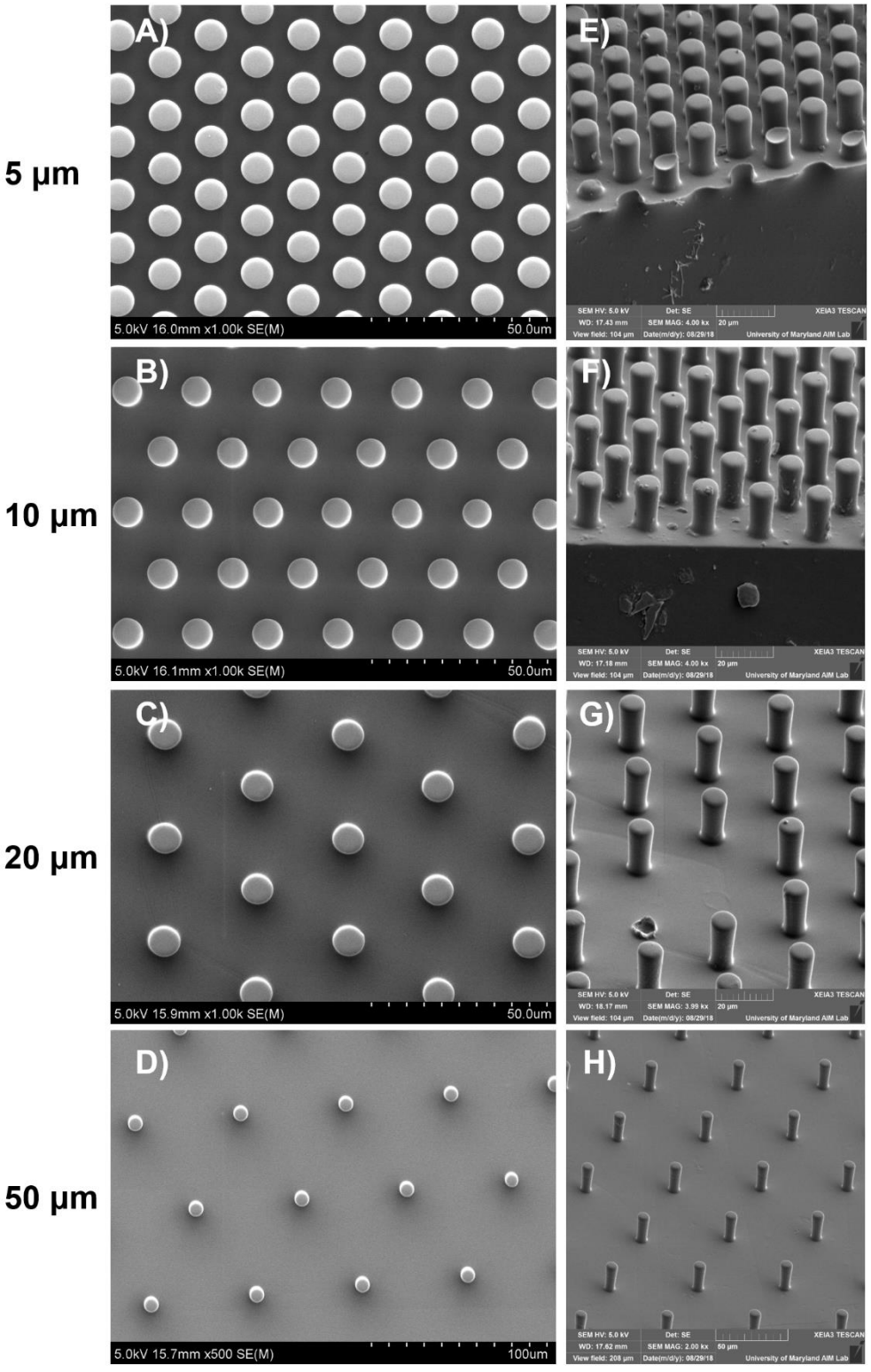
5 µm
10 µm
20 µm
50 µm
A)
B)
C)
D)
E)
F)
G)
H)
5.0kV 16.0mm x1.00k SE(M)
50.0um
5.0kV 16.1mm x1.00k SE(M)
50.0um
5.0kV 15.9mm x1.00k SE(M)
50.0um
5.0kV 15.7mm x500 SE(M)
100um

Table 5.1 Measurements of SEM images

Pillar spacing (theorized)	Pillar spacing (mean ± SD)	Pillar diameter (mean ± SD)	Pillar height (mean ± SD)
5 μm	5.861 ± 0.21 μm	9.160 ± 0.16 μm	12.82 ± 0.29 μm
10 μm	10.95 ± 0.30 μm	8.622 ± 0.19 μm	14.27 ± 0.21 μm
20 μm	20.35 ± 0.25 μm	9.217 ± 0.25 μm	13.26 ± 0.20 μm
50 μm	51.57 ± 0.60 μm	9.011 ± 0.51 μm	16.94 ± 0.92 μm

5.3.2 Cell density is consistent across micropillar spacings in short-term culture

After cells were seeded atop the micropillar arrays and incubated overnight, cells appeared to have infiltrated between the micropillars. A change in cell culture medium removed any cells remaining in suspension, but did not dislodge most cells within pillars. Cells remained within the micropillars after 48 hours, ensuring cell infiltration was not transient and could withstand media changes. Despite this, we wanted to ensure that cell density was fairly constant between micropillar arrays and for cells from multiple MSC donors. We quantified cell density within the micropillars at both 24 and 48 hours post-seeding. For Donor 1 cells, at 24 hours, there was no difference in the cell density between micropillar arrays (Fig. 5.4A). However, for Donor 1 cells, by 48 hours, there were less cells within 50 μm spaced pillars than any other pillar spacing (Fig. 5.4B). To investigate whether this observation was donor-specific, we seeded MSCs

from a second donor (Donor 2) within micropillar arrays. There was no difference in cell density between micropillar spacings at 24 or 48 hours, suggesting that cell seeding density may need to be optimized for each MSC donor and carefully considered when interpreting biological outcomes from the experiments (Fig. 5.4C-D).

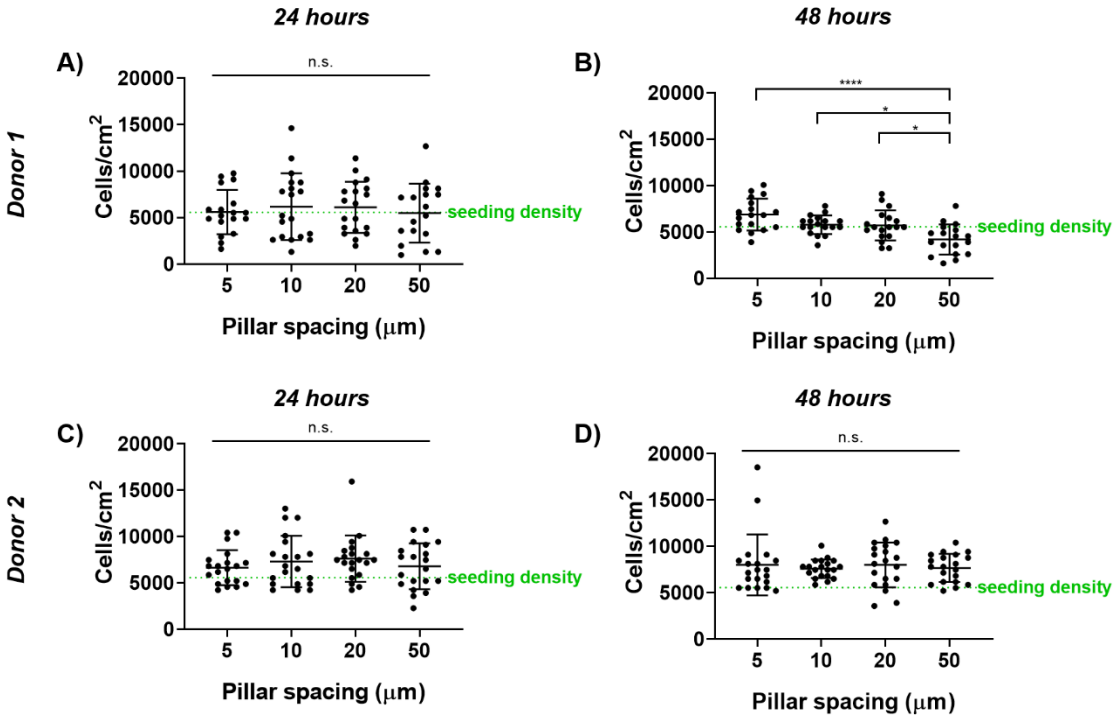

Figure 5.4 MSC density within micropillars. Donor 1 MSC density within micropillars for A) 24 hours or B) 48 hours. Donor 2 MSC density within micropillars for A) 24 hours or B) 48 hours. Dot plots report mean ± SD. *p<0.05, ****p<0.0001. Each dot indicates one analyzed image, pooled from N=2 independent experiments.

5.3.3 Cell and nucleus morphology within micropillars is altered by micropillar spacing

Fluorescence images of cell actin demonstrated that micropillar spacing drastically affected cell and nucleus morphology (Fig. 5.5A-D). Qualitatively, we observed cell spreading behaviors typical of 2D substrates in the 50 μm spaced pillars, while cells in the narrow spacings displayed much more spindly, protrusive morphologies with most cells physically wrapping around micropillars. At both 24 and 48 hours, cells within arrays of 20 μm and 50 μm spaced pillars were significantly larger in area than those in arrays of 5 μm spaced pillars (Fig. 5.5E). At both time points, cells within arrays of 5 μm spaced pillars were significantly less solid than cells in any other micropillar array and significantly less circular than cells within 20 μm arrays (Figs. 5.5F, 5.5H), which was expected given their spindly, protrusive morphology. There was no significant difference in any cell morphology measure within any pillar spacing from 24 to 48 hours (Fig. 5.5E-H).

Figure 5.5 MSC morphology within micropillars. MSC actin cytoskeleton and nucleus after 48 hours in micropillar arrays with spacings of A) 5 µm, B) 10 µm, C) 20 µm, or D) 50 µm. In panels (A-D) cells were fixed and stained for actin (green) and the nucleus (blue). E) Area, F) solidity, G) roundness, and H) circularity of MSC body as a function of pillar spacing after 24 hours and 48 hours within the micropillars. Dot plots report mean ± SEM. *p<0.05, **p<0.005, ***p<0.0005, ****p<0.0001. Each dot indicates one cell, pooled from N=2 independent experiments with n(5 µm, 24 hours)=56, n(5 µm, 48 hours)=94, n(10 µm, 24 hours)=45, n(10 µm, 48 hours)=78, n(20 µm, 24 hours)=47, n(20 µm, 48 hours)=66, n(50 µm, 24 hours)=35, n(50 µm, 48 hours)=42.

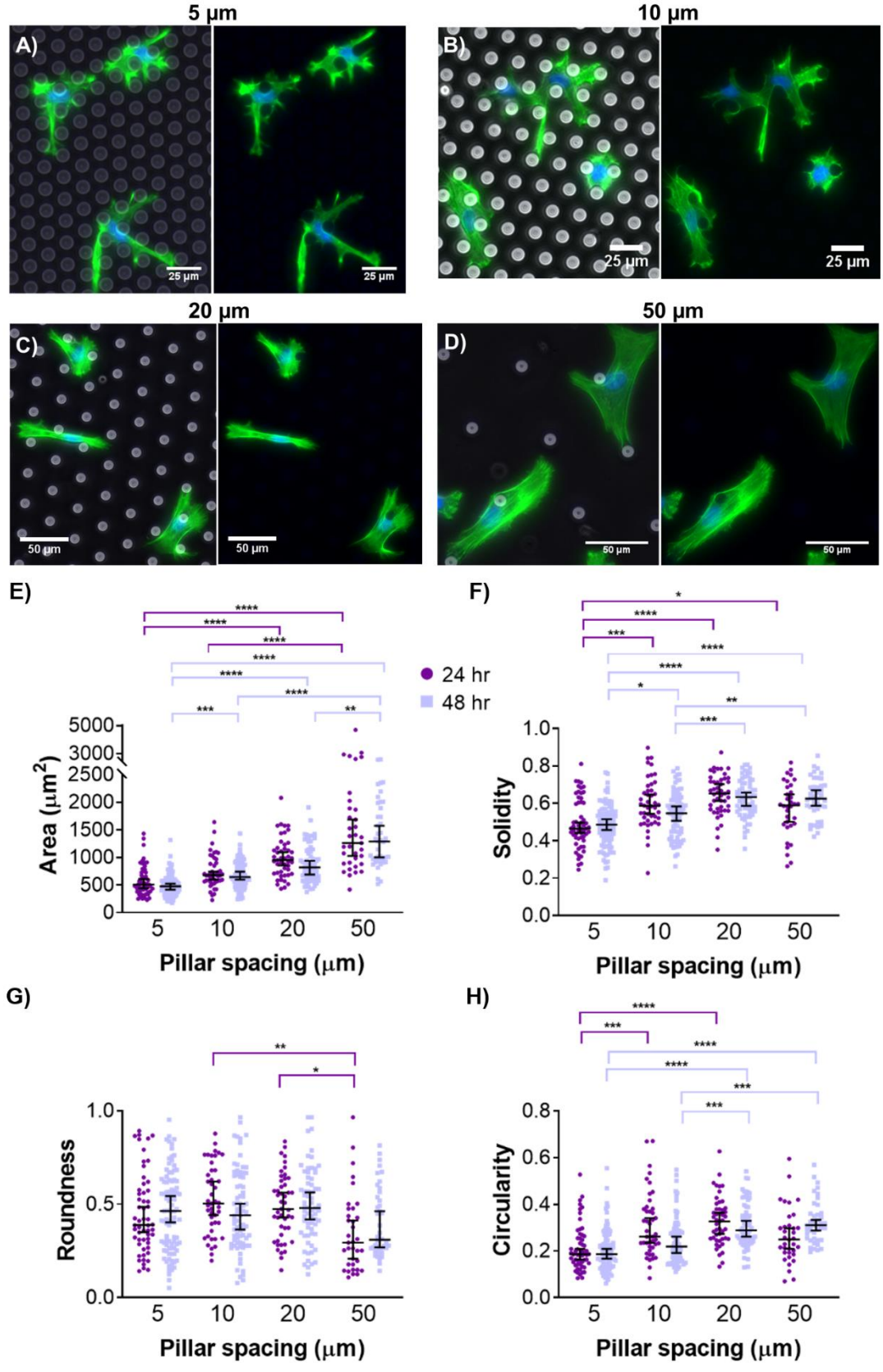
5 µm
10 µm
20 µm
50 µm
A)
B)
C)
D)
25 µm
50 µm
E)
F)
G)
H)
24 hr
48 hr
Area (µm²)
Solidity
Roundness
Circularity
Pillar spacing (µm)
5
10
20
50

Cell nuclei followed a slightly more consistent trend. Nucleus morphology was measured as above, and we additionally measured the major and minor axis. Major and minor axis indicate the longest and shortest axis, respectively, of an ellipse fit to the nucleus (Fig. 5.6A-B). In pillar arrays of 5 μm spacing, the fitted ellipse was typically larger than the nucleus (Fig. 5.6A). In pillar arrays of 10 μm spacing or wider, the nuclei were naturally ellipsoidal (Fig. 5.6B). At both 24 and 48 hours, cell nuclei within pillar arrays of 5 μm spacing were significantly smaller in 2D area, less solid, less round, and less circular than cell nuclei in any other array (Fig. 5.6C-F). Interestingly, there was no significant difference in the nucleus major axis among micropillars of different spacing, but the nucleus minor axis was significantly smallest in arrays with 5 μm pillar spacing (Fig. 5.6G-H). Future studies should examine if cell nuclei alter their volume in response to confinement within micropillars.

Figure 5.6 MSC nucleus morphology within micropillars. MSC nucleus in micropillar arrays with spacings of A) 5 μm and B) 10 μm. In panels (A-B) cells were fixed and stained for actin (green) and the nucleus (blue). C) Area, D) solidity, E) roundness, F) circularity, G) major axis, and J) minor axis of MSC nucleus as a function of pillar spacing after 24 hours and 48 hours within the micropillars. Dot plots report mean ± SEM. *p<0.05, **p<0.005, ***p<0.0005, ****p<0.0001. Each dot indicates one cell, pooled from N=2 independent experiments with n(5 μm, 24 hours)=56, n(5 μm, 48 hours)=94, n(10 μm, 24 hours)=45, n(10 μm, 48 hours)=78, n(20 μm, 24 hours)=47, n(20 μm, 48 hours)=66, n(50 μm, 24 hours)=35, n(50 μm, 48 hours)=42.

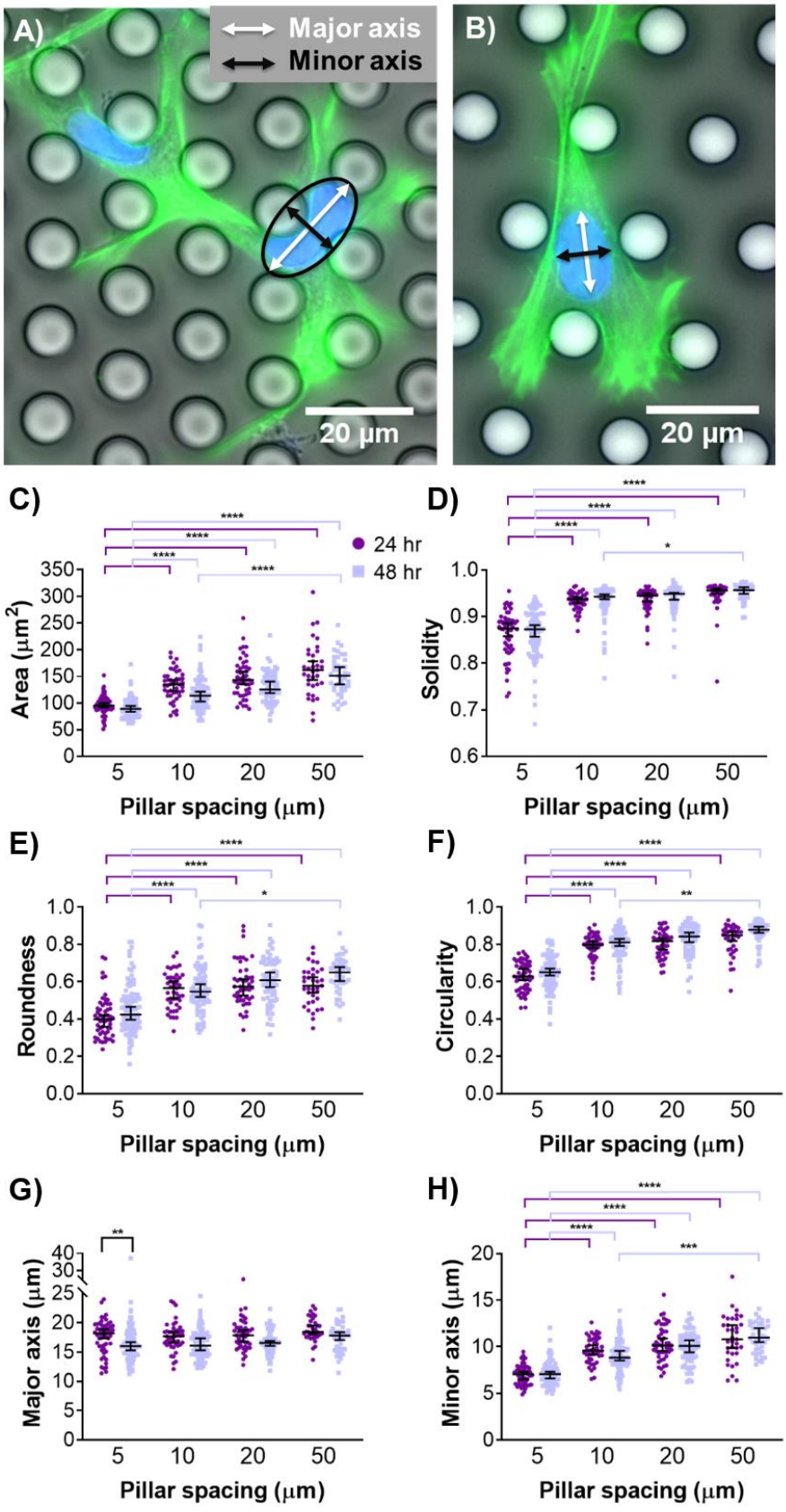
A)
Major axis
Minor axis
20 µm
B)
20 µm
C)
24 hr
48 hr
Area (µm²)
Pillar spacing (µm)
D)
Solidity
Pillar spacing (µm)
E)
Roundness
Pillar spacing (µm)
F)
Circularity
Pillar spacing (µm)
G)
Major axis (µm)
Pillar spacing (µm)
H)
Minor axis (µm)
Pillar spacing (µm)

We have also demonstrated that cells can remain viable and integrated within the micropillar confinement array for at least 3 weeks, and likely longer. When MSCs were cultured in micropillars for 3 weeks, they formed elongated networks within the narrowest micropillar arrays (Fig. 5.7A-B). MSCs cultured within the widest micropillar arrays for 3 weeks were similar in appearance to a two-dimensional monolayer (Fig. 5.7C-D). In addition to network formation, some cells began to protrude over the pillar tops (Fig. 5.7A). There were fewer cells within pillar arrays of 5 μm than those of 20 or 50 μm; thus, quantitative biological readouts may need to be normalized to cell density (Fig. 5.7E). Such long-term culture and high cell counts may allow for the examination of cell response to confinement in situations relevant for tissue engineering applications, such as the changing secretome or differentiation status of the cells.

Figure 5.7 MSCs within micropillars for 3 weeks. MSCs in micropillar arrays with spacings of A) 5 μm, B) 10 μm, C) 20 μm, or D) 50 μm. E) MSC density after 3 weeks. In panels (A-D) cells were fixed and stained for actin (green) and the nucleus (blue). Scale bars represent 50 μm. In panel (E) dot plots report mean ± SEM. **p<0.005. Each dot indicates one analyzed image.

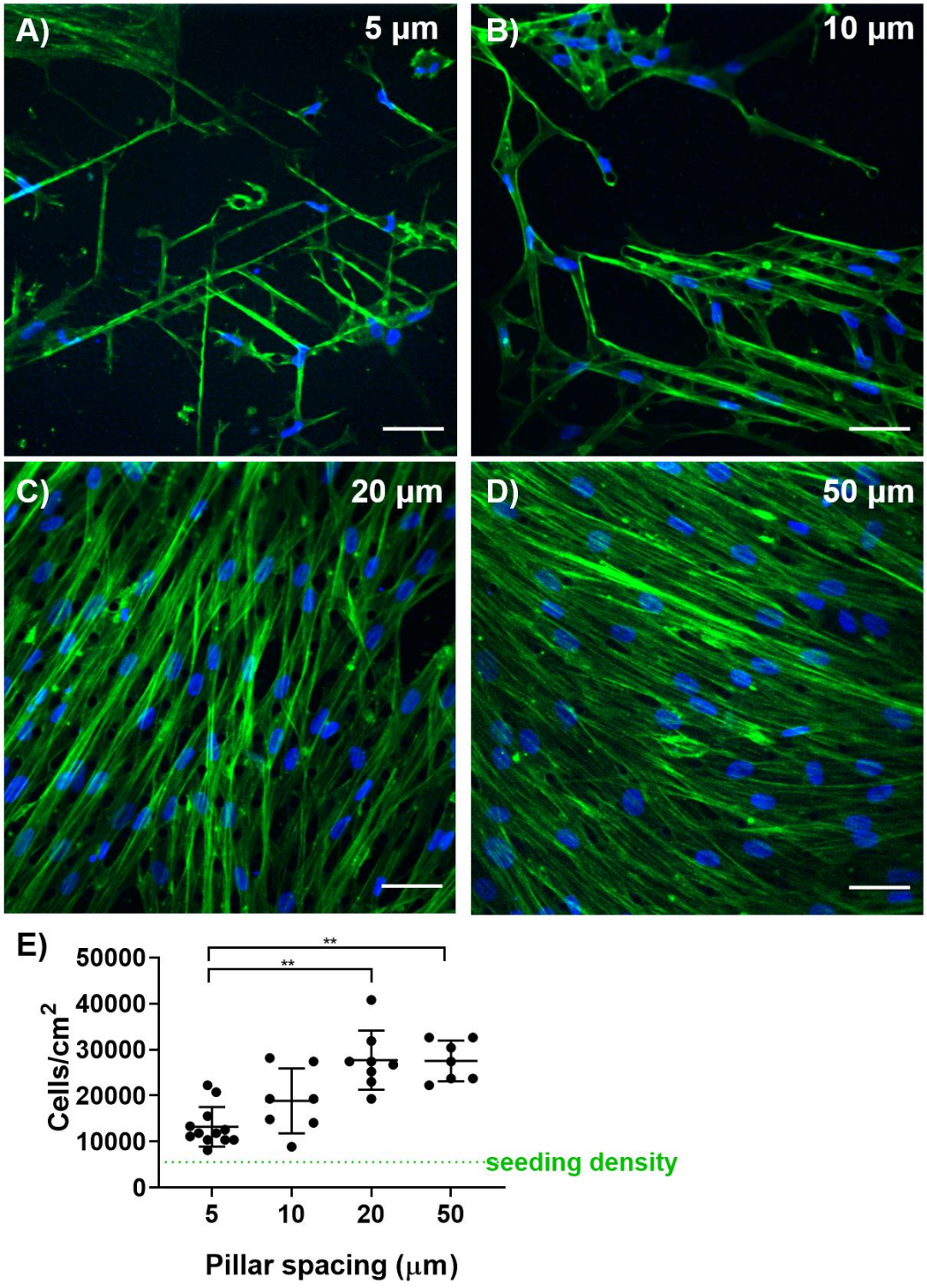
A)
5 µm
B)
10 µm
C)
20 µm
D)
50 µm
E)
**
**
50000
40000
30000
20000
10000
0
Cells/cm2
seeding density
5
10
20
50
Pillar spacing (µm)

5.3.4 MSC cytoskeletal elements become more diffuse with increasing confinement

We next investigated whether the changes in cellular morphology as a function of micropillar array spacing were accompanied by alterations in organization of the cell cytoskeleton. Within all micropillar arrays, regardless of pillar spacing, some cells exhibited f-actin-rich protrusions wrapping entirely around the pillars (Fig. 5.8). To determine whether cells were adhering to the pillars via focal adhesions, we immunostained for tyrosine-phosphorylated (py-) paxillin, a protein associated with focal adhesions. Indeed, we observed areas of high py-paxillin signal associated with the micropillars (Fig. 5.8A-B). MSCs within 50 μm spaced micropillars exhibited many linear, mature focal adhesions at the end of f-actin stress fibers, indicative of highly contractile cells (Fig. 5.8D). These linear, mature focal adhesions decreased with each subsequent decrease in pillar spacing (Fig. 5.8B-C). MSCs within 5 μm spaced micropillars exhibited mostly punctate py-paxillin dispersed through the cell (Fig. 5.8A). These results are consistent with our own previous work in microchannels (Chapter 3).

We also examined how microtubules were arranged within MSCs via immunostaining of α-tubulin. Microtubules were fairly well-localized to regions of f-actin in confined MSCs within 5 μm and 10 μm spaced micropillars (Fig. 5.8E-F). MSCs within 20 μm and 50 μm spaced micropillar arrays exhibited the strongest microtubule signal surrounding the cell nucleus, while f-actin mainly resided along the cell perimeter (Fig. 5.8G-H). Similar to f-actin, microtubules also wrapped around individual

micropillars. Together, these results provide further confirmation that the cell cytoskeleton and adherence patterns can be altered by physical confinement, which we also hypothesized could result in cell phenotypes with altered functionality in behaviors, such as cell migration, relevant to tissue engineering strategies.

Figure 5.8 MSC cytoskeleton within micropillars. Basal plane of MSC cytoskeleton in micropillar arrays with spacing of A) 5 µm, B) 10 µm, C) 20 µm, and D) 50 µm. Maximum projection of MSC cytoskeleton in micropillar arrays with spacing of E) 5 µm, F) 10 µm, G) 20 µm, and H) 50 µm. In panels (A-D) cells were fixed and stained for py-paxillin (red), actin (green), and the nucleus (blue). Areas of strong signal are indicated by white arrows. In panels (E-H) cells were fixed and stained for α-tubulin (red), actin (green), and the nucleus (blue). Color channels were altered individually for optimal visualization. Scale bars represent 10 µm.

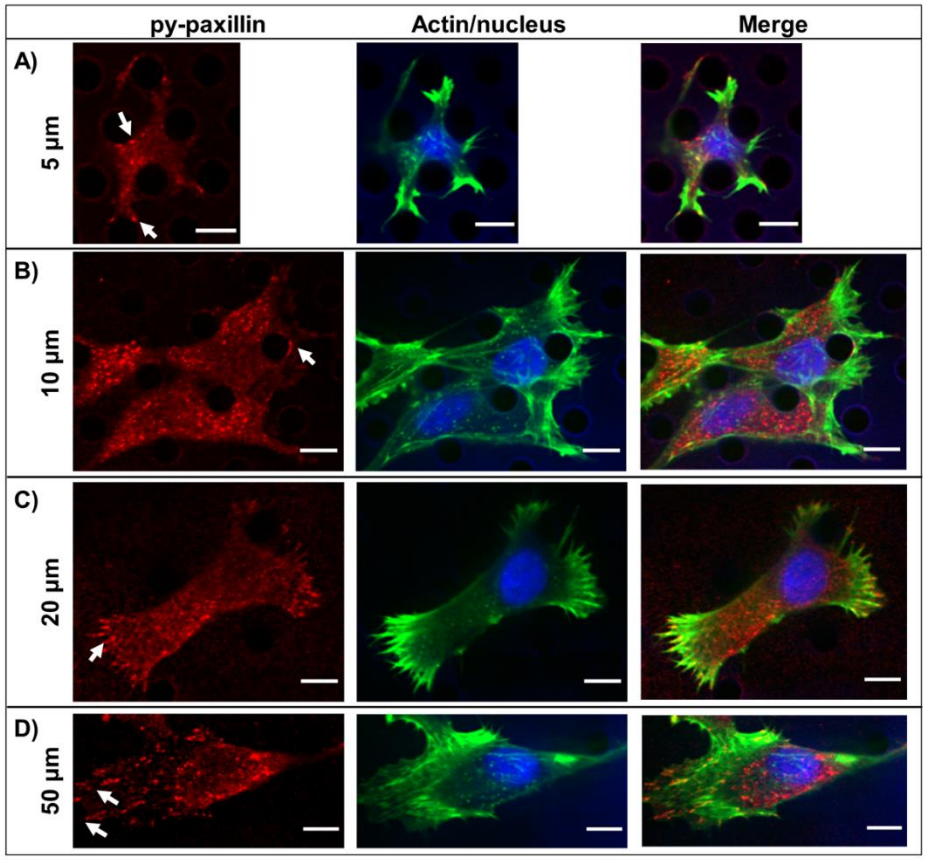
py-paxillin
Actin/nucleus
Merge
A)
5 µm
B)
10 µm
C)
20 µm
D)
50 µm

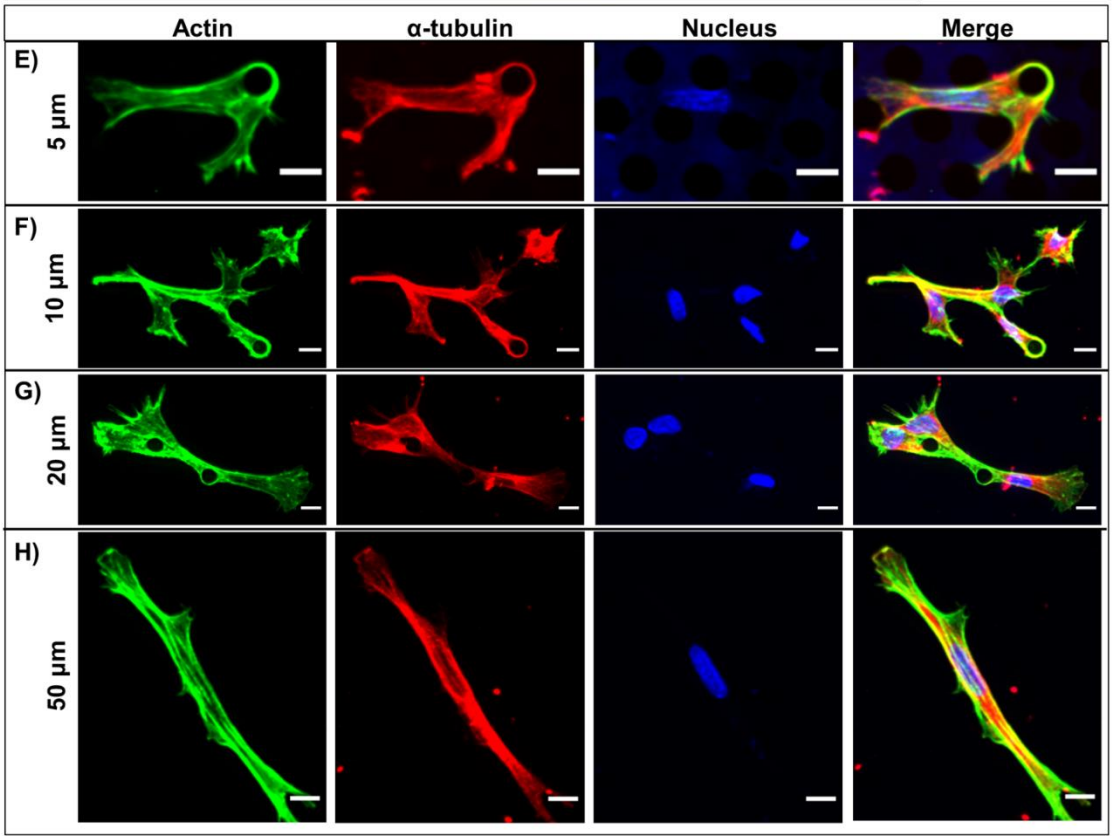
Actin
α-tubulin
Nucleus
Merge
E)
5 µm
F)
10 µm
G)
20 µm
H)
50 µm

5.3.5 MSCs migrate within micropillar arrays

Our next goal was to use phase contrast imaging to confirm that cells were capable of robust migration within the micropillars (Fig. 5.9). Cells displayed several interesting behaviors when migrating within the micropillars. In arrays where pillars were 5 μm or 10 μm apart, cells remained mostly elongated. MSCs typically approached a pillar, probed around both sides, and "chose" one of those two sides to migrate around (Fig. 5.9A). Occasionally, cells appeared to engulf a pillar entirely to migrate around it. In arrays where pillars were 20 μm or 50 μm apart, different migration patterns emerged. The cells often migrated in a mesenchymal mode, like their behavior in 2D (Fig. 5.9B). However, cells also migrated in a somewhat amoeboidal mode, characterized by alternating periods of fast, directional migration and slower, more random migration (Fig. 5.9C). Occasionally, another mode appeared where cells attached to a pillar, clung to it for some time, and then rapidly migrated to another pillar where it attached and rounded up yet again (Fig. 5.9D). These observations of different migration modes encouraged us to further analyze MSC migration within the micropillar arrays.

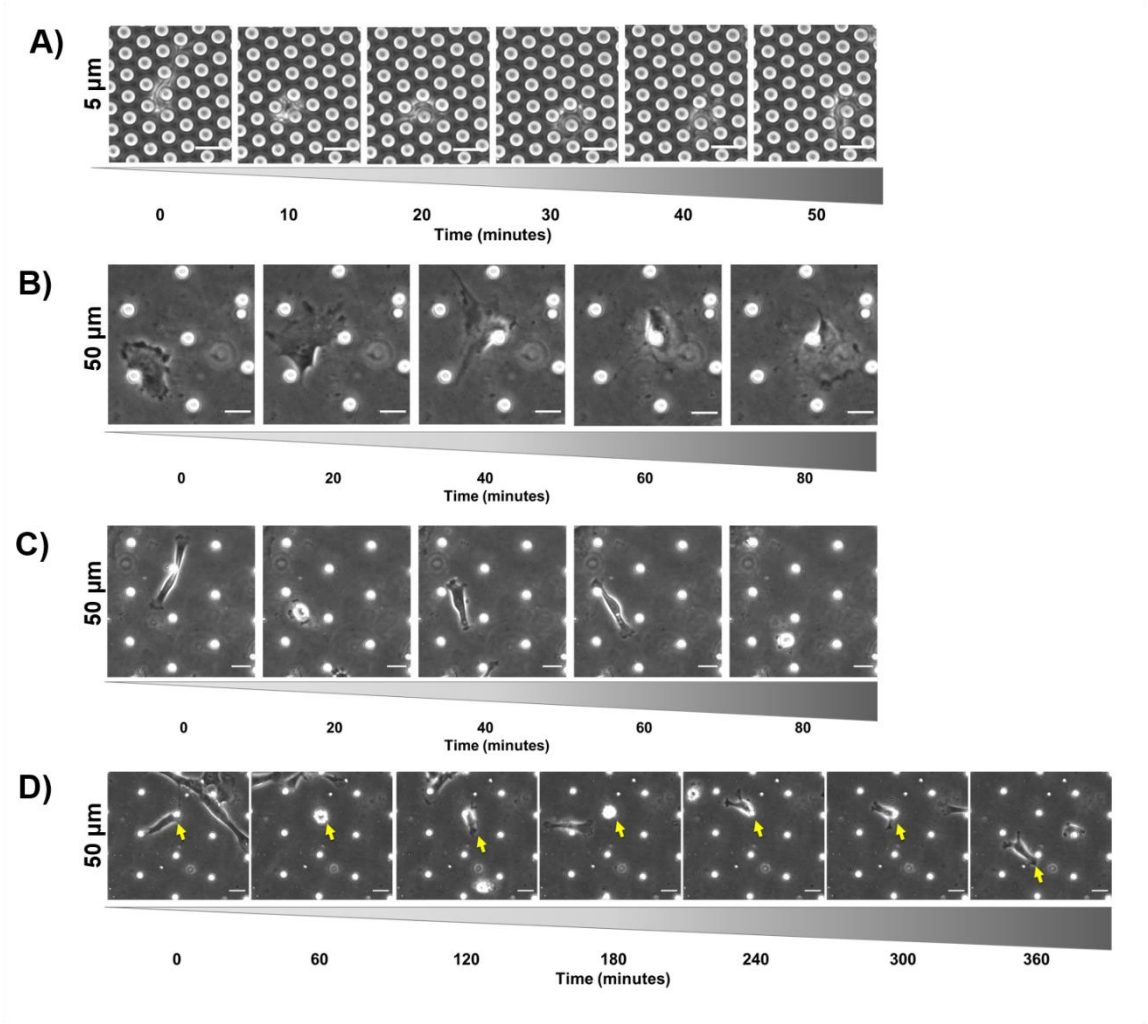

Figure 5.9 MSC migration phenotypes within micropillars. Representative image sequences of A) MSC migrating in confined 5 µm pillar spacing, B) MSC migrating in a mesenchymal mode within wide 50 µm pillar spacing, C) MSC migrating in amoeboidal mode within wide 50 µm pillar spacing, and D) MSC attaching to a micropillar within wide 50 µm pillar spacing (MSC of interest denoted by yellow arrow). Scale bars represent 25 µm.

To investigate cell migration, we manually tracked each cell's movement every 10 minutes or every 30 minutes. We hypothesized that cell migration parameters, including speed and turning angle distribution, would depend on time interval chosen for analysis, where, at short timescales, cells may be more persistent, but turn more or measure slower speeds when undergoing random migration. Qualitatively, MSC trajectories within the 5 μm spaced micropillars appeared to migrate with more "straight" paths, presumably due to guidance by the constricting pillars (Fig. 5.10A-B). As pillar spacing was increased, cell motion appeared more random (Fig. 5.10A-B). We quantified the turning angle of each cell for each time point as it migrated and plotted the relative frequency of turning angles (Fig. 5.10C-F). The turning angle represents the angle between a cell's previous trajectory and its current trajectory. We observed most turning angles were close to 0°, and there was a slight increase in the frequency of angles very close to 180° for cells in 5 μm micropillars (Fig. 5.10C). In this definition, a turning angle of 0° indicates a cell continued moving forward in a straight line, while a turning angle of 180° indicates a cell completely reversed its direction. However, we also considered straightness of cell migration without considering directionality. In this definition, we considered turning angles from 0° to 90°, by subtracting the angle from 180° if it was over 90° (Fig. 5.10D). For example, a previous turning angle of 175° (nearly complete reversal of migration direction) would now be represented as 5°. In this case, turning angles within all micropillar spacings were most frequently close to 0°, with 5 μm being the most extreme case (Fig. 5.10D). Interestingly, different trends emerged when we analyzed cell turning angles using 30-minute time steps instead of 10-minute time steps (Fig. 5.10E-F). Specifically, we found an increase in the

distribution of turning angles close to 180° (complete reversal of direction), especially for the 5 μm pillar spacing. We subsequently quantified the skewness of each histogram and found that, when considering turning angles from 0° to 90°, there was an increase in skewness with increasing confinement, which provided quantitative confirmation that more confined cells migrated in straighter paths than less confined cells (Fig. 5.10G). MSCs migrated faster in 50 μm spaced pillars than 3 μm spaced pillars when tracked every 10 minutes, but there were no differences in speed when cells were tracked every 30 minutes (Fig. 5.10H-I). The mean squared displacement (MSD) versus time of the MSCs appeared very similar for all micropillar spacings over short timescales (up to ~200 minutes), but began to diverge (with no monotonic trend) between micropillar spacings at larger timescales (Fig. 5.10J-K). Therefore, physical confinement of MSCs in this micropillar assay affects not only cell morphology and cytoskeletal organization, but also functional behaviors such as cell migration.

Figure 5.10 Quantitative MSC migration parameters within micropillars. Trajectories of MSCs within 5 μm, 10 μm, 20 μm, or 50 μm micropillar arrays tracked every A) 10 minutes or B) 30 minutes. Histogram displaying relative frequencies of turning angles for cells tracked every 10 minutes within micropillars, and considered from C) 0-180° where 0° corresponds to no deviation in migration path from previous timestep and 180° corresponds to a complete reversal of direction; or D) 0 to 90° where there is no distinction between forward and backward motion. Histogram displaying relative frequencies of turning angles for cells tracked every 30 minutes within micropillars, and considered from E) 0-180° or F) 0 to 90°. G) Skewness of histograms in panel (C-F). Speed of MSCs as a function of pillar spacing tracked every H) 10 minutes or I) 30 minutes. G) MSD as a function of time for cells within micropillars spacing tracked every J) 10 minutes or K) 30 minutes. Panels (C-K) display data for 5 μm (green), 10 μm (blue), 20 μm (red), or 50 μm (cyan). Dot plots in panels (H-I) report mean ± SEM, and each dot represents one cell. n.s. = not significant, *p<0.05. Cells pooled from N=4 independent experiments with n(5 μm)=25, n(10 μm)=30, n(20 μm)=32, n(50 μm)=21.

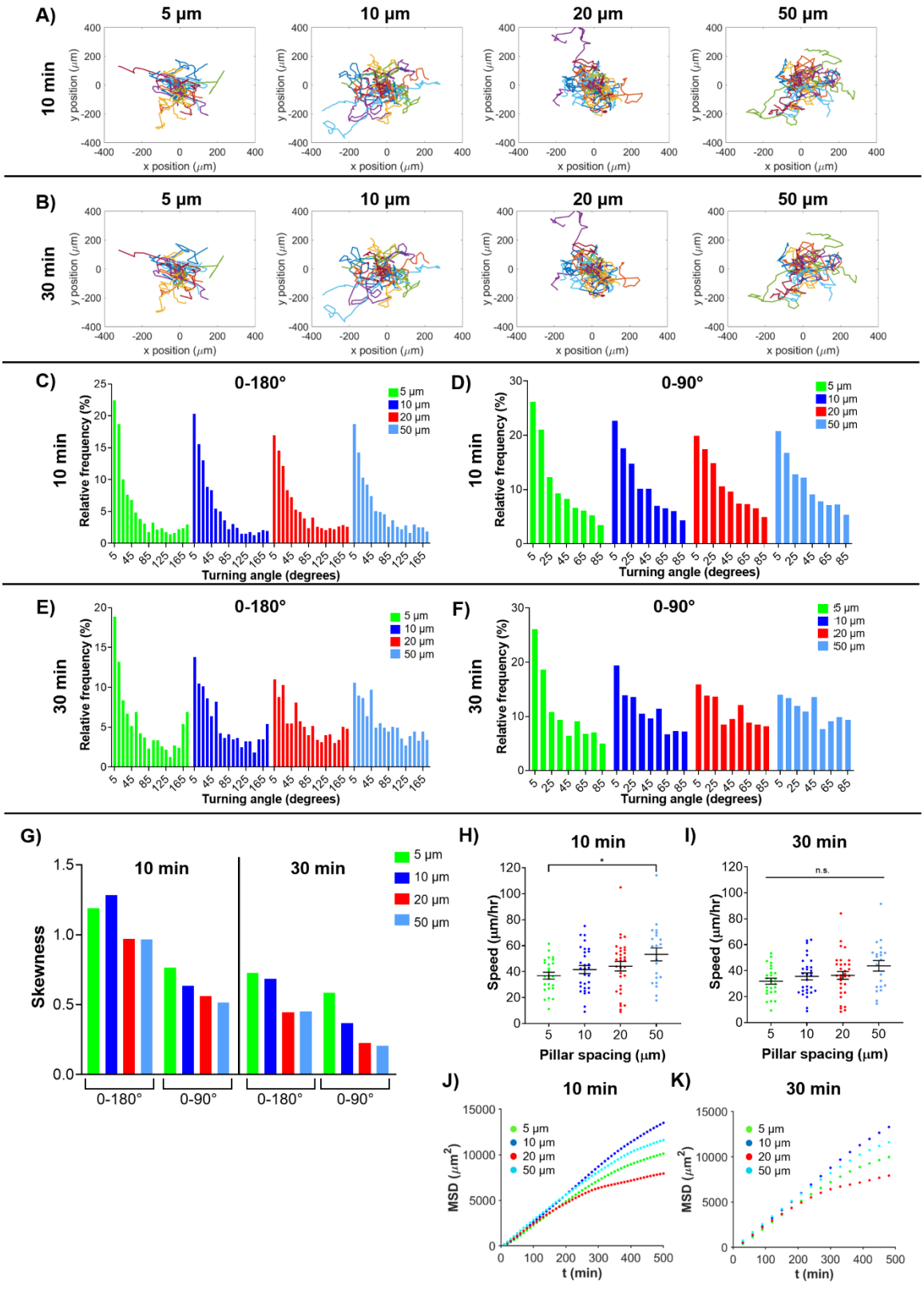
A)
5 µm
10 µm
20 µm
50 µm
10 min
y position (µm)
x position (µm)
B)
30 min
C)
0-180°
D)
0-90°
Relative frequency (%)
Turning angle (degrees)
5 µm
10 µm
20 µm
50 µm
E)
F)
G)
Skewness
10 min
30 min
0-180°
0-90°
H)
I)
Speed (µm/hr)
Pillar spacing (µm)
n.s.
J)
K)
MSD (µm²)
t (min)

5.4 Discussion

We have demonstrated the potential of using a micropillar array for confining cells and studying their mechanobiology with a downstream goal of providing information that could help optimize cell culture systems for tissue engineering purposes. Our system was developed using information learned from many previous studies using micropillars in various applications. An excellent review of how micropillars have been used to evaluate cell behavior is found in Roca-Cusachs *et al*. [256]. In Table 5.2, we summarize studies where cells were cultured within [153]–[155], within and atop [209], [257]–[259], or solely atop [152], [260]–[263] micropillar arrays. Our system herein is distinct in that we use a wide range of micropillar spacings and show that cells can be maintained within micropillars over long periods of time (Table 5.2). Additionally, cells infiltrate directly into the micropillar array, in contrast to other systems in which cells migrate from 2D into micropillars [153], [155]. In fact, collagen-coated micropillar arrays can be placed within a non- cell-adhesive plate to disallow cell attachment to any 2D surface. This allows one to investigate the effect of confinement on cell behavior by ensuring no cells are attached to a 2D surface.

Table 5.2 Micropillars used in literature.

	Pillar size and spacing	Unique features	Cells	Functional assessment	Paper
Within pillars	10 μm diameter 14-16 μm height 5, 10, 20, 50 μm spacing	Wide range of pillar spacings, long-term culture	human MSCs	Cell morphology, cytoskeletal arrangement, cell migration	The work herein
	7.6x7.7 μm^2 to 3.7x5.7 μm^2 dimensions 15 μm height ~3 μm spacing	Anisotropically stiff	human MSCs	Cell alignment	[154]
	10 μm diameter 20 μm height 8,10,12 μm spacing	Correlated invasiveness to nucleus mechanical properties	human MSCs	Invasiveness, persistence length	[153]
	10 μm diameter 20 μm height 6, 8, 12 μm spacing	Cells migrate from 2D into pillars	3T3 fibroblasts, Hutchinson–Gilford Progeria Syndrome patient fibroblasts	Morphology, invasiveness, trajectory, MSD, diffusion coefficient	[155]
Atop and within pillars	5 μm diameter 20 μm height 4-12 μm spacing	Cells sit atop and deform pillars	REF52 fibroblasts	Displacement of pillars, force exerted on pillars during spreading	[257]
	3 μm side length 7 μm height 6 μm spacing	Examined effect of osteogenesis on nuclear deformation	rat MSCs, osteoblasts	Nuclear height, nuclear deformation	[209]
	2-15 μm side length 6 μm height 2-20 μm spacing	Compared pillar materials	osteosarcoma cells	Nuclear deformation	[258]

	5-15 μm side length 5 μm height 5-15 μm spacing	Compared pillars to grooves	rat MSCs	Proliferation, morphology, cytoskeletal elements	[259]
Atop pillars	3 μm diameter 9 μm height 6 μm spacing	Micropillars within microchannels	3T3 fibroblasts, osteosarcoma cells	Traction forces	[152]
	3 μm diameter 10 μm height 9 μm spacing	Magnetic microposts to apply forces to cells	3T3 fibroblasts	Traction forces, focal adhesion area	[260]
	1-2 μm diameter 3-8 μm height 2-4 μm spacing	Improved resolution	MDCK epithelial cells	Traction forces	[261]
	2-10 μm diameter 3-50 μm height 6 μm spacing	Origin of micropillars	Pulmonary artery smooth muscle cells, endothelial cells, 3T3 fibroblasts	Traction forces	[262]
	2-7 μm diameter 12 μm height 10 μm spacing	Stiffness gradient of pillars	C2C12 myoblasts, 3T3 fibroblasts, HeLa cells	Traction forces, cell migration	[263]

An additional important feature of our system is the non-deformability of micropillars by cells. Our micropillar arrays are fabricated with a stiff polymer that has previously been measured to be approximately 1.75 MPa [264]. Even in the most extreme case, if cells were to reach the top of the pillar and exert a force perpendicular to the pillar, the bending stiffness, $k = {3\pi D^4}/{64L^3}$ [265], of the tallest pillar would be 629 nN/μm, assuming a pillar diameter (D) of 10 μm and a pillar height (L) of 16 μm.

Cells typically exert traction forces through focal adhesions of ~100-1000 nN [266]. Therefore, the micropillars should be primarily non-deformable to the cells and induce the specified degree of confinement. Although the PDMS used here is quite stiff, it is similar to the stiffness of various tissues *in vivo* such as bone, cartilage, and ligament [267]. To mimic other anatomical features, future studies may use gels of lower elastic modulus, thus enabling investigation into the coupled effects of confinement and stiffness.

Distinct morphological differences appeared between MSCs in 5 μm spaced pillars and wider spaced pillars. Morphology is an important indicator of MSC behavior, as morphology alone can be used to predict the long term mineralization potential or the immunosuppressive capacity of MSCs [268], [269]. Future work may leverage freely available software such as CellProfiler to create high throughput pipelines and analyze cells on a population level. Such high throughput analysis may be applied to this micropillar confinement system to reveal subsets of distinct cells within a heterogeneous population or between different populations, such as different MSC donors.

Similar to what we saw within micropillar arrays, it has been shown previously that mesenchymal cells can spontaneously switch to an amoeboidal migration mode when they experience both vertical confinement and low adhesion [183]. One of these amoeboidal migration modes is initiated by an external polarization signal, such as a piece of debris. In our case, the micropillars may act as an external polarizer, even though MSCs herein attach well to the micropillars on three sides and show evidence of some focal adhesions. Similar to our migration assays, another group also observed cells alternate between fast, directed migration and slow, random migration when cells

encountered micropillars [270]. Furthermore, the cell and nuclear deformation and altered cytoskeletal organization that occur in the most confining micropillar arrays may lead to differences in cell growth, as we have shown for sarcoma cells [173], or cell fate, which is influenced by other mechanical cues that have similar impact on cell morphology.

Interestingly, we saw different trends in turning angles when cells were tracked every 10 minutes compared to when they were tracked every 30 minutes. When cell migration is tracked using a 10 minute interval, the subsequent analysis is representative of changes in cell migration at short timescales. This potentially increases the histogram's skewness towards small turning angles, as cells make small probing motions. Increasing the time interval to 30 minutes could be more representative of cell migration over long time periods, as cells move through the micropillars. Regardless of the time interval, cells migrated straighter within more confined micropillar arrays, perhaps due to the high density of micropillars guiding their migration.

The migration patterns of MSCs we observed within micropillar arrays is in slight contrast to our previous reports of MSC behavior within microchannels (chapter 3). Herein, MSCs migrated faster in 50 μm spaced pillars than 5 μm spaced pillars when tracked every 10 minutes. However, when MSCs migrated through microchannels, cells within 50 μm wide channels migrated slower than or with similar speed to those in 6 μm or 10 μm wide channels, depending on MSC passage (chapter 3). We hypothesize that contact guidance has a larger influence on cell migration in microchannels than in micropillar arrays, as cells tend to follow the surface to which they are attached [141]. Cells have more choice over their path within micropillar arrays, potentially slowing

them in narrower spacings. Furthermore, our previous results in microchannels were in the presence of a chemotactic gradient, which in combination with contact guidance from the microchannel walls, may lead to altered trends in migration. Overall, different methods of confinement may induce different cell behaviors.

It was critical that our micropillar design yield adequate sample sizes for downstream quantitative assays to investigate the concentration of secreted factors as well as gene and protein expression. We have successfully performed an ELISA on MSC-conditioned media at various time points (data not shown). This is possible due to the capacity of our micropillar arrays to support long-term cell growth. Analysis of cell density after 3 weeks in micropillars showed that cells did indeed proliferate within the micropillar arrays, yet there were significantly fewer cells within the 5 μm spaced micropillars. We speculate this may be due to there being less planar surface area for cell attachment and growth in the narrowest spaced micropillars. Additionally, we have previously shown that increasing confinement (in microchannels) decreases the percentage of cells that successfully divide [173], which may explain cells being more sparse in 5 μm arrays. Despite differences after 3 weeks in culture, the majority of seeded cells infiltrated into the micropillars, yielding a sample size of ~$5x10^4$ cells per micropillar array at 24 hours. This was fairly consistent for 2 different MSC donors, but minor differences suggest that cell seeding parameters be optimized for each new cell type. This cell count could provide enough RNA to allow for qRT-PCR and analysis. However, an order of magnitude more cells are necessary for one Western blot. This could be achieved by running multiple wells in parallel, increasing the area of the micropillar array, or increasing the seeding density. However, we note that when the

seeding density was increased to a very high number (5-10x10^5 cells per array), some groups of cells began to aggregate and did not infiltrate into the pillars (data not shown). The combination of our confinement assay with Western blot or PCR will reveal downstream effects of mechanical confinement, making it an even more powerful tool for tissue engineering. Through deeper understanding of cell mechanotransduction in the context of confinement, we can fine tune tissue engineered constructs to produce cell phenotypes that are optimal for a given purpose.

5.5 Conclusion

In summary, we have successfully developed and validated a PDMS micropillar array that systematically confines cells, allows for easy visualization and scale up, allows for long term cell culture, and provides an adequate sample size for analysis of the genome, secretome, or proteome. Future modifications of the micropillar confinement assay, including fabrication of micropillar arrays with more narrow spacing and applying a top confining post to the micropillar array, would enable us to study the effects of physical confinement on cell behaviors in greater depth. This knowledge is critical to improve the design of cell-laden tissue engineered constructs and *in vivo* cell therapies. By combining confinement with other physical cues, we can harness mechanical properties in order to encourage or inhibit cell migration, direct cells down a particular lineage, induce cell secretion of specific cytokines or extracellular vesicles, and ultimately direct cells to behave in a way conducive to tissue engineering.

The PDMS micropillar array is an advantageous tool to study the effect of mechanical confinement on the lung fibroblast to myofibroblast transition (FMT). FMT

is a key phenomenon related to idiopathic pulmonary fibrosis (IPF) progression, and requires a system that can support long-term culture and downstream biological readouts, while still exerting known amounts of mechanical confinement and retaining easy visualization of cells. Therefore, in the next Chapter, we utilize the micropillar assay developed in this chapter to investigate the effect of confinement on FMT.

Chapter 6: Fibroblast to myofibroblast transition is cell density dependent

6.1 Introduction

Idiopathic pulmonary fibrosis (IPF) is a chronic disease of the lung caused by a rampant inflammatory response that results in the deposition of excessive extracellular matrix (ECM). The excess ECM presents as scarring of the lung parenchyma and impairs gas exchange, making it difficult for patients to breathe [21]. There are no effective treatments for IPF, and the median survival time after diagnosis is approximately 3 years, making IPF a critical disease to investigate and treat [40].

Lung tissue explanted from patients diagnosed with IPF is stiffer than healthy lung tissue, due to the increased protein content of the ECM and altered collagen crosslinking [41], [42]. Concomitant with increased ECM deposition and crosslinking, there is increased confinement imposed on cells by the ECM. In concert with increased confinement imposed by the ECM, there is increased confinement imposed by increased cell density as fibroblastic foci develop. Another characteristic feature of IPF, fibroblastic foci within the lung consist of activated fibroblasts and myofibroblasts [41].

Myofibroblasts are contractile, matrix-depositing cells characterized by α-SMA-positive stress fibers. Myofibroblasts are essential in the recovery of damaged tissues and critical in the inflammatory response, but cause pathology when they persist in tissue. Although the origin of myofibroblasts in IPF is continually under investigation, there is evidence that resident fibroblasts can differentiate into myofibroblasts, termed

the fibroblast to myofibroblast transition (FMT), when given certain physical and/or chemical cues [44]. For example, fibroblasts cultured on stiff substrates are more likely to differentiate into myofibroblasts than those on soft substrates, due to increased actomyosin contractility [44]. Concomitantly, stiff matrices encourage stress fiber formation within cells, which compress the nucleus [45]. However, it is unknown to what degree, if any, direct nuclear compression in the absence of increased contractility alters FMT. We are able to induce nuclear deformation within low-contractile cells by confining cells within the micropillar assay detailed in Chapter 5. This micropillar array also allows us to investigate if increased confinement, such as that imposed by the dense ECM within IPF, influences FMT.

Confining forces can also come from neighboring cells within a tissue. In fibroblastic foci, fibroblasts and myofibroblasts are more densely packed than in healthy lung tissue. Cell density is known to affect the behavior of lung fibroblasts, such as how they contract a 3D collagen gel [271]. In this work, we investigated the role of mechanical and cell-cell imposed confinement in FMT.

One treatment being targeted as a therapy for IPF is MSC injection [54]. Several pre-clinical trials have proved MSCs effective in ameliorating inflammation and fibrosis, and clinical trials have begun [18], [55]. However, other studies indicate that MSC therapy worsens outcome, particularly in late stage IPF [19]. Less than 1% of all injected MSCs remain in the body one week after systemic injection, suggesting a paracrine mechanism of action [56]. Accordingly, secreted factors derived from MSCs have been shown to block fibroblast differentiation into myofibroblasts [57].

Recently, manipulating the physical microenvironment, such as by applying strain or altering substrate protein coating, has been shown to alter the MSC secretome, which includes cytokines and extracellular vesicles [203]. To obtain MSC secreted factors, MSCs are typically cultured in 2D on standard tissue culture plastic and their media harvested [204], [205]. However, MSCs cultured in 3D spheroids have been shown to have enhanced therapeutic effects [206]. Herein, we investigated how increasing confinement may influence MSC secreted factors, aiming to increase our knowledge of how MSC culture conditions may enhance the therapeutic effects of MSCs. This work will enhance understanding of IPF progression at a mechanistic level and improve treatments for IPF.

6.2 Materials and methods

6.2.1 Cell culture

Human lung fibroblasts (HLFs) were purchased from ATCC (Manassass, VA, USA) and cultured in fibroblast basal medium (ATCC) supplemented with 7.5 mM L-glutamine, 5 ng/mL FGF basic, 5 µg/mL Insulin, 1 µg/mL Hydrocortisone, 50 µg/mL ascorbic acid, 2% fetal bovine serum (FBS, ATCC), and 1% Penicillin-Streptomycin 10,000 U/mL (Thermo Fisher Scientific, Waltham, MA, USA). HLFs were cultured and used until passage 5. Cells were washed with Phosphate-Buffered Saline (PBS) (VWR, Radnor, PA, USA), detached with Trypsin-EDTA for primary cells (ATCC), and resuspended in Trypsin Neutralizing Solution (ATCC). Bone marrow-derived human mesenchymal stem cells (Donor: 20 year-old female) were purchased from RoosterBio,

Inc. (Frederick, MD, USA). Cells were removed from liquid nitrogen and grown in RoosterBio basal media with media booster (RoosterBio, Inc.) for the first day post-thaw. Thereafter, cells were cultured in media composed of Dulbecco's Modified Eagle's Medium with high glucose (ThermoFisher Scientific), 10% Fetal Bovine Serum (FBS) (ThermoFisher Scientific), and 1% Penicillin-Streptomycin 10,000 U/mL (ThermoFisher Scientific). Cells were cultured and used until a population doubling level of 20 and cells were passaged at or below 80% confluency. Cells were washed with Phosphate-Buffered Saline (PBS) (VWR), and detached with TrypLE Express Enzyme (ThermoFisher Scientific). All cells were cultured at 37°C, 50% humidity, and 5% CO2:95% air.

6.2.2 Fibroblast to myofibroblast transition

To induce fibroblast to myofibroblast transition (FMT), HLFs were seeded and allowed to attach overnight. The following day, cells were washed with PBS before adding FBS-free media supplemented with 10 ng/mL TGF-β1 (Peprotech, Rocky Hill, NJ, USA) or vehicle control (10 mM citric acid) to induce FMT. For density-dependent experiments, cells were seeded at 500, 5000, and 50,000 cells/cm^2 for low, medium, and high densities, respectively and media was changed every 1-2 days.

6.2.3 Micropillar array fabrication

Micropillar arrays were fabricated as previously described [8]. Briefly, standard photolithographic techniques, as described previously [9], were used to create a silicon master of the micropillar array design, such that the pillars are 13-17 μm tall. All

photolithography procedures were carried out in the University of Maryland Nanocenter FabLab. Polydimethylsiloxane (PDMS, Krayden, Denver, CO, USA) was mixed at a 10:1 base:curing agent ratio, poured over the silicon master and baked to create a PDMS master, which was then removed and silanized overnight under vacuum using tridecafluoro-1,1,2,2,tetrahydrooctyl-1-trichlorosilane (OTS, 97%) (UCT Inc., Bristol, PA, USA). Then, PDMS was mixed at a 10:1 base:curing agent ratio, poured onto the PDMS master, baked at 80°C overnight, and removed, yielding the final PDMS micropillar arrays. The micropillar arrays were placed in a plasma cleaner (Harrick Plasma, Ithaca, NY, USA) and plasma treated with air for 2.5 minutes in order to increase hydrophilicity. PDMS blocks were simultaneously coated in 8% Pluronic F127 (Sigma-Aldrich) solution for 1 hour at room temperature, then washed with DI water. Micropillar arrays were subsequently stamped with the Pluronic F127-coated PDMS blocks such that the pillar tops were rendered non-adhesive to cells, and placed into 6-well plates. The micropillar-containing plates were UV sterilized for 10 minutes, and 20 μg/mL collagen I (Sigma-Aldrich) was added to all wells and incubated for at least one hour at 37°C. The collagen I solution was then removed, and devices were washed with PBS before seeding cells at a density of $5x10^4$ cells/well. Cell media was changed every 1-2 days.

6.2.4 Immunofluorescence

The following steps were carried out at room temperature, unless otherwise specified. Cells were fixed in 3.7% formaldehyde (Fisher Scientific) for 10 minutes, then washed twice in PBS (VWR). Cells were permeabilized with 0.5% Triton-X 100

(Sigma-Aldrich) for 5 minutes, washed in PBS twice, and blocked for nonspecific binding in 2.5% goat serum (Abcam, Cambridge, MA, USA) for at least one hour. Mouse anti-α-smooth muscle actin antibody (Sigma-Aldrich, St. Louis, MO, USA, #A5228, 1:100) in 1% goat serum was added to cells and incubated at 4°C overnight. Cells were washed three times in PBS, blocked in 2.5% goat serum for at least one hour, then incubated with AlexaFluor 488 Phalloidin (Thermo Fisher Scientific, 1:500), Hoechst (Thermo Fisher Scientific, 1:2500), and AlexaFluor 568 goat anti-mouse (ThermoFisher Scientific #A11004, 1:200) for one hour. Cells were washed three times in PBS, then imaged. Images were acquired on an Olympus IX83 microscope (Olympus, Center Valley, PA, USA) using a 10x or 20x objective.

6.2.5 Cell lysis

Cells were washed with cold PBS, placed on ice, then incubated for 5 minutes in ice cold RIPA lysis buffer (Thermo Fisher Scientific) supplemented with 1:100 protease inhibitor cocktail (Sigma-Aldrich) and 1:500 10 mg/mL phenylmethylsulfonyl fluoride (PMSF) in ethanol. Cells were collected using a cell scraper, and samples were incubated on ice for 1 hour, with vortexing every 15 minutes. Samples were centrifuged at 300xg for 6 minutes, and the cell lysate supernatant was collected. A Pierce BCA assay (Thermo Fisher Scientific) was performed to determine total protein concentration of each cell lysate against bovine serum albumin (BSA) standard.

6.2.6 Western blotting

Cell lysates were diluted in RIPA such that each sample was of the same concentration and final volume. Lysates were mixed 1:1 with 2x Laemmli sample buffer with 1:20 β-mercaptoethanol (BioRad, Hercules, CA, USA), then incubated for 10 minutes at 100°C. Samples were loaded into precast 10% polyacrylamide gels (BioRad) and subject to SDS-PAGE at 120V for 1 hour. Protein was then transferred to a polyvinylidene difluoride (PVDF) membrane (BioRad) at 100V for 1 hour. Membranes were blocked in Tris-buffered saline (TBS)-based blocking buffer (Thermo Fisher Scientific) for 1 hour at room temperature, then incubated in primary antibody overnight at 4°C. Primary antibodies used include mouse anti-α-smooth muscle actin antibody (Sigma-Aldrich #A5228, 1:1000), rabbit anti-GAPDH (Cell Signaling Technology, Danvers, MA, USA, #2118, 1:2000), rabbit anti-OB-cadherin (Cell Signaling Technology #4442, 1:1000), rabbit anti-N-cadherin (Cell Signaling Technology #4061, 1:1000), rabbit anti-vimentin (Cell Signaling Technology #5741, 1:1000), and mouse anti-vimentin (Santa Cruz Biotechnology, Dallas, TX, USA, 1:2000). Membranes were then washed thrice in TBS with 1:500 Tween 20 (TBST buffer, BioRad) at 4°C. Membranes were then incubated in HRP linked secondary antibody for 1 hour at room temperature. Secondary antibodies used were anti-mouse IgG (Cell Signaling Technology, #7076, 1:5000) and anti-rabbit IgG (Cell Signaling Technology, #7074, 1:5000). Membranes were then washed thrice in TBST buffer and once in TBS buffer. Clarity Western ECL substrate was mixed 1:1 Peroxide solution:Luminol/Enhancer (BioRad), then added to the membrane and incubated for 5 minutes. Membranes were imaged using FluorChem E Gel Imaging System. Imaging was performed in the

BioWorkshop core facility in the Fischell Department of Bioengineering at the University of Maryland, College Park.

6.2.7 MSC-CM

MSCs were seeded atop micropillar arrays and allowed to infiltrate overnight. The following day, media was changed to remove suspended cells. After 3 days in culture, MSC-CM was harvested, centrifuged at 500xg for 10 minutes, and filtered through a cell strainer. The MSC-CM was then frozen at -20°C until use. For some experiments MSC-CM was concentrated using a centrifugal filter unit (Millipore Sigma). HLFs were seeded on 2D TCPS and treated with 10 ng/mL TGF-β1 or vehicle control for 3 days. Subsequently, HLFs were washed once in PBS and MSC-CM was added with HLF media.

6.3 Results

6.3.1 TGF-β1 concentration and incubation time alters α-SMA expression within HLFs

TGF-β1 is a pro-inflammatory and pro-fibrotic cytokine that is upregulated in IPF [272]. TGF-β1 has been shown to induce FMT *in vitro* as evidenced by increased α-SMA expression within HLFs [273]. Our first aim was to optimize the concentration and timing of TGF-β1 treatment to induce FMT by examining α-SMA expression via immunofluorescent straining. We observed α-SMA within HLFs after a 48-hour incubation with TGF-β1 at 2, 5, or 10 ng/mL, and to a much greater extent after 72 hours (Fig. 6.1). However, we noticed a decrease in the percentage of cells expressing α-SMA

when we seeded HLFs at a 50% lower density (Fig. 6.2). At low densities, HLFs did not express significant amounts of α-SMA even when treated with 20 ng/mL TGF-β1 (Fig. 6.3). With the potential cytotoxic effects of the citric acid carrier in mind, we chose 10 ng/mL TGF-β1 as our standard treatment concentration for subsequent experiments.

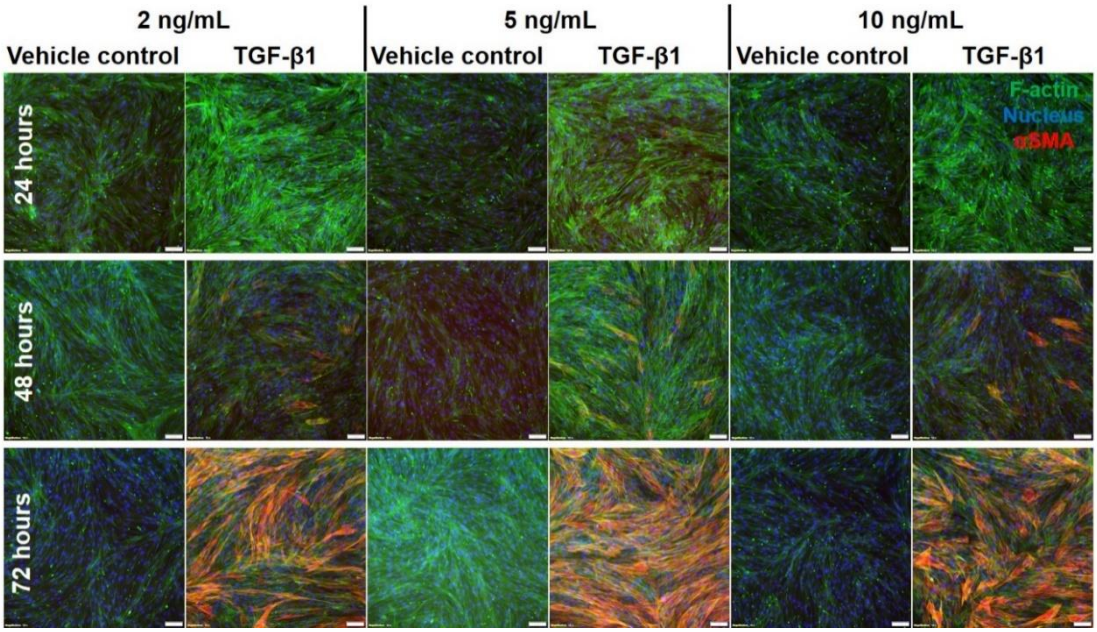

Figure 6.1 HLFs increase α-SMA in response to TGF-β1. HLFs were treated with 2, 5, or 10 ng/mL TGF-β1 or vehicle control for 24, 48, or 72 hours. Cells were fixed and stained for α-SMA (red), f-actin (green), and the nucleus (blue). Scale bars represent 100 µm.

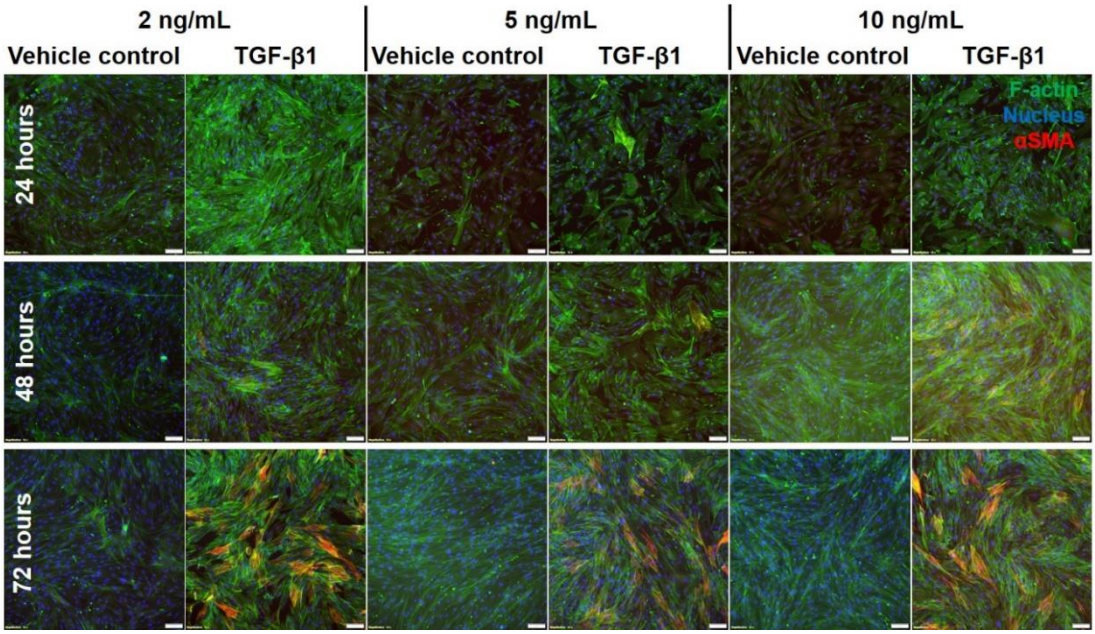

Figure 6.2 HLFs increase α-SMA expression in response to TGF-β1 to a lesser degree at lower density. HLFs were treated with 2, 5, or 10 ng/mL TGF-β1 or vehicle control for 24, 48, or 72 hours. Cells were fixed and stained for α-SMA (red), f-actin (green), and the nucleus (blue). Scale bars represent 100 μm.

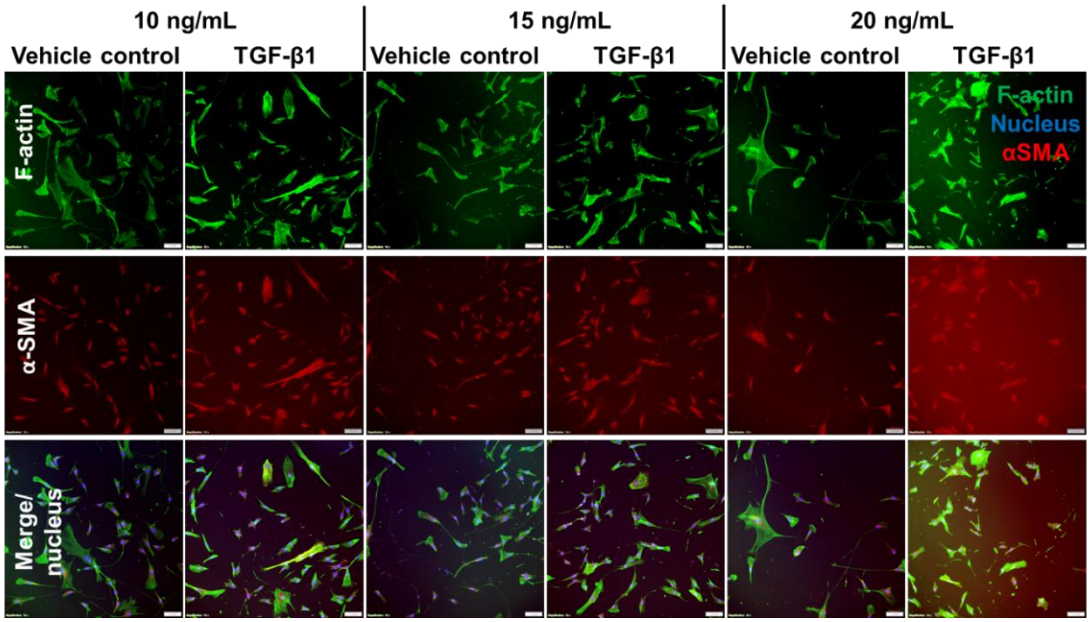

Figure 6.3 HLFs do not increase α-SMA expression in response to TGF-β1 at a low density. HLFs were treated with 10, 15, or 20 ng/mL TGF-β1 or vehicle control for 72 hours. Cells were fixed and stained for α-SMA (red), f-actin (green), and the nucleus (blue). Scale bars represent 100 μm.

6.3.2 HLF seeding density alters α-SMA expression within HLFs

We next investigated if HLF response to TGF-β1 remained density-dependent at a time beyond 72 hours. We seeded 500, 5000, or 50,000 cells/cm^2 (low, medium, and high density, respectively) and treated with 10 ng/mL TGF-β1 for 5 days. We then examined α-SMA expression via immunofluorescent straining. We observed expression of α-SMA in HLFs seeded at a medium density or high density and treated with TGF-β1, but this effect was most prominent in HLFs seeded at high density (Fig. 6.4A). Additionally, f-actin stress fibers were more prominent in medium and high density groups. All groups treated with vehicle control and low density cells treated with TGF-β1 were mostly devoid of α-SMA staining (Fig. 6.4A). We confirmed these results via

western blot for the medium and high density groups, as the low density group did not contain adequate protein for analysis (Fig. 6.4B-C). TGF-β1 induced much higher α-SMA protein expression in the high density than the medium density group. However, the high density group treated with vehicle control had higher levels of α-SMA than the medium density vehicle control group by one order of magnitude. Consequently, TGF-β1 induced an approximately 14-fold increase in expression of α-SMA in the medium density group and approximately 21-fold increase in the high density group. The increased α-SMA expression was present in both the cytosol and cytoskeleton portions of the HLFs (data not shown).

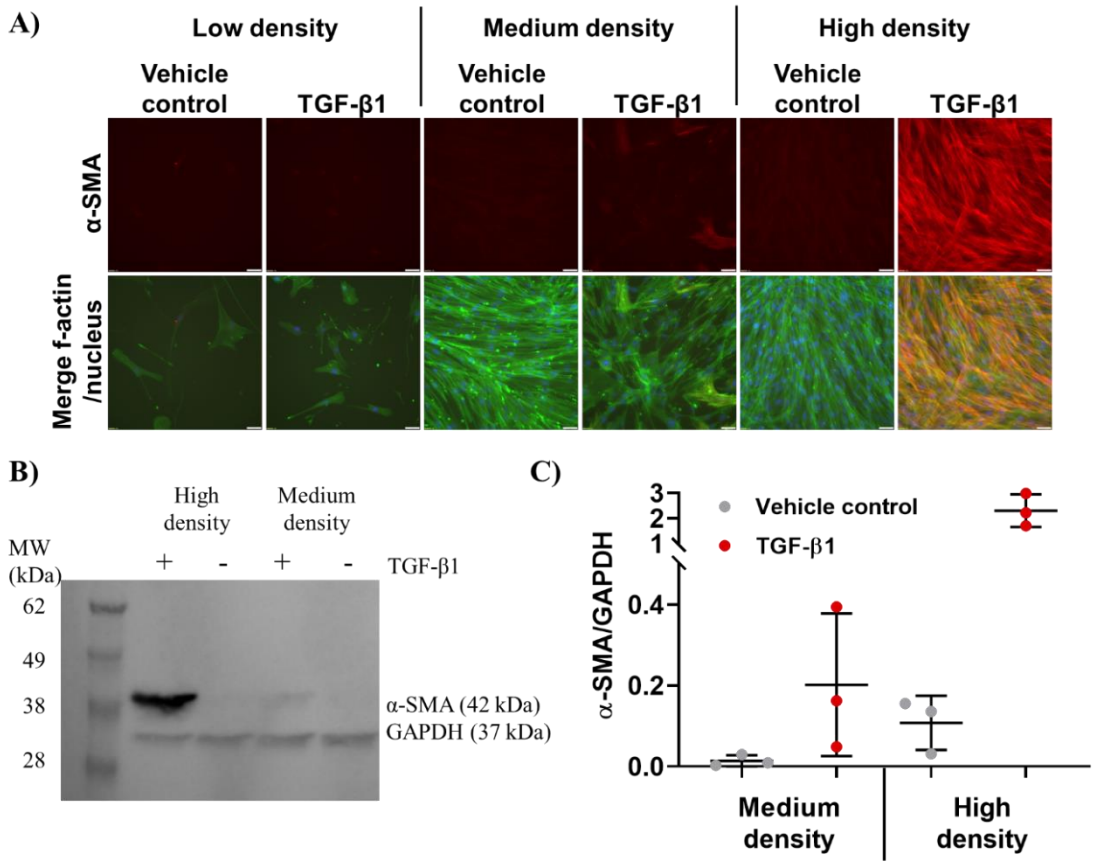

Figure 6.4 HLFs increase α-SMA expression with increasing cell density. HLFs were treated with 10 ng/mL TGF-β1 or vehicle control for 5 days. A) Representative images. Cells were fixed and stained for α-SMA (red), f-actin (green), and the nucleus (blue). Scale bars represent 50 µm. B) Representative western blot. C) Quantification of western blots. Dot plots report mean ± SD.

6.3.3 HLF seeding density, but not TGF-β1, alters OB-cadherin expression

It has been proposed that a transition within fibroblasts from N-cadherin expression to OB-cadherin expression is a hallmark of FMT [274]. We seeded low, medium, and high density HLFs and treated them with 10 ng/mL TGF-β1 for 5 days. We then performed a western blot and noted that no group appeared to express N-

cadherin (Fig. 6.5). Conversely, HLFs seeded at high density expressed more OB-cadherin then the medium density group, irrespective of TGF-β1 treatment. Interestingly, TGF-β1 treatment reduced lamin A/C in all density groups by approximately 50% on average (data not shown).

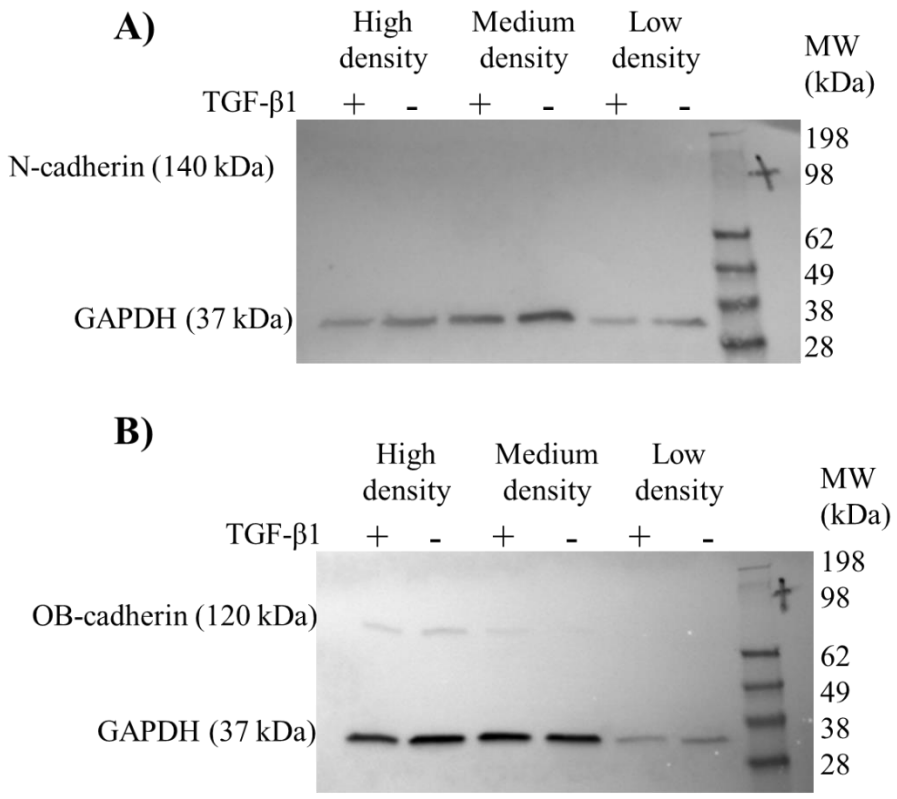

Figure 6.5 HLFs increase OB-cadherin expression with increasing cell density. A) N-cadherin and B) OB-cadherin expression expressed by cells of differing cell density and TGF-β1 treatment.

6.3.4 Confinement does not affect FMT

To investigate whether nuclear compression contributes to the observed density-dependent FMT, we used the micropillar assay developed in Chapter 5 to confine cells. We used PDMS micropillar arrays that are 5, 10, 20, or 50 μm apart from one another,

as well as a 2D PDMS and 2D tissue culture polystyrene (TCPS) controls. This system allows for nuclear deformation even in a reduced contractile state, i.e. in the most confined micropillar array. TGF-β1 increased α-SMA expression in all levels of confinement by a small amount, with planar PDMS having slightly higher α-SMA expression than the 5, 10, 20, or 50 μm confined groups (Fig. 6.6). However, α-SMA expression was highest in HLFs treated with TGF-β1 on 2D TCPS. When we visualized cells via immunofluorescent staining, we noted that HLFs began to grow over the micropillar tops in the 5 μm group (Fig. 6.7). This may explain why α-SMA expression within the 5 μm groups was slightly higher than the 10, 20, and 50 μm groups (Fig. 6.6). Additionally, HLFs treated with TGF-β1 tended to have higher f-actin signal and form discrete clumps, while control HLFs were more evenly distributed (Fig. 6.7). It has been suggested that the formation of small contractile units is the most effective for inducing a high net force on a matrix.

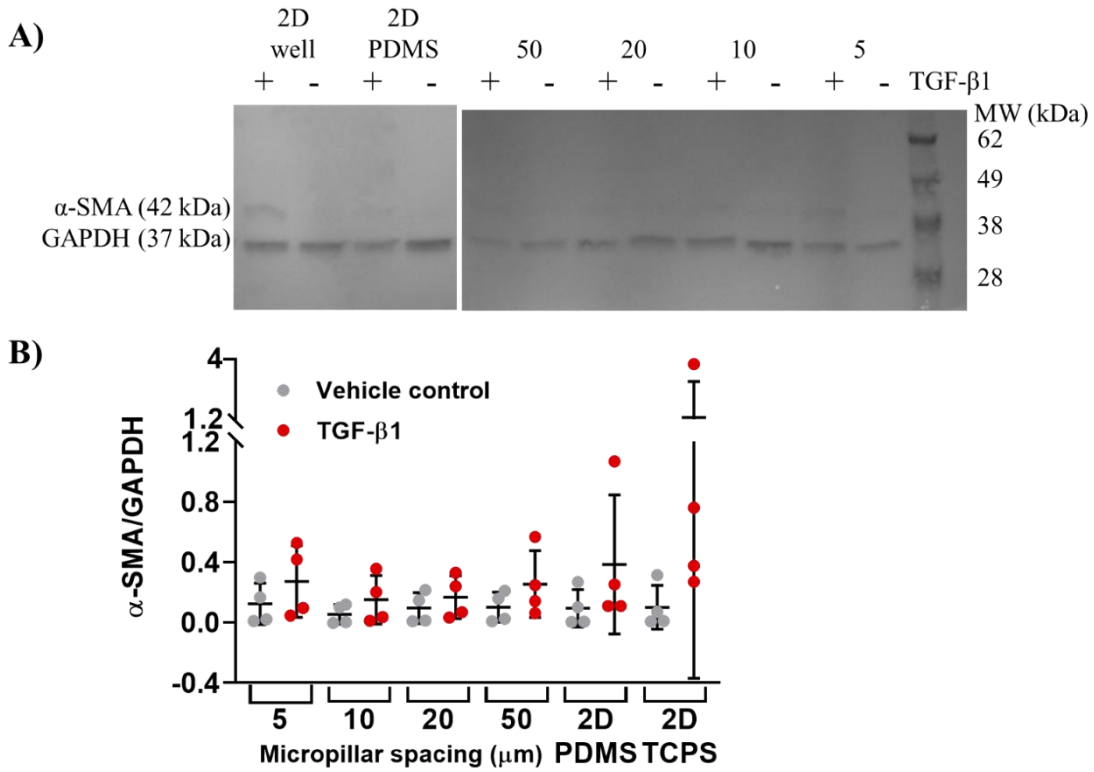

Figure 6.6 Confinement does not affect FMT. HLFs were treated with 10 ng/mL TGF-β1 or vehicle control for 5 days. A) Representative western blot. B) Quantification of western blots. Dot plots report mean ± SD.

Figure 6.7 Confinement does not affect FMT. HLFs were treated with 10 ng/mL TGF-β1 or vehicle control for 5 days. Cells were fixed and stained for α-SMA (red), f-actin (green), and the nucleus (blue). Scale bars represent 50 μm.

Merge micropillars
Merge f-actin /nucleus
α-SMA
5 µm
10 µm
20 µm
50 µm
Vehicle control
TGF-β1
Merge f-actin /nucleus
α-SMA
2D PDMS
2D well
Vehicle control
TGF-β1

6.3.5 MSC-CM does not affect FMT

We next investigated if MSC-CM harvested from confined MSCs would affect its efficacy in reducing FMT. We cultured MSCs in 5, 10, 20, or 50 μm micropillars or on 2D TCPS and harvested their MSC-CM. Simultaneously, we induced FMT by culturing HLFs on 2D TCPS with TGF-β1. We then applied MSC-CM to the HLFs. Surprisingly, we did not see any decrease in α-SMA expression in any group relative to the blank control (data not shown). We concentrated the MSC-CM to potentially enhance the effects, but again did not see any changes relative to the blank control (Fig. 6.8).

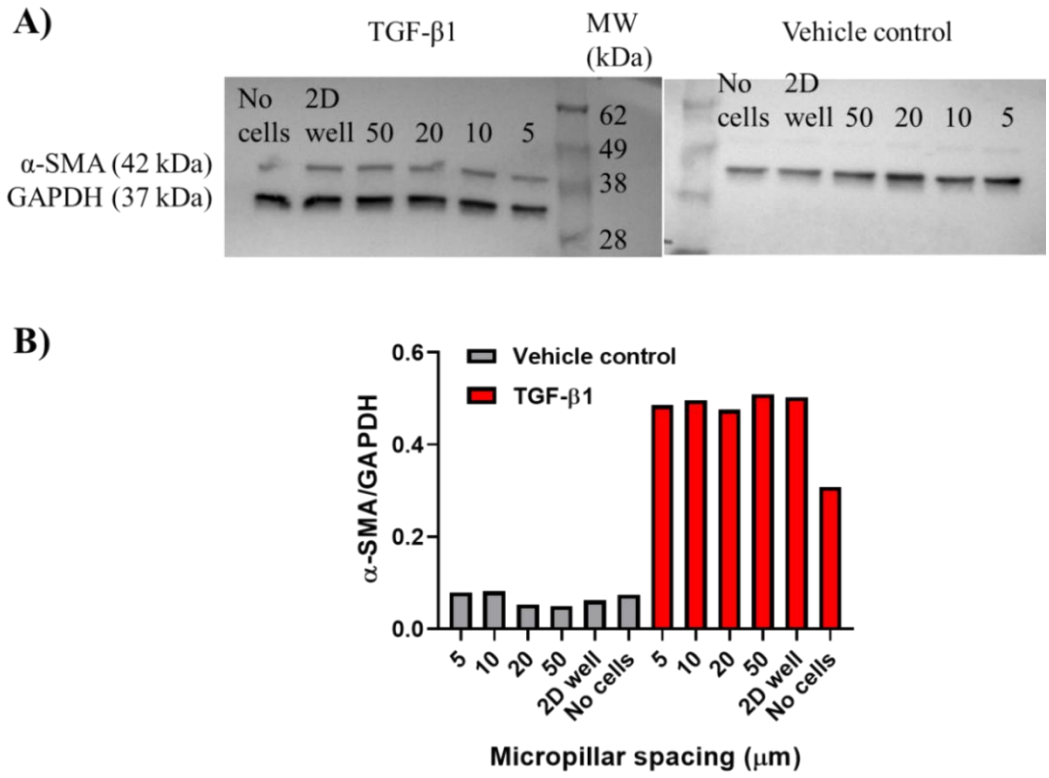

Figure 6.8 MSC-CM does not affect FMT. HLFs were treated with TGF-β1 or vehicle control for 3 days, followed by MSC-CM for 3 days. A) Representative western blot of TGF-β1 treated cells. B) Quantification of western blot. Bar graph reports mean.

6.4 Discussion

IPF is a terminal disease with an average mortality rate of 3 years. There are no effective treatments for IPF, which highlights the urgent need for improved understanding of disease progression in order to elucidate new drug targets. We investigated how confining forces from neighboring cells or from physical features influences the lung FMT. We observed that HLFs seeded at high density expressed more α-SMA in response to TGF-β1 than those seeded at a low or medium density.

This is in contrast to other results using fibroblasts sourced from different tissues. For example, one group showed that α-SMA expression increased when corneal fibroblasts were plated at low density (500 cells/cm^2) when compared to high density (50,000 cells/cm^2), even in the absence of TGF-β1 [275]. However, this study analyzed cells in each group once they reached confluence. Therefore, low density cells were cultured for a longer time than high density cells, on the order of days. This is problematic, because substrate stiffness influences FMT, and traditional culture plastic is extremely stiff. Prolonged exposure to stiff plastic may induce FMT, and it has been shown that culture itself can induce FMT [276]. Others have demonstrated that medium density bronchial fibroblasts (5000 cells/cm^2) undergo FMT more readily than high density bronchial fibroblasts (50,000 cells/cm^2) [277]. However, this study investigated asthmatic bronchial fibroblasts, which is localized to a proximal site within the lung, while IPF affects distal alveoli. Medium density dermal fibroblasts undergo FMT more readily than high density cells, potentially involving the upregulation of OB-cadherin [278]. Again, this study analyzed cells upon reaching confluence, such that low density cells were cultured 8 days longer than high density cells.

There is a shift from N-cadherin to OB-cadherin expression in fibroblasts during wound healing [279]. We observed an increase in OB-cadherin in HLFs seeded at high density when compared to HLFs seeded at medium or low density. Interestingly, we did not see N-cadherin expression in any group. Previously, blocking N-cadherin in bronchial fibroblasts was shown to reduce FMT [277]. FOXF1 was recently demonstrated to be a key protein in preventing the switch from N-cadherin to

OB-cadherin expression in FMT [280]. Adherens junctions have been implicated in transferring mechanical strain between myofibroblasts, thereby opening mechanosensitive ion channels, inducing a calcium ion influx, and subsequently inducing contraction in the neighbor cell [281].

Despite being FBS-deprived, HLFs were still able to proliferate at a very low rate. HLFs seeded at low and medium density doubled approximately 2-3 times in 6 days. HLFs seeded at high density doubled approximately 1-2 times in 6 days. This decrease in proliferation in the high-density group may be a confounding factor, as marked by the increase in α-SMA expression in the high density control group compared to the medium density group. Indeed, others have shown that quiescent myofibroblasts have reduced α-SMA turnover when compared to proliferating cells [282].

We did not observe any effect of confinement on FMT within HLFs. Interestingly, our 2D PDMS control consistently had lower α-SMA expression than on 2D TCPS. We attribute this to several factors. PDMS is an innately hydrophobic material that we make hydrophilic via plasma treatment and then add a coating of collagen I. There is a possibility that collagen I attaches differently on PDMS vs TCPS. Additionally, there is the potential that PDMS may have adsorbed a portion of TGF-β1, a hydrophobic molecule, making it inaccessible to the cells. We addressed this by changing media every 1-2 days, but the potential for PDMS acting as a TGF-β1 sink should be investigated further. Additionally, the PDMS used herein is approximately 1.75 MPa in stiffness, while TCPS is approximately 3 GPa [264].

While both materials are extremely stiff, the 3 orders of magnitude increase in stiffness of TCPS could have induced a greater incidence of FMT.

We investigated if MSC-CM from MSCs cultured in different levels of confinement will alter FMT resolution. FMT can be a reversible process as a tissue begins to heal [283]. However, there are limitations to this reversal, as lung fibroblasts have been shown to have a "mechanical memory" [284]. For example, cells cultured on stiff substrates for 3 weeks sustained their myofibroblast activity even when returned to a softer substrate for 2 weeks [284]. Future studies may test the reversibility of FMT in our system. Additionally, future studies should utilize lung cells from an age-matched healthy patient to an IPF patient. Our HLFs were isolated from a young female, which likely behave different than an older or sick individual because disease state has been shown to influence FMT. For example, bronchial fibroblasts derived from a patient with asthma underwent FMT with higher frequency than those from a non-asthmatic patient [277].

6.5 Conclusion

In summary, we found that HLFs express more α-SMA in response to TGF-β1 when seeded at a high density compared to a medium or a low density. This likely indicates that HLFs undergo FMT more readily in response to TGF-β1 when cells are densely packed. This effect could be dependent on increased OB-cadherin expression and/or increased quiescence within high density cultures. This work demonstrates that cell density is an important factor to consider when modelling IPF *in vitro*, and may

suggest decreasing cell density within fibroblastic foci as a strategy to reduce IPF burden.

Chapter 7: Conclusions and contributions to science

7.1 Physical confinement alters cytoskeletal contributions towards human mesenchymal stem cell migration

In Chapter 3, we showed that mesenchymal stem cells (MSCs) respond differently to pharmacological inhibitors of cytoskeletal and contractile machinery in narrow vs. wide microchannels, suggesting that cells rely on this machinery to different degrees in confined vs. unconfined microenvironments. Inhibition of actin significantly hindered cell migration in both confined and unconfined microchannels. However, MSC migration in narrow channels was overall less sensitive to perturbations to the MSC cytoskeleton than MSCs in wide channels. These insights could allow for specific control of MSC infiltration into tissue engineered scaffolds and could also inform whether the degree of confinement in microchannels between anatomical structures directs cell migration during homing *in vivo*. Furthermore, it is possible that physical confinement, in conjunction with other microenvironmental cues, can be exploited to engineer and direct stem cells for use in regenerative therapies and/or *in vitro* models.

7.2 Nuclear deformation in response to physical confinement is cell type dependent

In Chapter 4, we observed that MSCs and L929 cells deform differently in response to mechanical confinement. Microtubule polymerization and myosin II contractility do not appear essential to L929 cells for regulation of nuclear volume and

dimensionality. Conversely, microtubule polymerization and myosin II contractility seem to play a role in maintaining nuclear volume and dimensionality in unconfined, but not confined, MSCs. This work informs our understanding of nuclear mechanics in microenvironments related to tissue homeostasis and disease and suggests diverging roles of the cytoskeleton in regulating nuclear deformation in different cell types. These dissimilarities may ultimately lead to differences in cell behaviors, such as differentiation or migration.

7.3 Micropillar arrays successfully confine cells

In Chapter 5, we successfully developed and validated a polydimethylsiloxane (PDMS) micropillar assay that systematically confines cells, allows for easy visualization and scale up, allows for long term cell culture, and provides an adequate sample size for analysis of the genome, secretome, or proteome. Additionally, MSCs may use different modes of migration within the various micropillar arrays. Future modifications of the micropillar confinement assay, including fabrication of micropillar arrays with more narrow spacing and applying a top confining post to the micropillar array, would enable investigation into the effects of physical confinement on cell behaviors in greater depth. This knowledge is critical to improve the design of cell-laden tissue engineered constructs and *in vivo* cell therapies. By combining confinement with other physical cues, we can harness mechanical properties in order to encourage or inhibit cell migration, direct cells down a particular lineage, induce cell secretion of specific cytokines or extracellular vesicles, and ultimately direct cells to behave in a way conducive to tissue engineering.

7.4 Lung fibroblast to myofibroblast transition is dependent on cell density, but not confinement

In Chapter 6, we observed that increased cell density increases the incidence of fibroblast to myofibroblast transition (FMT), but mechanical confinement imposed by micropillars has no effect on FMT incidence. We found that human lung fibroblasts (HLFs) express more α-SMA, a marker of myofibroblasts, in response to TGF-β1 when seeded at a high density compared to a medium or a low density. This likely indicates that HLFs undergo FMT more readily in response to TGF-β1 when cells are densely packed. This effect could be dependent on increased OB-cadherin expression or increased quiescence within high density cultures. This work demonstrates that cell density is an important factor to consider when modelling IPF *in vitro*, and it may suggest decreasing cell density within fibroblastic foci as a strategy to reduce IPF burden.

7.5 Concluding remarks

In summary, this work presents the physiological relevance of confinement as well as its major impact on cell phenotype and cell behaviors. The importance of all aspects of the mechanical microenvironment to many facets of cell behavior continues to be demonstrated over the years. Our use of engineered confining microchannels and the development of engineered confining micropillar arrays (Chapter 5) allowed us to investigate diverse aspects of cell phenotype within confinement. Microchannels enabled us to begin to elucidate the migration mechanisms (Chapter 3) and nuclear

volume maintenance mechanisms (Chapter 4) of MSCs within confinement, while confining micropillars allowed us to explore the effect of confinement on FMT (Chapter 6). Future examination of confinement's effects on cell behaviors will improve our basic understanding of biology, thereby improving therapeutics and improving human health.

7.6 Contributions to the field

7.6.1 Scientific contributions to the field

- Determined that MSC migration speed is biphasic and chemotactic index decreases as a function of increasing confinement (Chapter 3).
- Determined that MSC actin and microtubules become more diffuse and focal adhesions become smaller and sparser with increasing confinement (Chapter 3).
- Determined that MSCs require actin polymerization to migrate, but may not require myosin contractility to efficiently migrate. MSCs require microtubules to efficiently migrate only in less confined spaces (Chapter 3).
- Determined that nucleus volume decreases in L929 cells and MSC cells in a highly confined environment (Chapter 4).
- Determined that microtubules and myosin contractility are not essential in maintaining nucleus volume in confinement, but play a role in wide channels (Chapter 4).
- Developed an improved micropillar confining assay (Chapter 5).

- Observed MSCs migrate straighter within the most confining micropillar arrays (Chapter 5).
- Determined that increased cell density, but not increased mechanical confinement imposed by micropillars, increases incidence of FMT in lung fibroblasts (Chapter 6).

7.6.2 Scientific contributions to the Stroka lab

- Created PDMS micropillar confining device and protocol for its use.
- Contributed photolithography protocol updates.
- Contributed MSC maintenance and MSC tri-lineage differentiation protocols.
- Expanded HLFs and optimized HLF maintenance protocol as well as FMT protocol.
- Executed collaborations with Dr. Amy Karlsson's lab (University of Maryland) resulting in 2 publications (see Chapter 7.6.3).
- Initiated collaborations with Dr. Alex Dunn (Stanford University) and Dr. Daniel Conway (Virginia Commonwealth University).
- Established protocols for working with DN-KASH adenovirus and lentivirus (provided by Dr. Daniel Conway).
- Established protocol for working with FRET tension sensor (provided by Dr. Alex Dunn) and analyzing FRET images.
- Established safety guidelines and protocols for expanding, titering, and using DN-KASH lentivirus.

- Trained and mentored 2 graduate students (Rebecca Moriarty, Ariana Decastro) and 2 undergraduate students (Thea Ornstein, Katelyn Kunert).

7.6.3 Peer-reviewed journal publications

Published:

- **M.T. Doolin*,** R.A. Moriarty*, and K.M Stroka, Mechanosensing of Physical Confinement by Mesenchymal-Like Cells, *Frontiers in Physiology*, 11:365 (2020). - Invited manuscript for special issue on "Mechanosensing at Biointerfaces."
- S.P. Ikonomova, P. Moghaddam-Taaheri, Y. Wang, **M.T. Doolin**, K.M. Stroka, B. Hube, and A.J. Karlsson, Effects of Histatin-5 Modifications on Antifungal Activity and Kinetics of Proteolysis, *Protein Science*, 29(2): 480-493 (2020).
- Z. Gong, **M.T. Doolin,** S. Adhikari, K.M. Stroka, and A.J. Karlsson, Role of Charge and Hydrophobicity in Translocation of Cell-Penetrating Peptides into *Candida albicans* Cells, *AIChE Journal*, 65(12): e16768 (2019). - Invited manuscript for special issue on "Future of Chemical Engineering."
- **M.T. Doolin** and K.M. Stroka, Integration of Mesenchymal Stem Cells into a Novel Micropillar Confinement Assay, *Tissue Engineering Part C: Methods*, 25(11): 662-676 (2019). - Invited manuscript for special issue on "Methods in Biomechanics and Mechanobiology for Tissue Repair and Regeneration."
- **M.T. Doolin*,** T.S. Ornstein*, and K.M. Stroka, Nuclear Deformation in Response to Mechanical Confinement is Cell Type Dependent, *Cells*, 8(5): 427

(2019). - Invited manuscript for special issue on “Frontiers in Cytoskeleton Research—From Development to Disease.”

- **M.T. Doolin** and K.M. Stroka, Physical confinement alters cytoskeletal contributions towards human mesenchymal stem cell migration, *Cytoskeleton*, 75(3): 103-117 (2018). - Featured on cover.

In preparation:

- **M.T. Doolin** and K.M. Stroka, The Fibroblast to Myofibroblast Transition is Enhanced by Increased Cell Density, (in preparation, 2020).

7.6.4 Conference presentations

- **M.T. Doolin** and K.M. Stroka, *Lung Fibroblast to Myofibroblast Transition is Cell Density Dependent* (poster, Cellular and Molecular Bioengineering Conference, January 2020, Rio Grande, Puerto Rico).
- **M.T. Doolin** and K.M. Stroka, *Human Mesenchymal Stem Cell Nuclei Deform Anisotropically in Response to Mechanical Confinement* (poster, Bioscience Day, November 2018, College Park, MD).
- **M.T. Doolin** and K.M. Stroka, *Micropillar Arrays to Confine Cells in Three Dimensions* (presentation, Fischell Department of Bioengineering Retreat, August 2018, College Park, MD). **Voted “Best Presentation” by FDB Retreat attendees.
- **M.T. Doolin** and K.M. Stroka, *Human Mesenchymal Stem Cell Nuclei Deform Anisotropically in Response to Mechanical Confinement* (poster, Graduate Research Appreciation Day, April 2018, College Park, MD).

- **M.T. Doolin** and K.M. Stroka, *Human Mesenchymal Stem Cell Nuclei Deform Anisotropically in Response to Mechanical Confinement* (poster, Cellular and Molecular Bioengineering Conference, January 2018, Key Largo, FL).
- **M.T. Doolin** and K.M. Stroka, *Physical Confinement Alters Cytoskeletal Requirements for Mesenchymal Stem Cell Migration* (poster, BMES Annual Meeting, October 2017, Phoenix, AZ).
- **M.T. Doolin** and K.M. Stroka, *I like the way you move: The Impact of Mechanical Confinement on Stem Cell Migration and Mechanobiology* (presentation, Graduate Student Research Seminar, June 2017, College Park, MD).
- **M.T. Doolin** and K.M. Stroka, *The Impact of Mechanical Confinement on Stem Cell Migration and Mechanobiology* (presentation, ResearchFest, June 2017, College Park, MD).
- **M.T. Doolin**, M.A. Baird, and K.M. Stroka, *The Impact of Mechanical Confinement on Stem Cell Migration and Mechanobiology* (poster, Biophysics Symposium, May 2017, College Park, MD).
- **M.T. Doolin**, M.A. Baird, and K.M. Stroka, *The Impact of Mechanical Confinement on Stem Cell Migration and Mechanobiology* (poster, Graduate Research Appreciation Day, April 2017, College Park, MD).
- **M.T. Doolin**, M.A. Baird, and K.M. Stroka, *The Impact of Mechanical Confinement on Stem Cell Migration and Mechanobiology* (poster, Cellular and Molecular Bioengineering Annual Conference, January 2017, Kohala Coast, HI).

Chapter 8: Future Work and Outlook

This dissertation has presented new results which contribute to the fields of mechanobiology, mesenchymal stem cell (MSC)-based therapies, and therapies for idiopathic pulmonary fibrosis (IPF). There are many questions remaining, and we outline our future work below based on preliminary results.

8.1 Traction forces in confined migration and the fibroblast to myofibroblast transition

As explained in Chapter 3, we observed a decrease in the size and quantity of focal adhesions within confined cells. Additionally, microtubule and actin filaments presented as more diffuse, typically indicative of a low contractile state. We hypothesize that if there is reduced contractility and smaller focal adhesions within confined cells, their traction forces are reduced. Traction forces are generated as cells adhere to a substrate and contract via actomyosin, thereby moving the cell forward [76]. Determination of the precise traction forces exerted by a cell migrating in 3D has been technically challenging [80], [152]. We propose a simpler approach, utilizing a Förster resonance energy transfer (FRET) tension sensor, supplied by Dr. Alexander Dunn at Stanford University, within microchannels to measure traction forces exerted by MSCs in confinement (Fig. 8.1). FRET is the energy transfer from a donor fluorophore to an acceptor fluorophore, such that the donor fluorescence is quenched and the acceptor fluorescence is enhanced [285]. This occurs provided that the two fluorophores are in close enough proximity and that there is spectral overlap between the two [285].

This FRET tension sensor will also be useful in evaluating fibroblast to myofibroblast transition (FMT). We propose to coat microfabricated micropillar devices with FRET tension sensor, thereby visualizing cell traction forces in various degrees of confinement (Fig. 8.1). By measuring cell traction forces in confinement, we may be able to begin to decouple the effects of cellular contractility and nuclear deformation on cell behaviors.

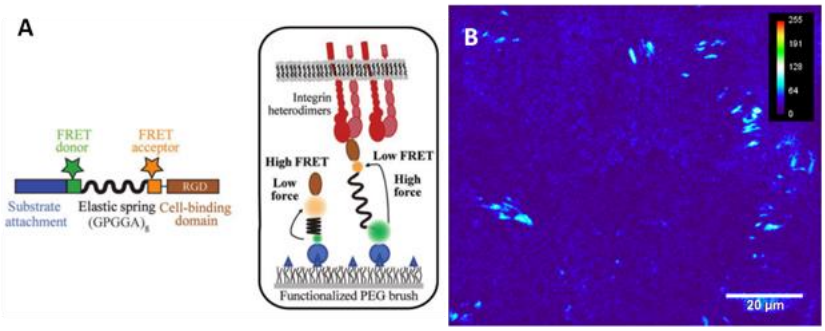

Figure 8.1 FRET tension sensor to measure cell traction forces. A) FRET tension sensor (modified from [286]**). B) FRET index map of adherant MSC. Dark areas = high FRET/low tension. Light areas = low FRET/high tension.**

8.2 The role of the LINC complex in confinement

Disruption of the linker of nucleoskeleton and cytoskeleton (LINC) complex in cells migrating in 3D decreased their pseudopodial activity and speed, implicating the LINC complex in supporting 3D cell migration [50]. Disruption of the LINC complex prohibited cells from responding to low magnitude signals, indicating the LINC complex as a critical component of the MSC mechanosensing machinery as well [73]. It was shown that low magnitude signals encourage adipogenesis of MSCs via the LINC complex, giving the LINC complex a role in lineage specification [73]. In line

with this, transfer of strain from the cytoskeleton to the nucleus via the LINC complex has been shown to be essential for stretch-induced activation of the Yes-associated protein (YAP)/transcriptional co-activator with PDZ-binding motif (TAZ) pathway [74]. The YAP/TAZ mechanotransduction pathway plays a fundamentally important role in regulating gene expression and MSC differentiation. We plan to investigate the role of the LINC complex, specifically the KASH-domain proteins, nesprins, in MSC migration and nuclear volume, as well as lung FMT. We plan to repeat the experiments performed in Chapters 3, 4, and 6, but instead use cells transfected with a dominant negative (DN)-KASH construct or control donated to us by Dr. Daniel Conway at Virginia Commonwealth University. These experiments will elucidate the role of the LINC complex in MSC migration, nucleus volume, and FMT in confinement.

8.3 Role of chromatin condensation in confined MSC migration and nucleus volume

Chapter 4 showed that microtubule polymerization and myosin II-mediated contractility do not affect MSC nuclear dimensions or volume within confinement, but play a role in unconfined nuclear dimensions and volume. Previous work which confined cells within microwells has shown that chromatin becomes more densely packed as nucleus volume decreases [85]. Chromatin decondensation or lamina disruption have both been demonstrated to decrease or increase, respectively, the anisotropic nucleus deformation in response to force [101]. As microtubules and myosin contractility did not affect nucleus volume in confinement, we hypothesize

that intrinsic nuclear components, such as the nuclear lamina and chromatin, regulate nucleus volume within confinement.

We have begun to investigate how chemically inhibiting chromatin condensation via a histone deacetylase inhibitor, Trichostatin A (TSA), affects MSCs in confined microenvironments. TSA decondenses chromatin within the cell, typically increasing nucleus volume in 2D. MSCs were treated with TSA or vehicle control (DMSO) for various times, then lysed and analyzed via western blot to determine each group's expression of acetyl-histone H3 and actin as a control. We determined that TSA begins to increase acetyl-histone H3 expression after 2 hours, peaking around 4 hours. Cells remain viable for approximately 22 hours after treatment with TSA, then begin to undergo apoptosis. Therefore, we performed overnight timelapses of MSCs treated with TSA or DMSO control and analyzed MSC speed and chemotactic index (Fig. 8.2A-B). We also fixed cells after 4 of TSA treatment and analyzed nucleus volume (Fig. 8.2C). Our preliminary data suggests that TSA does not affect speed or chemotactic index in any degree of confinement. However, TSA may increase nucleus volume in unconfined channels. Future work is necessary to determine if this is true in confined microchannels as well.

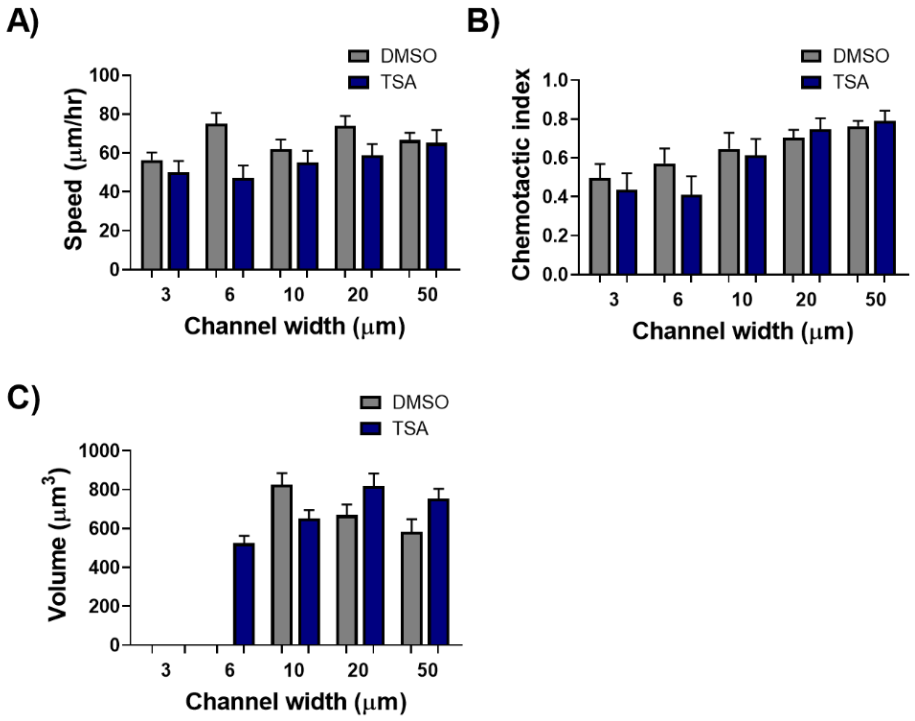

Figure 8.2 MSCs treated with TSA. Effect of TSA on A) speed, B) chemotactic index, and C) nucleus volume.

8.4 Effect of confinement on lamin A/C expression and MSC multipotency

Lamin A/C provides mechanical support to the nucleus, and its expression has been shown to scale with substrate stiffness. Cells isolated from stiff tissues contain higher lamin A/C levels than cells isolated from soft tissues [287]. In stem cells, low nuclear stress promotes lamin A/C degradation and turnover, while cytoskeletal stress and tension promote lamin A/C maintenance [252]. This pathway acts through myosin contractility and turnover, and it ultimately influences gene expression [252]. Lamin A/C overexpression has been shown to increase the degree of anisotropic nuclear

deformation in response to an applied force, underscoring its importance in nuclear mechanics and response to external forces [101]. Additionally, lamin A/C overexpression encourages osteogenesis, and lamin A/C silencing inhibits osteogenesis [287]–[289]. In contrast, it has been shown that culturing MSCs on nanogratings decreases lamin A/C expression, yet shifts cell lineage away from adipogenesis [290]. Lamin A overexpression has also been shown to inhibit chondrogenesis [291]. We aim to determine how mechanical confinement may modulate lamin A/C expression in MSCs and, in turn, influence MSC differentiation.

Preliminary data from two independent trials indicates that lamin A/C expression is reduced on 2D PDMS compared to tissue culture polystyrene (TCPS, Fig. 8.3). Interestingly, there may be a slight increase in lamin A/C expression in MSCs confined within micropillar arrays compared to those on 2D PDMS (Fig. 8.3). However, future work is needed to expand on these preliminary studies. MSCs were also cultured within micropillars in basal media or media containing adipogenic or osteogenic factors. We subsequently stained the cells using Oil Red O to evaluate adipogenesis, or Alizarin Red to investigate osteogenesis efficiency. Due to imaging limitations, these results were inconclusive, but this should certainly be investigated further in the future. The impact of confinement on MSC differentiation could have major implications for tissue engineering and MSC-based therapies.

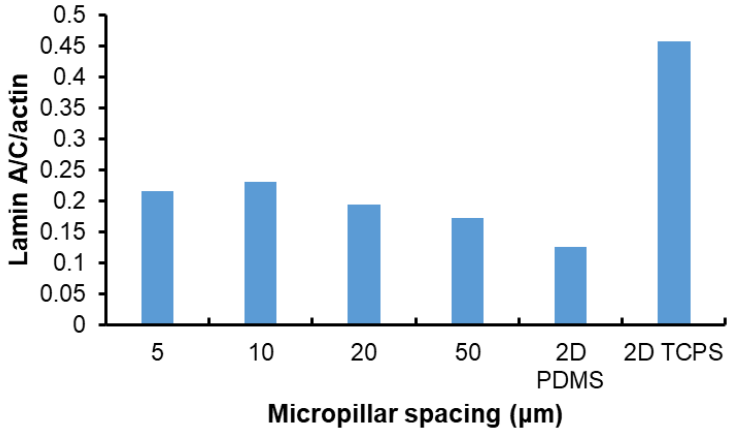

Figure 8.3 Effect of confinement on lamin A/C expression in MSCs. Averaged data from 2 independent western blots, with lamin A/C expression normalized to actin.

8.5 Effect of MSC co-culture on fibroblast differentiation

We did not observe any effect of MSC-CM on FMT, which was surprising given other reports describing the therapeutic effects of MSC-CM on IPF. Therefore, we propose to explore the role of MSC co-culture on FMT. Hydrogels containing MSCs only, fibroblasts only, or no cells will serve as controls. ECM deposition by cells will be evaluated via second harmonic generation imaging after each day in culture. Additionally, we will stain cells within hydrogels for α-SMA. We expect co-culture hydrogels to decrease incidence of α-SMA positive cells. These experiments will reveal how a more in vivo-type co-culture environment influences fibroblast differentiation and, therefore, IPF progression.

8.6 Outlook

This dissertation provides further evidence that mechanical confinement alters cell mechanosensing and cell behaviors. However, there is still a need to link these two areas in greater depth. Merely observing a behavior without elucidating the mechanism behind it or, conversely, learning of a mechanosensing mechanism without observing its impact is not enough to significantly improve therapeutic outcomes. Due to the pervasive nature of mechanical confinement *in vivo*, it is critical to understand how and why confinement alters cell phenotype. Furthermore, it is becoming increasingly evident that we must also make these links in the context of tissue-specific physical and biochemical microenvironments. Together, this knowledge has the potential to improve a wide range of therapeutics.

Appendix

For all movies: First frame represents the x-y plane, and the nucleus revolves around the y-axis. Stacks were thresholded and cut according to the workflow described in Fig. 4.2 before being rendered.

Movie S1. 3D rendering of MSC nucleus in 3 μm channel.

Movie S2. 3D rendering of L929 nucleus in 3 μm channel.

Movie S3. 3D rendering of MSC nucleus in 50 μm channel.

Movie S4. 3D rendering of L929 nucleus in 50 μm channel (center cell).

Movie S5. 3D rendering of MSC nucleus in 3 μm channel treated with vehicle control.

Movie S6. 3D rendering of MSC nucleus in 3 μm channel treated with nocodazole.

Movie S7. 3D rendering of L929 nucleus in 3 μm channel treated with vehicle control.

Movie S8. 3D rendering of L929 nucleus in 3 μm channel treated with nocodazole.

Movie S9. 3D rendering of MSC nucleus in 50 μm channel treated with vehicle control.

Movie S10. 3D rendering of MSC nucleus in 50 μm channel treated with nocodazole.

Movie S11. 3D rendering of L929 nucleus in 50 μm channel treated with vehicle control (bottom right cell).

Movie S12. 3D rendering of L929 nucleus in 50 μm channel treated with nocodazole (top cell).

Movie S13. 3D rendering of MSC nucleus in 3 μm channel treated with vehicle control.

Movie S14. 3D rendering of MSC nucleus in 3 μm channel treated with blebbistatin.

Movie S15. 3D rendering of L929 nucleus in 3 μm channel treated with vehicle control.

Movie S16. 3D rendering of L929 nucleus in 3 μm channel treated with blebbistatin.

Movie S17. 3D rendering of MSC nucleus in 50 μm channel treated with vehicle control.

Movie S18. 3D rendering of MSC nucleus in 50 μm channel treated with blebbistatin.

Movie S19. 3D rendering of L929 nucleus in 50 μm channel treated with vehicle control.

Movie S20. 3D rendering of L929 nucleus in 50 μm channel treated with blebbistatin.

Bibliography

[1] A. J. Engler, S. Sen, H. L. Sweeney, D. E. Discher, L. H. Sweeney, and D. E. Discher, “Matrix Elasticity Directs Stem Cell Lineage Specification,” *Cell*, vol. 126, no. 4, pp. 677–689, Aug. 2006, doi: 10.1016/j.cell.2006.06.044.

[2] S. C. Wei *et al.*, “Matrix stiffness drives epithelial-mesenchymal transition and tumour metastasis through a TWIST1-G3BP2 mechanotransduction pathway,” *Nat. Cell Biol.*, vol. 17, no. 5, pp. 678–688, 2015, doi: 10.1038/ncb3157.

[3] F. Martino, A. R. Perestrelo, V. Vinarský, S. Pagliari, and G. Forte, “Cellular mechanotransduction: From tension to function,” *Front. Physiol.*, vol. 9, no. JUL, pp. 1–21, 2018, doi: 10.3389/fphys.2018.00824.

[4] K. A. Jansen, D. M. Donato, H. E. Balcioglu, T. Schmidt, E. H. J. Danen, and G. H. Koenderink, “A guide to mechanobiology: Where biology and physics meet,” *Biochim. Biophys. Acta - Mol. Cell Res.*, vol. 1853, no. 11, pp. 3043–3052, 2015, doi: 10.1016/j.bbamcr.2015.05.007.

[5] T. Iskratsch, H. Wolfenson, and M. P. Sheetz, “Appreciating force and shape—the rise of mechanotransduction in cell biology.,” *Nat. Rev. Mol. Cell Biol.*, vol. 15, no. 12, pp. 825–33, 2014, doi: 10.1038/nrm3903.

[6] T. J. Kirby and J. Lammerding, “Emerging views of the nucleus as a cellular mechanosensor,” *Nat. Cell Biol.*, vol. 20, no. April, pp. 373–381, Feb. 2018, doi: 10.1038/s41556-018-0038-y.

[7] L. Lv, Y. Tang, P. Zhang, Y. Liu, X. Bai, and Y. Zhou, “Biomaterial Cues Regulate Epigenetic State and Cell Functions—A Systematic Review,” *Tissue*

Eng. Part B Rev., vol. 24, no. 2, p. ten.teb.2017.0287, 2017, doi: 10.1089/ten.teb.2017.0287.

[8] M. C. Lampi and C. A. Reinhart-King, "Targeting extracellular matrix stiffness to attenuate disease: From molecular mechanisms to clinical trials," *Sci. Transl. Med.*, vol. 10, no. 422, p. eaao0475, 2018, doi: 10.1126/scitranslmed.aao0475.

[9] P. Friedl and S. Alexander, "Cancer invasion and the microenvironment: Plasticity and reciprocity," *Cell*, vol. 147, no. 5, pp. 992–1009, 2011, doi: 10.1016/j.cell.2011.11.016.

[10] K. M. Stroka, Z. Gu, S. X. Sun, and K. Konstantopoulos, "Bioengineering paradigms for cell migration in confined microenvironments," *Curr. Opin. Cell Biol.*, vol. 30, no. 1, pp. 41–50, 2014, doi: 10.1016/j.ceb.2014.06.001.

[11] Y.-H. V. Ma, K. Middleton, L. You, and Y. Sun, "A review of microfluidic approaches for investigating cancer extravasation during metastasis," *Microsystems Nanoeng.*, vol. 4, no. October 2017, p. 17104, 2018, doi: 10.1038/micronano.2017.104.

[12] C. D. Paul, P. Mistriotis, and K. Konstantopoulos, "Cancer cell motility: lessons from migration in confined spaces," *Nat. Rev. Cancer*, vol. 17, no. 2, pp. 131–140, Feb. 2017, doi: 10.1038/nrc.2016.123.

[13] C. M. Denais *et al.*, "Nuclear envelope rupture and repair during cancer cell migration," *Science (80-.).*, vol. 352, no. 6283, pp. 353–358, Apr. 2016, doi: 10.1126/science.aad7297.

[14] J. M. Karp and G. S. Leng Teo, "Mesenchymal Stem Cell Homing: The Devil Is in the Details," *Cell Stem Cell*, vol. 4, no. 3, pp. 206–216, Mar. 2009, doi:

10.1016/j.stem.2009.02.001.

[15] X.-L. Fan, Y. Zhang, X. Li, and Q.-L. Fu, “Mechanisms underlying the protective effects of mesenchymal stem cell-based therapy,” *Cell. Mol. Life Sci.*, Jan. 2020, doi: 10.1007/s00018-020-03454-6.

[16] A. Uccelli, L. Moretta, and V. Pistoia, “Mesenchymal stem cells in health and disease,” *Nat. Rev. Immunol.*, vol. 8, pp. 726–736, Sep. 2008, doi: 10.1038/nri2395.

[17] A. Trounson and C. McDonald, “Stem Cell Therapies in Clinical Trials: Progress and Challenges,” *Cell Stem Cell*, vol. 17, no. 1, pp. 11–22, 2015, doi: 10.1016/j.stem.2015.06.007.

[18] S. Wecht and M. Rojas, “Mesenchymal stem cells in the treatment of chronic lung disease,” *Respirology*, vol. 21, no. 8, pp. 1366–1375, 2016, doi: 10.1111/resp.12911.

[19] X. Li, S. Yue, and Z. Luo, “Mesenchymal stem cells in idiopathic pulmonary fibrosis,” *Oncotarget*, vol. 8, no. 60, pp. 102600–102616, 2017, doi: 10.18632/oncotarget.18126.

[20] J. A. Kropski and T. S. Blackwell, “Progress in Understanding and Treating Idiopathic Pulmonary Fibrosis,” *Annu. Rev. Med.*, vol. 70, no. 1, pp. 211–224, Jan. 2019, doi: 10.1146/annurev-med-041317-102715.

[21] F. J. Martinez *et al.*, “Idiopathic pulmonary fibrosis,” *Nat. Rev. Dis. Prim.*, vol. 3, no. 17074, pp. 1–19, Oct. 2017, doi: 10.1038/nrdp.2017.74.

[22] P. J. Wolters, H. R. Collard, and K. D. Jones, “Pathogenesis of Idiopathic Pulmonary Fibrosis,” *Annu. Rev. Pathol. Mech. Dis.*, vol. 9, no. 1, pp. 157–179,

2013, doi: 10.1146/annurev-pathol-012513-104706.

[23] B. Hinz, “Myofibroblasts,” *Exp. Eye Res.*, vol. 142, pp. 56–70, 2015, doi: 10.1016/j.exer.2015.07.009.

[24] M. W. Moore and E. L. Herzog, “Regulation and Relevance of Myofibroblast Responses in Idiopathic Pulmonary Fibrosis,” *Curr. Pathobiol. Rep.*, vol. 1, no. 3, pp. 199–208, 2013, doi: 10.1007/s40139-013-0017-8.

[25] Z. Tong, E. M. Balzer, M. R. Dallas, W.-C. Hung, K. J. Stebe, and K. Konstantopoulos, “Chemotaxis of Cell Populations through Confined Spaces at Single-Cell Resolution,” *PLoS One*, vol. 7, no. 1, p. e29211, Jan. 2012, doi: 10.1371/journal.pone.0029211.

[26] E. M. Balzer *et al.*, “Physical confinement alters tumor cell adhesion and migration phenotypes,” *FASEB J.*, vol. 26, no. 10, pp. 4045–4056, Oct. 2012, doi: 10.1096/fj.12-211441.

[27] B. Weigelin, G.-J. Bakker, and P. Friedl, “Intravital third harmonic generation microscopy of collective melanoma cell invasion,” *IntraVital*, vol. 1, no. 1, pp. 32–43, 2012, doi: 10.4161/intv.21223.

[28] K. Wolf *et al.*, “Collagen-based cell migration models in vitro and in vivo,” *Semin. Cell Dev. Biol.*, vol. 20, no. 8, pp. 931–941, Oct. 2009, doi: 10.1016/j.semcdb.2009.08.005.

[29] M. Dominici *et al.*, “Minimal criteria for defining multipotent mesenchymal stromal cells. The International Society for Cellular Therapy position statement,” *Cytotherapy*, vol. 8, no. 4, pp. 315–317, 2006, doi: 10.1080/14653240600855905.

[30] A. Naji, M. Eitoku, B. Favier, F. Deschaseaux, N. Rouas-Freiss, and N. Suganuma, “Biological functions of mesenchymal stem cells and clinical implications,” *Cell. Mol. Life Sci.*, vol. 76, no. 17, pp. 3323–3348, Sep. 2019, doi: 10.1007/s00018-019-03125-1.

[31] M. Kabat, I. Bobkov, S. Kumar, and M. Grumet, “Trends in mesenchymal stem cell clinical trials 2004-2018: Is efficacy optimal in a narrow dose range?,” *Stem Cells Transl. Med.*, vol. 9, no. 1, pp. 17–27, 2020, doi: 10.1002/sctm.19-0202.

[32] M. Hay, D. W. Thomas, J. L. Craighead, C. Economides, and J. Rosenthal, “Clinical development success rates for investigational drugs,” *Nat. Biotechnol.*, vol. 32, no. 1, pp. 40–51, 2014, doi: 10.1038/nbt.2786.

[33] C. H. Wong, K. W. Siah, and A. W. Lo, “Estimation of clinical trial success rates and related parameters,” *Biostatistics*, vol. 20, no. 2, pp. 273–286, 2019, doi: 10.1093/biostatistics/kxx069.

[34] J. Galipeau and L. Sensébé, “Mesenchymal Stromal Cells: Clinical Challenges and Therapeutic Opportunities,” *Cell Stem Cell*, vol. 22, no. 6, pp. 824–833, 2018, doi: 10.1016/j.stem.2018.05.004.

[35] E. K. F. Yim, E. M. Darling, K. Kulangara, F. Guilak, and K. W. Leong, “Nanotopography-induced changes in focal adhesions, cytoskeletal organization, and mechanical properties of human mesenchymal stem cells,” *Biomaterials*, vol. 31, no. 6, pp. 1299–1306, 2010, doi: 10.1016/j.biomaterials.2009.10.037.

[36] R. McBeath, D. M. Pirone, C. M. Nelson, K. Bhadriraju, and C. S. Chen, “Cell

shape, cytoskeletal tension, and RhoA regulate stem cell lineage commitment," *Dev. Cell*, vol. 6, no. 4, pp. 483–495, 2004, doi: 10.1016/S1534-5807(04)00075-9.

[37] J. H. Wen *et al.*, "Interplay of matrix stiffness and protein tethering in stem cell differentiation," *Nat. Mater.*, vol. 13, no. 10, pp. 979–987, Aug. 2014, doi: 10.1038/nmat4051.

[38] B. D. Riehl, J. S. Lee, L. Ha, and J. Y. Lim, "Fluid-flow-induced mesenchymal stem cell migration: role of focal adhesion kinase and RhoA kinase sensors.," *J. R. Soc. Interface*, vol. 12, no. 104, p. 20141351, Jan. 2015, doi: 10.1098/rsif.2014.1351.

[39] P. A. Galie and J. P. Stegemann, "Injection of mesenchymal stromal cells into a mechanically stimulated in vitro model of cardiac fibrosis has paracrine effects on resident fibroblasts," *Cytotherapy*, vol. 16, no. 7, pp. 906–914, 2014, doi: 10.1016/j.jcyt.2014.01.416.

[40] Y.-W. Lan *et al.*, "Hypoxia-preconditioned mesenchymal stem cells attenuate bleomycin-induced pulmonary fibrosis.," *Stem Cell Res. Ther.*, vol. 6, p. 97, 2015, doi: 10.1186/s13287-015-0081-6.

[41] G. Burgstaller, B. Oehrle, M. Gerckens, E. S. White, H. B. Schiller, and O. Eickelberg, "The instructive extracellular matrix of the lung: basic composition and alterations in chronic lung disease," *Eur. Respir. J.*, vol. 50, no. 1, p. 1601805, Jul. 2017, doi: 10.1183/13993003.01805-2016.

[42] M. G. Jones *et al.*, "Nanoscale dysregulation of collagen structure-function disrupts mechano-homeostasis and mediates pulmonary fibrosis," *Elife*, vol. 7,

pp. 1–24, 2018, doi: 10.7554/eLife.36354.

[43] J. K. Burgess, T. Mauad, G. Tjin, J. C. Karlsson, and G. Westergren-Thorsson, "The extracellular matrix – the under-recognized element in lung disease?," *J. Pathol.*, vol. 240, no. 4, pp. 397–409, 2016, doi: 10.1002/path.4808.

[44] X. Huang *et al.*, "Matrix stiffness-induced myofibroblast differentiation is mediated by intrinsic mechanotransduction," *Am. J. Respir. Cell Mol. Biol.*, vol. 47, no. 3, pp. 340–348, 2012, doi: 10.1165/rcmb.2012-0050OC.

[45] J. Swift *et al.*, "Nuclear Lamin-A Scales with Tissue Stiffness and Enhances Matrix-Directed Differentiation," vol. 341, no. August, 2013, doi: 10.1126/science.1240104.

[46] Y. Shi, Y. Dong, Y. Duan, X. Jiang, C. Chen, and L. Deng, "Substrate stiffness influences TGF-β1-induced differentiation of bronchial fibroblasts into myofibroblasts in airway remodeling," *Mol. Med. Rep.*, vol. 7, no. 2, pp. 419–424, 2013, doi: 10.3892/mmr.2012.1213.

[47] R. S. Oh *et al.*, "RNAi screening identifies a mechanosensitive ROCK-JAK2-STAT3 network central to myofibroblast activation," *J. Cell Sci.*, vol. 131, no. 10, 2018, doi: 10.1242/jcs.209932.

[48] Y. Zhou *et al.*, "Inhibition of mechanosensitive signaling in myofibroblasts ameliorates experimental pulmonary fibrosis," *J. Clin. Invest.*, vol. 123, no. 3, p. 1096, 2013, doi: 10.1172/JCI66700DS1.

[49] S. S. Htwe, B. H. Cha, K. Yue, A. Khademhosseini, A. J. Knox, and A. M. Ghaemmaghami, "Role of Rho-Associated Coiled-Coil Forming Kinase Isoforms in Regulation of Stiffness-Induced Myofibroblast Differentiation in

Lung Fibrosis," *Am. J. Respir. Cell Mol. Biol.*, vol. 56, no. 6, pp. 772–783, Jun. 2017, doi: 10.1165/rcmb.2016-0306OC.

[50] L. Leinhos *et al.*, "Hypoxia suppresses myofibroblast differentiation by changing RhoA activity," *J. Cell Sci.*, vol. 132, no. 5, pp. 1–13, 2019, doi: 10.1242/jcs.223230.

[51] V. Dugina, L. Fontao, C. Chaponnier, J. Vasiliev, and G. Gabbiani, "Focal adhesion features during myofibroblastic differentiation are controlled by intracellular and extracellular factors," *J. Cell Sci.*, vol. 114, no. 18, pp. 3285–3296, 2001.

[52] M. E. Blaauboer, T. H. Smit, R. Hanemaaijer, R. Stoop, and V. Everts, "Cyclic mechanical stretch reduces myofibroblast differentiation of primary lung fibroblasts," *Biochem. Biophys. Res. Commun.*, vol. 404, no. 1, pp. 23–27, 2011, doi: 10.1016/j.bbrc.2010.11.033.

[53] A. Trounson, R. G. Thakar, G. Lomax, and D. Gibbons, "Clinical trials for stem cell therapies," *BMC Med.*, vol. 9, no. 1, p. 52, Dec. 2011, doi: 10.1186/1741-7015-9-52.

[54] K. M. Akram, N. Patel, M. A. Spiteri, and N. R. Forsyth, "Lung regeneration: Endogenous and exogenous stem cell mediated therapeutic approaches," *Int. J. Mol. Sci.*, vol. 17, no. 1, 2016, doi: 10.3390/ijms17010128.

[55] S. Geiger, D. Hirsch, and F. G. Hermann, "Cell therapy for lung disease," *Eur. Respir. Rev.*, vol. 26, p. 170044, Jun. 2017, doi: 10.1183/16000617.0044-2017.

[56] B. Parekkadan and J. J. Milwid, "Mesenchymal Stem Cells as Therapeutics," *Annu Rev Biomed Eng*, vol. 12, pp. 87–117, 2010, doi: 10.1146/annurev-

bioeng-070909-105309.Mesenchymal.

[57] T. P. Shentu *et al.*, “Thy-1 dependent uptake of mesenchymal stem cell-derived extracellular vesicles blocks myofibroblastic differentiation,” *Sci. Rep.*, vol. 7, no. 1, pp. 1–11, 2017, doi: 10.1038/s41598-017-18288-9.

[58] A. I. Caplan, “Mesenchymal stem cells,” *J. Orthop. Res.*, vol. 9, no. 5, pp. 641–650, Sep. 1991, doi: 10.1002/jor.1100090504.

[59] K.-C. Hwang *et al.*, “Chemicals that modulate stem cell differentiation,” *Proc. Natl. Acad. Sci.*, vol. 105, no. 21, pp. 7467–7471, May 2008, doi: 10.1073/pnas.0802825105.

[60] A. Huang, M. Farrell, M. Kim, and R. Mauck, “Long-term dynamic loading improves the mechanical properties of chondrogenic mesenchymal stem cell-laden hydrogel,” *Eur. Cells Mater.*, vol. 19, no. 215, pp. 72–85, Feb. 2010, doi: 10.22203/eCM.v019a08.

[61] S. Oh *et al.*, “Stem cell fate dictated solely by altered nanotube dimension,” *Proc. Natl. Acad. Sci.*, vol. 106, no. 7, pp. 2130–2135, Feb. 2009, doi: 10.1073/pnas.0813200106.

[62] G. Yourek, S. M. McCormick, J. J. Mao, and G. C. Reilly, “Shear stress induces osteogenic differentiation of human mesenchymal stem cells,” *Regen. Med.*, vol. 5, no. 5, pp. 713–724, Sep. 2010, doi: 10.2217/rme.10.60.

[63] L. Li and J. Jiang, “Regulatory factors of mesenchymal stem cell migration into injured tissues and their signal transduction mechanisms,” *Front. Med. China*, vol. 5, no. 1, pp. 33–39, 2011, doi: 10.1007/s11684-011-0114-1.

[64] M. T. Doolin and K. M. Stroka, “Physical confinement alters cytoskeletal

contributions towards human mesenchymal stem cell migration," *Cytoskeleton*, vol. 75, no. 3, pp. 103–117, Mar. 2018, doi: 10.1002/cm.21433.

[65] W.-C. Hung *et al.*, "Distinct signaling mechanisms regulate migration in unconfined versus confined spaces," *J. Cell Biol.*, vol. 202, no. 5, pp. 807–824, Sep. 2013, doi: 10.1083/jcb.201302132.

[66] R. J. Petrie, H. Koo, and K. M. Yamada, "Generation of compartmentalized pressure by a nuclear piston governs cell motility in a 3D matrix," *Science (80-.).*, vol. 345, no. 6200, pp. 1062–1065, Aug. 2014, doi: 10.1126/science.1256965.

[67] K. M. Stroka *et al.*, "Water permeation drives tumor cell migration in confined microenvironments.," *Cell*, vol. 157, no. 3, pp. 611–23, Apr. 2014, doi: 10.1016/j.cell.2014.02.052.

[68] S. K. Kang, I. S. Shin, M. S. Ko, J. Y. Jo, and J. C. Ra, "Journey of Mesenchymal Stem Cells for Homing: Strategies to Enhance Efficacy and Safety of Stem Cell Therapy," *Stem Cells Int.*, vol. 2012, p. 342968, 2012, doi: 10.1155/2012/342968.

[69] E. Eggenhofer, F. Luk, M. H. Dahlke, and M. J. Hoogduijn, "The Life and Fate of Mesenchymal Stem Cells," *Front. Immunol.*, vol. 5, no. MAY, p. 148, May 2014, doi: 10.3389/fimmu.2014.00148.

[70] A. Ode *et al.*, "CD73 and CD29 concurrently mediate the mechanically induced decrease of migratory capacity of mesenchymal stromal cells," *Eur. Cells Mater.*, vol. 22, no. 030, pp. 26–42, Jul. 2011, doi: 10.22203/eCM.v022a03.

[71] J. Leibacher and R. Henschler, "Biodistribution, migration and homing of

systemically applied mesenchymal stem/stromal cells," *Stem Cell Res. Ther.*, vol. 7, no. 1, p. 7, Dec. 2016, doi: 10.1186/s13287-015-0271-2.

[72] M. F. Pittenger and B. J. Martin, "Mesenchymal stem cells and their potential as cardiac therapeutics," *Circ. Res.*, vol. 95, no. 1, pp. 9–20, 2004, doi: 10.1161/01.RES.0000135902.99383.6f.

[73] F. Nitzsche, C. Müller, B. Lukomska, J. Jolkkonen, A. Deten, and J. Boltze, "Concise Review: MSC Adhesion Cascade-Insights into Homing and Transendothelial Migration," *Stem Cells*, vol. 35, no. 6, pp. 1446–1460, Jun. 2017, doi: 10.1002/stem.2614.

[74] G. S. L. Teo *et al.*, "Mesenchymal Stem Cells Transmigrate Between and Directly Through Tumor Necrosis Factor-α-Activated Endothelial Cells Via Both Leukocyte-Like and Novel Mechanisms," *Stem Cells*, vol. 30, no. 11, pp. 2472–2486, Nov. 2012, doi: 10.1002/stem.1198.

[75] E. Zamir and B. Geiger, "Molecular complexity and dynamics of cell-matrix adhesions.," *J. Cell Sci.*, vol. 114, no. 20, pp. 3583–90, Oct. 2001, doi: 10.1016/0014-4827(75)90636-9.

[76] M. L. Gardel, I. C. Schneider, Y. Aratyn-Schaus, and C. M. Waterman, "Mechanical Integration of Actin and Adhesion Dynamics in Cell Migration," *Annu. Rev. Cell Dev. Biol.*, vol. 26, no. 1, pp. 315–333, Nov. 2010, doi: 10.1146/annurev.cellbio.011209.122036.

[77] J. Xie, M. Bao, S. M. C. Bruekers, and W. T. S. Huck, "Collagen Gels with Different Fibrillar Microarchitectures Elicit Different Cellular Responses," *ACS Appl. Mater. Interfaces*, vol. 9, no. 23, pp. 19630–19637, Jun. 2017, doi:

10.1021/acsami.7b03883.

[78] N. Huebsch *et al.*, “Harnessing traction-mediated manipulation of the cell/matrix interface to control stem-cell fate,” *Nat. Mater.*, vol. 9, no. 6, pp. 518–526, Jun. 2010, doi: 10.1038/nmat2732.

[79] S. Khetan, M. Guvendiren, W. R. Legant, D. M. Cohen, C. S. Chen, and J. a Burdick, “Degradation-mediated cellular traction directs stem cell fate in covalently crosslinked three-dimensional hydrogels,” *Nat. Mater.*, vol. 12, no. 5, pp. 458–465, May 2013, doi: 10.1038/nmat3586.

[80] W. R. Legant, J. S. Miller, B. L. Blakely, D. M. Cohen, G. M. Genin, and C. S. Chen, “Measurement of mechanical tractions exerted by cells in three-dimensional matrices,” *Nat. Methods*, vol. 7, no. 12, pp. 969–971, 2010, doi: 10.1038/nmeth.1531.

[81] A. D. Doyle, M. L. Kutys, M. A. Conti, K. Matsumoto, R. S. Adelstein, and K. M. Yamada, “Micro-environmental control of cell migration - myosin IIA is required for efficient migration in fibrillar environments through control of cell adhesion dynamics,” *J. Cell Sci.*, vol. 125, no. 9, pp. 2244–2256, 2012, doi: 10.1242/jcs.098806.

[82] E. Cukierman, R. Pankov, D. R. Stevens, and K. M. Yamada, “Taking cell-matrix adhesions to the third dimension.,” *Science (80-.).*, vol. 294, no. 5547, pp. 1708–12, Nov. 2001, doi: 10.1126/science.1064829.

[83] O. Chaudhuri *et al.*, “Hydrogels with tunable stress relaxation regulate stem cell fate and activity,” *Nat. Mater.*, vol. 15, no. 3, pp. 326–334, Mar. 2016, doi: 10.1038/nmat4489.

[84] S. I. Fraley *et al.*, “A distinctive role for focal adhesion proteins in three-dimensional cell motility,” *Nat. Cell Biol.*, vol. 12, no. 6, pp. 598–604, Jun. 2010, doi: 10.1038/ncb2062.

[85] M. Bao, J. Xie, A. Piruska, and W. T. S. Huck, “3D microniches reveal the importance of cell size and shape,” *Nat. Commun.*, vol. 8, no. 1, p. 1962, Dec. 2017, doi: 10.1038/s41467-017-02163-2.

[86] B. Pontes *et al.*, “Membrane tension controls adhesion positioning at the leading edge of cells,” *J. Cell Biol.*, vol. 216, no. 9, pp. 2959–2977, Jul. 2017, doi: 10.1083/jcb.201611117.

[87] A. R. Houk *et al.*, “Membrane Tension Maintains Cell Polarity by Confining Signals to the Leading Edge during Neutrophil Migration,” *Cell*, vol. 148, no. 1–2, pp. 175–188, Jan. 2012, doi: 10.1016/J.CELL.2011.10.050.

[88] A. D. Doyle and K. M. Yamada, “Mechanosensing via cell-matrix adhesions in 3D microenvironments,” *Exp. Cell Res.*, vol. 343, no. 1, pp. 60–66, 2016, doi: 10.1016/j.yexcr.2015.10.033.

[89] W.-C. Hung *et al.*, “Confinement Sensing and Signal Optimization via Piezo1/PKA and Myosin II Pathways,” *Cell Rep.*, vol. 15, no. 7, pp. 1430–1441, May 2016, doi: 10.1016/j.celrep.2016.04.035.

[90] M. M. Pathak *et al.*, “Stretch-activated ion channel Piezo1 directs lineage choice in human neural stem cells,” *Proc. Natl. Acad. Sci. U. S. A.*, vol. 111, no. 45, pp. 16148–16153, Nov. 2014, doi: 10.1073/pnas.1409802111.

[91] K. Salaita *et al.*, “Restriction of receptor movement alters cellular response: physical force sensing by EphA2.,” *Science*, vol. 327, no. 5971, pp. 1380–5,

Mar. 2010, doi: 10.1126/science.1181729.

[92] C. F. Natale, M. Ventre, and P. A. Netti, “Tuning the material-cytoskeleton crosstalk via nanoconfinement of focal adhesions,” *Biomaterials*, vol. 35, pp. 2743–2751, 2014, doi: 10.1016/j.biomaterials.2013.12.023.

[93] B. Willipinski-Stapelfeldt *et al.*, “Changes in Cytoskeletal Protein Composition Indicative of an Epithelial-Mesenchymal Transition in Human Micrometastatic and Primary Breast Carcinoma Cells,” *Clin. Cancer Res.*, vol. 11, no. 22, pp. 8006–8014, Nov. 2005, doi: 10.1158/1078-0432.CCR-05-0632.

[94] D. W. Dumbauld *et al.*, “How vinculin regulates force transmission,” *Proc. Natl. Acad. Sci.*, vol. 110, no. 24, pp. 9788–9793, Jun. 2013, doi: 10.1073/pnas.1216209110.

[95] R. Windoffer, M. Beil, T. M. Magin, and R. E. Leube, “Cytoskeleton in motion: The dynamics of keratin intermediate filaments in epithelia,” *J. Cell Biol.*, vol. 194, no. 5, pp. 669–678, 2011, doi: 10.1083/jcb.201008095.

[96] J. Kim *et al.*, “Actin remodelling factors control ciliogenesis by regulating YAP/TAZ activity and vesicle trafficking,” *Nat. Commun.*, vol. 6, no. 1, p. 6781, Dec. 2015, doi: 10.1038/ncomms7781.

[97] C. A. Carter, G. P. Parham, and T. Chambers, “Cytoskeletal Reorganization Induced by Retinoic Acid Treatment of Human Endometrial Adenocarcinoma (RL95-2) Cells Is Correlated with Alterations in Protein Kinase C-α,” *Pathobiology*, vol. 66, no. 6, pp. 284–292, 1998, doi: 10.1159/000028035.

[98] D.-H. Kim, S. Cho, and D. Wirtz, “Tight coupling between nucleus and cell migration through the perinuclear actin cap,” *J. Cell Sci.*, vol. 127, no. 11, pp.

2528–2541, Jun. 2014, doi: 10.1242/jcs.144345.

[99] S. P. Desai, S. N. Bhatia, M. Toner, and D. Irimia, “Mitochondrial Localization and the Persistent Migration of Epithelial Cancer cells,” *Biophys. J.*, vol. 104, no. 9, pp. 2077–2088, May 2013, doi: 10.1016/J.BPJ.2013.03.025.

[100] K. Wang *et al.*, “Nanotopographical Modulation of Cell Function through Nuclear Deformation,” *ACS Appl. Mater. Interfaces*, vol. 8, no. 8, pp. 5082–5092, Mar. 2016, doi: 10.1021/acsami.5b10531.

[101] K. Haase *et al.*, “Extracellular Forces Cause the Nucleus to Deform in a Highly Controlled Anisotropic Manner,” *Sci. Rep.*, vol. 6, no. 1, p. 21300, Feb. 2016, doi: 10.1038/srep21300.

[102] P. M. Davidson, C. Denais, M. C. Bakshi, and J. Lammerding, “Nuclear deformability constitutes a rate-limiting step during cell migration in 3-D environments,” *Cell. Mol. Bioeng.*, vol. 7, no. 3, pp. 293–306, 2014, doi: 10.1007/s12195-014-0342-y.

[103] Y. Fu, L. K. Chin, T. Bourouina, A. Q. Liu, and A. M. J. Vandongen, “Nuclear deformation during breast cancer cell transmigration,” *Lab Chip*, vol. 12, pp. 3774–3778, 2012, doi: 10.1039/c2lc40477j.

[104] B. Enyedi and P. Niethammer, “Nuclear membrane stretch and its role in mechanotransduction,” *Nucleus*, vol. 8, no. 2, pp. 156–161, Mar. 2017, doi: 10.1080/19491034.2016.1263411.

[105] S. Cho, J. Irianto, and D. E. Discher, “Mechanosensing by the nucleus: From pathways to scaling relationships,” *J. Cell Biol.*, vol. 216, no. 2, pp. 305–315, Feb. 2017, doi: 10.1083/jcb.201610042.

[106] S. B. Khatau *et al.*, “The distinct roles of the nucleus and nucleus-cytoskeleton connections in three-dimensional cell migration,” *Sci. Rep.*, vol. 2, no. 1, p. 488, Dec. 2012, doi: 10.1038/srep00488.

[107] A. Buxboim *et al.*, “Matrix elasticity regulates lamin-A,C phosphorylation and turnover with feedback to actomyosin,” *Curr. Biol.*, vol. 24, no. 16, pp. 1909–1917, 2014, doi: 10.1016/j.cub.2014.07.001.

[108] E. M. Hatch and M. W. Hetzer, “Nuclear envelope rupture is induced by actin-based nucleus confinement,” *J. Cell Biol.*, vol. 215, no. 1, pp. 27–36, Oct. 2016, doi: 10.1083/jcb.201603053.

[109] M. Raab *et al.*, “ESCRT III repairs nuclear envelope ruptures during cell migration to limit DNA damage and cell death.,” *Science*, vol. 352, no. 6283, pp. 359–62, Apr. 2016, doi: 10.1126/science.aad7611.

[110] X. Cao *et al.*, “A Chemomechanical Model for Nuclear Morphology and Stresses during Cell Transendothelial Migration,” *Biophys. J.*, vol. 111, no. 7, pp. 1541–1552, Oct. 2016, doi: 10.1016/J.BPJ.2016.08.011.

[111] D. M. Graham and K. Burridge, “Mechanotransduction and nuclear function,” *Curr. Opin. Cell Biol.*, vol. 40, pp. 98–105, Jun. 2016, doi: 10.1016/j.ceb.2016.03.006.

[112] K.-H. Chow, R. E. Factor, and K. S. Ullman, “The nuclear envelope environment and its cancer connections,” *Nat. Rev. Cancer*, vol. 12, no. 3, pp. 196–209, Mar. 2012, doi: 10.1038/nrc3219.

[113] E. Infante *et al.*, “LINC complex-Lis1 interplay controls MT1-MMP matrix digest-on-demand response for confined tumor cell migration,” *Nat. Commun.*,

vol. 9, no. 1, p. 2443, Dec. 2018, doi: 10.1038/s41467-018-04865-7.

[114] D. G. Thomas *et al.*, “Non-muscle myosin IIB is critical for nuclear translocation during 3D invasion,” *J. Cell Biol.*, vol. 210, no. 4, pp. 583–594, 2015, doi: 10.1083/jcb.201502039.

[115] P. T. Arsenovic *et al.*, “Nesprin-2G, a Component of the Nuclear LINC Complex, Is Subject to Myosin-Dependent Tension,” *Biophys. J.*, vol. 110, no. 1, pp. 34–43, 2016, doi: 10.1016/j.bpj.2015.11.014.

[116] G. Uzer *et al.*, “Cell Mechanosensitivity to Extremely Low-Magnitude Signals Is Enabled by a LINCed Nucleus,” *Stem Cells*, vol. 33, no. 6, pp. 2063–2076, Jun. 2015, doi: 10.1002/stem.2004.

[117] T. P. Driscoll, B. D. Cosgrove, S.-J. Heo, Z. E. Shurden, and R. L. Mauck, “Cytoskeletal to Nuclear Strain Transfer Regulates YAP Signaling in Mesenchymal Stem Cells,” *Biophys. J.*, vol. 108, no. 12, pp. 2783–2793, Jun. 2015, doi: 10.1016/j.bpj.2015.05.010.

[118] J. Kind *et al.*, “Single-Cell Dynamics of Genome-Nuclear Lamina Interactions,” *Cell*, vol. 153, no. 1, pp. 178–192, Mar. 2013, doi: 10.1016/j.cell.2013.02.028.

[119] J. Lammerding *et al.*, “Lamin A / C deficiency causes defective nuclear mechanics and mechanotransduction,” *J. Clin. Invest.*, vol. 113, no. 3, pp. 370–378, 2004, doi: 10.1172/JCI200419670.Introduction.

[120] J. Chang *et al.*, “NF-κB inhibits osteogenic differentiation of mesenchymal stem cells by promoting β-catenin degradation,” *Proc. Natl. Acad. Sci.*, vol. 110, no. 23, pp. 9469–9474, Jun. 2013, doi: 10.1073/pnas.1300532110.

[121] J. Irianto *et al.*, “Nuclear constriction segregates mobile nuclear proteins away

from chromatin," *Mol. Biol. Cell*, vol. 27, no. 25, pp. 4011–4020, Dec. 2016, doi: 10.1091/mbc.e16-06-0428.

[122] E. Makhija, D. S. Jokhun, and G. V Shivashankar, "Nuclear deformability and telomere dynamics are regulated by cell geometric constraints," *Proc. Natl. Acad. Sci.*, vol. 113, no. 1, pp. E32–E40, Jan. 2016, doi: 10.1073/pnas.1513189113.

[123] I. Bronshtein *et al.*, "Loss of lamin A function increases chromatin dynamics in the nuclear interior," *Nat. Commun.*, vol. 6, no. 1, p. 8044, Dec. 2015, doi: 10.1038/ncomms9044.

[124] S. Talwar, N. Jain, and G. V. Shivashankar, "The regulation of gene expression during onset of differentiation by nuclear mechanical heterogeneity," *Biomaterials*, vol. 35, no. 8, pp. 2411–2419, 2014, doi: 10.1016/j.biomaterials.2013.12.010.

[125] H. Bian, J. Z. Lin, C. Li, and S. R. Farmer, "Myocardin-related transcription factor A (MRTFA) regulates the fate of bone marrow mesenchymal stem cells and its absence in mice leads to osteopenia," *Mol. Metab.*, vol. 5, no. 10, pp. 970–979, Oct. 2016, doi: 10.1016/j.molmet.2016.08.012.

[126] M. Le Berre, J. Aubertin, and M. Piel, "Fine control of nuclear confinement identifies a threshold deformation leading to lamina rupture and induction of specific genes," *Integr. Biol.*, vol. 4, no. 11, p. 1406, 2012, doi: 10.1039/c2ib20056b.

[127] A. L. McGregor, C.-R. Hsia, and J. Lammerding, "Squish and squeeze — the nucleus as a physical barrier during migration in confined environments," *Curr.*

Opin. Cell Biol., vol. 40, pp. 32–40, Jun. 2016, doi: 10.1016/j.ceb.2016.01.011.

[128] L. A. Lautscham *et al.*, "Migration in Confined 3D Environments Is Determined by a Combination of Adhesiveness, Nuclear Volume, Contractility, and Cell Stiffness," *Biophys. J.*, vol. 109, no. 5, pp. 900–913, Sep. 2015, doi: 10.1016/j.bpj.2015.07.025.

[129] K. Wolf *et al.*, "Physical limits of cell migration: Control by ECM space and nuclear deformation and tuning by proteolysis and traction force," *J. Cell Biol.*, vol. 201, no. 7, pp. 1069–1084, Jun. 2013, doi: 10.1083/jcb.201210152.

[130] H.-R. Thiam *et al.*, "Perinuclear Arp2/3-driven actin polymerization enables nuclear deformation to facilitate cell migration through complex environments," *Nat. Commun.*, vol. 7, p. 10997, 2016, doi: 10.1038/ncomms10997.

[131] T. Harada *et al.*, "Nuclear lamin stiffness is a barrier to 3D migration, but softness can limit survival," *J. Cell Biol.*, vol. 204, no. 5, pp. 669–682, Mar. 2014, doi: 10.1083/jcb.201308029.

[132] C. D. Paul, W.-C. Hung, D. Wirtz, and K. Konstantopoulos, "Engineered Models of Confined Cell Migration," *Annu. Rev. Biomed. Eng.*, vol. 18, no. 1, pp. 159–180, Jul. 2016, doi: 10.1146/annurev-bioeng-071114-040654.

[133] M. Junkin and P. K. Wong, "Probing cell migration in confined environments by plasma lithography," *Biomaterials*, vol. 32, no. 7, pp. 1848–1855, Mar. 2011, doi: 10.1016/J.BIOMATERIALS.2010.11.009.

[134] J. Y. Lim and H. J. Donahue, "Cell Sensing and Response to Micro- and Nanostructured Surfaces Produced by Chemical and Topographic Patterning," *Tissue Eng.*, vol. 13, no. 8, pp. 1879–1891, Aug. 2007, doi:

10.1089/ten.2006.0154.

[135] A. D. Doyle, F. W. Wang, K. Matsumoto, and K. M. Yamada, “One-dimensional topography underlies three-dimensional fibrillar cell migration,” *J. Cell Biol.*, vol. 184, no. 4, pp. 481–490, Feb. 2009, doi: 10.1083/jcb.200810041.

[136] S. S. Chang, W.-H. Guo, Y. Kim, and Y.-L. Wang, “Guidance of Cell Migration by Substrate Dimension,” *Biophys. J.*, vol. 104, no. 2, pp. 313–321, Jan. 2013, doi: 10.1016/j.bpj.2012.12.001.

[137] A. Ray *et al.*, “Anisotropic forces from spatially constrained focal adhesions mediate contact guidance directed cell migration,” *Nat. Commun.*, vol. 8, p. 14923, Apr. 2017, doi: 10.1038/ncomms14923.

[138] A. I. Teixeira, “Epithelial contact guidance on well-defined micro- and nanostructured substrates,” *J. Cell Sci.*, vol. 116, no. 10, pp. 1881–1892, May 2003, doi: 10.1242/jcs.00383.

[139] H. Zhang *et al.*, “Single cell migration dynamics mediated by geometric confinement,” *Colloids Surfaces B Biointerfaces*, vol. 145, pp. 72–78, Sep. 2016, doi: 10.1016/j.colsurfb.2016.04.039.

[140] D. Kim, K. Han, K. Gupta, K. W. Kwon, K.-Y. Suh, and A. Levchenko, “Mechanosensitivity of fibroblast cell shape and movement to anisotropic substratum topography gradients,” *Biomaterials*, vol. 30, no. 29, pp. 5433–5444, Oct. 2009, doi: 10.1016/j.biomaterials.2009.06.042.

[141] C. D. Paul *et al.*, “Interplay of the physical microenvironment, contact guidance, and intracellular signaling in cell decision making,” *FASEB J.*, vol.

30, no. 6, pp. 2161–2170, Jun. 2016, doi: 10.1096/fj.201500199R.

[142] J. Ballester-Beltrán, M. Lebourg, and M. Salmerón-Sánchez, “Dorsal and ventral stimuli in sandwich-like microenvironments. Effect on cell differentiation,” *Biotechnol. Bioeng.*, vol. 110, no. 11, pp. 3048–3058, 2013, doi: 10.1002/bit.24972.

[143] M. Le Berre, E. Zlotek-Zlotkiewicz, D. Bonazzi, F. Lautenschlaeger, and M. Piel, “Methods for two-dimensional cell confinement,” *Methods Cell Biol.*, vol. 121, no. March, pp. 213–229, 2014, doi: 10.1016/B978-0-12-800281-0.00014-2.

[144] P. M. Davidson, J. Sliz, P. Isermann, C. Denais, and J. Lammerding, “Design of a microfluidic device to quantify dynamic intra-nuclear deformation during cell migration through confining environments,” *Integr. Biol.*, vol. 7, no. 12, pp. 1534–1546, 2015, doi: 10.1039/C5IB00200A.

[145] C. G. Rolli, T. Seufferlein, R. Kemkemer, and J. P. Spatz, “Impact of Tumor Cell Cytoskeleton Organization on Invasiveness and Migration: A Microchannel-Based Approach,” *PLoS One*, vol. 5, no. 1, p. e8726, Jan. 2010, doi: 10.1371/journal.pone.0008726.

[146] M. A. Shumakovich, C. P. Mencio, J. S. Siglin, R. A. Moriarty, H. M. Geller, and K. M. Stroka, “Astrocytes from the brain microenvironment alter migration and morphology of metastatic breast cancer cells,” *FASEB J.*, vol. 31, no. 11, pp. 5049–5067, Nov. 2017, doi: 10.1096/fj.201700254R.

[147] D. Irimia and M. Toner, “Spontaneous migration of cancer cells under conditions of mechanical confinement,” *Integr. Biol.*, vol. 1, no. 8–9, pp. 506–

512, Sep. 2009, doi: 10.1039/b908595e.

[148] B. Koch *et al.*, “Dimensionality of Rolled-up Nanomembranes Controls Neural Stem Cell Migration Mechanism,” *Nano Lett.*, vol. 15, no. 8, pp. 5530–5538, 2015, doi: 10.1021/acs.nanolett.5b02099.

[149] W. Xi *et al.*, “Rolled-up Functionalized Nanomembranes as Three-Dimensional Cavities for Single Cell Studies,” *Nano Lett.*, vol. 14, no. 8, pp. 4197–4204, Aug. 2014, doi: 10.1021/nl4042565.

[150] E. Desvignes *et al.*, “Nanoscale Forces during Confined Cell Migration,” *Nano Lett.*, vol. 18, no. 10, pp. 6326–6333, Oct. 2018, doi: 10.1021/acs.nanolett.8b02611.

[151] J. K. Fisher and N. Kleckner, “Magnetic force micropiston: An integrated force/microfluidic device for the application of compressive forces in a confined environment,” *Rev. Sci. Instrum.*, vol. 85, no. 2, p. 023704, Feb. 2014, doi: 10.1063/1.4864085.

[152] P. S. Raman, C. D. Paul, K. M. Stroka, and K. Konstantopoulos, “Probing cell traction forces in confined microenvironments,” *Lab Chip*, vol. 13, no. 23, p. 4599, 2013, doi: 10.1039/c3lc50802a.

[153] S. T. Spagnol, W.-C. Lin, E. A. Booth, B. Ladoux, H. M. Lazarus, and K. N. Dahl, “Early Passage Dependence of Mesenchymal Stem Cell Mechanics Influences Cellular Invasion and Migration,” *Ann. Biomed. Eng.*, vol. 44, no. 7, pp. 2123–2131, Jul. 2016, doi: 10.1007/s10439-015-1508-z.

[154] Y. Alapan, M. Younesi, O. Akkus, and U. A. Gurkan, “Cell-Aligning Substrates: Anisotropically Stiff 3D Micropillar Niche Induces Extraordinary

Cell Alignment and Elongation," *Adv. Healthc. Mater.*, vol. 5, no. 15, pp. 1833–1833, Aug. 2016, doi: 10.1002/adhm.201670075.

[155] E. A. Booth-Gauthier, V. Du, M. Ghibaudo, A. D. Rape, K. N. Dahl, and B. Ladoux, "Hutchinson–Gilford progeria syndrome alters nuclear shape and reduces cell motility in three dimensional model substrates," *Integr. Biol.*, vol. 5, no. 3, pp. 569–577, 2013, doi: 10.1039/c3ib20231c.

[156] M. T. Doolin and K. M. Stroka, "Integration of Mesenchymal Stem Cells into a Novel Micropillar Confinement Assay," *Tissue Eng. Part C Methods*, vol. 25, no. 11, pp. 662–676, Nov. 2019, doi: 10.1089/ten.tec.2019.0083.

[157] A. Pathak and S. Kumar, "Independent regulation of tumor cell migration by matrix stiffness and confinement," *Proc. Natl. Acad. Sci.*, vol. 109, no. 26, pp. 10334–10339, 2012, doi: 10.1073/pnas.1118073109.

[158] C. M. Kraning-Rush, S. P. Carey, M. C. Lampi, and C. A. Reinhart-King, "Microfabricated collagen tracks facilitate single cell metastatic invasion in 3D," *Integr. Biol.*, vol. 5, no. 3, p. 606, 2013, doi: 10.1039/c3ib20196a.

[159] O. Ilina, G.-J. Bakker, A. Vasaturo, R. M. Hofmann, and P. Friedl, "Two-photon laser-generated microtracks in 3D collagen lattices: principles of MMP-dependent and -independent collective cancer cell invasion," *Phys. Biol.*, vol. 8, no. 1, p. 015010, Feb. 2011, doi: 10.1088/1478-3975/8/1/015010.

[160] A. L. Carlson *et al.*, "Microfibrous substrate geometry as a critical trigger for organization, self-renewal, and differentiation of human embryonic stem cells within synthetic 3-dimensional microenvironments," *FASEB J.*, vol. 26, no. 8, pp. 3240–3251, Aug. 2012, doi: 10.1096/fj.11-192732.

[161] A. D. Doyle, N. Carvajal, A. Jin, K. Matsumoto, and K. M. Yamada, “Local 3D matrix microenvironment regulates cell migration through spatiotemporal dynamics of contractility-dependent adhesions,” *Nat. Commun.*, vol. 6, no. 1, p. 8720, Dec. 2015, doi: 10.1038/ncomms9720.

[162] N. Peela *et al.*, “A three dimensional micropatterned tumor model for breast cancer cell migration studies,” *Biomaterials*, vol. 81, pp. 72–83, 2016, doi: 10.1016/j.biomaterials.2015.11.039.

[163] N. Luciani *et al.*, “Successful chondrogenesis within scaffolds, using magnetic stem cell confinement and bioreactor maturation,” *Acta Biomater.*, vol. 37, pp. 101–110, Jun. 2016, doi: 10.1016/j.actbio.2016.04.009.

[164] D. Robert *et al.*, “Magnetic micro-manipulations to probe the local physical properties of porous scaffolds and to confine stem cells,” *Biomaterials*, vol. 31, no. 7, pp. 1586–1595, Mar. 2010, doi: 10.1016/j.biomaterials.2009.11.014.

[165] F. A. Pennacchio, C. Fedele, S. De Martino, S. Cavalli, R. Vecchione, and P. A. Netti, “Three-Dimensional Microstructured Azobenzene-Containing Gelatin as a Photoactuable Cell Confining System,” *ACS Appl. Mater. Interfaces*, vol. 10, no. 1, pp. 91–97, Jan. 2018, doi: 10.1021/acsami.7b13176.

[166] M. A. Kinney, T. A. Hookway, Y. Wang, and T. C. McDevitt, “Engineering Three-Dimensional Stem Cell Morphogenesis for the Development of Tissue Models and Scalable Regenerative Therapeutics,” *Ann. Biomed. Eng.*, vol. 42, no. 2, pp. 352–367, Feb. 2014, doi: 10.1007/s10439-013-0953-9.

[167] H.-C. Chen, “Boyden Chamber Assay,” in *Cell Migration. Methods in Molecular Biology™, vol 294*, vol. 294, J.-L. Guan, Ed. Totowa, NJ: Humana

Press, 2005, pp. 15–22.

[168] S. M. Hamilla, K. M. Stroka, and H. Aranda-Espinoza, “VE-cadherin-independent cancer cell incorporation into the vascular endothelium precedes transmigration.,” *PLoS One*, vol. 9, no. 10, p. e109748, 2014, doi: 10.1371/journal.pone.0109748.

[169] K. M. Stroka, H. N. Hayenga, and H. Aranda-Espinoza, “Human Neutrophil Cytoskeletal Dynamics and Contractility Actively Contribute to Trans-Endothelial Migration,” *PLoS One*, vol. 8, no. 4, p. e61377, 2013, doi: 10.1371/journal.pone.0061377.

[170] M. A. Pranda, K. M. Gray, A. J. L. DeCastro, G. M. Dawson, J. W. Jung, and K. M. Stroka, “Tumor Cell Mechanosensing During Incorporation into the Brain Microvascular Endothelium,” *Cell. Mol. Bioeng.*, vol. 12, no. 5, pp. 455–480, 2019, doi: 10.1007/s12195-019-00591-2.

[171] T. M. Farooque, C. H. Camp, C. K. Tison, G. Kumar, S. H. Parekh, and C. G. Simon, “Measuring stem cell dimensionality in tissue scaffolds,” *Biomaterials*, vol. 35, no. 9, pp. 2558–2567, Mar. 2014, doi: 10.1016/j.biomaterials.2013.12.092.

[172] M. T. Doolin, T. S. Ornstein, and K. M. Stroka, “Nuclear Deformation in Response to Mechanical Confinement is Cell Type Dependent,” *Cells*, vol. 8, no. 5, p. 427, May 2019, doi: 10.3390/cells8050427.

[173] R. A. Moriarty and K. M. Stroka, “Physical confinement alters sarcoma cell cycle progression and division,” *Cell Cycle*, vol. 17, no. 19–20, pp. 2360–2373, Oct. 2018, doi: 10.1080/15384101.2018.1533776.

[174] C. L. Gilchrist, D. S. Ruch, D. Little, and F. Guilak, “Micro-scale and meso-scale architectural cues cooperate and compete to direct aligned tissue formation,” *Biomaterials*, vol. 35, no. 38, pp. 10015–10024, Dec. 2014, doi: 10.1016/j.biomaterials.2014.08.047.

[175] K. A. Kyburz and K. S. Anseth, “Three-dimensional hMSC motility within peptide-functionalized PEG-based hydrogels of varying adhesivity and crosslinking density,” *Acta Biomater.*, vol. 9, no. 5, pp. 6381–6392, May 2013, doi: 10.1016/j.actbio.2013.01.026.

[176] E. K. Paluch, I. M. Aspalter, and M. Sixt, “Focal Adhesion–Independent Cell Migration,” *Annu. Rev. Cell Dev. Biol.*, vol. 32, no. 1, pp. 469–490, Oct. 2016, doi: 10.1146/annurev-cellbio-111315-125341.

[177] R. J. Petrie and K. M. Yamada, “Fibroblasts Lead the Way: A Unified View of 3D Cell Motility,” *Trends Cell Biol.*, vol. 25, no. 11, pp. 666–674, Nov. 2015, doi: 10.1016/j.tcb.2015.07.013.

[178] R. J. Petrie and K. M. Yamada, “Multiple mechanisms of 3D migration: the origins of plasticity,” *Curr. Opin. Cell Biol.*, vol. 42, pp. 7–12, Oct. 2016, doi: 10.1016/j.ceb.2016.03.025.

[179] A. J. S. Ribeiro, P. Khanna, A. Sukumar, C. Dong, and K. N. Dahl, “Nuclear Stiffening Inhibits Migration of Invasive Melanoma Cells,” *Cell. Mol. Bioeng.*, vol. 7, no. 4, pp. 544–551, Dec. 2014, doi: 10.1007/s12195-014-0358-3.

[180] S. R. Peyton *et al.*, “Marrow-Derived stem cell motility in 3D synthetic scaffold is governed by geometry along with adhesivity and stiffness,” *Biotechnol. Bioeng.*, vol. 108, no. 5, pp. 1181–1193, 2011, doi: 10.1002/bit.23027.

[181] R. J. Mills, J. E. Frith, J. E. Hudson, and J. J. Cooper-White, “Effect of Geometric Challenges on Cell Migration,” *Tissue Eng. Part C Methods*, vol. 17, no. 10, pp. 999–1010, Oct. 2011, doi: 10.1089/ten.tec.2011.0138.

[182] N. Huebsch *et al.*, “Matrix elasticity of void-forming hydrogels controls transplanted-stem-cell-mediated bone formation,” *Nat. Mater.*, vol. 14, no. 12, pp. 1269–1277, Dec. 2015, doi: 10.1038/nmat4407.

[183] Y. J. Liu *et al.*, “Confinement and low adhesion induce fast amoeboid migration of slow mesenchymal cells,” *Cell*, vol. 160, no. 4, pp. 659–672, 2015, doi: 10.1016/j.cell.2015.01.007.

[184] S. S. Ho, A. T. Keown, B. Addison, and J. K. Leach, “Cell Migration and Bone Formation from Mesenchymal Stem Cell Spheroids in Alginate Hydrogels Are Regulated by Adhesive Ligand Density,” *Biomacromolecules*, vol. 18, no. 12, pp. 4331–4340, Dec. 2017, doi: 10.1021/acs.biomac.7b01366.

[185] K. M. Schultz, K. A. Kyburz, and K. S. Anseth, “Measuring dynamic cell–material interactions and remodeling during 3D human mesenchymal stem cell migration in hydrogels,” *Proc. Natl. Acad. Sci.*, vol. 112, no. 29, pp. E3757–E3764, 2015, doi: 10.1073/pnas.1511304112.

[186] P. Neth, M. Ciccarella, V. Egea, J. Hoelters, M. Jochum, and C. Ries, “Wnt Signaling Regulates the Invasion Capacity of Human Mesenchymal Stem Cells,” *Stem Cells*, vol. 24, no. 8, pp. 1892–1903, Aug. 2006, doi: 10.1634/stemcells.2005-0503.

[187] A. Ray, Z. M. Slama, R. K. Morford, S. A. Madden, and P. P. Provenzano, “Enhanced Directional Migration of Cancer Stem Cells in 3D Aligned Collagen

Matrices," *Biophys. J.*, vol. 112, no. 5, pp. 1023–1036, Mar. 2017, doi: 10.1016/j.bpj.2017.01.007.

[188] A. Guzman, M. J. Ziperstein, and L. J. Kaufman, "The effect of fibrillar matrix architecture on tumor cell invasion of physically challenging environments," *Biomaterials*, vol. 35, no. 25, pp. 6954–6963, Aug. 2014, doi: 10.1016/j.biomaterials.2014.04.086.

[189] A. Haeger, M. Krause, K. Wolf, and P. Friedl, "Cell jamming: collective invasion of mesenchymal tumor cells imposed by tissue confinement.," *Biochim. Biophys. Acta*, vol. 1840, no. 8, pp. 2386–95, Aug. 2014, doi: 10.1016/j.bbagen.2014.03.020.

[190] S. Kumar, R. Kulkarni, and S. Sen, "Cell motility and ECM proteolysis regulate tumor growth and tumor relapse by altering the fraction of cancer stem cells and their spatial scattering," *Phys. Biol.*, vol. 13, no. 3, p. 036001, Apr. 2016, doi: 10.1088/1478-3975/13/3/036001.

[191] A. Matsiko, J. P. Gleeson, and F. J. O'Brien, "Scaffold Mean Pore Size Influences Mesenchymal Stem Cell Chondrogenic Differentiation and Matrix Deposition," *Tissue Eng. Part A*, vol. 21, no. 3–4, pp. 486–497, Feb. 2015, doi: 10.1089/ten.tea.2013.0545.

[192] Y.-P. Lo, Y.-S. Liu, M. G. Rimando, J. H.-C. Ho, K. Lin, and O. K. Lee, "Three-dimensional spherical spatial boundary conditions differentially regulate osteogenic differentiation of mesenchymal stromal cells," *Sci. Rep.*, vol. 6, no. 1, p. 21253, Aug. 2016, doi: 10.1038/srep21253.

[193] K. M. McAndrews, M. J. Kim, T. Y. Lam, D. J. McGrail, and M. R. Dawson,

"Architectural and Mechanical Cues Direct Mesenchymal Stem Cell Interactions with Crosslinked Gelatin Scaffolds," *Tissue Eng. Part A*, vol. 20, no. 23–24, pp. 3252–3260, Dec. 2014, doi: 10.1089/ten.tea.2013.0753.

[194] V. Serpooshan *et al.*, "Reduced hydraulic permeability of three-dimensional collagen scaffolds attenuates gel contraction and promotes the growth and differentiation of mesenchymal stem cells," *Acta Biomater.*, vol. 6, no. 10, pp. 3978–3987, Oct. 2010, doi: 10.1016/j.actbio.2010.04.028.

[195] W. Wang *et al.*, "3D spheroid culture system on micropatterned substrates for improved differentiation efficiency of multipotent mesenchymal stem cells," *Biomaterials*, vol. 30, no. 14, pp. 2705–2715, May 2009, doi: 10.1016/j.biomaterials.2009.01.030.

[196] N. Tanaka, T. Yamashita, A. Sato, V. Vogel, and Y. Tanaka, "Simple agarose micro-confinement array and machine-learning-based classification for analyzing the patterned differentiation of mesenchymal stem cells," *PLoS One*, vol. 12, no. 4, p. e0173647, Apr. 2017, doi: 10.1371/journal.pone.0173647.

[197] M. Caiazzo, Y. Okawa, A. Ranga, A. Piersigilli, Y. Tabata, and M. P. Lutolf, "Defined three-dimensional microenvironments boost induction of pluripotency," *Nat. Mater.*, vol. 15, no. 3, pp. 344–352, Mar. 2016, doi: 10.1038/nmat4536.

[198] C. Luni *et al.*, "High-efficiency cellular reprogramming with microfluidics," *Nat. Methods*, vol. 13, no. 5, pp. 446–452, 2016, doi: 10.1038/nmeth.3832.

[199] B. Roy *et al.*, "Laterally confined growth of cells induces nuclear reprogramming in the absence of exogenous biochemical factors," *Proc. Natl.*

Acad. Sci., vol. 115, no. 21, pp. E4741–E4750, May 2018, doi: 10.1073/pnas.1714770115.

[200] J. Cmielova *et al.*, "Gamma radiation induces senescence in human adult mesenchymal stem cells from bone marrow and periodontal ligaments," *Int. J. Radiat. Biol.*, vol. 88, no. 5, pp. 393–404, May 2012, doi: 10.3109/09553002.2012.666001.

[201] G. G. Giobbe *et al.*, "Confined 3D microenvironment regulates early differentiation in human pluripotent stem cells," *Biotechnol. Bioeng.*, vol. 109, no. 12, pp. 3119–3132, Dec. 2012, doi: 10.1002/bit.24571.

[202] E. Redondo-Castro, C. J. Cunningham, J. Miller, H. Brown, S. M. Allan, and E. Pinteaux, "Changes in the secretome of tri-dimensional spheroid-cultured human mesenchymal stem cells in vitro by interleukin-1 priming," *Stem Cell Res. Ther.*, vol. 9, no. 1, p. 11, Dec. 2018, doi: 10.1186/s13287-017-0753-5.

[203] M. De Lisio, T. Jensen, R. A. Sukiennik, H. D. Huntsman, and M. D. Boppart, "Substrate and strain alter the muscle-derived mesenchymal stem cell secretome to promote myogenesis," *Stem Cell Res. Ther.*, vol. 5, no. 3, pp. 1–12, 2014, doi: 10.1186/scrt463.

[204] S.-Y. Kim *et al.*, "Mesenchymal stem cell-conditioned media recovers lung fibroblasts from cigarette smoke-induced damage," *Am. J. Physiol. - Lung Cell. Mol. Physiol.*, vol. 302, no. 9, pp. L891–L908, 2012, doi: 10.1152/ajplung.00288.2011.

[205] K. E. Hostettler *et al.*, "Multipotent mesenchymal stem cells in lung fibrosis," *PLoS One*, vol. 12, no. 8, pp. 1–22, 2017, doi: 10.1371/journal.pone.0181946.

[206] Y. Petrenko, E. Syková, and Š. Kubinová, “The therapeutic potential of three-dimensional multipotent mesenchymal stromal cell spheroids,” *Stem Cell Res. Ther.*, vol. 8, no. 1, p. 94, 2017, doi: 10.1186/s13287-017-0558-6.

[207] M. Carmo-Fonseca, “The Contribution of Nuclear Compartmentalization to Gene Regulation,” *Cell*, vol. 108, no. 4, pp. 513–521, Feb. 2002, doi: 10.1016/S0092-8674(02)00650-5.

[208] A. Elosegui-Artola *et al.*, “Force Triggers YAP Nuclear Entry by Regulating Transport across Nuclear Pores,” *Cell*, vol. 171, no. 6, pp. 1397–1410, Nov. 2017, doi: 10.1016/j.cell.2017.10.008.

[209] X. Liu, R. Liu, Y. Gu, and J. Ding, “Nonmonotonic Self-Deformation of Cell Nuclei on Topological Surfaces with Micropillar Array,” *ACS Appl. Mater. Interfaces*, vol. 9, no. 22, pp. 18521–18530, Jun. 2017, doi: 10.1021/acsami.7b04027.

[210] J. Zhang *et al.*, “Enhanced multi-lineage differentiation of human mesenchymal stem/stromal cells within poly(N -isopropylacrylamide-acrylic acid) microgel-formed three-dimensional constructs,” *J. Mater. Chem. B*, vol. 6, no. 12, pp. 1799–1814, 2018, doi: 10.1039/C8TB00376A.

[211] D. Y. Ko, M. Patel, H. J. Lee, and B. Jeong, “Coordinating Thermogel for Stem Cell Spheroids and Their Cyto-Effectiveness,” *Adv. Funct. Mater.*, vol. 28, no. 7, p. 1706286, Feb. 2018, doi: 10.1002/adfm.201706286.

[212] B.-N. B. Nguyen, R. A. Moriarty, T. Kamalitdinov, J. M. Etheridge, and J. P. Fisher, “Collagen hydrogel scaffold promotes mesenchymal stem cell and endothelial cell coculture for bone tissue engineering,” *J. Biomed. Mater. Res.*

Part A, vol. 105, no. 4, pp. 1123–1131, Apr. 2017, doi: 10.1002/jbm.a.36008.

[213] A. Dolatshahi-Pirouz *et al.*, "A combinatorial cell-laden gel microarray for inducing osteogenic differentiation of human mesenchymal stem cells," *Sci. Rep.*, vol. 4, no. 1, p. 3896, May 2015, doi: 10.1038/srep03896.

[214] M. K. Nguyen, O. Jeon, M. D. Krebs, D. Schapira, and E. Alsberg, "Sustained localized presentation of RNA interfering molecules from in situ forming hydrogels to guide stem cell osteogenic differentiation," *Biomaterials*, vol. 35, no. 24, pp. 6278–6286, 2014, doi: 10.1016/j.biomaterials.2014.04.048.

[215] J. P. Winer, P. a Janmey, M. E. McCormick, and M. Funaki, "Bone marrow-derived human mesenchymal stem cells become quiescent on soft substrates but remain responsive to chemical or mechanical stimuli.," *Tissue Eng. Part A*, vol. 15, no. 1, pp. 147–54, 2009, doi: 10.1089/ten.tea.2007.0388.

[216] D. B. Patel, K. M. Gray, Y. Santharam, T. Lamichhine, K. M. Stroka, and S. M. Jay, "Impact of Cell Culture Parameters on Production and Vascularization Bioactivity of Mesenchymal Stem Cell-Derived Extracellular Vesicles," *Bioeng. Transl. Med.*, vol. In Press, no. May, pp. 170–179, 2017, doi: 10.1002/btm2.10065.

[217] Y.-C. Chang, P. Nalbant, J. Birkenfeld, Z.-F. Chang, and G. M. Bokoch, "GEF-H1 Couples Nocodazole-induced Microtubule Disassembly to Cell Contractility via RhoA," *Mol. Biol. Cell*, vol. 19, no. 5, pp. 2147–2153, May 2008, doi: 10.1091/mbc.E07-12-1269.

[218] A. A. Birukova *et al.*, "Microtubule disassembly induces cytoskeletal remodeling and lung vascular barrier dysfunction: Role of Rho-dependent

mechanisms,” *J. Cell. Physiol.*, vol. 201, no. 1, pp. 55–70, 2004, doi: 10.1002/jcp.20055.

[219] M. Krendel, F. T. Zenke, and G. M. Bokoch, “Nucleotide exchange factor GEF-H1 mediates cross-talk between microtubules and the actin cytoskeleton.,” *Nat. Cell Biol.*, vol. 4, no. 4, pp. 294–301, 2002, doi: 10.1038/ncb773.

[220] A. Rape, W. -h. Guo, and Y. -l. Wang, “Microtubule depolymerization induces traction force increase through two distinct pathways,” *J. Cell Sci.*, vol. 124, no. 24, pp. 4233–4240, 2011, doi: 10.1242/jcs.090563.

[221] A. M. Pasapera, I. C. Schneider, E. Rericha, D. D. Schlaepfer, and C. M. Waterman, “Myosin II activity regulates vinculin recruitment to focal adhesions through FAK-mediated paxillin phosphorylation,” *J. Cell Biol.*, vol. 188, no. 6, pp. 877–890, 2010, doi: 10.1083/jcb.200906012.

[222] K. M. Stroka and K. Konstantopoulos, “Physical Biology in Cancer. 4. Physical cues guide tumor cell adhesion and migration,” *AJP Cell Physiol.*, vol. 306, no. 2, pp. C98–C109, 2014, doi: 10.1152/ajpcell.00289.2013.

[223] A. Banfi, A. Muraglia, B. Dozin, M. Mastrogiacomo, R. Cancedda, and R. Quarto, “Proliferation kinetics and differentiation potential of ex vivo expanded human bone marrow stromal cells,” *Exp. Hematol.*, vol. 28, no. 6, pp. 707–715, 2000, doi: 10.1016/S0301-472X(00)00160-0.

[224] J. M. Maloney *et al.*, “Mesenchymal stem cell mechanics from the attached to the suspended state,” *Biophys. J.*, vol. 99, no. 8, pp. 2479–2487, 2010, doi: 10.1016/j.bpj.2010.08.052.

[225] S. Geißler *et al.*, “Functional Comparison of Chronological and In Vitro Aging:

Differential Role of the Cytoskeleton and Mitochondria in Mesenchymal Stromal Cells," *PLoS One*, vol. 7, no. 12, 2012, doi: 10.1371/journal.pone.0052700.

[226] C. M. Kraning-Rush, S. P. Carey, J. P. Califano, B. N. Smith, and C. A. Reinhart-King, "The role of the cytoskeleton in cellular force generation in 2D and 3D environments.," *Phys. Biol.*, vol. 8, no. 1, p. 015009, 2011, doi: 10.1088/1478-3975/8/1/015009.

[227] H. Polioudaki, M.-C. Kastrinaki, H. A. Papadaki, and P. A. Theodoropoulos, "Microtubule-interacting drugs induce moderate and reversible damage to human bone marrow mesenchymal stem cells," *Cell Prolif*, vol. 42, pp. 434–447, 2009, doi: 10.1111/j.1365-2184.2009.00607.x.

[228] A. L. Blajeski, V. A. Phan, T. J. Kottke, and S. H. Kaufmann, "G(1) and G(2) cell-cycle arrest following microtubule depolymerization in human breast cancer cells.," *J. Clin. Invest.*, vol. 110, no. 1, pp. 91–9, Jul. 2002, doi: 10.1172/JCI13275.

[229] J. C. Martens and M. Radmacher, "Softening of the actin cytoskeleton by inhibition of myosin II," *Pflugers Arch. Eur. J. Physiol.*, vol. 456, no. 1, pp. 95–100, 2008, doi: 10.1007/s00424-007-0419-8.

[230] B. G. Jaganathan *et al.*, "Rho inhibition induces migration of mesenchymal stromal cells.," *Stem Cells*, vol. 25, no. 8, pp. 1966–1974, 2007, doi: 2007-0167 [pii]\r10.1634/stemcells.2007-0167 [doi].

[231] S. Liu, R. H. Goldstein, E. M. Scepansky, and M. Rosenblatt, "Inhibition of Rho-Associated Kinase Signaling Prevents Breast Cancer Metastasis to Human

Bone," *Cancer Res.*, vol. 69, no. 22, 2009, Accessed: Sep. 03, 2017. [Online]. Available: http://cancerres.aacrjournals.org/content/69/22/8742.long.

[232] J. Lane, T. A. Martin, G. Watkins, R. E. Mansel, and W. G. Jiang, *The expression and prognostic value of ROCK I and ROCK II and their role in human breast cancer*, vol. 33, no. 3. University of Crete, Faculty of Medicine, Laboratory of Clinical Virology, 2008.

[233] M. Nagayama, H. Haga, M. Takahashi, T. Saitoh, and K. Kawabata, "Contribution of cellular contractility to spatial and temporal variations in cellular stiffness," *Exp. Cell Res.*, vol. 300, no. 2, pp. 396–405, 2004, doi: 10.1016/j.yexcr.2004.07.034.

[234] M. A. Wozniak, R. Desai, P. A. Solski, C. J. Der, and P. J. Keely, "ROCK-generated contractility regulates breast epithelial cell differentiation in response to the physical properties of a three-dimensional collagen matrix," *J Cell Biol*, vol. 163, no. 3, pp. 583–595, 2003, doi: 10.1083/jcb.200305010.

[235] D. Ingber, "Mechanobiology and diseases of mechanotransduction," *Ann. Med.*, vol. 35, no. 8, pp. 564–577, 2003, doi: 10.1080/07853890310016333.

[236] I. L. Ivanovska, J.-W. Shin, J. Swift, and D. E. Discher, "Stem cell mechanobiology: diverse lessons from bone marrow.," *Trends Cell Biol.*, vol. 25, no. 9, pp. 523–532, 2015, doi: 10.1016/j.tcb.2015.04.003.

[237] P. Isermann and J. Lammerding, "Consequences of a tight squeeze: Nuclear envelope rupture and repair," *Nucleus*, vol. 8, no. 3, pp. 268–274, 2017, doi: 10.1080/19491034.2017.1292191.

[238] A. Tajik *et al.*, "Transcription upregulation via force-induced direct stretching

of chromatin," *Nat. Mater.*, vol. 15, no. 12, pp. 1287–1296, 2016, doi: 10.1038/nmat4729.

[239] D. Tremblay, L. Andrzejewski, A. Leclerc, and A. E. Pelling, "Actin and microtubules play distinct roles in governing the anisotropic deformation of cell nuclei in response to substrate strain," *Cytoskeleton*, vol. 70, no. 12, pp. 837–848, 2013, doi: 10.1002/cm.21148.

[240] C. Guilluy *et al.*, "Isolated nuclei adapt to force and reveal a mechanotransduction pathway in the nucleus," *Nat. Cell Biol.*, vol. 16, no. 4, pp. 376–381, 2014, doi: 10.1038/ncb2927.

[241] B. Koch, S. Sanchez, C. K. Schmidt, A. Swiersy, S. P. Jackson, and O. G. Schmidt, "Confinement and Deformation of Single Cells and Their Nuclei Inside Size-Adapted Microtubes," *Adv. Healthc. Mater.*, vol. 3, no. 11, pp. 1753–1758, Nov. 2014, doi: 10.1002/adhm.201300678.

[242] S. Neelam *et al.*, "Direct force probe reveals the mechanics of nuclear homeostasis in the mammalian cell," *Proc. Natl. Acad. Sci.*, vol. 112, no. 18, pp. 5720–5725, 2015, doi: 10.1073/pnas.1502111112.

[243] A. Mazumder and G. V. Shivashankar, "Emergence of a prestressed eukaryotic nucleus during cellular differentiation and development," *J. R. Soc. Interface*, vol. 7, no. SUPPL. 3, 2010, doi: 10.1098/rsif.2010.0039.focus.

[244] H. V. Prentice-Mott, C.-H. Chang, L. Mahadevan, T. J. Mitchison, D. Irimia, and J. V. Shah, "Biased migration of confined neutrophil-like cells in asymmetric hydraulic environments," *Proc. Natl. Acad. Sci.*, vol. 110, no. 52, pp. 21006–21011, Dec. 2013, doi: 10.1073/pnas.1317441110.

[245] J. Swift *et al.*, “Nuclear Lamin-A Scales with Tissue Stiffness and Enhances Matrix-Directed Differentiation - supplement,” pp. 1–36, 2013, doi: 10.1126/science.1240104.

[246] D.-H. Kim, B. Li, F. Si, J. M. Phillip, D. Wirtz, and S. X. Sun, “Volume regulation and shape bifurcation in the cell nucleus,” *J. Cell Sci.*, vol. 129, no. 2, pp. 457–457, 2016, doi: 10.1242/jcs.185173.

[247] A. M. Greiner *et al.*, “Cell type-specific adaptation of cellular and nuclear volume in micro-engineered 3D environments,” *Biomaterials*, vol. 69, pp. 121–132, 2015, doi: 10.1016/j.biomaterials.2015.08.016.

[248] M. Guo *et al.*, “Cell volume change through water efflux impacts cell stiffness and stem cell fate,” *Proc. Natl. Acad. Sci.*, vol. 114, no. 41, pp. e8618–e8627, Sep. 2017, doi: 10.1073/pnas.1705179114.

[249] Z. Tariq *et al.*, “Lamin A and microtubules collaborate to maintain nuclear morphology,” *Nucleus*, vol. 8, no. 4, pp. 433–446, 2017, doi: 10.1080/19491034.2017.1320460.

[250] F.-Y. Chu, S. C. Haley, and A. Zidovska, “On the origin of shape fluctuations of the cell nucleus,” *Proc. Natl. Acad. Sci.*, vol. 114, no. 39, pp. 10338–10343, Sep. 2017, doi: 10.1073/pnas.1702226114.

[251] Z. Al-Rekabi, K. Haase, and A. E. Pelling, “Microtubules mediate changes in membrane cortical elasticity during contractile activation,” *Exp. Cell Res.*, vol. 322, no. 1, pp. 21–29, 2014, doi: 10.1016/j.yexcr.2013.12.027.

[252] A. Buxboim *et al.*, “Matrix Elasticity Regulates Lamin-A,C Phosphorylation and Turnover with Feedback to Actomyosin,” *Curr. Biol.*, vol. 24, no. 16, pp.

1909–1917, Aug. 2014, doi: 10.1016/j.cub.2014.07.001.

[253] R. Zhu, S. Antoku, and G. G. Gundersen, “Centrifugal Displacement of Nuclei Reveals Multiple LINC Complex Mechanisms for Homeostatic Nuclear Positioning,” *Curr. Biol.*, vol. 27, no. 20, pp. 3097-3110.e5, 2017, doi: 10.1016/j.cub.2017.08.073.

[254] B. Weigelin, G.-J. Bakker, and P. Friedl, “Intravital third harmonic generation microscopy of collective melanoma cell invasion,” *IntraVital*, vol. 1, no. 1, pp. 32–43, Jul. 2012, doi: 10.4161/intv.21223.

[255] K. I. Hulkower and R. L. Herber, “Cell migration and invasion assays as tools for drug discovery,” *Pharmaceutics*, vol. 3, no. 1, pp. 107–124, 2011, doi: 10.3390/pharmaceutics3010107.

[256] P. Roca-Cusachs, V. Conte, and X. Trepat, “Quantifying forces in cell biology,” *Nat. Cell Biol.*, vol. 19, no. 7, pp. 742–751, 2017, doi: 10.1038/ncb3564.

[257] M. Ghibaudo, J. M. Di Meglio, P. Hersen, and B. Ladoux, “Mechanics of cell spreading within 3D-micropatterned environments,” *Lab Chip*, vol. 11, no. 5, pp. 805–812, 2011, doi: 10.1039/c0lc00221f.

[258] F. Badique *et al.*, “Directing nuclear deformation on micropillared surfaces by substrate geometry and cytoskeleton organization,” *Biomaterials*, vol. 34, no. 12, pp. 2991–3001, 2013, doi: 10.1016/j.biomaterials.2013.01.018.

[259] Z. Li *et al.*, “Differential regulation of stiffness, topography, and dimension of substrates in rat mesenchymal stem cells,” *Biomaterials*, vol. 34, no. 31, pp. 7616–7625, 2013, doi: 10.1016/j.biomaterials.2013.06.059.

[260] N. J. Sniadecki *et al.*, “Magnetic microposts as an approach to apply forces to

living cells," *Proc. Natl. Acad. Sci.*, vol. 104, no. 37, pp. 14553–14558, 2007, doi: 10.1073/pnas.0611613104.

[261] O. du Roure *et al.*, "Force mapping in epithelial cell migration," *Proc. Natl. Acad. Sci.*, vol. 102, no. 7, pp. 2390–2395, 2005, doi: 10.1073/pnas.0408482102.

[262] J. L. Tan, J. Tien, D. M. Pirone, D. S. Gray, K. Bhadriraju, and C. S. Chen, "Cells lying on a bed of microneedles: An approach to isolate mechanical force," *Proc. Natl. Acad. Sci.*, vol. 100, no. 4, pp. 1484–1489, Feb. 2003, doi: 10.1073/pnas.0235407100.

[263] S. Lee, J. Hong, and J. Lee, "Cell motility regulation on a stepped micro pillar array device (SMPAD) with a discrete stiffness gradient," *Soft Matter*, vol. 12, no. 8, pp. 2325–2333, 2016, doi: 10.1039/c5sm00649j.

[264] I. D. Johnston, D. K. McCluskey, C. K. L. Tan, and M. C. Tracey, "Mechanical characterization of bulk Sylgard 184 for microfluidics and microengineering," *J. Micromechanics Microengineering*, vol. 24, no. 3, p. 035017, 2014, doi: 10.1088/0960-1317/24/3/035017.

[265] I. Schoen, W. Hu, E. Klitzsch, and V. Vogel, "Contribution of Substrate Warping to Pillar Deflection," *Nano Lett.*, vol. 10, no. 5, pp. 1823–1830, 2011, doi: 10.1021/nl100533c.Probing.

[266] J. Fu *et al.*, "Mechanical regulation of cell function with geometrically modulated elastomeric substrates," *Nat. Methods*, vol. 7, no. 9, pp. 733–736, Sep. 2010, doi: 10.1038/nmeth.1487.

[267] T. W. Chang, C. H. Wu, J. J. Liau, and C. K. Cheng, "The effect of graft

strength on knee laxity and the in-situ forces of grafts after posterior cruciate ligament reconstruction," *IFMBE Proc.*, vol. 25, no. 4, pp. 809–812, 2009, doi: 10.1007/978-3-642-03882-2-215.

[268] R. A. Marklein, J. L. Lo Surdo, I. H. Bellayr, S. A. Godil, R. K. Puri, and S. R. Bauer, "High Content Imaging of Early Morphological Signatures Predicts Long Term Mineralization Capacity of Human Mesenchymal Stem Cells upon Osteogenic Induction," *Stem Cells*, vol. 34, no. 4, pp. 935–947, 2016, doi: 10.1002/stem.2322.

[269] M. W. Klinker, R. A. Marklein, J. L. Lo Surdo, C.-H. Wei, and S. R. Bauer, "Morphological features of IFN-γ–stimulated mesenchymal stromal cells predict overall immunosuppressive capacity," *Proc. Natl. Acad. Sci.*, vol. 114, no. 13, pp. E2598–E2607, 2017, doi: 10.1073/pnas.1617933114.

[270] D. Arcizet *et al.*, "Contact-controlled amoeboid motility induces dynamic cell trapping in 3D-microstructured surfaces," *Soft Matter*, vol. 8, no. 5, pp. 1473–1481, 2012, doi: 10.1039/c1sm05615h.

[271] R. A. Redden and E. J. Doolin, "Complementary roles of microtubules and microfilaments in the lung fibroblast-mediated contraction of collagen gels: Dynamics and the influence of cell density," *Vitr. Cell. Dev. Biol. - Anim.*, vol. 42, no. 3–4, pp. 70–74, 2006, doi: 10.1290/0509065.1.

[272] I. E. Fernandez and O. Eickelberg, "The impact of TGF-β on lung fibrosis: From targeting to biomarkers," *Proc. Am. Thorac. Soc.*, vol. 9, no. 3, pp. 111–116, 2012, doi: 10.1513/pats.201203-023AW.

[273] R. Kaarteenaho-Wiik, P. Pääkkö, and R. Sormunen, "Ultrastructural features of

lung fibroblast differentiation into myofibroblasts," *Ultrastruct. Pathol.*, vol. 33, no. 1, pp. 6–15, 2009, doi: 10.1080/01913120802608430.

[274] P. Pittet, K. Lee, A. J. Kulik, J. J. Meister, and B. Hinz, "Fibrogenic fibroblasts increase intercellular adhesion strength by reinforcing individual OB-cadherin bonds," *J. Cell Sci.*, vol. 121, no. 6, pp. 877–886, 2008, doi: 10.1242/jcs.024877.

[275] S. K. Masur, H. S. Dewal, T. T. Dinh, I. Erenburg, and S. Petridou, "Myofibroblasts differentiate from fibroblasts when plated at low density," *Proc. Natl. Acad. Sci. U. S. A.*, vol. 93, no. 9, pp. 4219–4223, 1996, doi: 10.1073/pnas.93.9.4219.

[276] U. Baranyi *et al.*, "Primary Human Fibroblasts in Culture Switch to a Myofibroblast-Like Phenotype Independently of TGF Beta," *Cells*, vol. 8, no. 7, p. 721, 2019, doi: 10.3390/cells8070721.

[277] M. Michalik *et al.*, "Transition of asthmatic bronchial fibroblasts to myofibroblasts is inhibited by cell-cell contacts," *Respir. Med.*, vol. 105, no. 10, pp. 1467–1475, 2011, doi: 10.1016/j.rmed.2011.04.009.

[278] H. P. Ehrlich, G. M. Allison, and M. Leggett, "The myofibroblast, cadherin, α smooth muscle actin and the collagen effect," *Cell Biochem. Funct.*, vol. 24, no. 1, pp. 63–70, 2006, doi: 10.1002/cbf.1188.

[279] B. Hinz, P. Pittet, J. Smith-Clerc, C. Chaponnier, and J.-J. Meister, "Myofibroblast Development Is Characterized by Specific Cell-Cell Adherens Junctions," *Mol. Biol. Cell*, vol. 15, no. 9, pp. 4310–4320, Sep. 2004, doi: 10.1091/mbc.e04-05-0386.

[280] M. Black *et al.*, “FOXF1 Inhibits Pulmonary Fibrosis by Preventing CDH2-CDH11 Cadherin Switch in Myofibroblasts,” *Cell Rep.*, vol. 23, no. 2, pp. 442–458, 2018, doi: 10.1016/j.celrep.2018.03.067.

[281] L. Follonier, S. Schaub, J. J. Meister, and B. Hinz, “Myofibroblast communication is controlled by intercellular mechanical coupling,” *J. Cell Sci.*, vol. 121, no. 20, pp. 3305–3316, 2008, doi: 10.1242/jcs.024521.

[282] P. D. Arora and C. A. G. McCulloch, “The deletion of transforming growth factor-β-induced myofibroblasts depends on growth conditions and actin organization,” *Am. J. Pathol.*, vol. 155, no. 6, pp. 2087–2099, 1999, doi: 10.1016/S0002-9440(10)65527-7.

[283] P. Kollmannsberger, C. M. Bidan, J. W. C. Dunlop, P. Fratzl, and V. Vogel, “Tensile forces drive a reversible fibroblast-to-myofibroblast transition during tissue growth in engineered clefts,” *Sci. Adv.*, vol. 4, no. 1, p. eaao4881, Jan. 2018, doi: 10.1126/sciadv.aao4881.

[284] J. L. Balestrini, S. Chaudhry, V. Sarrazy, A. Koehler, and B. Hinz, “The mechanical memory of lung myofibroblasts,” *Integr. Biol.*, vol. 4, no. 4, pp. 410–421, 2012, doi: 10.1039/c2ib00149g.

[285] C. Ballestrem and B. Geiger, “Application of microscope-based FRET to study molecular interactions in focal adhesions of live cells.,” *Methods Mol. Biol.*, vol. 294, no. 1, pp. 321–334, 2005, doi: 1-59259-860-9:321 [pii].

[286] A. H. Mekhdjian *et al.*, “Integrin-mediated traction force enhances paxillin molecular associations and adhesion dynamics that increase the invasiveness of tumor cells into a three-dimensional extracellular matrix,” *Mol. Biol. Cell*, vol.

28, no. 11, pp. 1467–1488, 2017, doi: 10.1091/mbc.E16-09-0654.

[287] J. Swift *et al.*, “Nuclear Lamin-A Scales with Tissue Stiffness and Enhances Matrix-Directed Differentiation,” *Science (80-.).*, vol. 341, no. 6149, pp. 1240104–1240104, Aug. 2013, doi: 10.1126/science.1240104.

[288] S. Bermeo, C. Vidal, H. Zhou, and G. Duque, “Lamin A/C Acts as an Essential Factor in Mesenchymal Stem Cell Differentiation Through the Regulation of the Dynamics of the Wnt/β-Catenin Pathway.,” *J. Cell. Biochem.*, vol. 116, no. 10, pp. 2344–53, 2015, doi: 10.1002/jcb.25185.

[289] R. Akter, D. Rivas, G. Geneau, H. Drissi, and G. Duque, “Effect of Lamin A/C Knockdown on Osteoblast Differentiation and Function,” *J. Bone Miner. Res.*, vol. 24, no. 2, pp. 283–293, Feb. 2009, doi: 10.1359/jbmr.081010.

[290] K. Kulangara, J. Yang, M. Chellappan, Y. Yang, and K. W. Leong, “Nanotopography alters nuclear protein expression, proliferation and differentiation of human mesenchymal stem/stromal cells,” *PLoS One*, vol. 9, no. 12, pp. 1–12, 2014, doi: 10.1371/journal.pone.0114698.

[291] J. Mateos, A. De la Fuente, I. Lesende-Rodriguez, P. Fernández-Pernas, M. C. Arufe, and F. J. Blanco, “Lamin A deregulation in human mesenchymal stem cells promotes an impairment in their chondrogenic potential and imbalance in their response to oxidative stress,” *Stem Cell Res.*, vol. 11, no. 3, pp. 1137–1148, 2013, doi: 10.1016/j.scr.2013.07.004.